TECHNISCHE UNIVERSITÄT MÜNCHEN

PHYSIK-DEPARTMENT
Lehrstuhl für funktionelle Materialien E13
Forschungsneutronenquelle Heinz Maier-Leibnitz (FRM II)

Ion Irradiation Studies of the Origins of Pressurized Water Reactor Fuel Assembly Deformation

Rosmarie Martina Hengstler-Eger

Vollständiger Abdruck der von der Fakultät für Physik der Technischen Universität München zur Erlangung des akademischen Grades eines

Doktors der Naturwissenschaften (Dr. rer. nat.)

genehmigten Dissertation.

Vorsitzender:	Univ.-Prof. Dr. Peter Vogl
Prüfer der Dissertation:	1. Univ.-Prof. Dr. Winfried Petry 2. Univ.-Prof. Dr. Erdmann Spiecker Friedrich-Alexander-Universität Erlangen-Nürnberg

Die Dissertation wurde am 12.09.2012 bei der Technischen Universität München eingereicht und durch die Fakultät für Physik am 15.11.2012 angenommen.

"The energy of the breaking down of the atom is a very poor kind of thing. Anyone who expects a source of power from the transformation of these atoms is talking moonshine."
(E. Rutherford, 1933)

Contents

Abstract

Fuel assembly (FA) deformation in pressurized water reactors (PWR) has become a larger issue during the last years, as a consequence of the continuous increase of FA lifetime, power level and burnup. Unexpectedly high FA growth was observed in some PWR, to an extent that constrained power plant operation. Therefore, a better scientific understanding of the microstructural processes in the FA structural components leading to this deformation is necessary to effectively address the phenomenon. As the FA component with the highest influence on the overall assembly growth are the guide tubes, the focus of this study was on irradiation growth of Zr-based alloys typically used for PWR guide tubes, and specifically on the still unknown effects of hydrogen content and external stress on FA growth.
Zirconium and its alloys show an increase in irradiation induced growth at high neutron fluences ("breakaway growth") which is generally being linked to the formation of vacancy-type <c>-component dislocation loops. Therefore, the characteristics of the irradiation induced microstructure, and particularly these "<c>-loops", were investigated in this work, in the typical guide tube alloys Zircaloy-4 (Zry-4) and M5®. As in-pile neutron irradiation requires irradiation times of several years, leads to high material activation and does not allow independent parameter studies or in-situ observation of damage formation, heavy ion irradiation was used for the neutron damage simulation. The largely applied post-irradiation examination technique was in-situ transmission electron microscopy for the direct observation of the dislocation loop structures, supplemented by positron Doppler broadening spectroscopy for the study of the general vacancy-type defect density.
At first, a feasibility study was conducted which showed that the irradiation induced microstructure forming under heavy ion irradiation at the chosen experimental conditions agreed in all main aspects with the known PWR neutron induced microstructure in Zr-based alloys. The comparison between the observed <c>-loop nucleation threshold in the ion irradiated samples with the known fluence range for the onset of breakaway growth under neutron irradiation confirmed the assumption of <c>-loop nucleation being at the source of the breakaway growth phenomenon. Also, in was shown for the first time that the <c>-loops' linear density increases linearly with the damage level, and the <c>-loop density increase rate was determined. After a set of successful experiments on the influence of temperature, the effect of hydrogen was studied in Zry-4. The hydrogen influence was found to be measurable, but to contain a discontinuous component, with a lower hydrogen content increasing the <c>-loop densities, while a higher hydrogen content led to the opposite effect. It was concluded that further studies on the hydrogen effect are necessary to provide a sufficiently large database for a clear correlation between hydrogen content and macroscopic component growth.
Finally, the effect of external tensile stress at the yield strength level was examined. The stress showed to have a most significant effect on the <c>-loop densities, with a strong dependence on the orientation of the stress direction towards the grains. While <c>-loop formation was comparable to samples without stress in the grain with its c-axis perpendicular to the stress direction, the <c>-loop density decreased with increasing stress component parallel to the c-axis and led to a complete suppression of <c>-loop formation in the grain with its c-axis parallel to the stress direction, despite the high damage level. This clear correlation between external tensile stress and the formation characteristics of basal plane vacancy loops in Zr-based alloys can be explained by the elastic properties of the hexagonal close-packed α-Zr lattice structure. It was proven experimentally for the first time, and the effect is surprising in both its clarity and its magnitude.

Chapter 1

Motivation

In 1934, E. Fermi published experimental results of the bombardment of uranium with neutrons [1]; during the following years, O. Hahn, L. Meitner and F. Strassmann studied the transmutation of uranium during interaction with slow and fast neutrons [2,3]. In February 1939, L. Meitner and O.R. Frisch identified the research results found by them and other research groups in the field as proof of the nuclear fission of uranium by neutron bombardment [4]. Less than four years later, a research group led by E. Fermi created the first controlled nuclear chain reaction in a reactor built underneath the University of Chicago's Stagg Field [5]. After electricity was produced by nuclear fission for the first time, in the nuclear Experimental Breeder Reactor EBR-I in Idaho on December 1951 [6], and after the first nuclear powered submarine, the U.S.S. Nautilus, was launched under president Eisenhower in January 1954 [7], the first nuclear power plant to be connected to the electricity grid was the Russian 5 MW_e APS-1 plant in June 1954 [6]. The first commercial nuclear power reactor worldwide, the 50 MW_e Calder Hall 1 plant, went operational in August 1956 in England [6], to be followed by nuclear power plants in most industrialized countries. By July 2012, 435 nuclear power plants are in operation[1] in 31 countries with a total net electric power of about 370 GW_e; 62 new plants are under construction (see Fig. 1.1) with a total net electric power of 59 GW_e [8]. In addition, 272 research reactors of different types are operational by July 2012, and 17 more are under construction [9].
The 435 operational nuclear power plants consist of 272 pressurized light-water moderated and cooled reactors (PWR), 84 boiling light-water moderated and cooled reactors (BWR), 47 pressurized heavy-water moderated and cooled reactors (PHWR), 15 gas-cooled, graphite-moderated reactors (GGR), 15 light-water cooled, graphite-moderated reactors (LWGR) and 2 fast breeder reactors (FBR) [8]. The focus of this work is on pressurized water reactors of western design.

Due to the widespread application of nuclear power, comprehensive research efforts have been dedicated for decades to study and develop materials for utilization in the nuclear field ("nuclear materials"). Nuclear materials consist of the two large groups of nuclear fuels, like uranium or plutonium dioxide, and nuclear structural materials. Next to stainless steel in various forms, studied for reactor pressure vessel (RPV) applications as well as cladding and other core components, Zirconium-based alloys are the dominating structural materials. In modern light-water moderated and cooled reactors (LWR), most fuel assembly (FA) structural components like fuel rod (FR) cladding, spacer grids, PWR guide tubes and BWR water channels and fuel channels consist of advanced Zr-based alloys.

[1] In consequence of the Fukushima accident, a number of these reactors are in temporary shutdown for safety review; they are listed as plants "in operation".

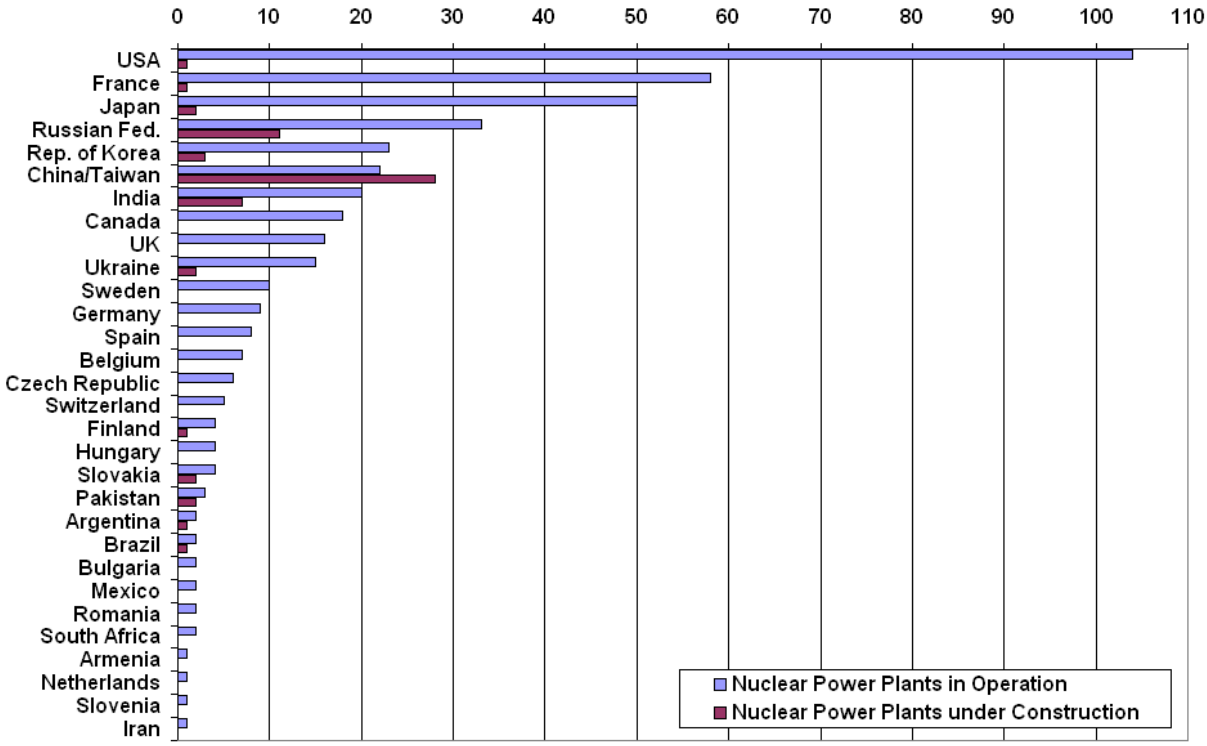

Figure 1.1: Nuclear power plants worldwide [6]

The dominating role of Zr-based alloys as structural material is due to their very advantageous properties with regard to nuclear reactor environments: Reactor-grade Zr in its natural isotopic composition has a low absorption cross section for thermal neutrons in the range of 0.2 barns, and a melting point of above 1800°C, thus providing enough margin to ensure thermal stability as cladding or structural material even in accidental scenarios. These two major qualities are shown in Fig. 1.2, compared to other elements used in industrial applications. Advanced Zr-based alloys possess a high corrosion resistance which allows for component lifetimes in the reactor core of several years, and they show a comparatively low hydrogen pickup. As hydrogen uptake can lead to material embrittlement, and high amounts of hydriding could favor material deformation, a low hydrogen uptake is an important nuclear material property. In addition, Zr-alloys feature sufficient mechanical stability to withstand transport and handling under normal operation as well as to fulfill stability requirements in design basis accidents like earthquakes. Finally, Zr is available in sufficient quantity and at price levels which allow for its industrial use.

A nuclear reactor requires the structural materials to tolerate extreme environmental conditions for many years during operation, particularly the neutron flux. Neutron irradiation of the in-core components produces irradiation defects with a number of consequences; in metals, one of the main effects of these defects is irradiation induced material deformation. Most metals under irradiation are known to experience this deformation, and the phenomenon can be divided into two contributing parts, creep and free growth. Creep is known as the constant volume material deformation process under stress, while growth is defined as the constant volume material defor-

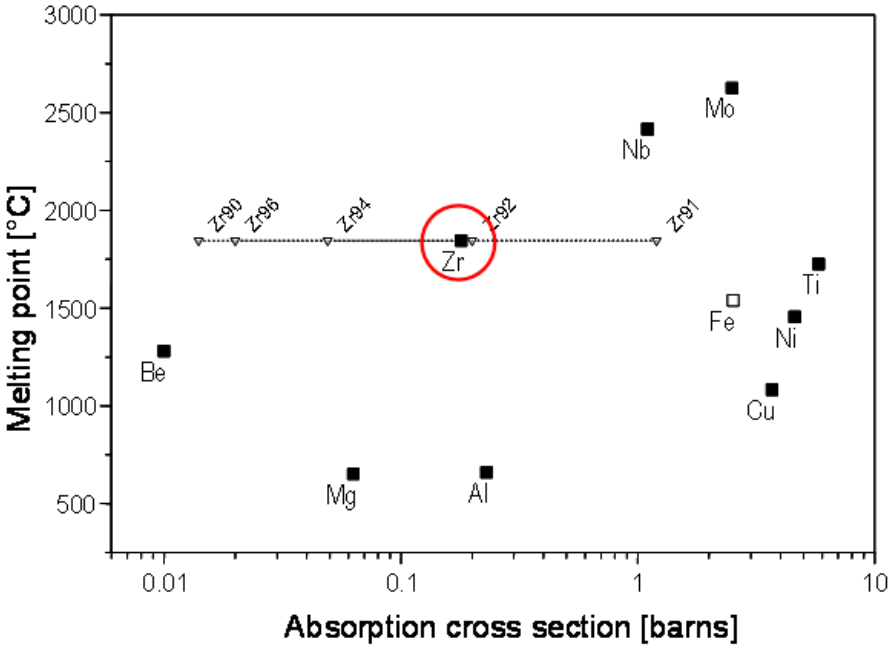

Figure 1.2: Material melting point vs. thermal neutron absorption cross section; courtesy of AREVA NP GmbH

mation in the absence of stress. Irradiation creep is observed in most metals; however, irradiation induced growth occurs in non-cubic crystal systems only, as it depends strongly on the anisotropy of the crystal lattice [10]. The irradiation-induced creep and growth occur simultaneously with each other and the thermally induced creep, which is a process that would also be present without the irradiation at the typical operating temperatures around 300°C. Therefore, the total observed material deformation is a combination of both thermally and irradiation induced deformation. One important part of the irradiation growth phenomenon is its development at high neutron fluences. Irradiated anisotropic materials in both single-crystal and polycrystal form show, after a certain fluence has been reached, an increase in their growth rate. This increase is designated as "breakaway growth", and its onset lies in fluence ranges that are relevant for nuclear reactor operation [11,12]. The occurrence of breakaway growth in fuel assembly components is therefore an important issue when discussing fuel assembly irradiation deformation.

A fuel assembly is a complex structure of fuel rods (which contain the fuel pellets), spacer grids and guide tubes. All these interconnected parts experience irradiation-induced deformation during operation, and the extent of their deformation varies due to their different geometry, texture, alloy, and local environmental situation. The deformation of the fuel assembly as a whole is then the result of the interaction of the deformation of these single components. It will be shown in chapter 2 that the PWR components whose deformation has the largest impact on the whole assembly's axial deformation are the guide tubes. Therefore, this work focusses on the irradiation behavior of typical guide tube alloys.
The phenomenon of fuel assembly deformation is, of course, known, and large experience databases containing FA deformation values from many years of operation exist. A certain amount of positive FA length change is even required to compensate for the irradiation induced relaxation of

the fuel assembly hold-down springs, which apply a load on the guide tubes to counteract the coolant flow's buoyant force. Based on the operational experience, fuel assembly design therefore allows for a specific amount of assembly growth; within these margins, a safe operation of the assemblies is ensured.

Due to economic and ecologic reasons, the nuclear fuel assembly market demands for FA designs which can reach higher fuel burnups, can withstand increased power levels at high operating temperatures and allow for longer cycle lengths and higher FA lifetimes [13]. By these developments, the number of assemblies for a fixed power output is reduced, thus decreasing FA acquisition and transport costs and the amount of nuclear waste. The required improvement of the fuel assembly operation behavior led to the development of advanced Zr-based alloys. However, due to these more demanding operating conditions, the issues of hydrogen uptake, corrosion and irradiation induced deformation of PWR fuel assembly structural components have become more significant than in the decades before [13].
King et al. reported unexpectedly high growth of PWR fuel assemblies with Zry-4 skeletons in the US Wolf Creek plant, which could not be accounted for by the operational experience based irradiation growth models [13]; similar FA behavior was observed in some other PWR plants. Such excessive and unexpected deformation of the assemblies can lead to issues disturbing power plant operation, like possible fuel assembly handling problems and interactions due to fuel assembly envelope increases caused by lateral spacer grid growth, or incomplete control rod insertion due to guide tube deformation [13]. As a consequence of this unexpected behavior, it has become clear that a more detailed understanding of the irradiation-induced microstructural processes leading to FA growth is necessary; such understanding could contribute to improve the fuel assembly deformation prediction codes and would facilitate the development of advanced growth-resistant Zr-based alloys [14].

The nuclear reactor environment offers a large number of possible reasons for FAs showing different levels of irradiation induced growth in different plants: variations in the FA design; neutron flux and fluence which depend on the plant, differ axially as well as with the FA position in the core and are influenced by varying control rod movements during start-up, shutdown and load changes; different fuel burnup, power levels and FA lifetimes; plant specific cooling water chemistry with a possible influence on hydrogen uptake at the components' beginning of life. Many of these possible parameters leading to FA growth have been investigated and could be excluded as the origin of the unexpected deformation. There are, however, two parameters whose influence on FA growth require further study: the guide tubes' hydrogen content and the influence of external stress.
Zr-alloys in a nuclear light water reactor environment absorb hydrogen during operation, with the total amount depending on a large number of factors like the FA's operating history, the component alloy's composition and its level of oxidation. With the hydrogen solubility limit in typical guide tube alloys in the range of 80 wt.-ppm at the operating temperatures in the range of 300°C, and possible hydrogen concentrations up to several 100 wt.-ppm, the excess hydrogen precipitates as zirconium hydrides. The Zr-alloy components' total hydride content therefore increases continuously during FA operation. The influence of both the hydrogen in solution in the Zr-alloy matrix and of the precipitated hydrides on the neutron irradiation induced microstructure remains unclear. The study of a possible correlation between hydrogen and irradiation-induced deformation is complex as the hydrogen content of the components increases not necessarily linearly with the total assembly time in the core and is further influenced by a

number of factors as mentioned above. It can also vary locally with the axial or radial guide tube position within one FA.
The second parameter of possible major influence on FA growth, external stress, can differ from unit to unit and assembly to assembly due to variations in coolant pressure and flow rate or differences in the chosen hold-down spring forces. Also, the applied axial stress by the hold-down springs is not constant, as the springs show relaxation as a consequence of material degradation due to the neutron irradiation. Additional stresses are caused by the irradiation deformation of the FA's components and their mechanical interaction, which can vary for different assembly designs and lead to consequential stress distributions in the assemblies that are different from the stress situation in other assemblies. Also, thermally and irradiation induced creep can lead to varying degrees of stress relaxation. Most of these factors are a function of the total assembly time in the core and of a number of other operation dependent parameters, such that the resulting local stress situation is complex.

As both the hydrogen content of the components and the applied stress depend on a large number of parameters that cannot be separated or measured with high accuracy in a nuclear reactor environment, the study of the effect of hydrogen level and stress on irradiation-induced creep and growth is difficult in in-pile experiments. Therefore, heavy ion irradiation was chosen as a method to simulate the neutron irradiation damage out-of-pile.
During heavy ion irradiation, experimental parameters like the material's temperature, hydrogen content, stress level and the irradiation dose and damage rate can be controlled and measured with accuracy. Also, in-situ transmission electron microscopy (TEM) facilities like the Argonne National Laboratory's IVEM Tandem Facility allow to observe the development of the irradiation damage with the dose dynamically in the TEM, such that defect nucleation, migration and interaction can be studied. Also, a defined material region can be imaged starting from its unirradiated state up to high dose levels; thus, the local microstructural properties before the irradiation are known, which avoids artifacts and measurement errors. Due to the significantly higher interaction cross sections of heavy charged particles with matter as compared to neutrons, irradiation times are strongly reduced. Typical guide tube end-of-life doses which are given in a PWR after about 5 years of operation can be reached by heavy ion irradiation in several hours. Finally, the absence of material activation avoids the decay times necessary for in-pile irradiated material, simplifies sample handling and laboratory access and saves large financial efforts for material transport and radiation protection issues. Heavy ion irradiation, especially coupled with in-situ TEM, is therefore a highly valuable tool for the study of neutron irradiation damage processes in nuclear materials.

The objective of this work is to provide a better understanding of the microstructural origins of PWR fuel assembly deformation, with specific focus on the effects of hydrogen content and external stress.
This objective is reached by three consecutive steps: First, the testing of appropriate heavy ion irradiation conditions for the simulation of PWR neutron damage in the chosen guide tube alloys, and of suitable post-irradiation examination methods to gain the maximal knowledge about the irradiation induced damage structures. Secondly, the conduction of a feasibility study to assess the comparability of heavy ion produced and PWR neutron induced irradiation damage. And finally, the investigation of the influence of hydrogen content and external stress on the irradiation induced microstructural changes in the guide tube alloys.

Chapter 2

Scientific and Industrial Background

2.1 Pressurized Water Reactor Nuclear Power Plants

Irradiation induced fuel assembly deformation is a known phenomenon in all nuclear power reactor designs. Since 272 of the 435 nuclear power reactors in operation worldwide as of July 2012 are pressurized water reactors, this work will focus on FA deformation in PWRs as the dominating reactor type. The studied fundamental processes of irradiation damage are, with reservation, also relevant to other reactors, as long as design differences like material compositions, coolant temperatures and neutron spectra are kept in mind.
This section provides an overview of the technical properties of the PWR design and of typical PWR fuel assemblies.

2.1.1 Thermal Nuclear Fission

The operation principle of a thermal nuclear power reactor is the production of electricity from the heat generated by a stable chain reaction of thermal nuclear fission. Energy gain by nuclear fission is in theory possible for elements with mass numbers higher than iron (A=56), while lighter elements would release energy by nuclear fusion. This is due to the dependency of the binding energy per nucleon on the mass number, as shown in Fig. 2.1 [15].
Elements with significant probability of undergoing nuclear fission after neutron absorption are those with Z>90. Neutron absorption leads, in a first step, to the formation of a so-called "compound nucleus" with the new mass number (A+1); following Fig. 2.1, the binding energy per nucleon is lowered by neutron absorption for heavy elements. This reduction in the binding energy per nucleon is sufficient, even if the captured neutron has low energy, to induce nuclear fission in several isotopes with odd neutron numbers like $^{233}_{92}$U, $^{235}_{92}$U, $^{239}_{94}$Pu and $^{241}_{94}$Pu [15]. These elements are designated as "fissile" and used as nuclear fuels for thermal nuclear reactors. Other isotopes of industrial interest are $^{232}_{90}$Th, $^{238}_{92}$U and $^{240}_{94}$Pu because of their high fission cross sections for neutron energies in the range of 1 MeV. This energy lies within the energy range of the neutrons produced by nuclear fission, which makes the isotopes candidates for fast nuclear fission. They are thus used in fast nuclear reactor designs like fast breeder reactors [15].
The probability of a neutron to interact with a target atom is described by the so-called "neutron reaction cross section" σ. σ is strongly energy and target isotope dependent and differs for each kind of neutron-target interaction, which include scattering, neutron capture with subsequent γ- or particle emission or capture with subsequent fission. The cross section is a measure for the effective interaction area a specific nucleus offers for an incoming neutron, and is thus measured

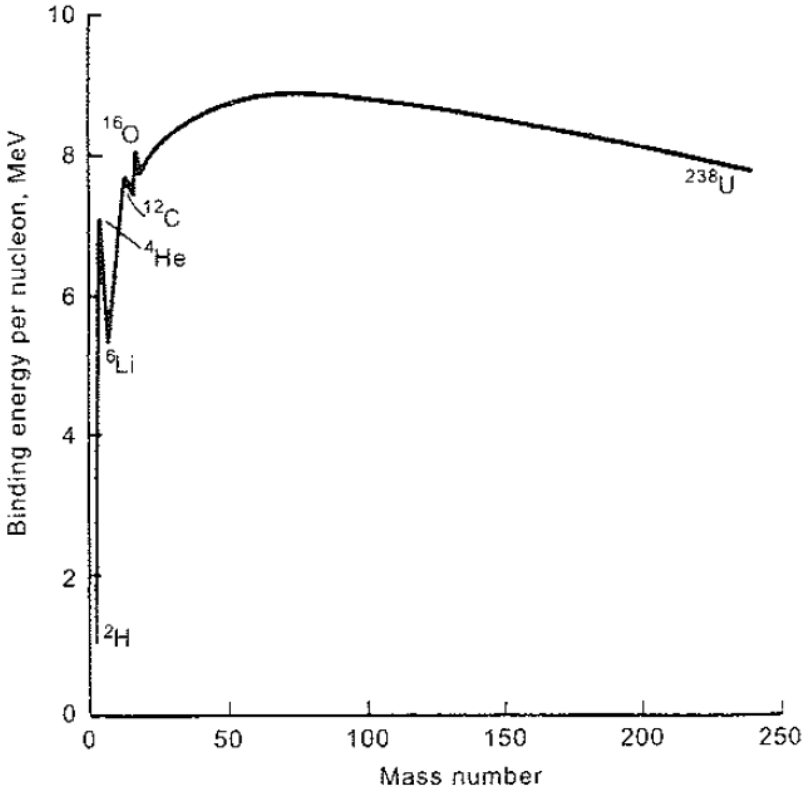

Figure 2.1: Binding energy per nucleon [15]

in the dimension of area; the established unit is $10^{-24}\mathrm{cm}^2 = 1\,\mathrm{barn}$. The total probability of a neutron to interact with a target consisting of isotopes i, by any possible neutron-target reaction k is the macroscopic cross section. It is the sum over the microscopic interaction cross sections σ_i of all isotopes in the target, multiplied with their respective atomic densities N_i, and over all interaction reaction types k [16]:

$$\Sigma(E) = \sum_{i,k} \sigma_{ik}(E) N_i.$$

Due to their lack of electric charge, neutrons travel freely in the target material between the collisions. Their mean free path between collisions, λ, is defined as $\lambda = 1/\Sigma$.
The probability of neutron capture and fission is quantified by the so-called capture and fission cross sections. Fig. 2.2 gives an overview of the low-energy neutron absorption (fission + capture) cross sections for the isotopes of main interest for thermal nuclear fission reactors, as well as a schematic of the fission product mass number distribution for thermal neutron and fast neutron induced fission of $^{235}_{92}$U.
The neutron absorption cross sections decrease with increasing neutron energy (except for the respective isotopes' specific resonance energy ranges, where the resonance cross sections reach high values for small energy bandwidths), as the probability for neutron-atom interaction is inversely proportional to the neutron's velocity [16]. To use the thus high fission cross sections at thermal neutron energies, the fission neutrons have to be decelerated from their energy of creation of up to several MeV to thermal energies before inducing subsequent fission reactions. This process

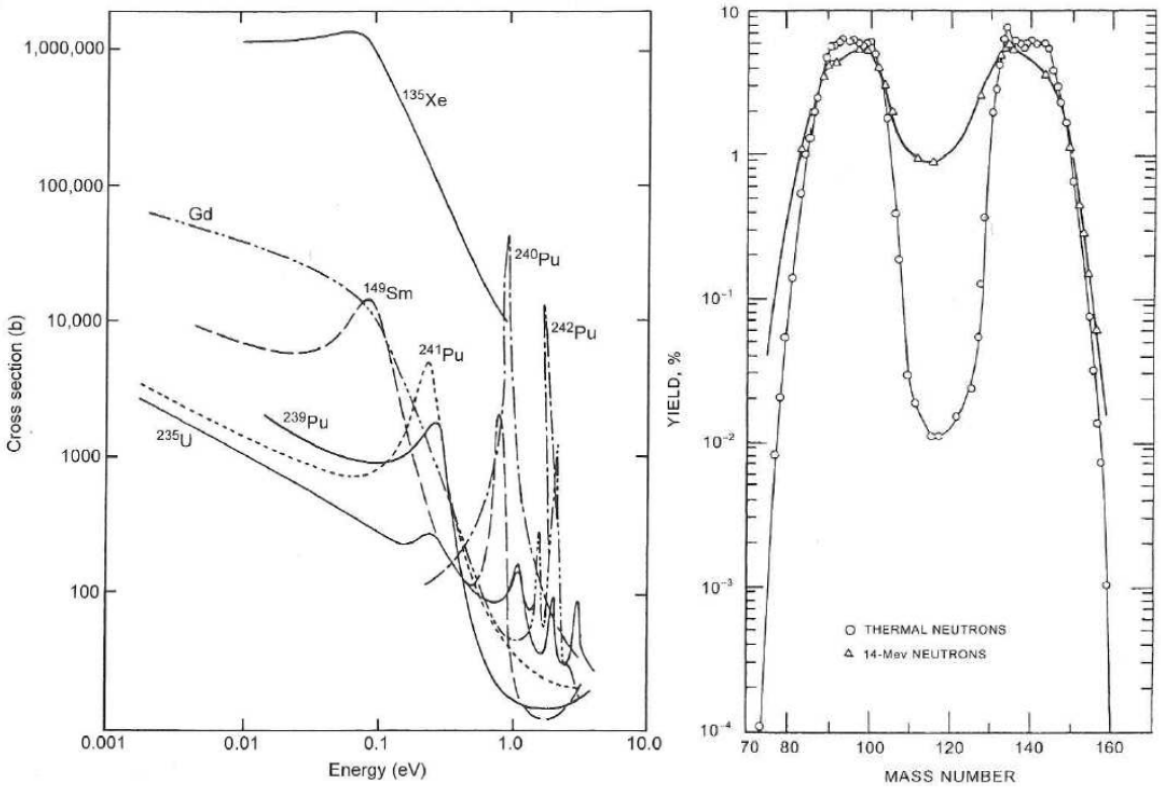

Figure 2.2: Neutron absorption (fission + capture) cross sections (left); fission product yield for $^{235}_{92}$U (right) [15]

is called "moderation" and is reached by a heterogeneous configuration of fissile material and a moderator. Moderators are chosen to have a high stopping power for neutrons combined with a low neutron absorption cross section in the relevant energy ranges. Typical moderators are light water (e.g. for PWR and BWR), heavy water (e.g. for PHWR like CANDU) or graphite (e.g. for LWGR).

For light water reactors of western design, uranium dioxide is the major fuel component, with the $^{235}_{92}$U content enriched up to 5 wt.-%. Due to neutron capture by the thermally non-fissile $^{238}_{92}$U, the thermally fissile isotopes $^{239}_{94}$Pu and $^{241}_{94}$Pu are bred during normal thermal reactor operation; their contribution to the energy from thermal nuclear fission goes up to about 1% at fuel assembly end-of-life. For mixed-oxide (MOX) fuel assemblies, the bred fissile Pu isotopes are recovered chemically from the burned UO_2 fuel assemblies after they have reached end-of-life and are mixed as plutonium dioxide with uranium dioxide to form new fuel.
^{235}U has an absorption cross section of 681 barn for thermal neutrons (E_{kin}=0.025 eV); the fission cross section is 586 barn [17]. The absorbed neutron leads to an excited ^{236}U* compound nucleus which parts with few exceptions into two excited fission products with the mass numbers of highest probability in the range of 90 and 140 (see Fig. 2.2). During the fission process, on average 2.43 prompt neutrons are emitted, as well as γ radiation. By the transitions of the excited fission product nuclei to their ground states, further γ-emission occurs. Delayed neutrons and anti-neutrinos emerge from the subsequent β^--decays and neutron emission of the neutron rich

fission products. The total energy gained by the nuclear fission of ^{235}U is 207 MeV; the majority of the energy, on average 168 MeV, is the kinetic energy of the fission products, divided according to momentum conservation. The remaining energy is partly borne by prompt γ's released directly during the fission event and prompt neutrons with a most likely energy of 0.7 MeV. After those neutrons slowed down, they are absorbed, thus producing γ emission subsequent to neutron capture ("capture γ's"). Further energy is released in the form of kinetic energy of β-particles and neutrinos resulting from the fission product decay. The energy caused by the delayed processes make up for about 7% of the total energy released (not counting the 12 MeV borne by neutrinos, as they are not deposited within the core due to the low neutrino interaction cross section) [15]. Those 7% are the origin of the afterheat of spent nuclear fuel after the chain reaction is stopped [16]. Table 2.1 summarizes the distribution of the energy released in the thermal nuclear fission of an $^{235}_{92}$U nucleus. Fig. 2.3 shows a schematic of the $^{235}_{92}$U fission chain reaction.

prompt processes	energy in MeV
kinetic energy of fission products	168
kinetic energy of prompt γ's	7
kinetic energy of prompt neutrons	5
delayed processes	**energy in MeV**
kinetic energy of capture γ's	7
kinetic energy of β-particles	8
kinetic energy of delayed neutrinos	12
kinetic energy of delayed neutrons	<<1

Table 2.1: Energy distribution after thermal nuclear fission of $^{235}_{92}$U [15, 16]

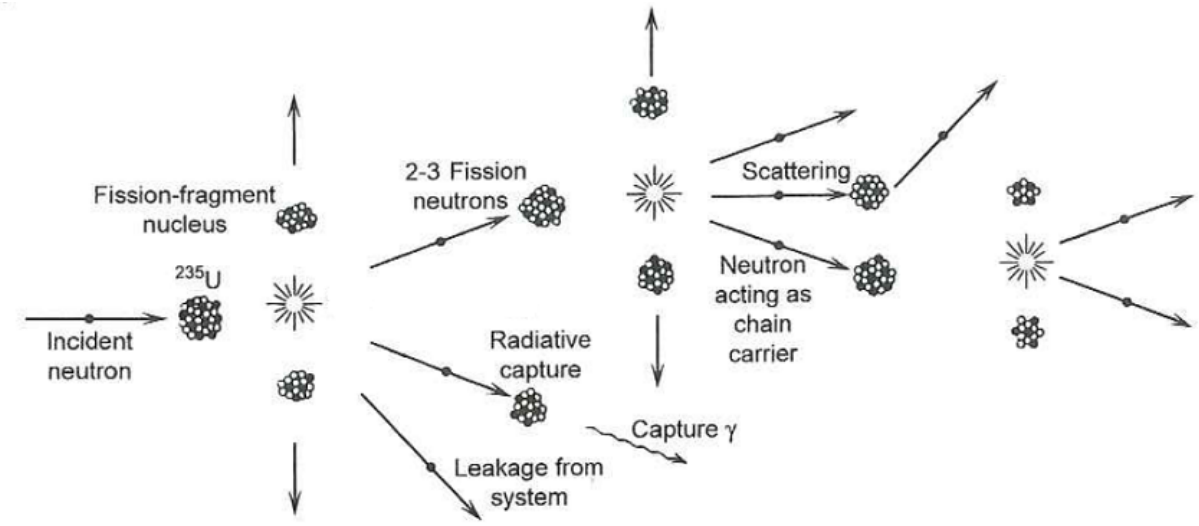

Figure 2.3: Fission chain reaction [15]

A stable nuclear fission chain reaction requires the number of neutrons available for nuclear fission in the $(i+1)^{th}$ generation of fission reactions to correspond to the neutron number in generation

i. For a homogeneous, infinite volume of fissile and absorbing material, the neutron density n(t)[1] as a function of time would be described by the neutron balance equation,

$$\frac{dn}{dt} = \nu\Sigma_f\varphi - \Sigma\varphi = n(t)v(\nu\Sigma_f - \Sigma) = n(t)C,$$

where ν is the number of neutrons produced per fission reaction, φ is the neutron flux, v the neutron velocity, Σ_f the macroscopic fission cross section and Σ the macroscopic absorption cross section of all reactions leading to neutron loss, i.e. neutron capture with subsequent fission and (n,γ) reactions e.g. in coolant, non-fissile fuel components or structural material. The neutron absorption in structural material or other core components leads to effective neutron loss and depends on a high number of parameters given by the reactor type and the specific plant, like the size and geometry of the reactor core and fuel assemblies, the choice of moderator, structural materials, fuel, and coolant. The constant C is given by

$$C = v(\nu\Sigma_f - \Sigma).$$

The neutron balance equation is solved by

$$n(t) = n_0 \exp(Ct),$$

and the desired state of a constant neutron density n(t) is given for C=0:

$$(\nu\Sigma_f - \Sigma) = 0 \;\Rightarrow\; \frac{\nu\Sigma_f}{\Sigma} = k = 1.$$

The thus defined ratio between neutron production and neutron loss, k, is designated the "multiplication factor". Using the neutrons' mean free path,

$$\lambda = \frac{1}{\Sigma}$$

and the neutrons' average lifetime

$$\bar{t} = \frac{\lambda}{v} = \frac{1}{v\Sigma},$$

C is related to the multiplication factor as follows:

$$C = v\Sigma\left(\frac{\nu\Sigma_f}{\Sigma} - 1\right) = \frac{k-1}{\bar{t}}.$$

Then, the time dependent neutron density is given as

$$n(t) = n_0 \exp\left[(k-1)\frac{t}{\bar{t}}\right].$$

For k=1, n(t)=n_0 is constant, leading to the desired state of a stable chain reaction which is designated as "critical". For k<1, the argument of the exponential function is negative, and the exponential function causes n(t) to approach zero; this state is called "subcritical", and the chain reaction cannot be held up. k>1 results in a positive argument of the exponential function and thus an exponential neutron density excursion; this state is known as "supercritical" [16]. For a stable nuclear chain reaction, fissile material has to be assembled in a way that enables k to keep the value 1 continuously. Such a configuration can be reached by different reactor designs, different fuels and for thermal, epithermal or fast neutron spectra.

[1] number of neutrons per unit volume

2.1.2 Pressurized Water Reactor Power Plant Design

Fig. 2.4 shows a schematic of a PWR power plant.

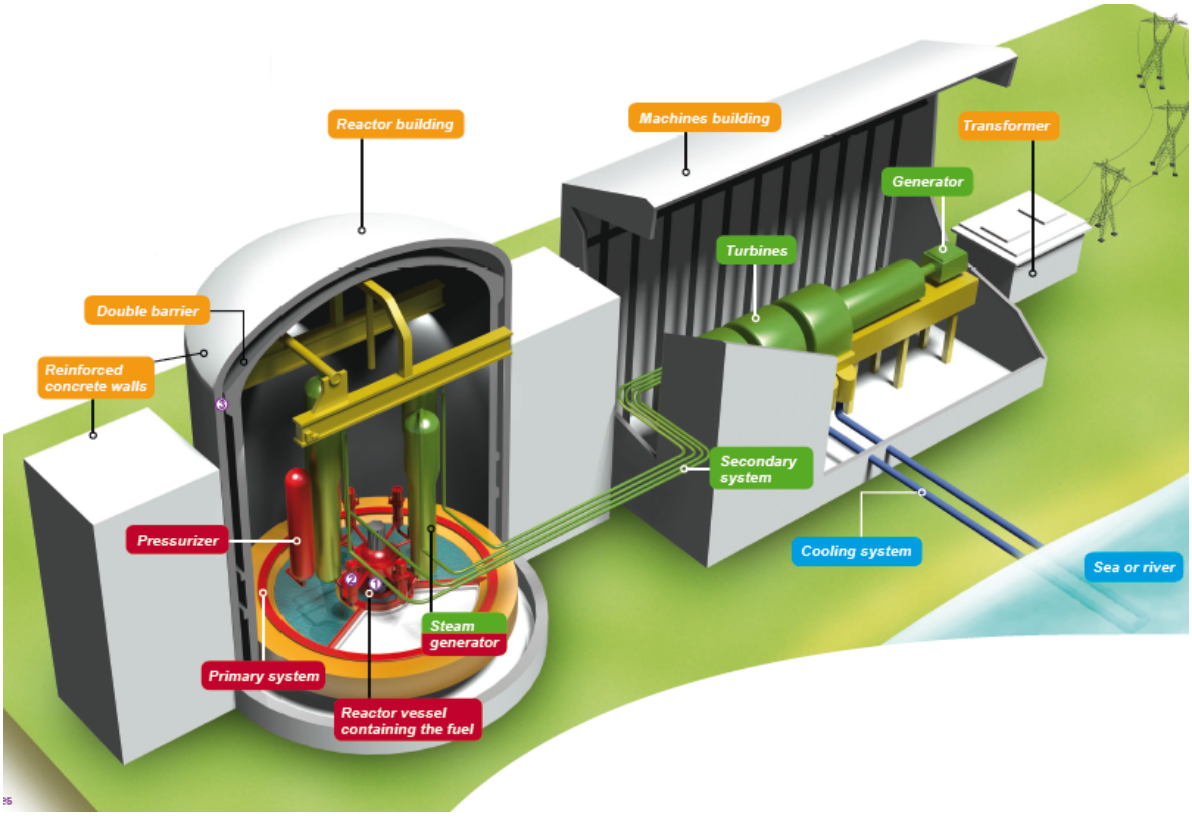

Figure 2.4: Schematic of a pressurized water reactor power plant [18]

The heart of a PWR is the reactor pressure vessel; for a German Vorkonvoi or Konvoi PWR, typical dimensions would be 5 m diameter, 12 m height and a wall thickness of 25 cm [19]. The reactor pressure vessel contains the fuel assemblies; German Vorkonvoi and Konvoi designs host FA with an active length of 3.90 m. Fig. 2.5 contains a more detailed schematic of the reactor pressure vessel and of a typical PWR fuel assembly design.
The top and bottom piece of the fuel assemblies are connected by about 20 - 24 guide tubes; together with the spacer grids, which are located at about every 500 mm of axial position, they make up the assembly skeleton. The spacer grids provide 14 x 14 to 18 x 18 positions; those which are not taken by the guide tubes are occupied by the fuel rods, which are held by the spacer springs, but do not have a fixed connection to top or bottom end piece. Typical modern AREVA PWR spacers are made of Zr-based alloys like M5®for the middle spacer positions and of alloy 718 ("Inconel"), a corrosion-resistant nickel-chromium-iron alloy, for the top and bottom spacer positions. PWR fuel rod cladding materials are Zircaloy-4 (Zry-4) or Zr-Nb alloys like AREVA's M5®alloy or Westinghouse's ZIRLO (Zr-1Nb-1Sn-0.1Fe). The fuel rods are filled with pellets of uranium dioxide or a mixture of uranium and plutonium dioxide in the case of MOX fuel. The pellets are held at their position by plenum springs within the top of each fuel rod; the fuel rods' free volume is filled with He gas at pressures of about 20 bar. With the cooling water acting as a moderator, the pellets create heat by thermal nuclear fission of $^{233}_{92}$U, $^{235}_{92}$U, $^{239}_{94}$Pu and $^{241}_{94}$Pu;

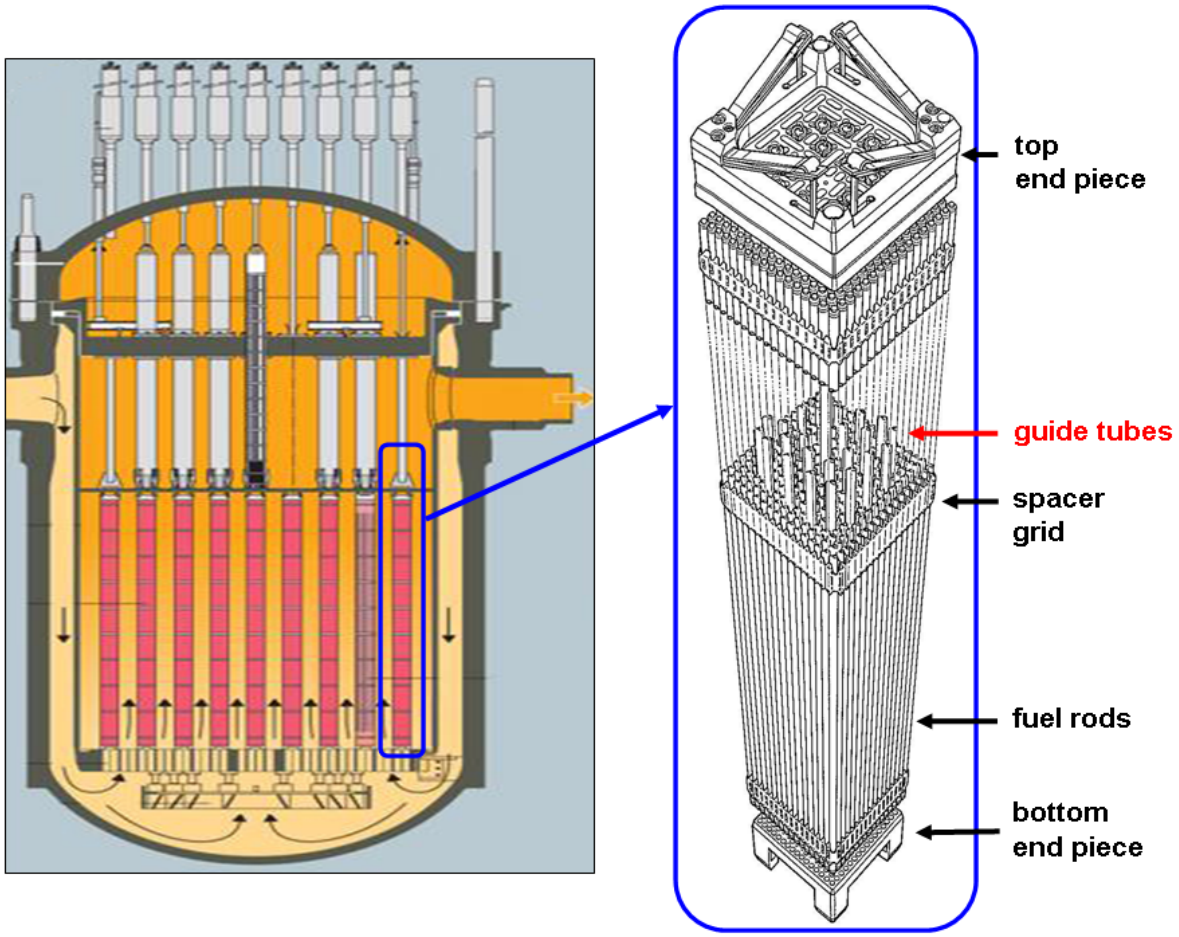

Figure 2.5: Schematic of a reactor pressure vessel and a PWR fuel assembly; courtesy of AREVA NP GmbH

the pellets' temperatures reach up to 1200°C in the pellet center and about 600°C at the pellets' surface. PWR local rod power levels can be as high as about 450 W/cm fuel rod length under normal operation in high duty plants. The neutron flux is relatively constant along the active length of the fuel assemblies. With a typical number of 193 fuel assemblies in German Konvoi PWR, the total uranium inventory at first loading is about 100 tons.
For Isar 2 as a typical German Konvoi plant, the pressurizer keeps the cooling water from boiling by pressures of about 150 bar and is pumped by four primary cooling pumps from pressure vessel bottom to top through the fuel assemblies (see Fig. 2.5), being heated from a typical inlet temperature of 293°C to an outlet temperature of 328°C [19]. The coolant temperature leads to fuel cladding outer temperatures of about 300-330 °C. The heated water from the pressure vessel outlet is led to four steam generators where heat exchangers between the primary and secondary cooling circuit with a total heating area of about 5400 m^2 evaporate the secondary cooling water; the primary cooling water continues to be reinjected into the pressure vessel. The created steam in the secondary circuit is led to one high pressure (HP) turbine with a vapor pressure of 64 bar at the HP turbine inlet and 11 bar at its outlet; it continues to two low pressure turbines before

reaching the condensor and being repumped into the steam generators. The heat sink for the condensor is provided by connection to a cooling tower; alternative heat sinks would be a river or the sea. The turbines with rotation speed of 1500 r/min drive a generator, producing net electrical power of 1410 MW_e [19].
German nuclear power plants have refuelling cycles of one year, while US or French plants prefer 18 - 24 months cycles; after each cycle, about a forth of the fuel assemblies will be exchanged with new assemblies. PWR fuel assembly lifetimes are in the range of five one-year cycles, corresponding to FA end-of-life burnups in the range of 55 - 60 MWd/kgU in typical German PWR. Refuelling involves a complete unloading and reloading of the core, with a new arrangement of the assemblies; based on neutronics calculations of assembly burnup and power levels, loading patterns are defined to provide a homogeneous power level throughout the core. Low leakage core loading pattern with high burnup assemblies and their associated lower power levels at the core periphery are being used for economic reasons and to reduce the neutron damage to the reactor pressure vessel.
Burnable poisons like boric acid in the coolant or gadolinium-doped fuel are used to compensate the excess reactivity at the beginning of the cycles. Load changes or reactor shutdown are done by partial or complete control rod insertion; the control rods, consisting of strong thermal neutron absorbers like B_4C or Ag-In-Cd, and with different absorber concentration and lengths depending on their function for shutdown or axial power regulation, are arranged in control rod banks above specific FA locations throughout the core and can be inserted into the guide tubes [15]. The guide tubes of fuel assemblies without control rod banks are closed by thimble plugs which control the coolant flow through the tubes.

2.1.3 Pressurized Water Reactor Guide Tubes

The focus of this work is on the study of irradiation damage in Zr-based alloys typically used for PWR guide tubes. There are two main groups of Zr-based alloys for light water reactor structural materials: The group of the Zr-Sn-Fe-Cr alloys, and the group of the Zr-Nb or Zr-Nb-Sn alloys. For this work, typical guide tube alloys from both groups were chosen: Zircaloy-4 from the group of the Zr-Sn-Fe-Cr and M5® from the group of the Zr-Nb alloys.

Material Properties of Zr-based Alloys

The group of Zr-Sn-Fe-Cr alloys contains the so-called Zircaloys (Zry) with the two major groups of Zry-2 and Zry-4. Both are Zr-based alloys with the main alloying elements Sn, Fe and Cr, differing mainly in their Ni content, which have been used for nuclear applications for decades [20]. Zry-4 is currently in use in both PWR and BWR, while Zry-2 is a BWR material only. The chemical composition of the Zry-4 and M5® ingots used in this work is given in Table 2.2. Both alloys have a mass density of 6.5 g/cm^3 at room temperature.
While tin and oxygen are in solid solution in α-Zr, iron and chromium are quasi-insoluble in Zr at typical component operating temperatures and precipitate nearly entirely as intergranular and intragranular $Zr(Fe,Cr)_2$ Laves phases[2] with hexagonal close-packed (hcp) lattice structure and typical diameters after the guide tube fabrication process of 200 nm [22].
The group of Zr-Nb alloys have been in operation in various reactor types for several years, e.g. Zr-2.5Nb for CANDU pressure tubes [23, 24], the Russian alloys E110 (Zr-1Nb) and E635 (Zr-1Nb-1.2Sn-0.35Fe) [25] or Westinghouse's ZIRLO alloy (Zr-1.0Sn-1.0Nb-0.1Fe) [13]. M5® is

[2]"Laves phases" desigate 3 highly close-packed structure types of defined composition AB_2; the high atomic density is enabled by the difference in atomic radii between A and B with an ideal radius ratio of 1.225 [21].

	Zry-4		M5®
Sn	1.3 wt.-%	Nb	0.99wt.-%
O	0.14 wt.-%	O	0.135 wt.-%
Fe	0.23 wt.-%	S	17 wt.-ppm
Cr	0.11 wt.-%		
Zr	98.2 wt.-%	Zr	98.9 wt.-%

Table 2.2: Alloying composition of the Zry-4 and M5® ingots used for this work

part of this group of Zr-Nb alloys; its major alloying elements are niobium, oxygen and sulfur. As compared to Zry-2 and Zry-4, M5® hosts only a low density of Laves phases which contain the impurity Fe of up to 500 wt.-ppm. The Laves phases' sizes correspond to typical sizes in Zircaloys; the Fe content of the M5 strips used for the samples was 389 wt.-ppm. The dominating second phase particle (SPP) type in M5® is a body-centered cubic zirconium-niobium phase ("β_{Nb}") with a Nb content of 85-90 wt.-% with spherical form and typical diameters between 30 and 50 nm [26,27]. Binary phase diagrams of Zr-Sn and Zr-Nb are given in the Appendix.

Zirconium and Zr-based alloys are in Zr's α-phase at room temperature and at typical component in-pile operating temperatures of around 300°C for guide tubes and 300 - 400°C for cladding. Zr's α-phase is hcp with space group 6/mmm; the atom layer sequence for hcp is ABABAB.... Pure Zr has lattice parameters of a=3.231 and c=5.147 and a density of 6.5 g/cm^3 [28,29]. The lattice parameters shift slightly with the alloying content. Fig. 2.6 shows a schematic of the hcp lattice structure, with the notation of the lattice planes of highest importance for irradiation defect accumulation. The basal planes are perpendicular to the basal pole, (0001); the prism planes can be divided into two different kinds, type I $(\bar{1}100)$ and type II $(11\bar{2}0)$[3] [10].

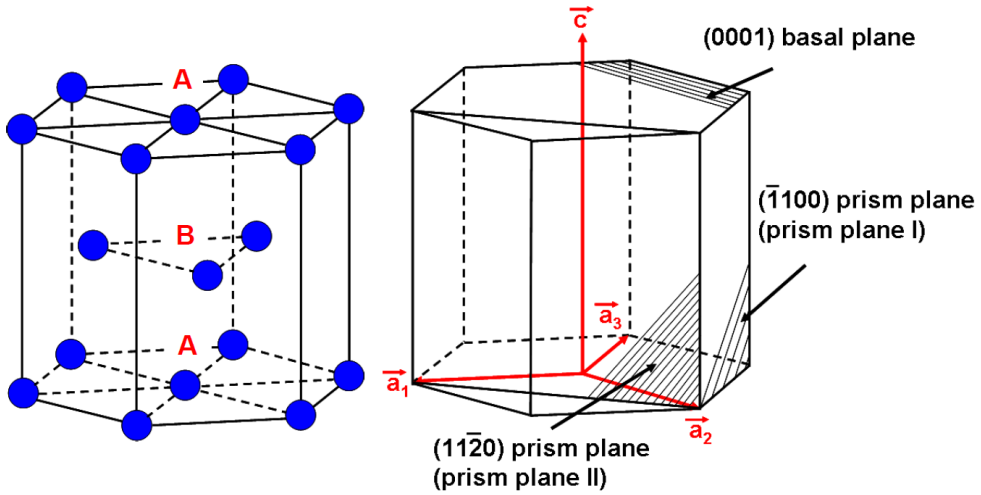

Figure 2.6: Hexagonal close-packed (hcp) lattice structure with main lattice planes

[3]Hexagonal crystal structures are sometimes described by using only the 3 Miller indices (hkl); the 4 index notation relates to the 3 Miller indices by (hkil) with i=-(h+k) [29].

The transition from the hcp α-Zr to body-centered cubic (bcc) β-Zr occurs, for very pure Zr, at 862°C; the β-phase has a lattice parameter of 3.545 Å [28]. The high temperature phase is, however, not present during normal reactor operation, where all Zr-based structures are in the α-phase.

Radiation damage in Zr-based alloys has shown to consist mainly of dislocation loops on the prism planes ("<a>-loops") and basal planes ("<c>-loops"). A dislocation loop develops if a significant number of vacancies or interstitials agglomerate on a particular plane; the vacancies or interstitials form a disc which has a circular edge dislocation as boundary [30]. The left image in Fig. 2.7 shows a schematic of an edge dislocation.

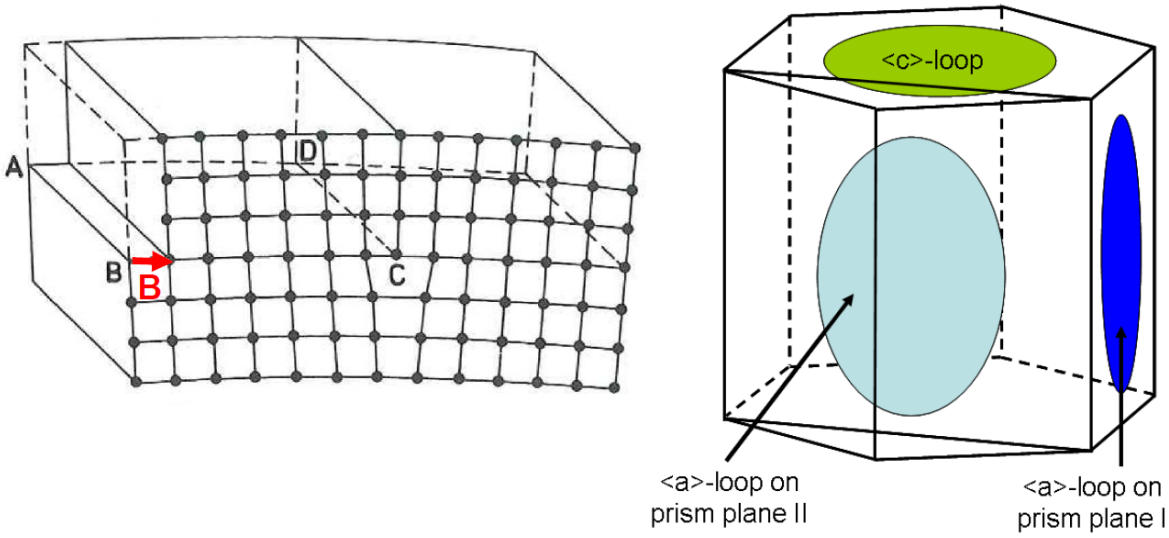

Figure 2.7: Edge dislocation [29] (left); <a>- and <c>-loop locations in the hcp lattice (right)

An edge dislocation can be imagined by cutting a crystal open along the plane ABCD as designated in Fig. 2.7, then shifting the left upper part of the crystal to the right by distance b, while the right upper part of the crystal remains unchanged. Then, both upper halfs of the crystal will be combined again, and the strain will release. The line CD is called a "dislocation line", and the displacement vector $\vec{B}$ is designated as "Burgers vector" [29]. The right side of Fig. 2.7 shows the schematic location of <a>- and <c>-loops on the hcp lattice planes. The loops are extended over several unit cells; typical diameters for <a>-loops, for example, would be 8 nm [10].

Guide Tube Fabrication

The guide tube fabrication process starts from an ingot of the respective Zr-based alloy, which is produced by several subsequent melting processes. After forging of a stock rod by a hot forging press, the bar undergoes a "forge forge quench" process to set the material's state with regard to second phase precipitate properties to a defined level. In a following forging process, billets will be formed, from which hollow billets will be produced by a drilling and milling process. The hollow billet will then be extruded to receive a so-called "tube shell" with an outer diameter of about 80 mm and a length in the range of 3 - 3.5 m. Then, a multistage cold pilgering process will start; during pilgering, the hollow cylinder will be deformed to a tube, by rotating cylinders ("rolling

dies") rolling the tube shell which is held centrically by a conic mandrel. The component after the first pilgering step is called a "tube reduced extrusion" (TREX), and such TREX material was used as base material for the Zry-4 samples in this work. Between the different rolling steps, the cylinder is rotated and shifted to allow for homogeneous deformation. In each step, after pilgering, the received tube is cleaned and recrystallization annealed to re-establish the material's ductility for further plastic deformation. The tube is then straightened and, depending on the quality of its inner surface, pickled. After drying and quality control, the next pilgering step is started. Guide tubes are typically pilgered to their final wall thickness in the range of 0.6 mm in four pilgering steps and then cut to their final length of about 4 m. The thus received material deformation is demonstrated in Fig. 2.8; the volume of the component shown in the schematic remains constant.

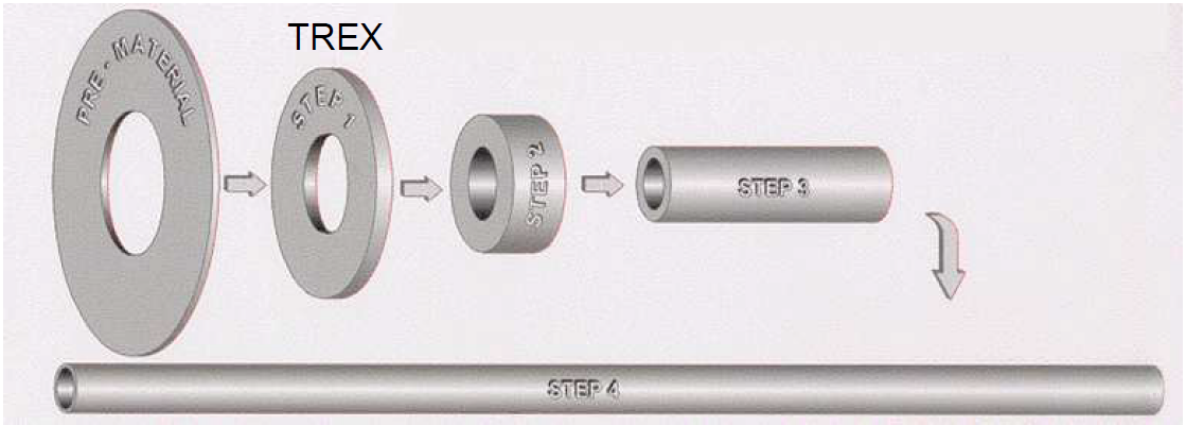

Figure 2.8: Schematic of the pilgering process; courtesy of AREVA NP GmbH

The annealing after pilgering leads to a recrystallized α-Zr microstructure in the guide tubes, with equiaxed grains of diameters in the range of 3 to 6 μm. The pilgering process for guide tubes results in a preferential crystallite orientation (texture) in the tubes; the α-Zr grains' c-axes will be directed radially, with an angular range of 30 to 40° from the radial vector. The a-axes range from axial to tangential orientation; a schematic of the guide tubes' texture is shown in Fig. 2.15 in the following section.
As an example for the typical microstructure of Zr-based alloys in their recrystallized state, Fig. 2.9 is a TEM image of unirradiated M5®. The structure shows the characteristic equiaxial grains of Zr-based alloys in their recrystallized α-phase. The small spherical β_{Nb}-precipitates can be seen, as well as some larger Laves phases. The main microstructural difference between Zry-4 and M5® would be the absence of β_{Nb}-SPPs and a higher density of Laves phases in Zry-4.

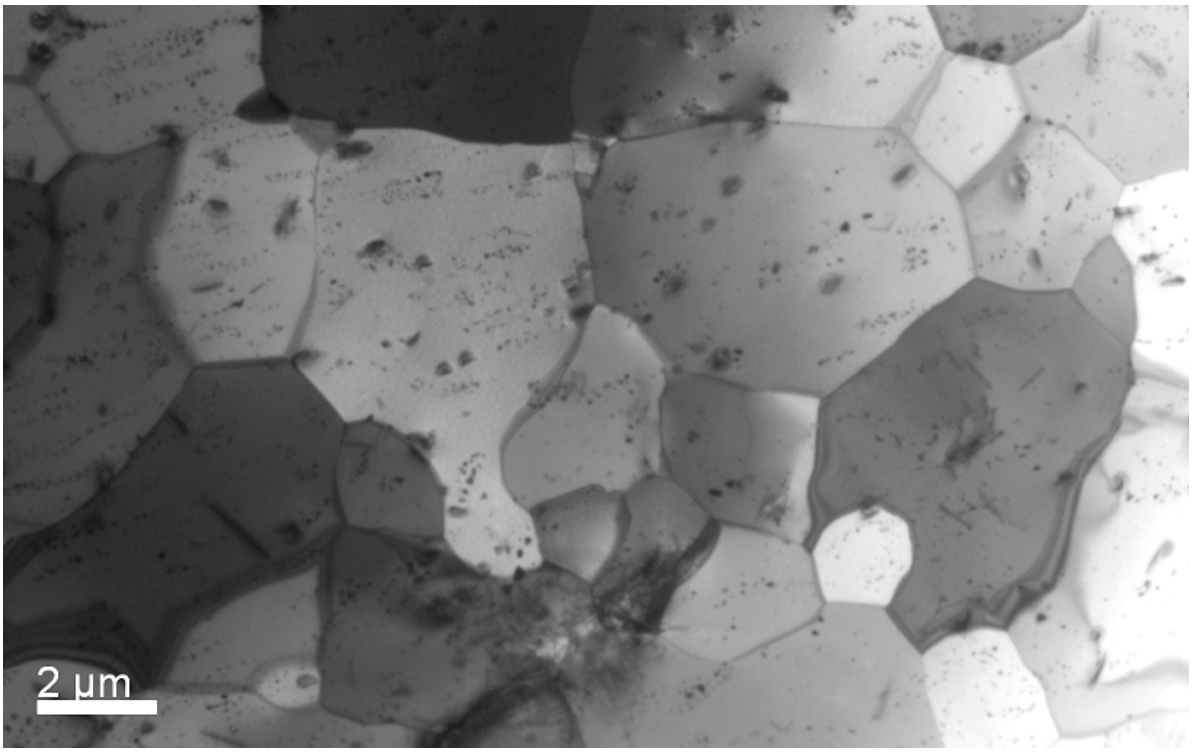

Figure 2.9: Microstructure of recrystallized, unirradiated standard M5®

2.2 Guide Tubes under Neutron Irradiation

PWR fuel assembly irradiation induced deformation is a complex process and the result of the irradiation induced deformation of the different structural components, i.e. guide tubes, spacer grids, fuel rods and hold down springs. In models that are phenomenologically describing the long-term deformation of Zr-based alloys in PWR environments, it has generally been assumed that the irradiation deformation consists of separable, additive components from the simultaneously occurring macroscopic component thermal and irradiation creep and irradiation growth [11].
Fuel assembly component deformation depends on a high number of partly interacting and time-dependent parameters; external parameters defined by the plant design like neutron spectrum, flux and fluence, coolant pressure and temperature, operating history, external stress and water chemistry, as well as internal parameters like component geometry, texture, alloy composition, initial microstructure and hydrogen content. This section gives a summary of the observed irradiation deformation in Zr-based alloys and the underlying microstructural processes, with a focus on guide tube deformation.

2.2.1 Observed Neutron Irradiation Effects in Zr-Based Alloys

Irradiation induced deformation of neutron irradiated zirconium and Zr-based alloys has been reported for decades. Buckley published in 1962 that fission fragment irradiation of Zr single crystals at 100°C and low fluence neutron irradiation of both Zr single crystals and Zry-2 at 90°C led to an expansion of the samples along their a-axes and a contraction along the c-axis, while the

sample volume remained constant. From the results, Buckley proposed the following widely-used model for the observed irradiation growth process: The irradiation induced interstitials condense on the prism planes while the vacancies, which are concentrated in the depleted regions of the damage cascades, collapse to form loops on the basal planes. This would lead to an effective atom transport from basal planes to prism planes and would thus explain the observed behavior [31]. Buckley's model was in agreement with following growth studies by Hesketh et al. on textured polycrystalline Zry-2; however, Hilditch found an a-axis expansion and also a very slight c-axis expansion in a neutron irradiated Zr single crystal. TEM analyses of the irradiated Zr, Zircaloy and Zr-2.5wt.-%Nb showed only dislocation loops on the prism planes (<a>-loops) with Burgers vectors $a/3(11\bar{2}0)$, while some authors reported measurements indicating a small fraction of loops with c-component Burgers vectors [32]. Northwood et al. described in 1976 the neutron irradiation of a Zr single crystal at 200 - 250°C. They found an initial elongation of the cylindric sample along the c-axis which decreased and led to a following shrinkage in c-direction with a final state of 0.03% lower length than at the initial state. All dislocation loops were reported to be prism plane loops with Burgers vector $a/3(11\bar{2}0)$ and an equal distribution among the three Burgers vectors. The loops after 10 min of annealing at 440°C were analyzed to consist of both vacancy and interstitial type with a 10% excess of interstitial loops [32]. In 1977, Jostsons et al. reported studies of both Zr and Zry-2 at irradiation temperatures of around 400°C which showed the dislocation structure to be again solely <a>-loops, which agrees with a report by Northwood et al. from 1979; however, in both these works, the <a>-loops are described to be primarily of vacancy-type, with the fraction of vacancy-loops between 53 to 91% of the total <a>-loop population [32,33]. Again in 1977, Jostsons et al. found faulted c-component dislocation loops with Burgers vector $1/6(20\bar{2}3)$ in high-purity Zr neutron irradiated at 450°C in addition to the <a>-loops of both interstitial and vacancy-type [34]. From the studies of the <a>-loop types in the following years until now, it can be concluded that the prism plane loops consist of both vacancy and interstitial loops with roughly equal fraction of the whole <a>-loop population [35]. Their density is reported to increase with the dose, but to saturate at comparatively low fluence in the range of $1 \times 10^{24} n/m^2$ [36]. According to G. Was, vacancy-type <a>-loops are unstable above 450°C due to thermal emission [10].

In 1986, Holt et al. described the neutron irradiation of annealed Zry-4 at about 290°C to lead to <c>-component loops in addition to a high density of <a>-loops, while annealed Zry-2 and Zry-4 irradiated to lower doses had only shown <a>-loops. They compared the dislocation loop observations to the samples' growth behavior and stated that "the appearance of the <c> component dislocations correlated with the reported onset of acceleration in the rate of irradiation growth of annealed Zircaloy at 550 K referred to as 'growth breakaway' " [12]. They concluded that the <c>-loops have an important role in the growth process, presumably as vacancy sinks. Further work by many authors confirmed that <a>-loops nucleate from the beginning of irradiation and are of both vacancy and interstitial type, while <c>-loops form above a threshold dose only and are of vacancy type [10,12,14,31–34,37–44].

Fig. 2.10 shows the typical <a>- and <c>-loop appearance in neutron irradiated Zircaloys. Fig. 2.11 is a summary of the growth strain observed in Zry-2 growth specimens and Zry-4 fuel guides as provided by Holt et al. [12]. It demonstrates that the observed irradiation growth follows a three-stage process. After the first stage of growth strain increase with the beginning of the irradiation, the strain remains constant in stage II before entering stage III of accelerated growth, designated as "breakaway".

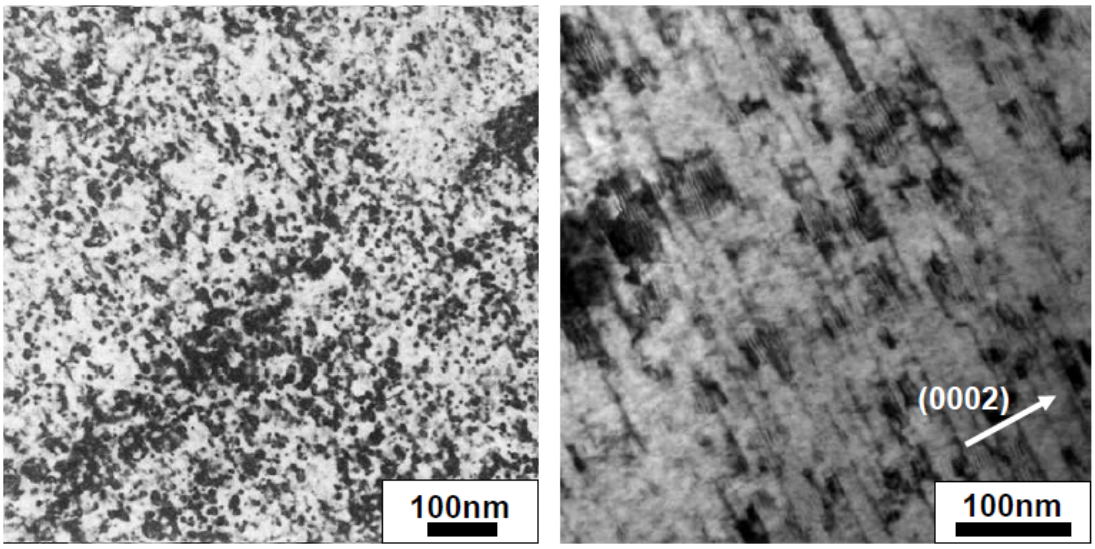

Figure 2.10: Dislocation loops in neutron irradiated Zircaloys. Left: <a>-loops in annealed Zry-2, irradiated at 300°C in Oak Ridge Research Reactor [45]; right: <c>-loops in recrystallized low-tin Zry-4, irradiated at 315°C in PWR [26]

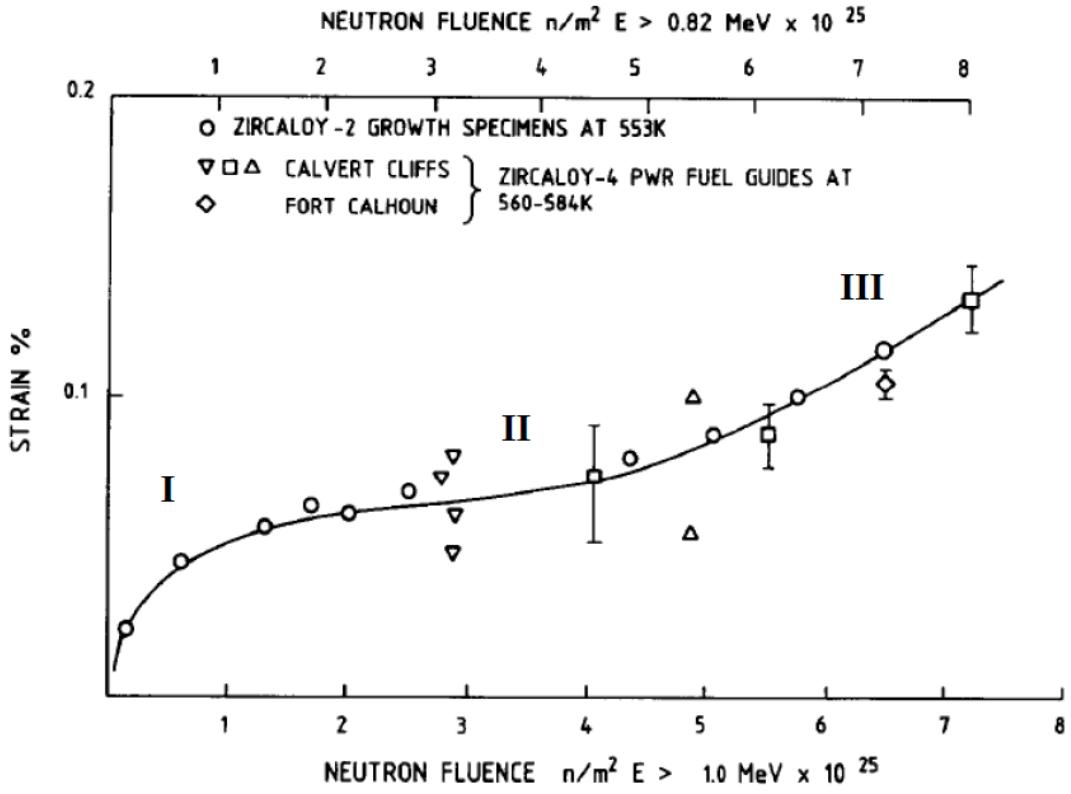

Figure 2.11: Irradiation growth in annealed Zircaloys at 277-307°C [12]

In the following years, irradiation induced deformation of components made of Zr-based alloys, and the implications on reactor performance were studied and discussed for different reactor types, Zr-alloys and irradiation conditions [11, 12, 43, 46–53]. Based on these studies and the fuel vendors' operational experience, empirical models were developed to predict (among others) PWR fuel assembly irradiation growth.
Even though these models are generally reliable, several cases of unexpectedly high fuel assembly growth were observed in some PWR plants during the last years. These observations led to more recent work on the phenomenon of irradiation-induced deformation of structural components. The transition from constant growth strain in stage II to breakaway in stage III as shown in Fig. 2.11 was observed in research studies on Zircaloy and ZrNb-alloys irradiated in the BOR 60 reactor in the scope of an NFIR (Nuclear Fuel Industry Research) program [54]; unpublished work on free growth samples of M5® and Zr-1%Nb alloys irradiated in different PWR as well as the BOR 60 test reactor also showed the transition to breakaway growth at high fluences.
In the light of the reported supposed correlation of the occurrence of <c>-loops with the onset of breakaway growth, a better understanding of the irradiation deformation phenomenon cannot only be reached by studying macroscopic component deformation, but also by investigating the nucleation mechanisms and characteristics of <c>-component dislocation loops.

2.2.2 Microstructural Origins of Irradiation Induced Guide Tube Deformation

The following section gives an overview of the irradiation induced deformation process. It begins with the neutron damage mechanisms in the structural material lattice, then describes the formation and characteristics of dislocation loops in Zr-based alloys and their impact on single grain geometry, and finally explains the transition from single grain irradiation deformation to component deformation.

Neutrons in Matter

At the very beginning of irradiation damage is the interaction process between the incoming neutron and the target material. The interaction of neutrons with matter can be divided into three groups of mechanisms. The first group contains the two processes of neutron scattering. "Elastic scattering" with the conservation of the kinetic energy of the initial neutron-nucleus system and without neutron absorption is referred to as "potential scattering" and can be treated as a hard sphere collision process [16, 55]. During "resonance scattering", also designated "inelastic scattering", the neutron forms a compound nucleus with the original nucleus, with the subsequent emission of a neutron with reduced energy. The residual nucleus remains in an excited state. While the neutron-nucleus system's total energy is conserved, the system's kinetic energy is not, as it is reduced by the excitation energy [55]. The excitation energy will eventually be emitted, e.g. in the form of γ-radiation or by internal conversion [15]. Inelastic scattering typically requires neutron energies in the keV to MeV range.
The second group are neutron capture reactions, associated with nucleus transmutation and radiation or particle emission. Typical examples are the neutron loss reactions A(n,γ)B, A(n,p)B* and A(n,α)B*, or the neutron producing A(n,2n)B* reaction where the capture of a fast neutron leads to the emission of two thermal neutrons. A and B are the initial and final nucleus, respectively. X* designate excited nuclei; their excitation energy is, again, typically emitted in the form of γ-radiation or internal conversion.

The third group of reactions is neutron induced nuclear fission, as described in 2.1.1 [16]. Zr-based alloys are non-fissile materials, with their elemental composition chosen in a way to keep neutron capture cross sections, and thus the probability of reactions of groups two and three, low. Therefore, the relevant neutron-nucleus reactions for guide tube materials are scattering reactions, with potential scattering being the dominant mechanism for light water reactor neutron spectra.

Fig. 2.12 shows the typical neutron energy distribution for the thermal fission of ^{235}U. The produced neutrons are quantified by the neutron flux $\varphi(\mathsf{E})$, which is the number of neutrons of energy E per unit area and unit time. While a fast nuclear reactor has the peak of its neutron flux spectrum near 1 MeV, thermal nuclear reactors show a continuous distribution from the fast neutrons down to thermal energies, with slight peaks in the range of 0.1 eV and 1 MeV (see right side of Fig. 2.12).

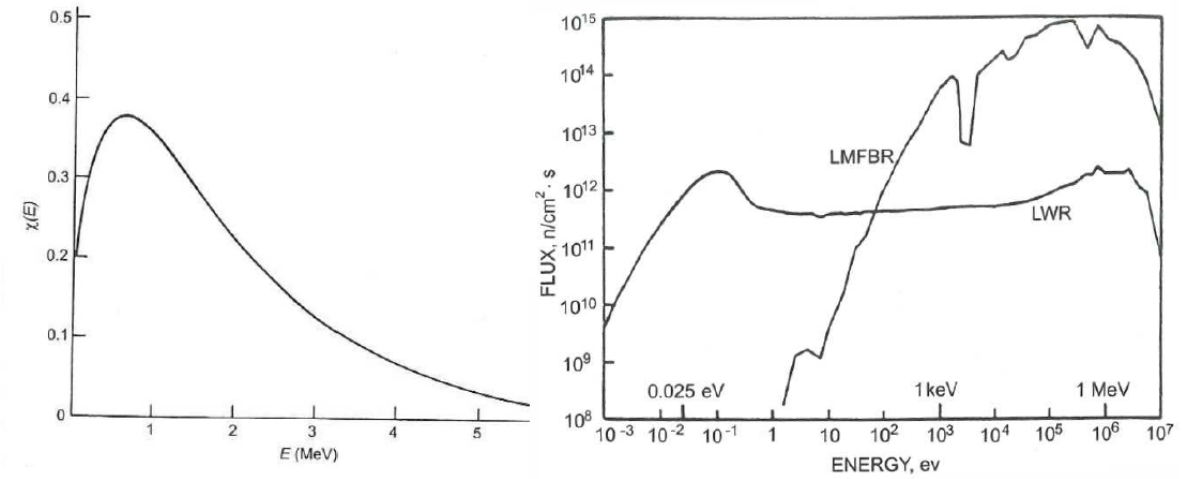

Figure 2.12: Neutron energy distribution after thermal fission of ^{235}U (left); representative PWR neutron flux, compared to LMFBR spectrum (right) [15]

To compare the magnitude of the elastic cross sections, which are the relevant cross sections for atom displacement in the structural materials, to the cross sections for neutron absorption with subsequent nuclear transformation, Fig. 2.13 shows the respective cross sections for ^{90}Zr, Zr's main isotope, for the typical LWR neutron energy range. The cross sections are taken from KAERI's pointwise ENDF-VII library at 300 K [56]. For a detailed calculation of the cross sections, they would have to be corrected for the different temperature at operating conditions; for a rough estimate, however, the data for 300 K is used. The general trend of the cross sections is comparable for all Zr isotopes. The total cross section is strongly dominated by the elastic cross section over all energy ranges up to about 1 MeV. While (n,γ) reactions show a contribution especially at thermal energies, their impact is small as compared to the elastic contribution for large parts of the spectrum. For energies higher than 1 MeV, the probability of nuclear reactions increases strongly, with (n,p) from about 2 MeV, (n,α) from about 3 MeV and a number of other reactions starting from higher energies. To estimate the importance of those reactions, the total macroscopic cross sections (Σ_{total}) and the macroscopic cross sections for all nuclear transformation reactions occurring in that energy range in addition to (n,γ) ($\Sigma_{\mathsf{transformation}}$), were

calculated for Zry-4 at the energies of 1 MeV, 2 MeV and 5 MeV; the contribution of all isotopes of the alloying elements as given in table 2.2 was taken into account. The resulting macroscopic cross sections and their ratio are given in table 2.3. The contributing nuclear reactions in that energy range are (n,p) and (n,α).

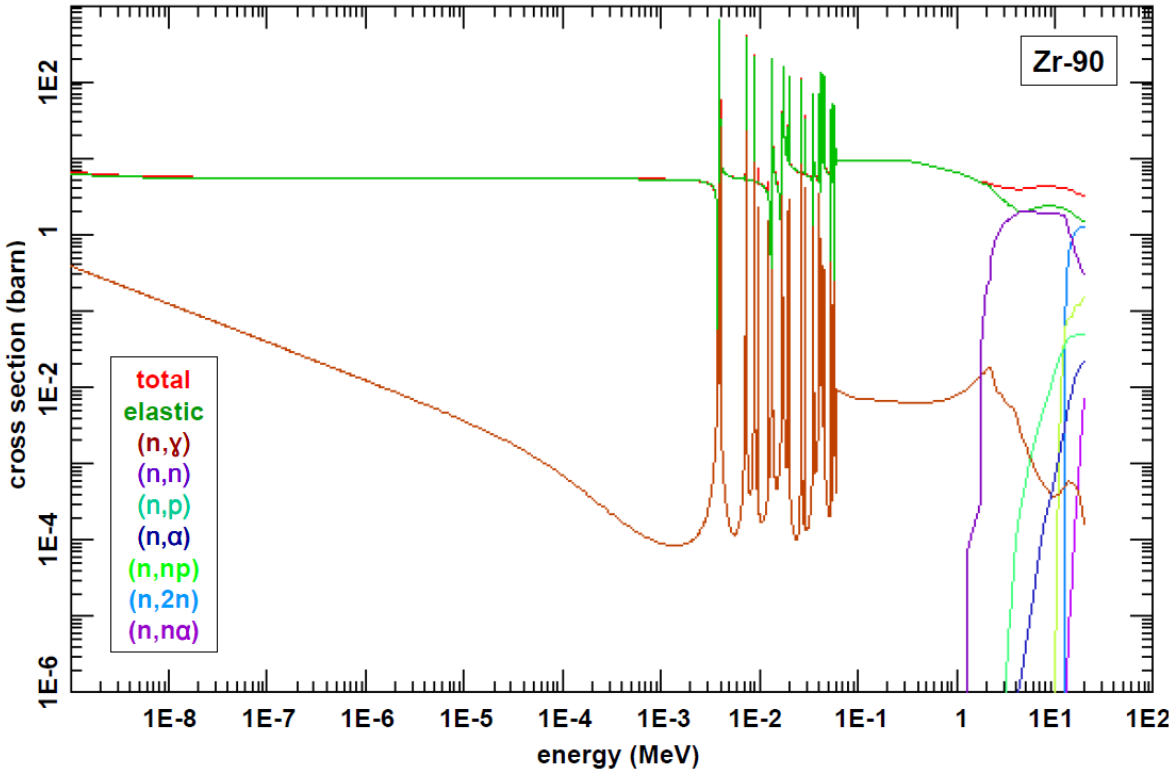

Figure 2.13: Neutron cross sections for ^{90}Zr at 300 K [56]

	Zry-4		
	1 MeV	2 MeV	5 MeV
Σ_{total} (cm^{-1})	0.27	0.20	0.15
$\Sigma_{transformation}$ (cm^{-1})	3.8×10^{-8}	4.3×10^{-7}	9.4×10^{-5}
$\Sigma_{transformation}/\Sigma_{total}$	1.4×10^{-7}	2.2×10^{-6}	6.3×10^{-4}

Table 2.3: Σ_{total} and $\Sigma_{transformation}$ (without (n,γ)) estimate for Zry-4

While those additional nuclear reactions reach significant contributions at 5 MeV, their fraction of the total reactions is low at 1 MeV and 2 MeV. While fission neutrons are produced with energies even higher than 5 MeV, their fraction of the whole neutron number is low, and their part of the overall light water moderated reactor spectrum is significantly smaller still (compare Fig. 2.12). Therefore, it can be concluded that the material impurities produced by nuclear transformation in the guide tube alloys, being either the hydrogen atoms or helium atoms from (n,p) and (n,α) reactions or the foreign atoms from the residuals of those reactions and the (n,γ) reactions, are

small as compared to the impurities already contained in the industrial alloys due to the fabrication process or the chemical interactions with the reactor environment.

To determine the level of irradiation damage, the first step is to calculate the number of elastic scattering reactions between neutrons and target atoms in the respective target volume. This quantity is defined by the neutron fluence $\Phi(E)$, which is the neutron flux integrated over the total irradiation time. The neutron fluence thus gives the total number of incoming neutrons after a certain irradiation time per unit area. The neutrons' mean free path between collisions, λ, is in the range of 1 cm in Zr-based alloys; in reactor core components like guide tubes with wall thicknesses less than 1 mm, the neutron-atom collision distribution can therefore be assumed to be homogeneous over the guide tube dimensions [16].

The number of elastic scattering reactions between neutron and target atoms per unit volume and unit time, the so-called "reaction rate" $\dot{R}$, can be calculated from the macroscopic elastic scattering cross section Σ_e by

$$\dot{R} = \int_{E_{min}}^{E_{max}} \varphi(E)\Sigma_e(E)\,dE.$$

For the assessment of irradiation damage, the total number of elastic neutron-target reactions in a defined irradiated material volume V_{irr} after a specific irradiation time t_{irr} is of interest. This total number of reactions, R, can be calculated by integration over V_{irr} and t_{irr}:

$$R = \int_0^{t_{irr}} \int_{V_{irr}} \int_{E_{min}}^{E_{max}} \varphi(E)\Sigma_e(E)\,dE\,dV\,dt.$$

From Point Defects to Defect Clusters

The number of elastic neutron-target nucleus collisions having occurred in a specific target volume after defined irradiation time can be calculated by the equation directly above. Whether the elastic collision reaction leads to atom displacement, and how much kinetic energy is transferred to the target atom, depends on the binding energy of the target atom in its crystal lattice and the target atom's mass. For α-Zr, an atom binding energy of 40 eV is specified in the ASTM[4] norm reference test standard [10,36]. Due to momentum conservation during the elastic collision, the transferred energy T from a neutron with initial energy E_i to an atom with mass A is given by [10]

$$T = \frac{2A}{(1+A)^2} E_i(1-\cos\theta)$$

with θ being the scattering angle. For the direct collision with maximal energy transfer, and the mass A = 91.22 for Zr with its natural isotopic composition, the minimal neutron energy necessary to displace a Zr atom is 932 eV. This energy is clearly covered by the majority of neutrons in the PWR spectrum.
Having been knocked out of its original lattice position and leaving a vacancy behind, the displaced Zr atom ("Primary Knock-on Atom", PKA) will travel through the matrix and loose its kinetic energy by Coulomb interaction with the target atoms' electrons as well as by elastic

[4] American Society for Testing and Materials

collisions, creating a displacement cascade. As the PKA and matrix atoms have equal mass for the majority of the atom collisions, half the PKA's current energy is transferred to the matrix atom [36]. Having lost its energy, the PKA comes to rest in the lattice, typically at an interstitial position. Thus, the primary defect types being caused by neutron irradiation are interstitials and vacancies. However, molecular dynamics computations showed that after the relaxation of the damage cascades, which initially consist of a core of high vacancy concentration and a periphery of high interstitial concentration, a large part of the point defects recombinate; in addition, the remaining defects are not all in point defect form but also constitute clusters which can contain up to 24 vacancies or 25 interstitials in the case of α-Zr. Those spatially separate point defect clusters as well as possible different numbers of vacancy and interstitial type point defects after the cascade relaxation can result in a disequilibrium in the interstitial to vacancy ratio, which is described as "production bias" and is of high importance for the resulting microstructure [36].
The point defects which remain in the material after the cascade collapse do not necessarily stay isolated in the target matrix but tend to form pairs and clusters. When a vacancy is induced into an atomic lattice, the lattice configuration changes slightly around it, adjusting to the new Coulomb potential. Thus, a strain is applied to the surrounding atoms that is absent in the equilibrium state without the vacancy and which increases the material's free energy. If two or more vacancies are located directly next to each other, the caused strain for the neighbouring atom positions is lower than the sum of the strains caused by two single vacancies. The same principle applies to interstitials, with the modification that the strain does not pull the surrounding atoms nearer to the vacancies' position but pushes them from the interstitials' location. Thus, clustering of defects lowers the system's free energy which is the reason for the tendency of defects to agglomerate [57].
Defect migration requires a defect type and lattice structure dependent activation energy to move the defect from its initial position where it is in a local potential minimum; at a sufficiently high material temperature, the thermal activation energy enables defect migration. Typical PWR coolant and thus structural component temperatures are in the range of 293°C to 328°C [19]. The migration and annihilation of point defects in single crystal α-Zr after 1.2 MeV electron irradiation at 120 K was studied by G.M Hood [58]; Frank then suggested the different defect annealing stages in α-Zr based on that work [37]. The onset of free vacancy migration in α-Zr, according to Hood, occurs between -23°C and +27°C [58]. According to Frank, free vacancy migration starts at around 30°C, while self-interstitials undergo long-range migration in annealing stages I and III, with the higher temperature limit of stage III at around 30°C [37]. At typical PWR component temperatures, the point defect migration threshold energies are thus clearly exceeded, and the point defects are free to migrate, recombinate or cluster in the material under irradiation. As compared to defect clusters like dislocations, single defects move on short time scales. Thus, the changes in cluster size are assumed to depend on the interstitial and vacancy migration rates. If an interstital reaches a vacancy cluster, the cluster shrinks, while an intestitial cluster would grow [10].

Zirconium alloys as non-cubic metals differ from a large number of other materials by their anisotropic crystal structure. The formation and characteristics of extended defect structures in irradiated materials are defined by the diffusion characteristics of point defects in these materials. As point defect diffusion strongly depends on the crystal structure, the anisotropy of the lattice structure has a major impact on the irradiation defect cluster formation and dislocation characteristics in Zr-based alloys.

Fig. 2.14 gives an overview of the two main processes leading from an irradiation induced population of interstitials and vacancies to the observed microstructural evolution in anisotropic metals. The focus of the schematic is on the behavior of point defects which is the primary factor determining the final material microstructure. However, it has to be taken into account that the behavior of defect clusters, like dislocation loop interaction or migration, does also influence the final microstructure.
The process shown in green takes place in isotropic as well as anisotropic materials and is, for isotropic metals, the main process of microstructural evolution. The process shown in blue is caused by the anisotropic crystal lattice and does not occur in isotropic materials; for anisotropic metals, the blue process is, according to Woo [41], the dominating one. Apart from the two presented processes, other minor influences are present.

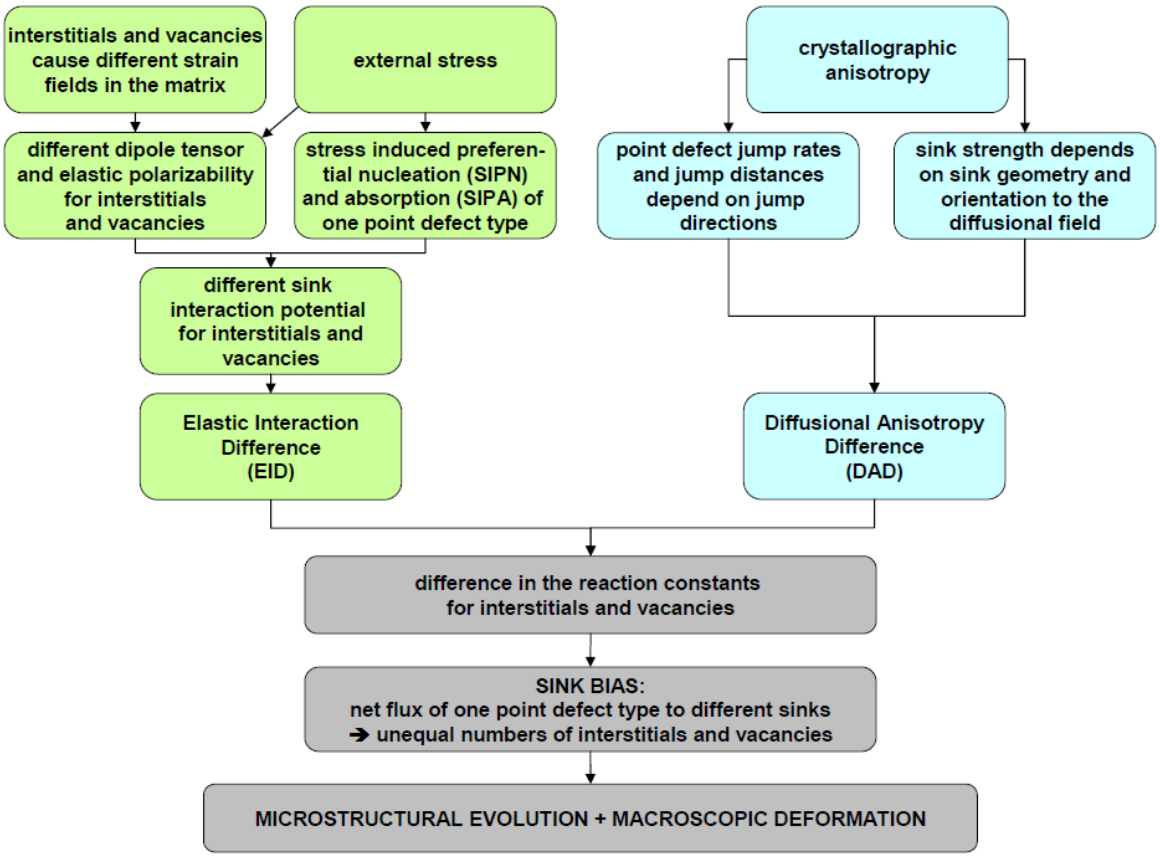

Figure 2.14: Schematic of the microstructural evolution processes in non-cubic metals

The conventional theoretical description of irradiation deformation in cubic metals is done by rate theory, based on the so-called Elastic Interaction Difference ("EID") between vacancies and interstitials. The EID shown in green results from a generally different interaction of interstitials and vacancies with defect sinks. While interstitials lead to an excess of atoms in a unit space that would contain less atoms in an ideal crystal, the neighboring atoms are pushed away from the interstitial. This is the inverse effect of a vacancy in the lattice, which provides additional space in the unit volume that would allow the neighboring atoms to move from their ideal crystal positions

nearer to the vacancy. Consequently, a strain of different mathematical sign is created in the lattice for the two different point defect types, and that different defect strain causes a different interaction of the point defects with the surrounding lattice atoms, dislocations and other sinks. That difference is mathematically expressed by the dipole tensor that describes the strain field created by the point defect in the perfect lattice, and the so-called "elastic polarizability" which specify the modification of the point defect strain by the total strain field that is present in the crystal, e.g. caused by defect sinks or external stress. The interaction of the point defects with sinks changes their migration characteristics and migration rates; therefore, the different dipole tensors and polarizabilities for interstitials and vacancies lead to different reaction constants of the two defect types with defect sinks [41].
If external stress is applied, it leads to an additional strain field that is superimposed on the existing dislocation and sink strain field in the material; such existing strain fields are small for recrystallized material but will grow during irradiation due to the developing defect structures. The external stress leads to the effects of stress-induced preferential nucleation ("SIPN") and stress-induced preferential absorption ("SIPA") of point defects. SIPN describes the preferred nucleation of dislocation loops on planes with a certain orientation to the external stress during irradiation. While interstitial loops are reported to nucleate with a higher probability on planes perpendicular to the applied tensile stress than parallel to it, vacancy loops are more likely to nucleate on planes parallel to the stress. Both effects lead to an increase in sample length parallel to the external tensile stress. However, the SIPN model is still controversely discussed and gives account only for a certain amount of the observed irradiation induced creep [10]. SIPA describes an unequilibrium in the point defect absorption by dislocations under external stress. The additional external strain field is reported to lead to a preferred absorption of interstitials by dislocations while vacancies are preferredly emitted by dislocations [10].
The result of the generally different interaction behavior of the different point defect types and the influence of the external stress is a different sink interaction potential for interstitials and vacancies which causes the elastic interaction difference.
For anisotropic metals, an additional process is triggered by the crystallographic anisotropy. In anisotropic crystalline materials, point defect jump directions and jump distances depend on the atom jump directions which leads to an anisotropy in point defect diffusion. Also, the sinks' attraction or repulsion for the different defect types depend on the sinks' geometry and their orientation to the diffusion field which causes the point defect sink interaction to become dependent on the spatial directions. The consequence of both effects is the so-called "Diffusional Anisotropy Difference" (DAD), a lattice direction dependent difference in the point defect diffusion of interstitials and vacancies [41].
The overall result of the described processes is a difference in the reaction constants for the interstitial-sink and vacancy-sink interactions which leads to the so-called "sink bias". The sink bias describes the difference between the different point defect fluxes to a certain defect sink. Even though interstitials and vacancies are produced in equal numbers during irradiation, and if it would be assumed that the production bias described above would be negligible, the sink bias in the material could lead to a local or general difference of the interstitial and vacancy number densities. This would result in the preferred nucleation of defect clusters like dislocation loops of specific type. The sink bias is thus generally observed as the dominant factor that determines the microstructural defect evolution and, on the long term, the macroscopic material deformation [10].

The explained process is, of course, an idealized one. It has to be considered that the described defect behavior will depend on parameters like the alloy's composition, chemical impurities, grain size and the associated grain boundary characteristics and second phase particle structure, to name but a few.

Based on the experimental and theoretical work during the last decades, the observed three-stage irradiation growth process can be described in more detail. Bacon [38] summarized the processes in hcp metals as follows: Stable interstitial loop nuclei are formed with a few self-interstitial atoms per loop, supposedly in replacement cascades under neutron irradiation. These loops are growing fast by self-interstitial diffusion parallel to the c-direction, leading to interstitial loops in the prism planes of type II. The extra material that is deposited on the prism planes leads to the growth transient that is observed at low doses (growth stage I). Then, vacancy loops nucleate and grow on the same planes; here, it is not known whether the loop nucleation is caused by neutron irradiation cascade collapse. Depositing vacancies at dislocations on the same type of planes as the interstitials decreases the growth rate to a very low value (growth stage II). The actually observed small rate could be caused by a small net deposition of self-interstitials at prism grain boundaries and vacancies at basal grain boundaries. The accumulation of more damage leads to the nucleation and growth of vacancy loops on the basal planes. This nucleation mechanism, which is possibly influenced by solute atoms, is unknown; however, the vacancy basal loops provide a ready sink for vacancies. Therefore, the presence of vacancy loops on the basal planes disturbs the balance of self-interstitial atoms and vacancies depositing on the prism planes, which leads to the acceleration of irradiation growth (growth stage III).

From Single Grain Growth to Component Growth

The described three-stage irradiation growth process leads to an expansion of Zr or Zr-based alloy single crystals along their a-axes and a shrinkage along their c-axis. How and to what degree this single crystal deformation affects the component as a whole depends strongly on the component's texture. For PWR guide tubes, the texture produced by the pilgering fabrication process consists of the majority of the grains' c-axes oriented radially, with their deviation from the radial vector within 30° to 40° [30]. The guide tube will thus shrink radially and expand axially, giving rise to the phenomenon of fuel assembly axial growth, as the guide tubes are in fixed connection to the assembly's top and bottom end piece. This process is demonstrated in Fig. 2.15. The schematic is, however, an idealized one. The real fuel assembly growth will occur simultaneously with irradiation creep and be a consequence of the irradiation induced dislocation structures in the single grains and the associated single grain deformation, the interaction of the single deforming grains via their grain boundaries and the macroscopic interaction of the different assembly components, i.e. guide tubes, spacer grids, fuel rods and hold-down springs. Each of these steps in itself is subject to a high number of variables which will be discussed in the following.

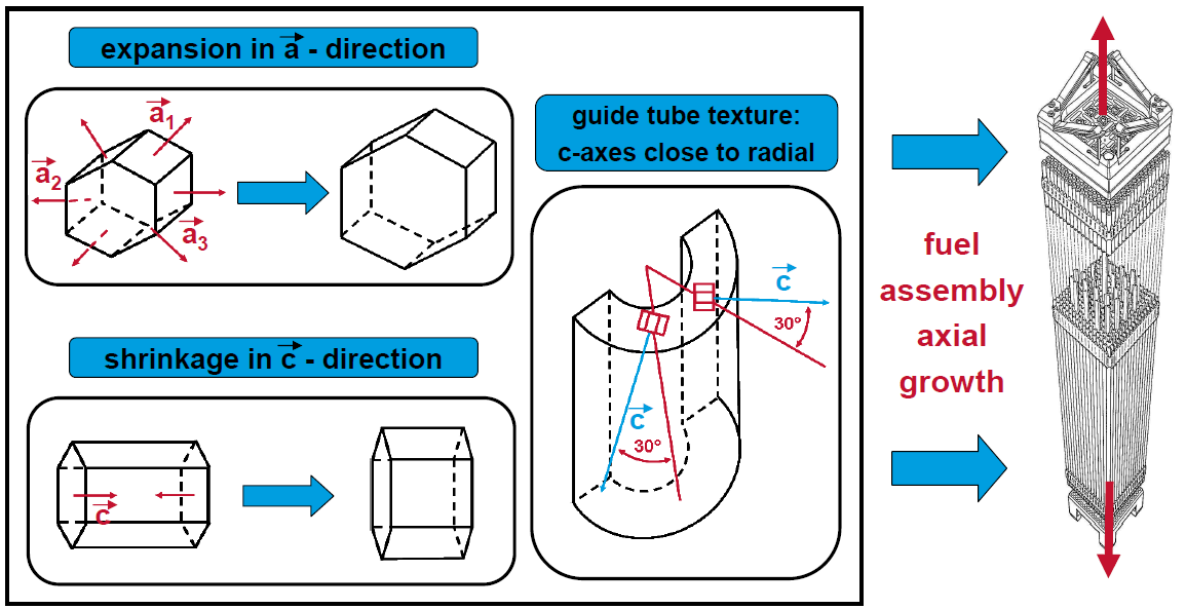

Figure 2.15: From single grain deformation to guide tube deformation; acc. to R.B. Adamson [30]

2.2.3 Parameters Affecting Irradiation Induced Guide Tube Deformation

Irradiation induced deformation of Zr-based alloys in PWR environments depends on various parameters. This section gives an overview of the relevant variables for irradiation deformation in general; then, it focusses on the factors that could be responsible for the unexpectedly high fuel assembly growth in several cases in some units, which occurred while other assemblies of similar design, reactor environment and operating history showed the predicted "normal" deformation behavior. Two of these parameters are the materials' hydrogen content and the external stress, whose effect was investigated in this work.

The following parameters are related to Zr-based alloy or fuel assembly deformation, as reported by Fidleris [11], Abromeit [59] and other authors [10]:

- **Neutron spectrum:** The neutron spectrum as the neutrons' energy distribution within a nuclear reactor defines the range of the energy transferred to the component material in neutron-target atom collisions. It is thus the decisive factor for the primary recoil energy distribution and the subsequent recoil cascade size and characteristics, which in turn define the initial point defect distribution and interaction in the target material. Irradiation damage in a test reactor with fast neutron spectrum can thus be expected to differ from the observed damage in a light water reactor with thermal spectrum.

- **Neutron flux:** The neutron flux defines the number of neutron-target interactions per unit volume and unit time. Time-dependent microstructural processes in the target material, like recoil cascade overlap or irradiation-induced dissolution of second phase particles can be expected to depend on the neutron flux.

- **Neutron fluence:** There is an obvious effect of neutron fluence on the irradiation induced deformation of Zr-based alloys: the observed three-stage growth process, and especially the occurrence of breakaway growth. From a microstructural point of view, the density of <a>-loops is described to first increase with the fluence and then approximate saturation, while the <c>-loops are reported to form only above a certain threshold fluence.

- **Temperature:** The irradiated material's temperature has a major influence on irradiation deformation. It directly affects the defect diffusion constants, as defect diffusion and migration increase with increasing temperature. Thompson described the defect migration rate, which defines the defect cluster growth and shrinkage and point defect recombination, to depend exponentially on the temperature [57].

- **Defect sink structure:** Due to the previously explained sink bias, the irradiation induced microstructure and the associated material deformation is strongly dependent on the presence, distribution and characteristics of defect sinks like initial dislocations from cold work, grain boundaries, second phase particles, alloying elements, foreign atoms and dislocations [10, 59]. These factors are usually defined by the fabrication process which leads to a given texture, grain size, alloying composition and second phase particle structure in the component. However, it has to be kept in mind that this defect sink structure is not a constant during the irradiation but changes continuously by the development of irradiation-induced defects, dislocations and local strain fields in the material or possible dissolution of second phases during irradiation.

- **Stability of second phase particles:** During the displacement process in the cascade, the material is locally in an overheated, molten state designated as "thermal spike". That phenomenon can lead to the formation of disordered or amorphous non-equilibrium phases, even though the local high temperatures fall to ambient temperature level in the range of 10^{-12} s. A damage cascade causes a shock wave in the material that can in certain cases result in a transport of interstitial displacement loops away from the interaction region [21]. The cascades lead to a disordering of the target's atomic structure that influences the behavior of alloy precipitates under heavy ion or neutron irradiation. Abromeit et al. [60] state two major atomic transport mechanisms under irradiation: atomic mixing and radiation-enhanced interdiffusion. The atomic mixing in the recoil cascade volume leads to dissolution of the preexisting mixtures of phases. Radiation-enhanced interdiffusion accelerates the system's return to the thermodynamical equilibrium and can either stabilize the previous mixture of phases or lead to flux-, defect- and atom species-dependent modified mixtures of phases.

- **Texture:** The respective component's texture defines how the irradiation growth of single grains affects the deformation of the component as a whole, as described above.

- **Alloying elements:** Hood reports that self-interstitial diffusion in α-Zr could be enhanced by Fe, Ni and Co due to an impurity-associated diffusion mechanism. Also, metallic solutes with small elemental radii are suspected to slow down the diffusion of vacancies and self-interstitial atoms: Undersized atoms in association with a self-interstitial are reported to build defects with lower mobility than the self-interstitials would have on their own [14]. Shishov et al. reported that the <a>- and <c>-loop population in neutron irradiated alloy Zr-1Nb-1.2Sn-0.35Fe ("E635") depends on the chemical composition, the phase mixture and the Fe/Nb-ratio [61]. For E635 with 0.15 %Fe, the evolution of <c>-loops and accelerated

growth was observed after a neutron dose of 15 dpa while E635 with 0.65 %Fe showed no <c>-loops up to 20 dpa. Hood specifically emphasized the role of Sn with regard to irradiation damage in α-Zr; Sn was observed to enhance interstitial-vacancy-recombination, as well as to attenuate vacancy clustering [14].

The parameters listed above are parameters that can be assumed to be relatively constant for fuel assemblies of the same design and production process, with comparable operating histories and in similar reactor environments. To better understand why some of these assemblies showed unexpectedly high growth, the focus is laid on the influence of two parameters which might vary even in otherwise comparable assemblies and reactor environments: the guide tubes' hydrogen content and the external stress.

Influence of the Alloy's Hydrogen Content

As all Zr-based alloy components in nuclear reactor environments, guide tubes pick up hydrogen during operation due to the corrosion reaction $Zr+2H_2O \rightarrow ZrO_2+2H_2$. Fig. 2.16 shows the typical range of hydrogen content in Zry-4 and ZIRLO guide tubes after fast fluences in the range of $9 \times 10^{21} cm^{-2}$ (E>1 MeV); the data was reported by King et al. for guide tubes from assemblies in the US units VC Summer and Wolf Creek [13]. The hydrogen content, which is strongly dependent on the alloy, increases with axial elevation due to the higher coolant temperature at higher axial positions which favors corrosion and thus hydrogen uptake. End-of-life hydrogen contents in Zry-4 guide tubes can reach ranges of up to 1000 wt.-ppm.

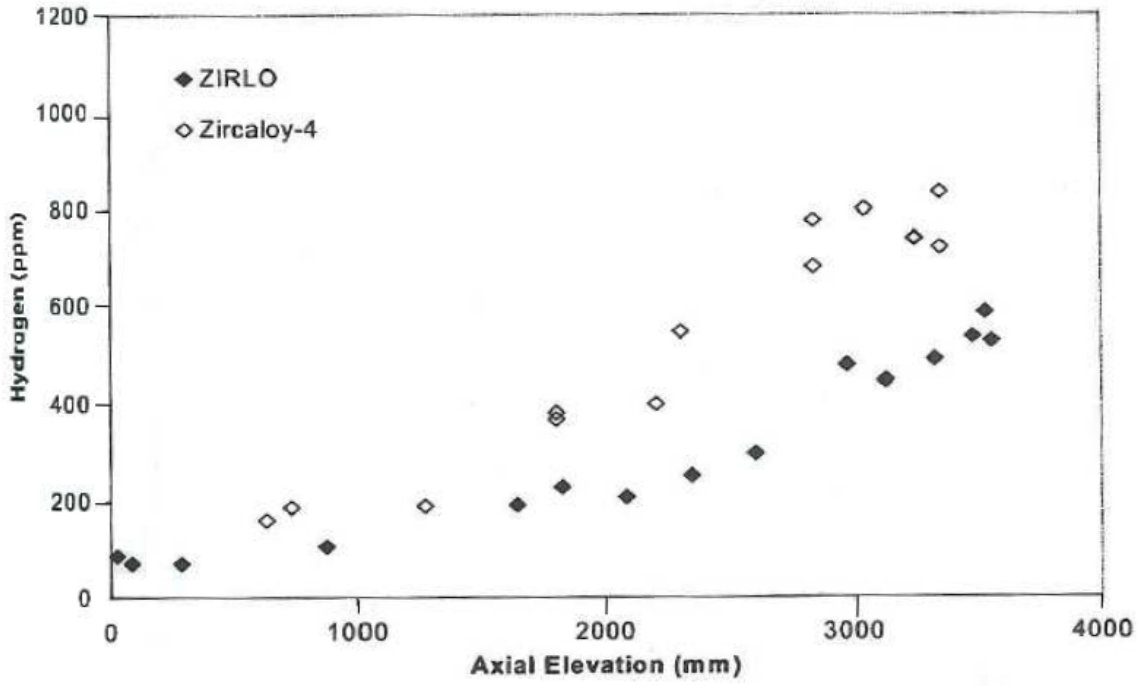

Figure 2.16: Hydrogen uptake in Zry-4 (fluence=$8.8 \times 10^{21} n/cm^2$, E>1 MeV) and ZIRLO (fluence=$9.5 - 9.6 \times 10^{21} n/cm^2$, E>1 MeV) guide tubes; H content in wt.-ppm [13]

Up to its solubility limit, the hydrogen is dissolved in the Zr matrix. Fig. 2.17 shows the terminal solid solubility of hydrogen in unirradiated Zry-4, measured by differential scanning calorimetry [62]. The T_{max} give the annealing temperatures of the samples; thus, the data in blue is from stress-relieved material while the data in red from recrystallized samples. The hydrogen solubility from the dissolution data shown in the plot at typical PWR temperatures of 300°C is in the range of 80 wt.-ppm. At room temperature, the solubility is close to 0 wt.-ppm.

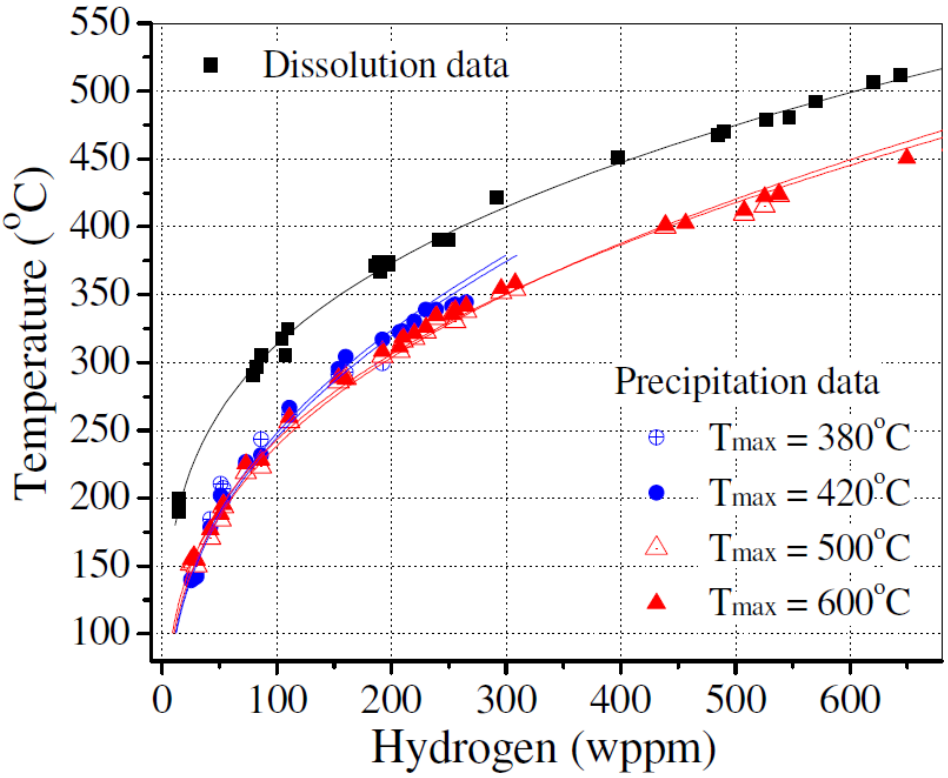

Figure 2.17: Hydrogen solubility in Zry-4 [62]

For hydrogen concentrations above the solubility limit, the hydrogen precipitates as zirconium hydride. At hydrogen levels lower than 1000 wt.-ppm, two hydride phases are reported to exist simultaneously in α-zirconium: the face-centered cubic δ-phase with the approximate composition of $ZrH_{1.6}$ and the face-centered tetragonal γ-phase, ZrH. While the δ-phase is described to form primarily intergranularly, the γ-phase tends to be intragranular; the hydrides are reported to precipitate with needle- or plate-like morphologies [63]. Cann et al. studied the influence of different parameters on the ratio between the δ- and γ-hydrides in α-zirconium. They found that the materials' oxygen content had a significant effect on the hydride ratio and concluded that the alteration of the yield strength by the oxygen may have an important effect on the nature of the formed hydride phases in α-Zr [63].
The hydrogen content under the solubility limit is in solution in the hcp α-Zr matrix. α-Zr with its large interatomic separation and a comparatively small ion-core radius of 0.079 nm [38] is a relatively open-structured metal; small atoms in α-Zr are reported to diffuse via the nominally empty interstitial sublattice generally faster than it would be possible by substitutional diffusion [14]. While substitutional diffusion would require the formation of a vacancy before the

substitute atom could jump to that new position and thus diffuse, interstitial diffusion needs only the activation energy for jumps between adjacent interstitial sites, thus leading to the observed higher diffusion coefficient. This corresponds to the observation that oxygen, nitrogen and hydrogen show, without exception, interstitial behavior in metal hosts. The relatively high solubility of these elements in α-Zr is assumed to cause a diffusion behavior that is largely insensitive to the state of the matrix [58].
The diffusion of hydrogen and oxygen in α-Zr is described to depend only weakly on the presence of alloying elements, at least at elevated temperatures. It was reported that the diffusion of small atoms in α-Zr is generally faster parallel to the c-axis than perpendicular to it, with the difference less than a factor of two [14].
McMinn et al. described the influence of chemical composition or microstructure on the terminal solid solubility to be small. They also studied the effect of CANDU reactor neutron irradiation on the hydrogen solubility in Zry-2 and Zry-4. They did not find an effect for fast fluences between $5.5\,\mathrm{x}\,10^{20}$ to $5.5\,\mathrm{x}\,10^{21}\,\mathrm{n/cm^2}$, but reported that Zry-2 with 75 wt.-ppm hydrogen irradiated to $1\,\mathrm{x}\,10^{22}\,\mathrm{n/cm^2}$ showed an increase of the hydrogen solubility that could not be completely recovered by annealing at 500°C for 1 h. From their observations, McMinn et al. formed the hypothesis that the irradiation damage sites after the high dose irradiation act as traps for hydrogen and keep the trapped hydrogen from contributing to the hydride precipitation and dissolution process. They based the hypothesis on reports of clear evidence for hydrogen trapping at vacancy defects and dislocation lines in Zr. Also, they referred to publications which describe that the irradiation induced microstructure inhibits hydrogen diffusion during irradiation [64]. The threshold fluence for the increase in solubility, and the fact that annealing at 500°C was insufficient to reverse the effect, would point to an important role of <c>-loops in the hydrogen trapping process.

To sum up, there are three different mechanisms to be considered when discussing the effect of hydrogen on irradiation induced guide tube deformation:

1) The material volume increase caused by hydride precipitation: With the hydrides' density lower than the density of Zr, the hydrogen precipitation leads to a volume increase of the Zr-based components. For a hydrogen concentration of about 1000 wt.-ppm in Zircaloy, this volume increase is in the range of 1 %, due to the density difference of about 16% between Zircaloy and zirconium hydride [65]. While King et al. [13] reported the guide tube and spacer grid volume increase due to precipitation to be independent of texture, a systematic preferential orientation of the needle-like hydrides in all hydrogen-loaded Zry-4 samples for this work was observed in the TEM. With guide tubes being textured components and Zr-based alloys having an anisotropic lattice structure, a possible preferential orientation of the hydrides, or the hydrides of a specific phase, with regard to the guide tube geometry cannot be excluded. Such preferential hydride precipitation would contribute to guide tube deformation. As guide tube hydrogen uptake increases with increasing axial position, following the oxide profile, [13] and depends on the assemblies' power history and time under irradiation, this effect can contribute with different strength to the deformation of guide tubes in different units, assemblies and also within one tube. Furthermore, the effect of hydride precipitation depends on the fluence: As described above, the hydrogen solubility in Zr increases for high fluences. Also, following the hypothesis of Cann et al. [63] on a dependence of the δ- to γ-hydride ratio on the material's yield strength, it might be possible that the irradiation hardening known to occur during neutron irradiation might lead to a different hydride type ratio. This would be relevant for deformation processes as the different hydride types have different densities and would thus contribute differently to the volume increase.

2) The direct interaction of hydrides with the irradiation induced defect structures: Second phase particles are typical sinks for point defects and can act as preferential defect type sinks in anisotropic materials [10]. The hydrides' size, density, phase, distribution and orientation to the lattice structure will thus define the interaction of the irradiation induced interstitials and vacancies with the hydrides, under the additional possible influence of external stress. Thus, the presence of hydrides could change the total number of point defects at a given fluence and also shift the interstitial to vacancy ratio in the material locally or generally; as a consequence, the presence of hydrides would directly influence the nucleation and development of the different dislocation loops.

3) The direct interaction of dissolved hydrogen with the irradiation induced defect structures: Gorodetsky et al. concluded from their studies on hydrogen-defect interaction in Mo and Ni (both cubic lattice structures) that hydrogen leads to an increase of the stability of radiation defects and defect clusters during their association and dissociation. They deduced a change in the defect cluster accumulation kinetics for defects of the same type. Also, they expected an essential increase in the probability of interstitial and vacancy recombination by the formation of stable and mobile self-interstitial-hydrogen-complexes. This might suppress the nucleation and growth of defect clusters [66]. In α-Zr, several experiments suggested an unexpectedly fast vacancy migration. Hood proposed the interaction of vacancies with another defect with a low migration energy as a possible explanation for this phenomenon; the interacting defect would either be another vacancy, a self-interstitial, a very mobile interstitial-like metallic solute or a hydrogen atom. He emphasized the fact that the interaction of hydrogen atoms with vacancies in metals is a well-known phenomenon [14]. Finally, the experiments and interpretations from McMinn et al. described above confirm an interaction between hydrogen and neutron irradiation induced defect structures, with an increase of the interaction for high fluences. This interaction was assumed to be due to hydrogen trapping in defects and dislocations [64]. Unpublished ab initio calculation work by other authors on the interaction between hydrogen and dislocation loops in α-Zr showed that the dislocation loops act as metastable and stable hydrogen traps, and that hydrogen can cause dislocation loop stabilization, depending on its position to the loops.

The sum of these interaction processes leads to the expectation that the hydrogen content of Zr-alloy components under neutron irradiation plays a major role in the components' irradiation induced deformation.

Influence of External Stress

The essential, and complex role of externally applied stress on the mechanisms leading from point defects to defect clusters, especially in the case of anisotropic lattice structures, was already described above (see the schematic in Fig. 2.15). A summarizing statement by G. Was on general loop nucleation, not only in anisotropic materials, should be emphasized again: "Interstitial loops will be more likely to nucleate on planes perpendicular to an applied tensile stress than parallel to the stress. Vacancy loops will be less likely to nucleate on planes perpendicular (non-aligned) to the tensile stress and more likely to nucleate on planes parallel (aligned) to the stress" [10].
It can therefore be assumed that external stress has a strong influence on the irradiation induced microstructure and the resulting irradiation induced component deformation. When discussing that influence, it has to be kept in mind that the stress distribution in the fuel assemblies can vary both in its magnitude and in its direction from assembly to assembly and also locally within single assemblies. Different initial hold-down spring forces and varying degrees of relaxation of

these spring forces during operation, the growth of an oxide layer that can cause axial tensile stress, coolant flow conditions and effects like cross flow, different irradiation deformation of spacer grids, fuel rods and guide tubes which can transfer mechanical stresses are some of the main contributors to the resulting final stress state of a specific part of the assembly.

2.3 Neutron Damage Simulation by Ion Irradiation

Neutron damage simulation by ion irradiation provides the advantages of very short irradiation times, the avoidance of target material activation, the easy experimental accessibility of the targets and the large parameter range for defined parameter studies. In addition, and most importantly, it offers the possibility of in-situ observation of the damage formation. However, the right selection of the experimental parameters for an ion irradiation experiment is crucial to the success of such a simulation. The essential parameters are the projectile element, its energy, the target temperature and the ion fluence and flux. In this section, the principal interaction mechanisms between ions and matter will be described, and the displacements per atom (dpa) concept will be introduced, a widely-used concept to match an ion or neutron dose to a specific irradiation spectrum and dose level. After a discussion of remaining constraints in the use of ion irradiation as a neutron irradiation analogue, a summary of several ion irradiation experiments for neutron damage simulation from the literature will be given.

2.3.1 Ions in Matter

Neutrons and charged particles interact with a target material by different physical processes. While neutron-target interaction is defined by the laws of strong interaction between the neutron and the target atom's nucleus, charged particle-target interaction is dominated by the laws of electromagnetical interaction of the charged projectile with the target atom's electron shell as well as with the target nuclei.
When an ion with kinetic energy in the MeV range enters a solid target material, it is stripped of all of its electrons; as a consequence, the initial charge state of the ion does not influence the damage it causes in the target. An atom passing through a crystal lattice loses energy by four different processes: collisions with nuclei, electronic excitation, ionization and emission of Bremsstrahlung. While mathematical descriptions of these processes are available, there is little experimental knowledge about the forces between metal atoms [10].
As long as the ion's energy is high, it is slowed down mainly by excitation and ionization of the target atoms' electron shells; during these processes, the ion's energy loss is small and its trajectory changes only insignificantly. In metals, the electron shell holes created by ionization or excitation are refilled by electrons from the conduction band in a short time frame; therefore, the result is the heating of the target, but no remaining changes in the target's structure as it would occur in insulators [57]. With the kinetic energy decreasing, the ion captures electrons from the target and thus reduces its Coulomb potential and the fraction of energy loss by excitation and ionization. The probability for atomic collisions with target atoms, which lead to higher energy loss and scattering angles, generally increases with decreasing ion energy and is the dominating energy loss mechanism at low ion energies. The projectile ion comes to rest in an interstitial site between lattice atom positions when its kinetic energy is too low for further displacement collisions. The total distance the ion passed before reaching that interstitial state, measured perpendicularly to the target surface, is called the ion's "range".

The energy loss per unit length can therefore be described by a parameter which consists of an elastic collision, electronic (excitation and ionization) interaction and radiation loss part, the stopping power S:

$$S = \left(-\frac{dE}{dx}\right)_{total} = \left(-\frac{dE}{dx}\right)_{elastic} + \left(-\frac{dE}{dx}\right)_{electronic} + \left(-\frac{dE}{dx}\right)_{radiation}$$

As energy loss by radiation is small, Bremsstrahlung can usually be neglected.

Collision processes between atoms are described by interatomic potentials V(r), r being the atoms' distance; the general form of an interatomic potential would be a central field repulsive force for small atom-atom distances and a Coulomb force dominating at larger distances. There is, however, not a single interatomic potential describing the whole atom mass and energy range; different energy ranges require the description by different interatomic potentials. According to Was [10], heavy ions with energies up to 1 MeV (as would be the case for the 1 MeV Kr irradiations in this work, and the main part of the recoil cascades following the collision) can best be described by an inverse square approximation:

$$V(r) = \frac{2E_r}{e}(Z_1 Z_2)^{5/6}\left(\frac{a_0}{r}\right)^2$$

where Z_i are the atoms' atomic numbers, e is the elementary charge, a_0 is the Bohr radius and E_r the Rydberg constant. Depending on projectile element, energy range and target properties, more refined interatomic potentials have been developed.
To receive the elastic collision part of the stopping power, the scattering cross section $\sigma(E_i,T)$ is calculated, with E_i being the energy of the incident atom and T the kinetic energy transferred during the collision. The differential scattering cross section is determined by the geometry of the collision [10]:

$$\sigma(E_i, T) = 2\pi T b \frac{db}{d\theta}\frac{d\theta}{dT}.$$

θ is the scattering angle and b the scattering parameter. The differential scattering cross section describes the probability of an incident particle of energy E_i to be scattered from an area 2πbdb into the angular element dθ at scattering angle θ with energy transfer T. The scattering geometry is defined by the specific interatomic potential for the scattering reaction.
With the scattering cross section known, the average transferred energy $\overline{T}$ can be calculated [10]:

$$\overline{T} = \frac{\int T\sigma dT}{\int \sigma dT}.$$

The mean free path of the atom between the collisions is defined as $\lambda = 1/\sigma N$, where N is the atom number density of the target. The ratio of the average energy transferred and the mean free path is then the stopping power [10]:

$$\left(-\frac{dE}{dx}\right)_{elastic} = -\frac{\overline{T}}{\lambda} = N\int_{T_{min}}^{T_{max}} T\sigma(E_i, T)dT.$$

As opposed to energy loss by collisions, energy loss by ionization or excitation is rather a continuous process than a sequence of single events. Electronic energy loss can be classically described by collisions between a moving heavy charged particle with an electron at rest; this approximation is valid for ion velocities higher than the velocity of the tightest bound electron [10]. A

more exact description is provided by the so-called "Bethe-Bloch formula", which is received by relativistic quantum mechanical calculations based on the Born approximation [10,67]:

$$\left(-\frac{dE}{dx}\right)_{electronic} = \frac{4\pi k_0^2 Z^2 e^4 n}{mc^2\beta^2}\left[\ln\frac{2mc^2\beta^2}{I(1-\beta^2)} - \beta^2\right] \tag{2.1}$$

$k_0 = \frac{1}{4\pi\epsilon_0}$ with ϵ_0 being the electric field constant, Z is the atomic number of the incoming ion, e the elementary charge, n the number of electrons per unit target volume and m the electron rest mass. $\beta = \frac{v}{c}$ with v the ion's velocity in the target and c being the speed of light in vacuum. I is the mean excitation energy of the target and describes the average necessary energy to excite target atom shell electrons. The mean excitation energy can be approximated by an empirically found formula [67]; for Z>13, I is given as $I \approx 52.8 + 8.71\,Z\,eV$; for Zr with atomic number 40, I is thus in the range of 400 eV. If the target material is an alloy, the mean excitation energy is calculated by the sum of the mean excitation energies of the different elements, weighted with their atomic fraction in the alloy. The Bethe-Bloch formula cannot be applied for very low ion energies because the logarithmic term would become negative [67,68].

The total stopping-power as a function of the target depth describes a peaked profile, increasing from high ion velocities to reach the peak when enough projectile energy is lost that atomic collisions become dominant, and decreasing for even lower energies. The defect profile in the target material follows that peak, as a high stopping power corresponds to a high energy transfer to recoils and consequently a high defect density in the region of that recoil. The damage peak is called the "Bragg peak"; in metals, its typical full width half maximum for heavy ions with energies in the MeV range is around 1 μm [67]. Fig. 2.19 gives an example for the resulting peaked recoil distribution for 1 MeV Kr in Zry-4, with a typical TEM foil thickness marked in the plot.

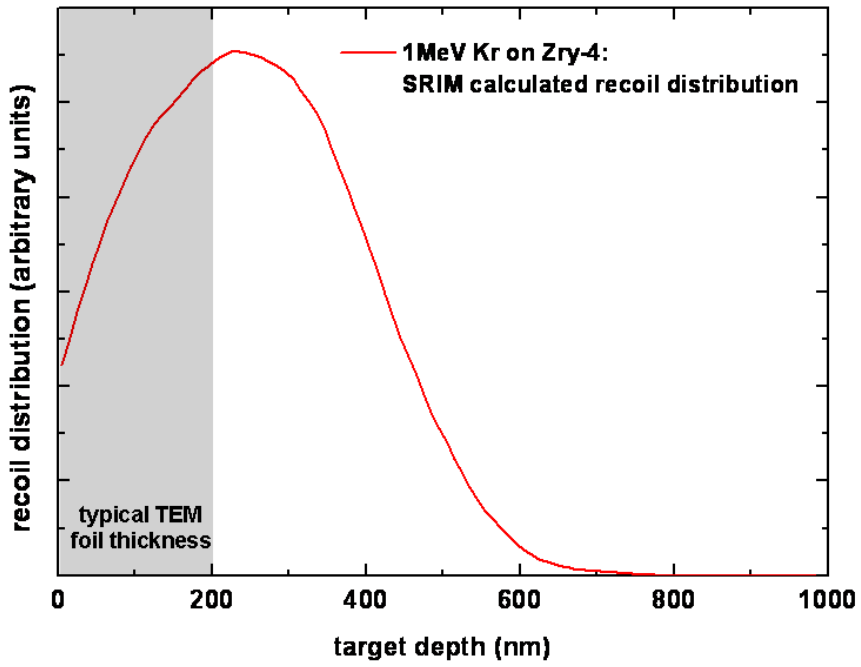

Figure 2.18: Position of the TEM foil within the 1 MeV Kr damage peak in Zry-4

This peaked stopping power profile is the reason why heavy ion damage is concentrated in a very thin layer with a depth of only several μm from the target's surface, while neutron irradiation leads for a spatially constant neutron flux to a homogeneous defect density over several cm depth of the target material. Consequently, for a comparable particle flux with the same average energy transfer to the target atoms, heavy ion irradiation reaches a specific target damage level orders of magnitude faster than neutron irradiation with the same particle flux.

The projectile-target interaction processes define the energy and trajectory of the primary knock-on atom, which is the starting point for the subsequent displacement cascade that takes place in the target. If ions are planned to be used for neutron simulation, the approach is to choose ion irradiation conditions that produce recoil cascade characteristics as similar as possible to the cascades produced by the respective neutron spectra. For the ion species, there are two self-evident choices. On the one hand, ions could be chosen with their mass and thus their collision characteristics as similar to neutrons as possible, to create similar kinetic energy transfer to the primary knock-on atoms; the best choice for this method would be protons with an energy spectrum comparable to LWR neutrons, as they have the same mass as neutrons. On the other hand, heavy ions could be chosen with their mass as similar to the target's main element as possible. By such an irradiation, the first collision process between neutron and nucleus would be skipped, and the projectile ion would take the role of the primary knock-on atom in the target. This process is demonstrated in Fig. 2.19. The process will match the neutron irradiation as closely as possible if self-ions are used for the irradiation, in this case Zr.

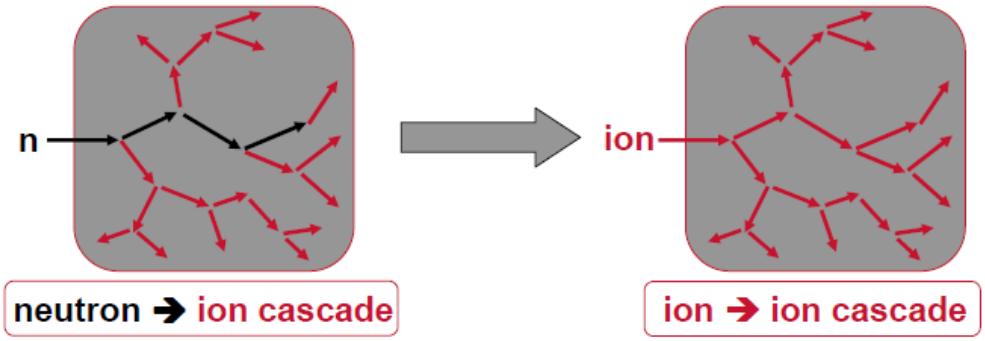

Figure 2.19: Schematic: self-ion irradiation as a neutron irradiation analogue

For the experiments in this work, heavy ion irradiation was chosen to simulate the neutron damage. The main argument for this choice was the significantly higher stopping power of heavy ions in matter as compared to light ions, which shortened the necessary irradiation times for dose levels comparable to PWR end-of-live conditions from several days to several hours. For the part of the irradiations where bulk foils were the targets and the projectile ions thus remained in the target, Zr projectiles were used. In the irradiation experiments with the projectiles in transmission, both Zr and Kr were chosen. It is not expected that the choice of Kr has significant influence on the irradiation microstructure, as it is close in mass to Zr, and only about 10 to 15% of the projectiles remain in the target for the chosen conditions, according to calculations with the SRIM code [69]. In addition, Kr as a nobel gas is chemically inert; therefore, chemical interaction between projectile and target is unlikely.

2.3.2 The Displacements per Atom Concept

For the simulation of PWR neutron damage with any other kind of projectile or energy spectrum than PWR neutrons, it is necessary to study the damage level and characteristics caused by PWR neutron irradiation; then, the irradiation parameters of the substitute particles have to be adjusted in a way that the same damage levels in the target material are reached. There are differences in the damage levels caused by the same neutron fluence in different nuclear reactors, depending on the neutron energy spectrum; the damage in a target material irradiated to the same neutron fluence in a material test reactor with a fast neutron spectrum will deviate from the damage caused by the same fluence in a light water reactor with thermal neutron spectrum. To be able to compare neutron damage in different reactor types, the displacements per atom (dpa) concept has been introduced; the dpa level is calculated by dividing the total number of displaced atoms in a certain material volume during irradiation by the total number of atoms in that volume. It is thus a measure of how often each atom in the target has been replaced from its lattice site. The dpa concept takes not only the total number of incoming neutrons, i.e. the fluence, into account, but also the amount of transferred energy to the material and the resulting number of atoms in the displacement cascades. The success of that concept is demonstrated in Fig. 2.20, taken from the textbook on radiation materials science by G. Was [10]. It compares the yield stress change in 316 stainless steels under irradiation for three neutron sources of different spectra: OWR is a test reactor with typical LWR spectrum, RTNS-II is a pure 14 MeV neutron source and LASREF has a broad high energy neutron spectrum. While a direct correlation cannot be seen when plotting the yield stress change against the fast fluence, the correlation is clearly given when comparing the data based on dpa.

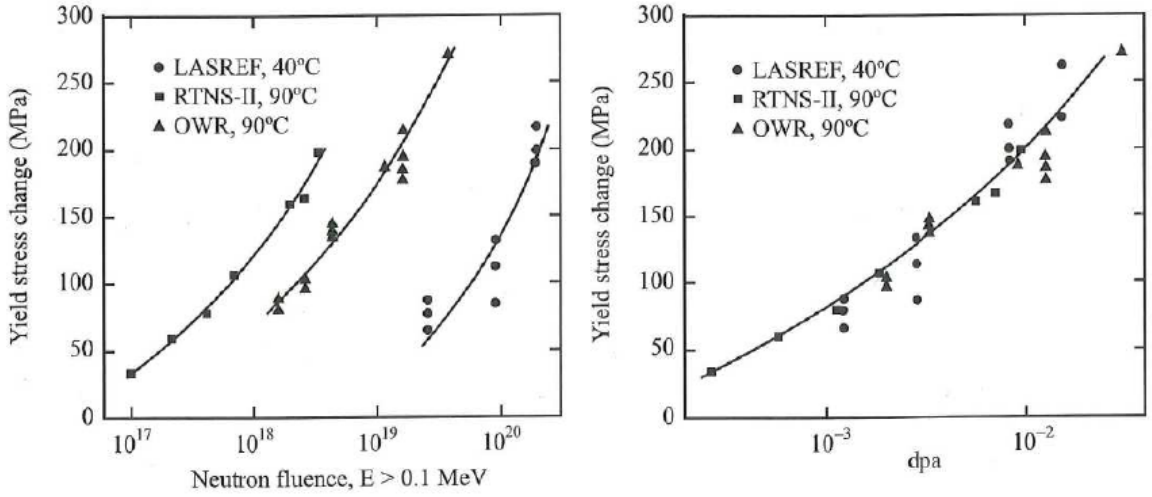

Figure 2.20: Irradiation effect correlation: fluence vs. dpa [10]

Due to the dpa concept's success in comparing different neutron spectra, it is also applied to compare radiation damage caused by different particle species, i.e. neutrons, electrons and light or heavy ions.

Dpa Calculation for Neutron Irradiation

The number of displacements in a target material unit volume under neutron irradiation occuring per unit time depends on the initial number of target atoms per unit volume N_0, the energy dependent neutron flux $\varphi(E)$ and the energy dependent damage cross section $\sigma_D(E)$, which describes how many target atoms are displaced per incoming neutron with energy E [10]:

$$\dot{N}_d = N_0 \int_{E_{min}}^{E_{max}} \varphi(E)\sigma_D(E)dE$$

The displacement cross section is given by

$$\sigma_D(E) = \int_{T_{min}}^{T_{max}} \sigma(E)\nu(T)dT$$

where T is the energy transferred from incoming particle to target atom and $\nu(T)$ the number of interstitial/vacancy-pairs produced by one incoming particle. $\sigma(E)$ is the elastic cross section for neutron-target atom collisions. The displacement cross section used for this calculation is the sum of the microscopic displacement cross sections of the different atom species in the target.
The total damage density D for an irradiation timeframe between t_0 and t_1 can then be calculated as follows [10]:

$$D = \frac{N_d}{N_0} = \int_{t_0}^{t_1} \int_{E_{min}}^{E_{max}} \int_{T_{min}}^{T_{max}} \varphi(E)\sigma(E)\nu(T)\, dT\, dE\, dt$$

A typical PWR neutron spectrum (see Fig. 2.12) shows an energy distribution over several orders of magnitude. Since neutrons with energies down to several 100 eV can displace target atoms, and since the number of recoil atoms in a cascade does not show a linear behavior with the neutron energy, a reliable dpa calculation has to be based not on an average neutron energy value but on a multigroup approximation of the neutron spectrum. For PWR cladding, Shishov et al. reported that a fast fluence of $6 \times 10^{24} nm^{-2}$ (E >1 MeV) correspond to 1 dpa [36]; this conversion factor will be used throughout this work for the comparison of neutron damage levels to ion damage.

Dpa Calculation for Ion Irradiation

The irradiation damage for ions is not spread homogeneously over the target material but leads, after a region with relatively low collision damage, to a damage peak. The peak's depth in the target depends on the projectile element and its kinetic energy as well as on the target's chemical composition and its lattice structure.
For ions, the displacements per atom in the target can be calculated from the number of displacements caused by ions in the damage peak region divided by the total number of atoms in the damage peak region:

$$D = \frac{N_d}{N_0}$$

The total number of atoms in the damage peak region, N_0, depends on the target's density ρ, the beam spot area A and the damage peak's thickness d. For ions being used in transmission, d would be the thickness of the irradiated sample region:

$$N_0 = \frac{\rho \cdot A \cdot d}{M_{mol}} \cdot N_A$$

M_{mol} is the molar mass of the target material, and N_A is Avogadro's constant.

For a measured beam current I at the accelerator with ion charge state C and beam spot area A, the ion flux ϕ is defined as the number of ions per unit area and unit time:

$$\phi = \frac{I}{e \cdot C \cdot A}$$

Integrating the ion flux over the total irradiation time t_{irr}, the total number of ions sent into the sample per unit area is given by the ion fluence F:

$$F = \int_0^{t_{irr}} \phi(t) dt$$

For constant ion flux, the fluence is the flux multiplied by the total irradiation time.

The total number of ions sent into the sample on the beam spot area A is given by

$$N_{ions} = F \cdot A$$

Then, the total number of displacements induced in the sample can be calculated as follows:

$$N_d^{tot} = N_{ions} \cdot N_d^{1ion}$$

N_d^{1ion} is the average number of displacements induced by one ion and can be calculated with the SRIM Monte Carlo code [69].
For the irradiation of bulk material, the number of displacements in the heavily damaged region, the damage peak, can be calculated by multiplying the total number of displacements with the fraction f of the displacements induced in the damage peak region:

$$N_d = N_d^{tot} \cdot f$$

The fraction of displacements in the damage region can be derived from the SRIM code results. For ions in transmission, the SRIM calculation input would include the low thickness of the material, and f would be set to 1.

Finally, the displacements per atom created in the damage peak region for a constant ion flux on the sample are defined as follows:

$$\boxed{\frac{N_d}{N_0} = \frac{I \cdot t_{irr} \cdot N_d^{1ion} \cdot f \cdot M_{mol}}{e \cdot C \cdot \rho \cdot V \cdot N_A}}$$

Based on the work by Shishov et al. [36,70], fast PWR neutron fluences (E>1 MeV) for end-of-life conditions in the range of 10 - 12 x 10^{21} n/cm^2 correspond to damage levels roughly between 17 to 20 dpa and PWR fuel assembly burnup in the range of 60 MWd/kgU. Therefore, the ion fluences for the irradiation experiments in this work have been chosen to correspond to or to exceed this range.

Deviations between Ion and Neutron Irradiation Experiments

Despite the many advantages offered by neutron damage simulation with heavy ions, there remain some deviations between the processes that cannot be overcome. For ion irradiation in transmission, the dominating effect can be assumed to be the low thickness of the irradiated TEM foil of around 200 - 300 nm as compared to the bulk guide tube material in a PWR. The TEM foil surfaces can be expected to act as defect sinks for defects forming near the surface region, which would reduce the point defect number in the foil. Therefore, defect densities in these regions might differ from the ones observed in bulk material, which might lead to differences in the microstructure. Another important point is the different damage rate; microstructural phenomena in general can be expected to show a variety of dose rate dependencies [71]. While guide tubes in a PWR take several years to reach their end-of-life dose, ion irradiated samples gain the same dose in a matter of hours. It is possible that long-term material relaxation or defect annealing effects that are active in a PWR environment cannot take place within the short irradiation time in an ion irradiation experiment. Also, the local high concentration of the damage events under ion irradiation as compared to neutron irradiation might lead to damage cascade overlap effects that might not occur in a nuclear reactor, due to the mean free path of neutrons in Zr of several cm.
However, the results presented in the next sections will show that despite those constraints, it is possible to produce typical PWR neutron damage structures by heavy ion irradiation in Zr-based alloys, under the chosen experimental conditions.

2.3.3 Selected Examples from the Literature

Experimental and theoretical work on neutron damage simulation by electrons or ions has been published for many years, mostly on materials with application in fission or fusion reactors. With zirconium alloys being a typical nuclear reactor structural material, there are many publications on charged particle irradiation of zirconium and its alloys. While most of the experiments compared the evolving ion irradiation damage to known neutron damage structures, there are also some publications available on ion irradiation induced macroscopic material creep and growth. The respective irradiation conditions and material parameters are differing over a wide range, due to the different objectives of the experiments and the available experimental capabilities.
Motta et al. [72] analyzed the different amorphization characteristics of $Zr(Cr,Fe)_2$ and $Zr_2(Ni,Fe)$ precipitates in Zircaloy under neutron, electron and ion irradiation in 1991. They reported that the critical temperatures, above which amorphization is not practically attainable, are varying for the three different projectiles. In their conclusion, they stated charged particle irradiation to be a useful tool for the studying of irradiation-induced processes; however, they warned that all comparisons to neutron irradiation damage should be done with care because of the different damage and annealing processes for the different projectiles.
In the IAEA technical meeting about "Accelerator Simulation and Theoretical Modelling of Radiation Effects" in 2008, Ryanzanov presented a comparison between neutron irradiated and proton (10 MeV) and helium (4 MeV) irradiated Russian Zr-based alloys with damage levels of 1 and 2 dpa [73]. The performed TEM analyses showed a similar <a>-type dislocation loop structure in all samples with regard to size and density. In the He irradiated samples, <c>-loops were found. Ryanzanov concluded that there is a good correlation between microstructural changes in irradiated Zr alloys after neutron and charged particle irradiation at comparable dpa level.
Tournadre et al. [74] presented work on 2 MeV proton and 600 keV Zr irradiation of Zry-4 at 300°C in 2011. They reported the observed <c>-loops to be smaller and more numerous after

Zr irradiation than found in neutron irradiated material; for proton irradiation, however, they described a homogeneous distribution of large <c>-loops, close to the known neutron-irradiation microstructure.

There is also some literature on the macroscopic creep and growth of Zr or Zr-based alloys under ion irradiation. Terasawa et al. [75] examined irradiation creep of pure zirconium under 4 MeV proton irradiation under stress in 1984. The used sample thickness was lower than the range of the protons to avoid hydrogen implantations in the material. At temperatures lower than 300 °C, they found that the creep strain was enhanced by irradiation, as it is also known to occur during in-pile neutron irradiation.
Chapman et al. [76] used 6 MeV protons in transmission at 280°C and 235°C to compare the creep and growth of Zircaloy-2 under proton irradiation with in-pile irradiation data from the DIDO material test reactor in Harwell in 1984. At 280 °C, the growth behavior under ion irradiation was stated to be in excellent agreement with the in-pile results. However, the results varied for the different irradiation methods for 235 °C. Based on profound data analysis, the authors concluded that the prediction of absolute creep and growth rates in thermal reactors by proton irradiation is generally good and that the respective creep equations are very close for both methods except for the dose dependence.

In conclusion, the available published work shows a wide range of experimental parameters, and different degrees of comparability between neutron damage and ion damage. The similarity between the ion induced damage structures to neutron damage is obviously strongly dependent on the chosen experimental and material parameters. Therefore, the experiments conducted in this work were not done on model alloys but industrial PWR guide tube alloys, and the irradiation temperatures and dpa levels were kept as closely as possible to PWR operating conditions. These conditions are expected to lead to the best possible similarity in the ion induced and neutron induced irradiation damage, and to the most reliable comparability of the observed microstructural effects to neutron irradiation damage.

Chapter 3

Experimental Methods

The following chapter provides an overview of the experimental methods used in this work. After a description of the ion damage level calculations with the SRIM Monte Carlo code, the tandem accelerator principle of operation is explained and the applied irradiation damage examination techniques are presented. Parts of the section are adopted from a first-author paper published in the Journal of Nuclear Materials in 2012 [77].

3.1 Ion Damage Simulation with the SRIM Code

The Stopping and Range of Ions in Matter program ("SRIM") is a widely used Monte Carlo code for the simulation of the energy loss and scattering behavior of ions in matter [69]. It allows the calculation of ion ranges and recoil numbers, distribution and energies for a wide spectrum of target elements and user-defined compounds in a large projectile ion energy range. However, it has to be kept in mind that the results are still an approximation, as details like the target's lattice structure or lattice orientation to the beam cannot be included; while the density of the target material can be defined by the user, the atoms are assumed to be homogeneously distributed as in an amorphous material. For the specific case of the samples in this work, this means to disregard the anisotropic lattice structure, the samples' texture and the presence of second phase particles. To minimize the error source from the neglected crystal lattice, the displacement energy of the target elements (the lattice and orientation dependent energy which is necessary to remove a lattice atom from its site in the crystal) can be defined.
For the ion induced damage level calculations, SRIM was used in the "detailed calculation with full damage cascades" mode for 1000 projectile ions with the kinetic energies used in the different irradiation experiments [69]. For the M5® samples irradiated at room temperature, the target was designed of 99 wt.-% Zr and 1 wt.-% Nb with the room temperature density of the alloy of ρ=6.50 g/cm^3. For the 300°C simulations, the target's thermal expansion was taken into account, which leads to a density of ρ=6.46 g/cm^3. A displacement energy of 40 eV for hcp Zr was chosen, as recommended by the ASTM norm reference test standard [10,36]. While only about 0.3 wt.% Nb are dissolved in the Zr matrix at 300°C [78], the remaining 0.7 wt.-% Nb are precipitated as bcc β_{Nb}; thus, based on the recommended displacement energy for bcc Nb, 60 eV [10], a weighted average binding energy of 54 eV was used for Nb in M5®. The calculations for Zry-4 were done for 1 MeV Kr on a target consisting of the main alloying elements as given by the samples' ingot's certificate: 98.22 wt.-%Zr, 1.3 wt.-%Sn, 0.23 wt.-%Fe, 0.11 wt.-%Cr and 0.14 wt.-%O; the displacement energies for all elements in Zry-4 were chosen to be 40 eV. The density corresponds

to the density of M5®. For all calculations, the lattice and surface binding energies were set to 0 eV, as advised by R. Stoller [79]. The number of displacements per ion, N_d^{1ion}, and the ion penetration depth d (for those samples that were not irradiated in transmission) are provided by the SRIM calculations. Then, the damage level D in dpa can be calculated as described in section 1.3.2.:

$$D = \frac{F \cdot N_d^{1ion} \cdot M_{mol}}{\rho \cdot d \cdot N_A}$$

F is the ion fluence, M_{mol} the target's molar mass and N_A Avogadro's constant.
For the in-situ ion irradiation, the ions were used in transmission; d is then the thickness of the electrolytically thinned TEM foil at the position of the observed grain. For the samples that were not irradiated in transmission but as bulk foils, the dpa calculation is based on the damage depth distribution given by SRIM. For sample M1 which was irradiated with 40 MeV Zr, the SRIM calculations provided a recoil distribution peak with full width half maximum of 1.5 μm; the calculation results showed 70 % of the displacements to have occurred within that peak region. For the foil samples irradiated at the lower energies of 2.5 and 3 MeV, the damage peak is spread out without significant variation to ion ranges of 1.2 μm and 1.3 μm, respectively. Thus, the whole ion range was used as "thickness" d of the irradiated layer, with 100% of the displacements occurring within that layer.
Table 3.1 summarizes the irradiated samples, the observed grains' thickness (or damage peak thickness for the foil samples) d, the calculated number of displacements per ion and the fraction of transmitted atoms per ion.

sample	alloy	type	H	d	ion	E_{ion}	displ./ion	transm. atoms/ion
M1	M5®	foil	≤ 3	1500	Zr	40	46538	0
I1	M5®	foil	≤ 3	1300	Zr	3	20973	0
I2	M5®	foil	≤ 3	1300	Zr	3	20973	0
I3	M5®	foil	≤ 3	1300	Zr	3	20973	0
I10	M5®	foil	≤ 3	1200	Zr	2.5	19548	0
A1*	M5®	TEM	≤ 3	150	Kr	1	2692	0.9
A2	M5®	TEM	≤ 3	181	Kr	1	3350	0.9
A3	M5®	TEM	110	197	Kr	1	3911	0.9
IA1*	Zry-4	TEM	≤ 7	200	Zr	1	4810	0.8
JA1	Zry-4	TEM	≤ 7	219	Kr	1	4651	0.9
PA2	Zry-4	TEM	≤ 7	247	Kr	1	5329	0.8
PB3	Zry-4	TEM	186	191	Kr	1	3782	0.9
PC4 grain 1	Zry-4	TEM	405	424	Kr	1	9236	0.3
PC4 grain 2	Zry-4	TEM	405	489	Kr	1	10123	0.1
PZ grain 1	Zry-4	St-TEM	≤ 7	337	Kr	1	7670	0.6
PZ grain 2	Zry-4	St-TEM	≤ 7	478	Kr	1	9871	0.2

Table 3.1: Summary of the irradiated samples:
H=hydrogen content in wt.-ppm, d=grain thickness/damage peak thickness in nm, E_{ion}=ion energy in MeV
"St-TEM"=tensile specimen for TEM
* = grain thickness not measured but estimated

3.2 Ion Irradiation and Post-Irradiation Examination

3.2.1 Ion Irradiation Facilities

Acceleration principles for heavy ions are, due to their electric charge, based on electric fields. The tandem accelerator principle has been established for decades and is used in accelerators for all mass numbers and an energy range from several tens of keV to several 100 MeV. Fig. 3.1 gives a schematic of the principle of operation.

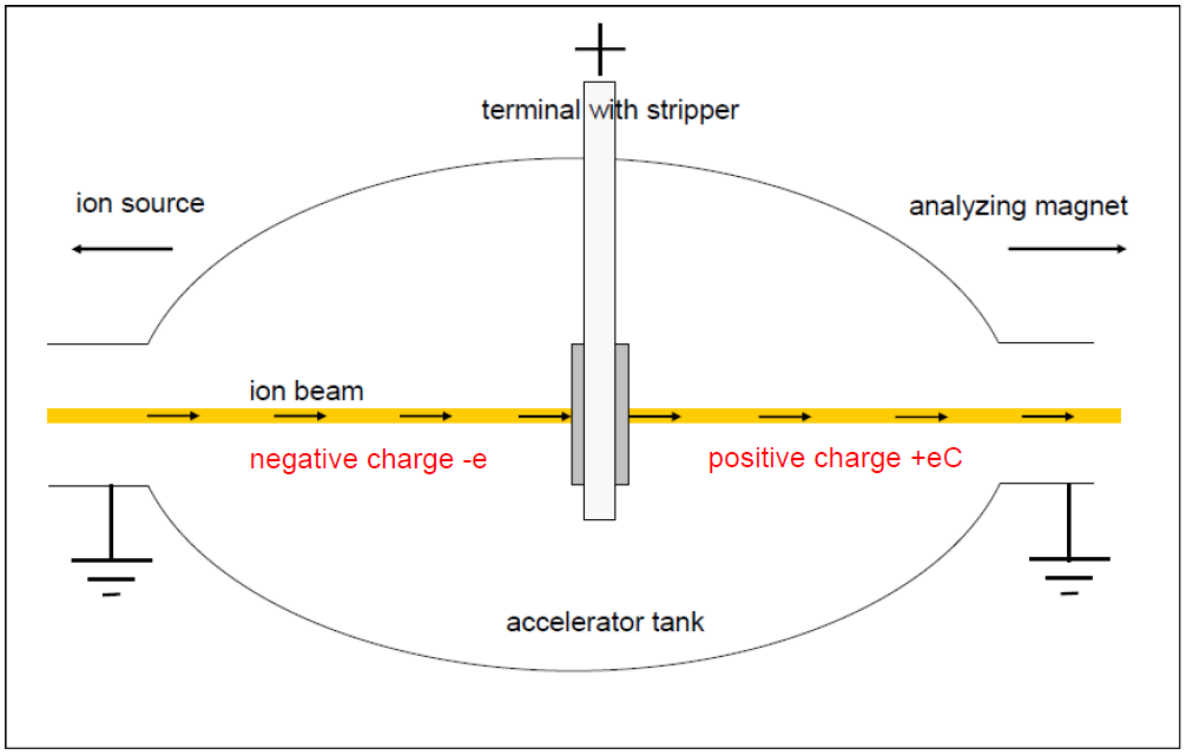

Figure 3.1: Schematic of the tandem accelerator principle of operation [80]; e=elementary charge, C=ion charge state

Ions of the desired element are produced in an ion source. While there are several different ion source principles, the Maier-Leibnitz Laboratorium's (MLL) and the Max-Planck Institut für Plasmaphysik's (IPP) accelerators use sputter ion sources. The projectile element in solid state, pure or in molecular form, is located in the sputter target, a cone-shaped copper form. Caesium is being evaporated adjacent to the cone, partly condensating on the cooled sputter target. Another part of the Cs steam is ionized at an ionizer and accelerated towards the target. The Cs ions' impact removes atoms from the target which pass through the condensed Cs layer, where they have a significant probability of taking up an electron. The then once negatively charged ions are accelerated from the source by an electric field towards the accelerator tank. The tandem accelerator tank is a vacuum tank with typical pressures in the range of 10^{-6} to 10^{-7} mbar. In the center of the tank, the positively charged high tension terminal is located with an electron stripping material in line with the ion beam; the stripper is either a carbon foil ("foil stripper", with thickness 4μg per cm^2 at MLL) or a volume filled with stripper gas ("gas

stripper", filled with air at $5 \cdot 10^{-4}$ mbar at MLL). With a positive high tension U_{acc} applied at the terminal, the once negatively charged ions are accelerated towards the terminal, gaining the kinetic energy $e \cdot U_{acc}$ until they pass the stripper. The stripper material removes, depending on ion type, stripper material and ion energy, one to several electrons, thus producing a beam of C times positively charged ions. Those ions are then repelled from the positively charged terminal to the end of the tank which is held at ground state, gaining $C \cdot e \cdot U_{acc}$ in kinetic energy. The ions then leave the tank with a total gain in kinetic energy of $(C+1) \cdot e \cdot U_{acc}$. The ion beam, which is focussed at several stages before and behind the tank with electromagnetic quadrupole lens systems, then passes an analyzing magnet, where the ions are radially deflected in the magnetic field, depending on their charge state. The desired charge state, which corresponds to the desired ion energy, is then focussed in the center of the beam tube and led to the experiment while the ions of other charge states are blocked [81–84]. The beam's intensity is typically measured by metallic cups ("Faraday Cups") which can be inserted into the beam or are located on the sample holder next to the target position within the beam spot or scanning area. They are electrically insulated against the beamtube and sample holder and measure the transported electric charge per unit time; this charge rate measure can be used to calculate the ion flux ϕ:

$$\phi = \frac{I}{C \cdot e \cdot A}$$

where I is the measured charge per time unit, C is the ions' charge state, e is the elementary charge and A the cross section area of the ion beam seen by the cup. Typical ion beam current measurement errors are in the range of 10%. The total number of ions per target area, the fluence F, is received by integration of the ion flux over the time of irradiation:

$$F = \int_0^{t_{irr}} \frac{I}{C \cdot e \cdot A}\, dt.$$

Three different tandem accelerators were used for the irradiation experiments in this work. The MLL tandem accelerator in Garching, Germany, is a high voltage accelerator for ion masses up to A=238 with a maximal terminal voltage of 14 MV [83]; depending on the projectile elements, it reaches ion energies from several MeV to more than 100 MeV. The second accelerator is part of the IPP in Garching, Germany, with a maximum accelerating voltage of 3 MV. Typical irradiations at that facility are hydrogen, deuterium or helium implantations with energies of several 100 keV; however, Zr with 1, 2.5 and 3 MeV showed to provide a stable beam as well, even though the beam current for 1 MeV was comparatively low. The third accerelator is the tandem accelerator of the IVEM (Intermediate Voltage Electron Microscope) Tandem Facility of Argonne National Laboratory (ANL) near Chicago, IL. The accelerator with a maximal terminal voltage of 500 kV is mostly used for intermediate mass elements in energy ranges of 1 MeV. The accelerator's beam tube is attached to a Hitachi H9000 300 keV transmission electron microscope (TEM) with an angle of 30° to the beam axis of the microscope, thus enabling in-situ TEM imaging during the ion irradiation. Fig. 3.2 shows photographs of the respective accelerators and the sample holders; the picture of the TEM holder is taken from a TEM lecture by D. Gerthsen [85]. For the irradiation of pre-thinned TEM samples at the IPP accelerator, a special sample holder was built to host four standard TEM samples simultaneously, corresponding to a sample holder design provided by T. Wiss from the Institute of Transuranium Elements (ITU) in Karlsruhe. Both sample holders used at IPP are shown in the pictures.
The major requirements of the sample holders were their capability for sample heating to 300°C and reliable temperature measurements; in all three sample holders, the defined heating was

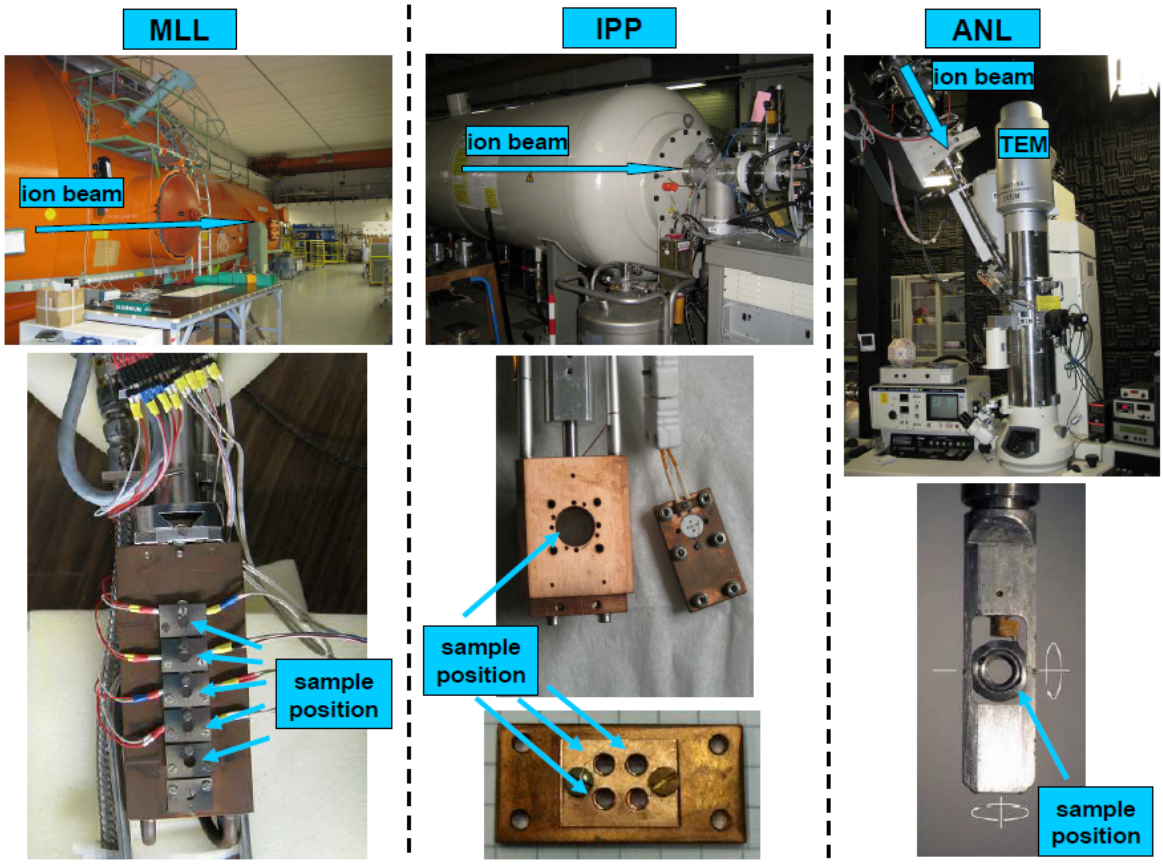

Figure 3.2: Pictures of the irradiation facilities with their respective sample holders

achieved by a combination of microheaters and water cooling systems. Temperature measurements were conducted by thermocouples pressed against or spot-welded to the samples. For the dislocation loop studies during in-situ TEM at ANL, a double-tilt heating sample holder was used to reach the respective grains' orientations which allow for the imaging of specific dislocation loop types. For the in-situ experiments with applied tensile stress at ANL, a single-tilt heating-straining sample holder was necessary. Table 3.2 summarizes the main technical and experimental parameters for the different accelerators.

accelerator	MLL	IPP	ANL
max. terminal voltage	14 MV	3 MV	500 kV
projectiles used	40 MeV Zr	1, 2.5 MeV and 3 MeV Zr	1 MeV Kr
ion beam mode	continuous	scanned	scanned
sample type	foil sample	foil and standard TEM samples	standard TEM + tensile TEM samples
target temperature	300°C	35°C and 300°C	300°C
temperature measurement	thermocouple spot-welded to sample	thermocouple pressed against sample	thermocouple pressed against sample
temperature control	heater + water cooling	heater + water cooling	heater + water cooling
beam current measurement	cup behind sample holder	cups around sample holder	cup with aperture in front of sample holder

Table 3.2: Technical and experimental parameters of the irradiation facilities

3.2.2 Post-Irradiation Examination Techniques

The ion damage structures in the irradiated samples were studied by three different methods: electron backscatter diffraction (EBSD), for the examination of the ions' penetration depth, positron Doppler broadening spectroscopy (DBS) for the examination of the vacancy-type defect densities and transmission electron microscopy (TEM) for direct observation of the irradiation-induced dislocation structures.

Electron Backscatter Diffraction (EBSD)

EBSD is an experimental technique that can be applied in scanning electron microscopes (SEM) which are equipped with electron backscatter detectors. These detectors are positioned close to the SEM's electron beam's axis and detect electrons that are reflected from the target material in the direction of the incoming beam. The method can be used for the study of crystalline materials to differentiate between sample regions with different degree of deviation from the ideal crystal structure.
When the SEM's electron beam with typical energies in the range of 2 to 30 keV [86] meets the target material, the beam widens up, being scattered in the target in all directions (see Fig. 3.3). For each lattice plane that is hit by the beam under the Bragg angle for constructive interference, the electron beam hits an adjacent plane at the mirrored Bragg angle. As this occurs for beams being deflected from the main beam in all angular directions, two cones of Bragg-reflected beams are formed for each set of lattice planes, so-called "Kossel cones". Due to their large radii, they appear on the detector as pairs of parallel straight lines, the so-called "Kikuchi lines". These lines can be observed by the SEM's backscatter detectors, or in the TEM for forward scattered electrons directly on the screen. The Kikuchi line patterns are specific for crystal lattice, lattice parameters and orientation of the target material to the beam. Fig. 3.3 shows a schematic of the Kikuchi line formation and a picture of the Kikuchi pattern of the $(1\bar{2}10)$ pole of a hexagonal lattice [87–89].
For imperfect crystallites, the Kikuchi lines appear with decreased intensity as compared to the perfect crystal; the higher the degree of disorder, the lower the lines' intensities. The parameter introduced to quantify this effect is the Band Slope (BS) parameter. It is a measure for the

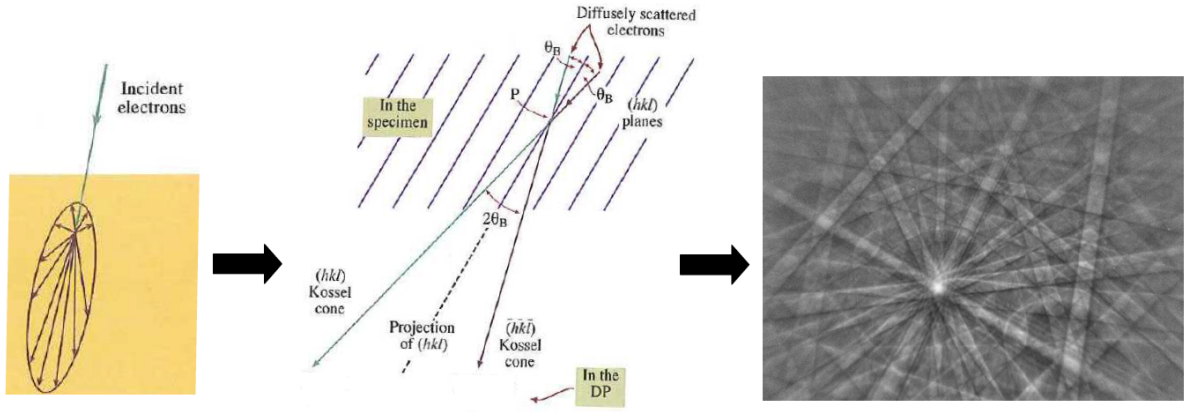

Figure 3.3: Kikuchi line formation schematic [88], with Kikuchi line pattern from hexagonal pole $(1\bar{2}10)$ [87]

intensity gradient between the Kikuchi band's rim and the background and thus decreases with increasing degree of crystal disorder. The target material of interest is prepared for SEM imaging by embedding into epoxy resin and polishing or etching. The area of interest is then mapped by the electron beam, with intensities being measured at each beam position. The resulting map can then be analysed by EBSD software, providing an area map of the degree of disorder in the crystal lattice. A Zeiss Neon 40 EsB scanning electron microscope with a Nordlys EBSD camera was used for the EBSD measurements.

Positron Doppler Broadening Spectroscopy (DBS)

Positron DBS is an experimental method to analyze the vacancy-type defect density in materials. The experiments described in this work were conducted at the high intensity positron source NEPOMUC at the research neutron source Heinz Maier-Leibnitz (FRM II) in Garching, Germany [90,91].
The FRM II is a 20 MW compact core light water cooled, heavy water moderated research reactor which went operational in 2004. With a single fuel assembly equipped with highly enriched uranium-silicide fuel dispersed in plates of an aluminum matrix, it offers an undisturbed maximum thermal neutron flux of about $8 \cdot 10^{14}\,\mathrm{cm}^{-2}\mathrm{s}^{-1}$. 11 beam tubes are located around the core, mostly in the region of maximum thermal neutron flux, leading the neutrons to different experimental facilities and neutron guides located around the core [92]. Fig. 3.4 provides a schematic of the positron source.

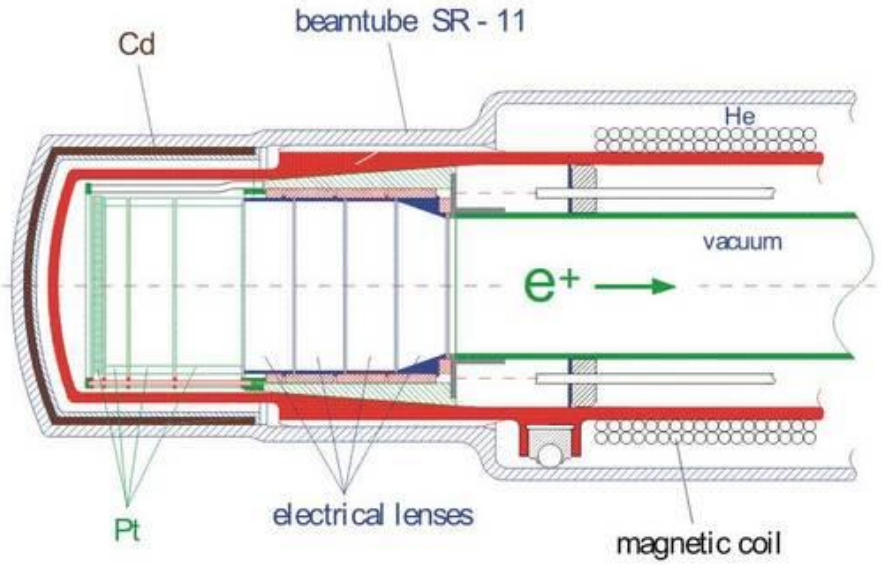

Figure 3.4: Design of the positron source in FRM II' beamtube SR11 [91]

In the beamtube SR11, which contains a ^{113}Cd shield, the high thermal neutron capture cross section of 20600 barn for the neutron-gamma reaction ^{113}Cd(n,γ)^{114}Cd is used to produce high energy γ-radiation. The γs fall onto a platinum plate where electron-positron pairs are created by pair production, with the maximum positron intensity at 800 keV. The positrons are moderated in a platinum layer to energies of 1 keV and led to the experiment facilities by electromagnetical lens systems in a beamtube. With an intensity of 9×10^8 moderated positrons per second, NEPOMUC is the world's positron source with the highest intensity of a monoenergetic positron beam [91]. After passing through an aperture and additional focussing systems, a positron beam of about 1 mm diameter is provided at the Doppler broadening spectroscopy facility. A voltage of up to 30 kV can be applied to the sample holder, thus offering positron energies between 1 and 30 keV; this enables depth dependent measurements in the target materials [91].
When a positron meets a metallic target, it is decelerated due to the Coulomb interaction and reaches a certain material depth, depending on its initial energy. The positron penetration depth can be approximated by the Makhov function as given by Puska and Nieminen [93], describing the positron probability distribution P in dependence of the material depth z:

$$P(z) = \frac{m z^{m-1}}{z_0^m} \exp\left[-\left(\frac{z}{z_0}\right)^m\right]$$

with m a dimensionless, material dependent parameter and z_0 being related to the mean stopping depth $\bar{z}$ by

$$z_0 = \frac{\bar{z}}{\Gamma[(1/m)+1]}.$$

Γ is the gamma function.

The mean stopping depth is defined as

$$\bar{z} = \frac{A}{\rho} E^n$$

with positron energy E, mass density ρ and fit parameters A and n [93,94].
As the parameters A, n and m for Zr were not available in the literature, they were calculated by linear interpolation between the parameters for Cu and Ag reported by Puska and Nieminen [93]; for the material density, the mass density of M5® and Zry-4, 6.5 g/cm^3, was used. The resulting parameters and calculated positron penetration depth distributions are given in Fig. 3.5.

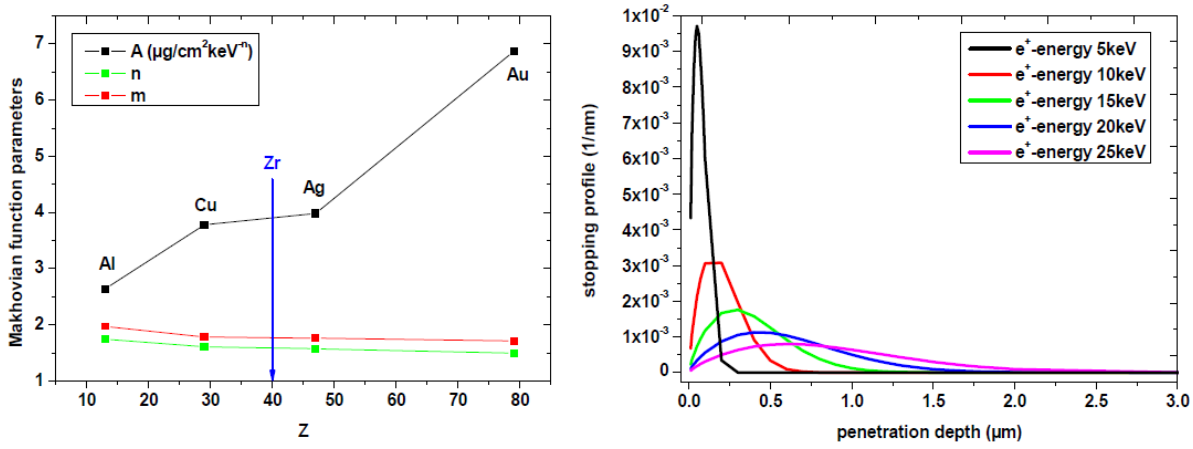

Figure 3.5: Calculated Makhov parameters and approximated positron penetration depth distributions in Zr

When entering the target material, the positrons will be thermalized (to energies of 0.04 eV at 300 K) in a timeframe of several picoseconds, which is about a factor 100 shorter than typical positron lifetimes in solids. The thermalized positrons are then diffusing through the solid within ranges of about 0.1 μm until they annihilate. During this diffusion, they can be trapped by potential sinks; such potential sinks are given by vacancy-type lattice defects, dislocations or grain boundaries. A missing atom in the lattice lowers the positive potential by about 1 eV as compared to the surrounding lattice and provides an attractive potential for the positrons. Positrons are thus captured in vacancy-type defects, and a trapped positron will not be able to escape from the vacancy until it annihilates with an electron. At the location of a vacancy-type defect, there is an increased probability of low-energy conduction and valence band electrons being present due to the missing higher energy electrons bound to the atomic nuclei. Therefore, positrons in crystalline materials with high vacancy-type defect density will annihilate with a higher probability with low-energy electrons than as they would in an undisturbed crystal. The electron-positron anihilation energy is released as two γ's in opposite directions, each bearing the electron/positron rest mass of 511 keV plus half of the electron's kinetic energy before the annihilation (the positron's kinetic energy after its thermalization can be approximated as zero). The emerging γ-radiation is detected at NEPOMUC's DBS facility with up to 4 high-purity, liquid N_2-cooled Ge-detectors with single count rates of up to 40000 counts/s and an energy resolution between 0.25 and 0.3% at 511 keV [91]. All measurements were done with an integration time of 60 s.
DBS experiments use the so-called "S-parameter" as a measure for the vacancy-type defect density

in the studied samples. The S-parameter is defined as the 511 keV γ-intensity within a previously defined energy band around 511 keV, divided by the total peak intensity and thus reflects the annihilations with low-momentum, i.e. valence or conduction band, electrons. In vacancies, the relative probability of positron annihilation with nuclei electrons with high energy is lower than in the perfect lattice. Thus, for a high vacancy concentration, a higher fraction of all annihilations occurs with low-momentum electrons, which leads to an increase of the S-parameter. The parameter is calculated after the subtraction of the background. Fig. 3.6 shows a schematic of the electron-positron annihilation and the definition of the S-parameter.

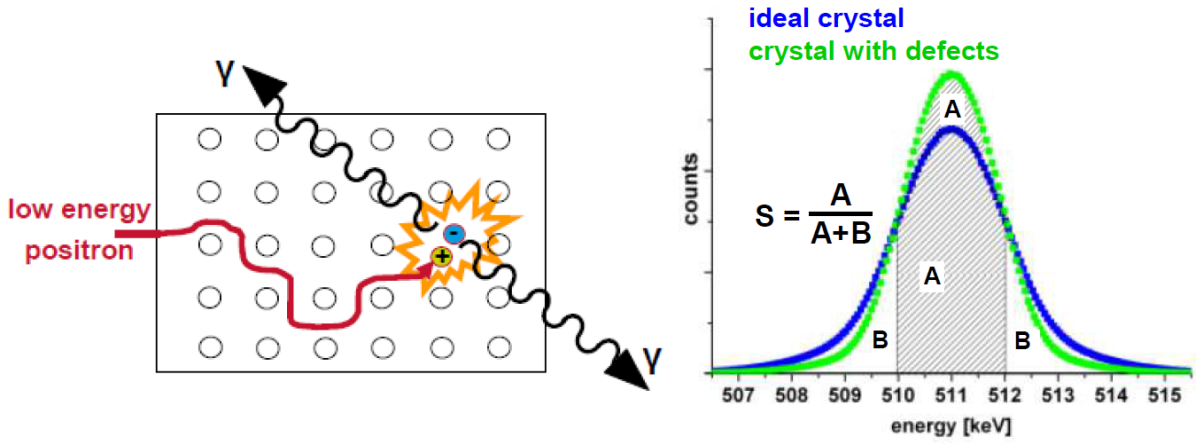

Figure 3.6: Electron-positron annihilation; definition of the S-parameter [95]

As the energy range limits around the 511 keV peak for the S-parameter are defined differently for each material and measurement setup to receive the highest possible resolution, absolute S-parameters can only be compared for samples measured with the same energy window in the same measurement campaign [77]. By normalizing the S-parameter to the parameters of an unirradiated standard of the respective material, a comparison between samples of different measuring campaigns can be achieved to a certain degree. By measuring the S-parameter of an unirradiated standard versus an irradiated sample of the same material, the increase in the vacancy-type defect density by the irradiation can be studied.
The positron annihilation spectra were analyzed by M_Spec 2 [96]; the S-parameters received from up to four detectors were averaged. The measurement errors given for the received S-parameters in the chapter "Results" are the statistical errors based on the standard deviation, as provided by M_Spec 2. Additional deviations of the S-parameters, which are not included in the error bars, can occur due to fluctuations of the Ge-detectors' energy resolution; such fluctuations can be caused by disturbances in the readout electronics. Also, mechanical vibrations of the DBS instrument environment which can influence the detector readout are a possible error source.
Due to the positron beam diameter of about 1 mm, the examined material area comprises of a high number of grains in the studied Zr-alloy samples, which have a typical grain size range of 3 - 6 μm. Therefore, the measured S-parameters provide a defect density averaged over a representative material volume, which minimizes the influence of possible local impurities.

Transmission Electron Microscopy (TEM)

Transmission electron microscopes offer spatial resolutions down to 0.05 nm and are mostly used for the study of defects, interfaces and nonperiodic structures in all kinds of materials [85]. Contrary to other electron microscope types, the TEM is used to view thin material samples in transmission. This leads to significant differences in imaging as compared to other electron microscope types, and specifically in TEM image interpretation; TEM images cannot be interpreted intuitively. A TEM image is a 2 D projection of a 3 D sample volume; in addition, the Bragg diffraction in crystalline materials causes a visibility or invisibility of structures with specific orientation to the beam. Dislocation structures visible at one crystal orientation to the beam under specific imaging conditions will be invisible at another tilt angle. These phenomena have to be considered in any interpretation of TEM images. Also, electron diffraction phenomena caused by the interaction of the beam with the thin foil can cause a number of additional image artifacts [88].
TEM imaging is a powerful and thus the dominating method for the direct observation of irradiation damage in materials [97]. Fig. 3.7 shows a schematic of a TEM, with a demonstration of the electron beam paths in the two basic operation modes of the TEM: diffraction mode (left) and imaging mode (right).

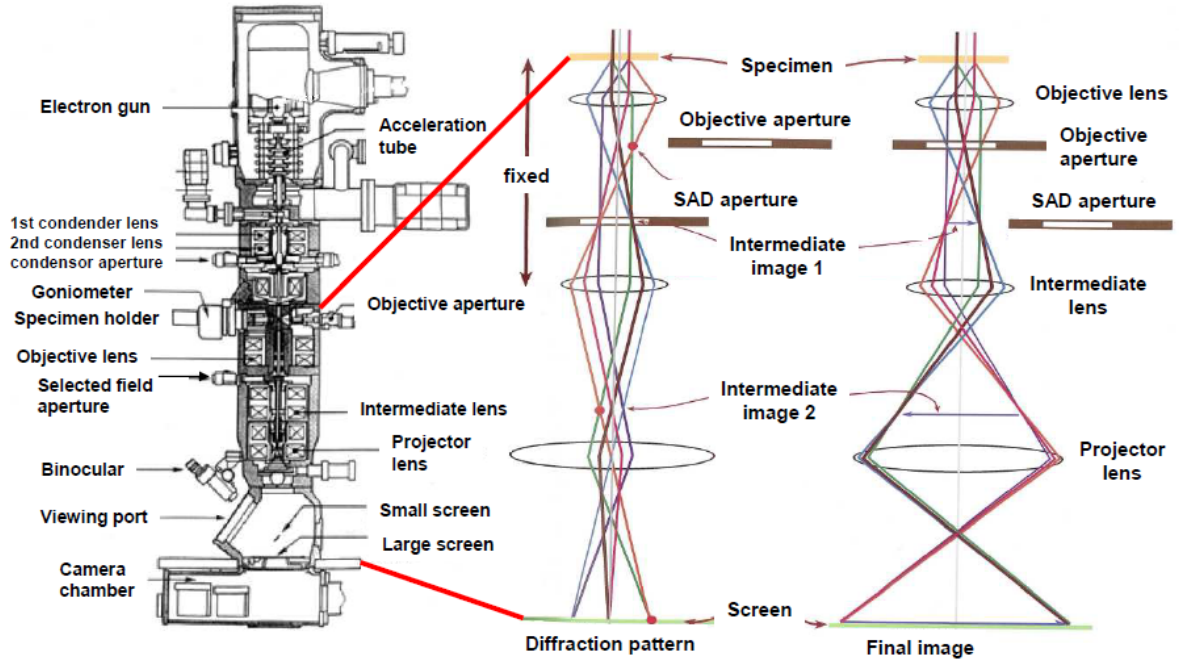

Figure 3.7: TEM schematic and electron beam path [88, 98]

The electron beam in the TEM is generated by an electron gun; typical guns are LaB_6 cathodes for thermal emission between 1700 - 2000°C, thermally supported field emission guns or cold field emission guns for highest resolution TEM, mostly made of tungsten with a ZrO_2 layer. The emitted electrons are accelerated towards the anode with typical voltages between 200 kV up to 1 MV. After passing the anode, the beam's intensity is defined by up to three electromagnetic condensor lenses which are used, in combination with the condensor aperture, to vary the angle

of convergence. The TEM sample with typical diameter of 3 mm is placed in a sample holder which is held in a goniometer; for analytical TEM, sample holders with two tilt axes are required. Depending on the desired experimental conditions, heating or cooling holders are available, as well as straining stages [85]. Below the sample, the objective aperture and the objective lens are located; the objective lens is the most important lens of the system [85,98]. The image aberrations of the objective lens determine the resolution of the TEM. The objective aperture's position defines whether the TEM is used in imaging or diffraction mode. The selected field aperture for selected area diffraction (SAD aperture) is used to confine the beam to a small sample area to receive diffraction pattern from detailed areas. After passing through the intermediate and projector lenses for the adjustment of the desired final magnification, the electron beam falls onto the fluorescent screen. A small fluorescent screen can be inserted into the beam and observed through a binocular for more detailed observations. The large fluorescent screen can be removed to let the beam pass to the CCD camera under the screen. For imaging in the diffraction mode, a beamstop can be inserted to protect the CCD camera from damage by the high intersity of the main beam [85,86,88].
The right side of Fig. 3.7 demonstrates the beam path in the two operating modes of a TEM. When the coherent electron beam falls on a crystalline sample, it is diffracted by the crystal's lattice planes according to Bragg's law

$$2d\sin\theta = n\lambda$$

with d being the lattice constant of the respective plane, θ the Bragg angle and λ the electron beam's wavelength. For an 300 keV electron beam, the wavelength would be 1.97 pm [85].
In diffraction mode (left schematic), the main beam and diffracted beams are focussed by the objective lens; the intermediate image 1 is formed in the plane of the SAD aperture which is used to select only a small material region for the diffraction. The main and diffracted beams are then focussed by the intermediate lens to form the intermediate image 2 in a plane above the projector lens, with the diffraction pattern in the focal point. The projector lens then focusses the main beam and the different diffracted beams onto the fluorescent screen, forming the diffraction pattern (DP). If the selected sample area consists of single crystal material, the DP shows the reciprocal lattice of the crystal lattice. For a polycrystalline or amorphous region, rings will form in the DP, as the electron beam meets small crystallites in all possible orientations towards the beam. For single crystal DPs, the individual reflexes of the pattern can be identified with their respective crystal planes ("indexing"), by using known lattice constants and geometries to identify the crystal lattice and its orientation towards the beam. For crystal lattices with a high symmetry like cubic or orthorhombic, indexing is straightforward. Lattices with low symmetry like hcp for Zr-based alloys require a more detailed analysis to identify the reflexes. Fig. 3.8 shows a diffraction pattern of hcp M5® for the beam axis parallel to the c-axis (pole (0001)), and for pole $(2\overline{1}\overline{1}0)$. The main reflexes are indexed, which was done by comparing the ratio of reflex distances, and the Kikuchi pattern at the poles, to the literature [88,99].
In imaging mode (right schematic in Fig. 3.7), the objective aperture is brought into the beam, cutting off the diffracted beams but letting the main beam pass. The intensity of the main beam is then varied at image areas where the Bragg condition has been met and parts of the beam were diffracted, by image regions with different lattice structures and different Bragg conditions than the matrix (e.g. second phase particles, bent or strained material regions) or by image regions with a higher thickness than the average sample thickness. The main beam reaches the intermediate lens whose strength is increased as compared to diffraction mode to focus the beam in the focal point of the projector lens. The beam then passes the projector lens and falls onto the fluorescent screen [85,88].

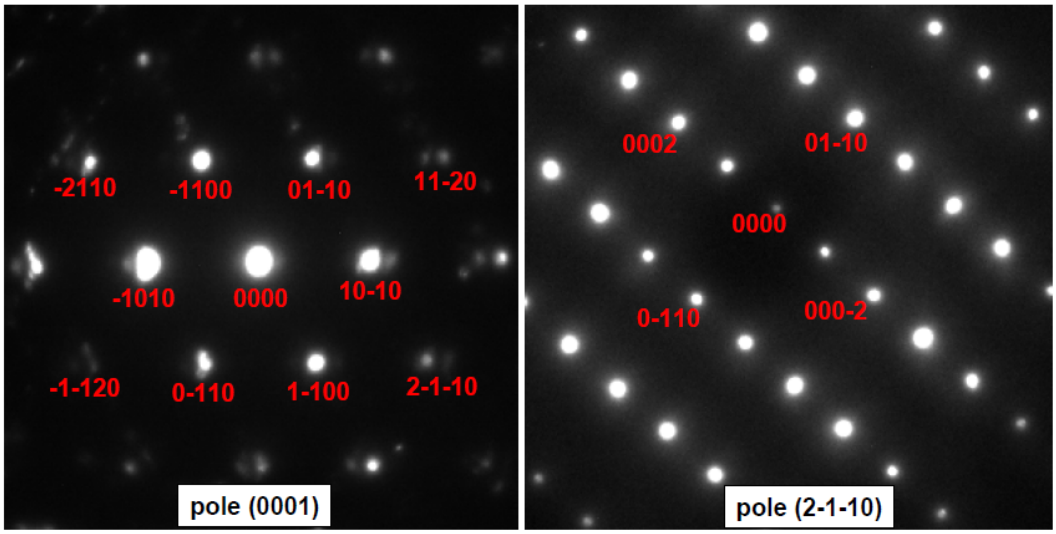

Figure 3.8: Diffraction pattern for hcp M5®, taken at ANL's IVEM Tandem Facility

The two main imaging modes for conventional TEM, where only one reflex is used for imaging, are bright field (BF) and dark field (DF) imaging. For BF imaging, the sample is tilted away from the pole until only the main beam and one reflex from the lattice plane of interest are excited and the intensity of all other reflexes is minimised. This condition is called "two-beam condition", and the excited reflex defines the diffraction vector $\vec{g}$. Then, a small objective aperture is chosen to block all reflexes except the main beam; the image then received in the imaging mode is formed by the main beam, with reduced intensity at all areas where the Bragg condition for the lattice plane corresponding to the excited reflex is met. For dark field imaging, the small objective aperture is set around the excited reflex, not the main beam. After shifting the reflected beam to the beam axis ("centered dark field") and changing to imaging mode, only those regions of the screen are lit where sample areas meet the Bragg condition for the chosen reflex; any other sample areas appear dark [85,88]. Fig. 3.9 shows a low magnification BF and the corresponding DF image of a grain in an unirradiated M5® standard sample loaded with hydrogen, containing microstructural features like the spherical second phase particles, needle-like hydrides and grain boundaries.
By tilting the sample to excite one higher order reflex and the main beam, and then setting up DF conditions by placing the objective aperture around the excited n-th order reflex, only the Bragg reflected beams of that order show intensity on the screen. This so-called $(\vec{g}, \mathsf{n}\vec{g})$-DF condition, or generally "weak-beam dark field condition", can be advantageous when imaging certain defect or dislocation types, as it is highly sensitive to regions of strain in the lattice [97].

A phenomenon of major importance for dislocation imaging in the TEM is the so-called "invisibility criterion":

Invisibility criterion:
$$\vec{B} \cdot \vec{g} = 0 \text{ and } \vec{g} \cdot (\vec{B} \times \vec{u}) = 0,$$

where $\vec{u}$ is the unit vector in direction of the dislocation line. As $\vec{B} \times \vec{u} = 0$ for screw dislocations, those with their Burgers vector $\vec{B}$ perpendicular to the diffraction vector $\vec{g}$ are

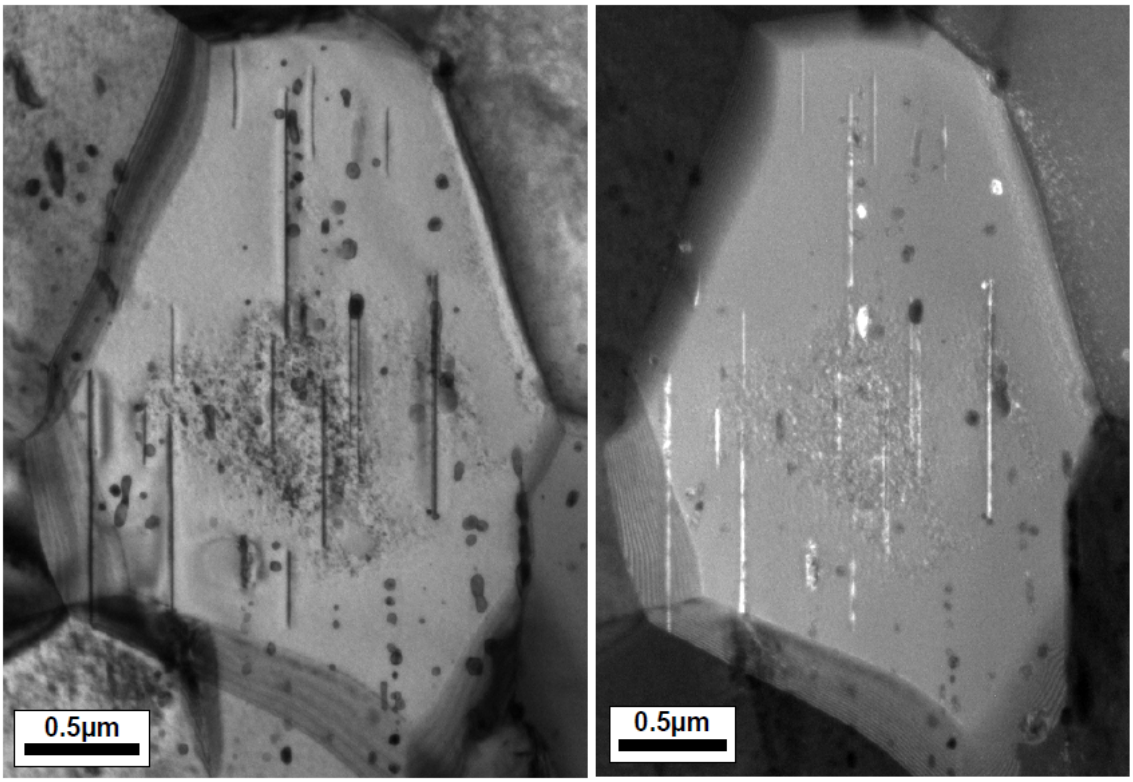

Figure 3.9: Bright field (left) and dark field (right) image of standard M5® after hydrogen loading

invisible in the image, while screw dislocations with $\vec{B}$ parallel to $\vec{g}$ show maximal contrast. For edge or mixed dislocations, both conditions of the invisibility criterion have to be fulfilled. The $\vec{B} \cdot \vec{g} = 0$ criterion can be explained as follows: The reflex intensity in two beam conditions with diffraction vector $\vec{g}$ for a crystal containing a dislocation with Burgers vector $\vec{B}$ is proportional to the square of the amplitude F of the Bragg reflex:

$$F = F_S \sum_{\text{all unit cells}} \exp[2\pi i(\vec{g} + \vec{s})(\vec{r_{pi}} + \vec{B})]$$

where F_S is the structure factor which depends on the atom positions in the lattice, $\vec{r_{pi}}$ is the position vector of atom i in the lattice and $\vec{s}$ is the excitation error. $\vec{s}$ is the distance of the reciprocal lattice point from the Ewald sphere[1] and a measure on how far the actual diffraction condition deviates from the ideal Bragg condition. The Ewald sphere with radius $1/\lambda$ is comparatively large, λ being in the range of 1 pm, with its surface appearing nearly as a plane, from the point of view of a small section of the diffraction pattern; thus, $\vec{s}$ is very small. As the reciprocal lattice points are not ideal points but extended to small rods whose length is proportional to 1/d with d being the sample thickness, the reflex intensity can be non-zero also for planes which do

[1]The Ewald sphere is a visualization of the Bragg condition in reciprocal space. It is constructed by drawing the wave vector of the incident electron beam such that it ends at the origin of the reciprocal lattice. The beginning of the wave vector is then the center of the Ewald sphere, its radius is $1/\lambda$, and the Bragg condition is fulfilled for all reciprocal lattice points that are intersected by the sphere.

not fulfill the Bragg condition exactly. The argument of the exponential function in the reflex amplitude then contains the sum of $\vec{g}$ and $\vec{s}$ [85,88,97].

Expanding the argument of the exponential function leads to the terms

$$(\vec{g} + \vec{s})(\vec{r_{pi}} + \vec{B}) = \vec{g} \cdot \vec{r_{pi}} + \vec{s} \cdot \vec{r_{pi}} + \vec{s} \cdot \vec{B} + \vec{g} \cdot \vec{B}$$

The first two terms correspond to the argument of the Bragg reflex from an undisturbed crystal plane; the third term is approximately zero, as $\vec{s}$ is very small as compared to $\vec{g}$. The fourth term, $\vec{g} \cdot \vec{B}$, is then the only term distinguishing the reflex amplitude of the disturbed material from the amplitude of the undisturbed crystal. If the Burgers vector is perpendicular to the diffraction vector, the scalar product in the fourth term will be zero, and the reflex amplitude will be the same as for the ideal crystal without the dislocation; the dislocation will be invisible in the image [85,88,97].

The origin of the additional $\vec{g} \cdot (\vec{B} \times \vec{u}) = 0$ condition for the invisibility of screw or mixed dislocations is the bending of the glide plane by the edge dislocation [88].

For the imaging of <a>-loops, two different diffraction vectors were used, depending on the textured samples' grain orientation.
The first diffraction vector for <a>-loop imaging was $\vec{g} = (11\bar{2}0)$ or equivalent with the foil tilted about 10° from the [0001] zone axis in bright field and $(\vec{g}, 3\vec{g})$ dark field conditions. While <c>-component dislocations with Burgers vectors (0001) are invisible under the chosen diffraction condition, all perfect <a>-component dislocation loops with Burgers vectors $(1\bar{2}10)$, $(\bar{1}2\bar{1}0)$ and $(2\bar{1}\bar{1}0)$ are visible, as well as all mixed <c+a>-types: $(11\bar{2}3)$, $(\bar{1}2\bar{1}3)$, $(\bar{2}113)$, $(11\bar{2}\bar{3})$, $(\bar{1}2\bar{1}\bar{3})$ and $(\bar{2}11\bar{3})$ [42]. The second diffraction vector was $\vec{g} = (01\bar{1}0)$ or equivalent with the foil tilted about 10° from the $[2\bar{1}\bar{1}0]$ zone axis. The $[2\bar{1}\bar{1}0]$ zone axis is particularly useful as it allows to reach both $\vec{g} = (01\bar{1}0)$ for <a>-loop imaging and $\vec{g} = (0002)$ for <c>-loop imaging (compare the diffraction pattern on the right side of Fig. 3.8). Thus, both <a>- and <c>-loops can be imaged if a grain is available with its orientation allowing imaging near that pole. Using $\vec{g} = (01\bar{1}0)$, two thirds of the <a>-loops are visible, those with Burgers vectors $(11\bar{2}0)$ and $(\bar{1}2\bar{1}0)$, and two thirds of the mixed <c+a>types, those with Burgers vectors $(11\bar{2}3)$, $(\bar{1}2\bar{1}3)$, $(11\bar{2}\bar{3})$ and $(\bar{1}2\bar{1}\bar{3})$. Pure <c>-type loops are invisible under that vector [42].
The <c>-loops were imaged using the $\vec{g} = (0002)$ diffraction vector, with the grain tilted approximately 10° from the $[2\bar{1}\bar{1}0]$ zone axis, in bright field, $(\vec{g}, 3\vec{g})$ and $(\vec{g}, 4\vec{g})$ dark field conditions. These diffraction conditions show all <c>-type and <c+a>-type contrasts while suppressing pure <a>-component contrasts [42].

To characterize the dislocation densities in the studied TEM samples, it was necessary to measure the thickness of the respective grains. The grain thicknesses were determined by imaging a grain boundary parallel to the sample holder's main tilt axis at different tilt angles and measuring the observable grain boundary thickness at these angles. The grain's real thickness can then be calculated from trigonometric relations, as described in more detail in Appendix C.

3.2.3 Sample Fabrication

The base material for the M5® samples studied in this work were polycrystalline M5®industrial strips with thicknesses of 0.38 mm and 0.43 mm. They were produced by subsequent hot and

cold rolling of a hot forged alloy slab with an original thickness of 110 mm, with the final heat treatment chosen to fully recrystallize the material. After cutting foil pieces from the strips by laser cutting and sample preparation steps, the samples were vacuum annealed for 2 hours at 580°C to restore an undisturbed recrystallized microstructure. According to the strips' material certificates, their hydrogen content was ≤ 3 wt.-ppm.
To study the thickness of the 40 MeV Zr irradiated layer in sample M1 by EBSD, a cross section of the sample was prepared and analyzed. To assure a good edge retention of the irradiated surface of the specimen, an unirradiated specimen was glued to the irradiated side of the irradiated specimen; then, both foils were embedded in a hot mounting resin. After grinding and polishing with colloidal silica, the cross section was swab etched with a specific electrolyte. The rounding of the edges of the irradiated foil during cross section grinding parallel to the foil normal showed to be in the range of several μm and thus near the expected irradiated layer's position. Therefore, the cross section was not ground and polished parallel to the foil normal but with an angle of 35° to the foil normal. As the irradiated layer was thus cut under an angle of 35°, its observable width was increased, improving the depth resolution.
For the low dose irradiation for DBS, the foil specimens' surface was pickled with an acid based etchant consisting of 30% H_2O, 30% H_2SO_4, 30% HNO_3 and 10% HF.
The M5® foils for the TEM samples were thinned by subsequent wet grinding with sandpaper of roughness 800, 1200 and 2400 to a thickness of about 150 μm; wet grinding was necessary due to the pyrophoric properties of zirconium. Then, their final thickness of about 100 μm was reached by etching with the described etchant. Discs of 3 mm diameter were punched from the foils, and the discs were electrolytically thinned to perforation using a twin-jet electrolytic process at - 50°C and an electrolyte consisting of 90% methanol and 10% perchloric acid.
Due to the rolling process during the strip production, the samples show a very strong texture with the majority of the grains' (0002) c-axes tilted with an angle of about 25° from the foil surface normal.

The Zry-4 samples were taken from an industrial Zry-4 tube reduced extrusion (TREX), a pre-product of the guide tube fabrication process, as described in section 1.1.3; the TREX was a hollow cylinder with wall thickness 15 mm. The hydrogen content of the ingot was given as $\leq$ 3 wt.-ppm, and the tubes produced from the ingot had a hydrogen content of 7 wt.-ppm. The hydrogen content of the TREX, which is not measured during the production process, is therefore given in this work as ≤ 7 wt.-ppm. For the samples loaded with hydrogen, the additional hydrogen put into the samples is given throughout the thesis.
Due to the pre-production steps, the TREX has the majority of the grains oriented with their c-axis radial to the cylinder axis. Thus, TEM samples with the majority of the grains' c-axes in the sample plane, as necessary for <c>-loop imaging, can be produced by cutting foils perpendicular to the cylinder axis. Fig. 3.10 shows the subsequent steps in the TEM sample production.
The Zry-4 TREX was cut axially by milling into six parts. Then, three of these parts were diffusion loaded with different amounts of hydrogen. The hydrogen loading was done by placing the vibratory ground part into a vacuum furnace after weighing it with a high accuracy scale; the vibratory grinding was necessary to remove the pickled TREX surface that inhibited the material from picking up the hydrogen. A defined pressure of hydrogen gas was then filled into the furnace, and the furnace heated to 400°C and held at that temperature for about 30 min, depending on the part's weight. By monitoring the decrease of the hydrogen pressure in the furnace, the amount of hydrogen that was taken up by the material can be estimated. After the end of the loading, the part was weighted a second time; the hydrogen uptake could then be

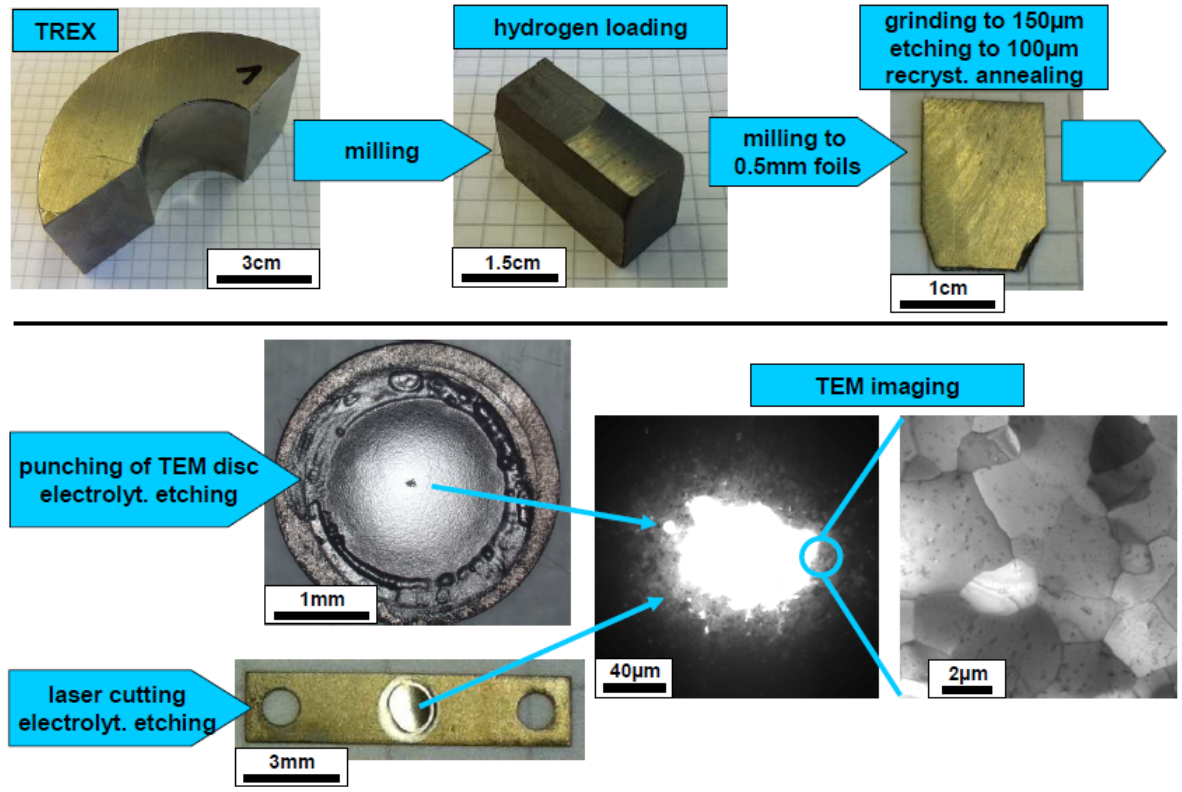

Figure 3.10: Sample fabrication process for Zry-4 TEM samples

calculated from the weight gain of the material. A cross section of one exemplary sample was done after the hydrogen loading to verify that the zirconium hydrides are distributed homogeneously in the sample. The accuracy of the hydrogen content values received by the described weighing method is in the range of 8%, as determined in former experiments where the such measured values were compared to the hydrogen contents provided by the hot vacuum extraction method. In the next step, thin slabs with a thickness of about 0.5 mm were milled perpendicular to the former cylinder axis from the unloaded and hydrogen loaded parts. The resulting foils were thinned to a final thickness of about 150 μm by subsequent wet grinding with sandpaper of roughness 800, 1200 and 2400. The thus received foils were then thinned to about 100 μm analogously to the M5® TEM sample fabrication. Afterwards, the foils were vacuum annealed for 2 hours at 600°C to remove any defects or dislocations produced by the cold working during fabrication, and to receive the material in its recrystallized state. Two different types of TEM samples were taken from these foils: The first type were standard TEM discs with 3 mm diameter, punched from the foils; the second type were tensile specimens cut from the slabs by laser cutting, corresponding to the required geometry of the straining stage from Gatan Inc. of the IVEM Tandem Facility. Both sample types were then electrolytically thinned to perforation by the same process as the M5® TEM samples.

It is important to note at this point that a high number of different TEM sample fabrication techniques were tested in the scope of this work. Before the proposal to the IVEM Tandem Facility was accepted, a different experimental process had been planned, consisting of irradiating foil samples with thicknesses in the range of 0.5 to 1 mm with or without external tensile stress,

kept at 300°C, and to afterwards prepare TEM samples out of the region of the foil where the ion damage peak was located. The advantage of that method would have been the easier accessibility of the accelerator facilities. The conducted TEM sample fabrication tests showed, however, that it was impossible to produce artifact free Zr-based alloy TEM samples from a defined position within the samples:
Focussed Ion Beam (FIB) would have been the method of choice for TEM sample preparation from a defined position within a foil [85, 88]. However, various test preparations with FIBs of different institutes (AREVA NP Technical Center, Erlangen; Universitäre Serviceeinrichtung für Transmissionselektronenmikroskopie (USTEM), Wien) showed that even using the lowest possible milling current, low milling angles and ion beam energies in the low keV range, it was impossible to keep the irradiation damage from the milling beam low enough. The unirradiated FIB-cut samples showed comparable irradiation damage as the irradiated samples from the accelerators. Also, the FIB lamellae kept bending during the FIB process, making it difficult to reach the necessary thinness for TEM imaging. Additional testing was done at USTEM using a Precision Ion Polishing System (PIPS) to remove the damaged layer from the FIB samples. As compared to FIB, which uses heavy ions like Gallium, PIPS is based on an Argon beam with typical energies between about 1 and 5 keV [85, 88]; also, the ion beam can be adjusted to meet the sample surface at a very low angle to produce a damaged layer of minimal thickness. However, PIPS itself showed to produce too much irradiation damage. An additional difficulty was the oxidation of the FIB lamellae during FIB, PIPS or during sample transfer between the devices or to the microscope. Finally, FIB at liquid nitrogen temperature was tested at USTEM, which showed an improved sample quality. However, artifacts from the preparation process could not be avoided completely and would have given strong doubts to any results of irradiation damage studies in those samples.
Then, several mechanical techniques were tried. Subsequent grinding, polishing and dimpling of standard TEM discs was tested at AREVA NP GmbH, the "Arbeitsgruppe für Elektronenmikroskopie" at the FAU Erlangen-Nürnberg and the Institute of Transuranium Elements (ITU) at Karlsruhe. The samples were dimpled to a minimal thickness at the center of about 10 to 30 μm; then, they were thinned to perforation by PIPS at the ITU. However, PIPS induced significant irradiation damage. Another tested method was thin edge polishing, a combination of mechanical and chemical polishing to produce an edge at one side of a foil sample with its thickness being low enough to view the material in the TEM. Problems with this method arose from sample oxidation as well as defect and dislocation production by the mechanical part of the polishing. Finally, sample cutting by an ultramicrotome [85,88] was tried by Leica Microsystems; this method is based on the mechanical cutting of very thin foils from soft materials, also soft metals, with a thin diamond blade; the resulting material slabs with thicknesses in the range of 150 nm are then collected on a copper grid TEM holder. However, the compression stress during cutting led to significant foil bending with parts of the foil thrown over each other; the defects induced by these high levels of strain would have made reliable irradiation damage studies impossible.

3.2.4 Summary of the Experiments

The experiments conducted in the course of this work consist of several groups.
First, the necessary ion damage levels were calculated based on the SRIM code, to define the ion fluence range necessary for the experiments. As a verification for the suitability of the SRIM code for Zr and Kr in Zr-based alloys, a M5® foil was irradiated, after several pre-tests and sample holder adjustments, at the MLL accelerator at the comparatively high ion energy of 40 MeV to receive an ion penetration depth of several μm. The resulting recoil distribution was then measured by electron backscatter diffraction to compare the actual recoil distribution with the simulation results.

Then, M5® foil samples were irradiated with 2.5 and 3 MeV Zr ions, both at 35°C and 300°C to different damage levels, at the IPP's accelerator for subsequent vacancy-type defect density studies with positron Doppler broadening spectroscopy. After test measurements at the NEPOMUC DBS facility, the samples were investigated with a number of different procedures: a lateral scan at a defined positron energy in the region of the maximal damage, depth scans from the sample's surface to the higher damage depths, a line scan from the unirradiated to the irradiated region and from sample surface to the region of highest damage, and finally an in-situ DBS annealing experiment to study the annealing behavior of the vacancy-type defects. By these experiments, information about the general defect behavior were found, in particular the influence of damage level and temperature on the overall vacancy type defect density.

However, for the direct observation of dislocation loop structures forming under irradiation, as necessary for the objective of this work, transmission electron microscopy was the method of choice. Therefore, the in-situ TEM irradiations comprise the widest part of the experiments, and some irradiations with subsequent TEM were done in addition. These TEM studies can be divided in several parts. At first, suitable TEM sample preparation conditions had to be established to receive the desired grain orientation and to minimize preparation artifacts, which included a high number of tests with all standard TEM sample preparation techniques at a number of different institutes and facilities as described above. Then, a first group of in-situ irradiations with both M5® and Zry-4 samples were done as a feasibility study for LWR neutron damage simulation with heavy ions. In addition, some irradiations with subsequent TEM were carried out at both ANL and IPP accelerators with Zr and Kr projectiles to exclude possible influences of projectile, accelerator or irradiation mode (irradiation in one step to the final damage level vs. irradiation in several steps with intermediate TEM imaging). After the successful results of this study, the effects of hydrogen content and tensile stress on the irradiation induced microstructure, which were the main issues to be investigated in this work, were studied in Zry-4.

Table 3.3 gives an overview of all irradiated samples described in this work, listing their irradiation conditions as well as the applied post-irradiation examination techniques. For the examined grains in samples A1 and IA1, where the grain thickness could not be measured due to geometry constraints, a thickness of 150 nm was assumed for the near-hole grain in sample A1 and a thickness of 200 nm for the grain in sample IA1 with a larger distance from the hole, estimated from the image quality and the experience with the other samples.

sample	alloy	type	H	acc.	ion	E_{ion}	T_{irr}	F_{ion}	D_{dpa}	$\dot{D}_{dpa}$	PIE
M1	M5®	foil	≤ 3	MLL	Zr	40	300	$3 \cdot 10^{15}$	21	10	EBSD
I1	M5®	foil	≤ 3	IPP	Zr	3	35	$2.5 \cdot 10^{13}$	0.1	7	DBS
I2	M5®	foil	≤ 3	IPP	Zr	3	35	$5 \cdot 10^{13}$	0.2	7	DBS
I3	M5®	foil	≤ 3	IPP	Zr	3	35	$1 \cdot 10^{14}$	0.4	7	DBS
I10	M5®	foil	≤ 3	IPP	Zr	2.5	300	$4 \cdot 10^{15}$	16	7	DBS;DBS+T
A1*	M5®	TEM	≤ 3	ANL	Kr	1	300	$5 \cdot 10^{15}$	18	22	IS-TEM
A2	M5®	TEM	≤ 3	ANL	Kr	1	300	$5 \cdot 10^{15}$	22	27	IS-TEM
A3	M5®	TEM	110	ANL	Kr	1	300	$6.25 \cdot 10^{15}$	27	27	IS-TEM;TEM+T
IA1*	Zry-4	TEM	≤ 7	IPP	Zr	1	300	$5 \cdot 10^{15}$	28	0.4	TEM
JA1	Zry-4	TEM	≤ 7	ANL	Kr	1	300	$5 \cdot 10^{15}$	25	31	TEM
PA2	Zry-4	TEM	≤ 7	ANL	Kr	1	300	$5 \cdot 10^{15}$	25	32	IS-TEM
PB3	Zry-4	TEM	186	ANL	Kr	1	300	$5 \cdot 10^{15}$	23	29	IS-TEM
PC4	Zry-4	TEM	405	ANL	Kr	1	300	$5 \cdot 10^{15}$	25	31	IS-TEM
PZ	Zry-4	St-TEM	≤ 7	ANL	Kr	1	300	$5 \cdot 10^{15}$	25**	32	IS-TEM+St

Table 3.3: Summary of the irradiated samples:
"St-TEM" = tensile specimen for TEM
"IS-TEM"=In-situ-TEM
"IS-TEM+St"=In-situ-TEM with straining stage
"DBS+T"=DBS with defect annealing
"TEM+T"=TEM with defect annealing
H = hydrogen content in wt.-ppm
E_{ion} = ion energy in MeV
T_{irr} = irradiation temperature in °C
F_{ion} = ion fluence in cm^{-2}
D_{dpa} = damage level in dpa
$\dot{D}_{dpa}$ = damage rate in 10^{-4}dpa/s
* = grain thickness not measured but estimated
** = average between the damage levels of two different grains

Chapter 4

Results and Discussion

This chapter consists of the description and discussion of the experimental results. It starts with a presentation of the confirmation of the SRIM calculations by electron backscatter diffraction (EBSD) and then focusses on the heavy ion irradiation experiments with M5® and Zry-4. Those experiments are structured into two parts. First, the feasibility studies will be described, which showed that typical PWR neutron damage can be simulated by heavy ion irradiation under the chosen conditions in M5® and Zry-4. Then, the investigation of the effect of different parameters on the irradiation induced microstructure will be presented: ion dose, temperature, hydrogen content and external stress.
Parts of this chapter have been published in a first-author publication in the Journal of Nuclear Materials [77].

4.1 SRIM Calculation Confirmation by Electron Backscatter Diffraction

The conversion of the ion fluence to displacements per atom, which is a key point in comparing neutron and ion damage, is based on recoil distribution simulations with the SRIM code [69]. To verify whether the code gives a realistic representation of the behavior of projectile ions in the Zr mass range in Zr-based alloys, a calculated ion recoil distribution was compared to the dimensions of the ion damage layer in a M5® sample. The sample (M1) was irradiated with 40 MeV Zr at the MLL accelerator at a temperature of 300°C to a total ion fluence of $3 \times 10^{15} \mathrm{cm}^{-2}$. After a cross-section was prepared from the sample, a total length of 330 μm along the irradiated and the unirradiated surface was analyzed with EBSD; the band slope distribution was averaged over the measured length. Fig. 4.1 shows the band slope mapping over the irradiated layer and the unirradiated bulk material near the surface; Fig. 4.2 gives the distribution of the normalized sum of the band slope (BS) parameter measured from the specimen's surface to the unirradiated bulk, compared to the recoil distribution caused by ^{90}Zr projectiles with 40 MeV in the alloy, calculated with SRIM for 100 projectiles. As the cross-section was polished with an angle of about 35° to the foil normal, the cut through the irradiated layer is inclined. Therefore, the EBSD image in Fig. 4.1 shows an enhanced thickness of the irradiated layer. The BS parameter given in Fig. 4.2 is corrected for the cross-section inclination and thus provides the actual thickness of the irradiated layer.

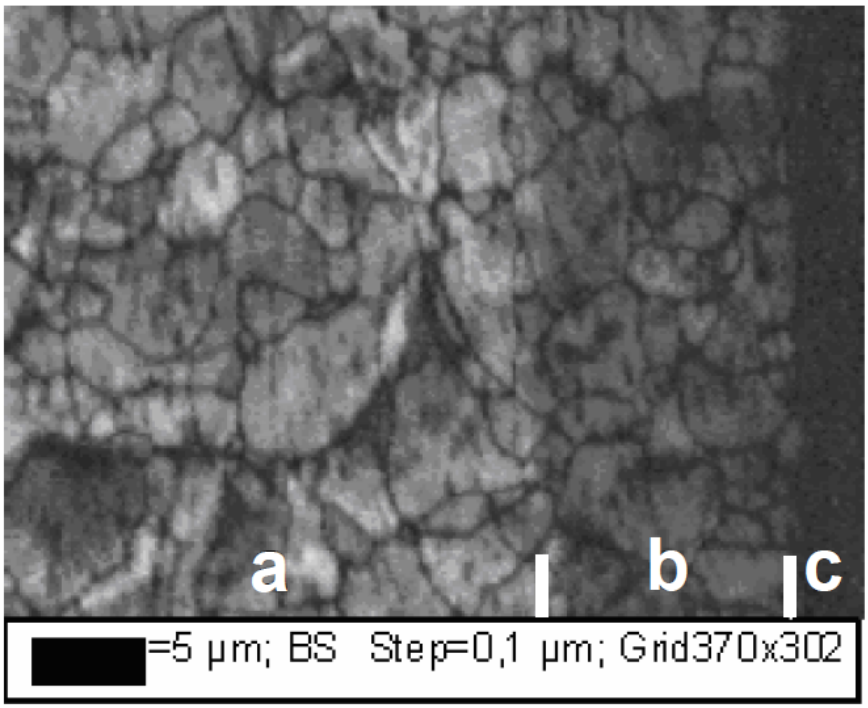

Figure 4.1: Band slope map of the irradiated M5® specimen (40 MeV Zr at 300°C) cut under 35°; a=unirradiated bulk; b=irradiated layer; c=gap to the stabilizing foil

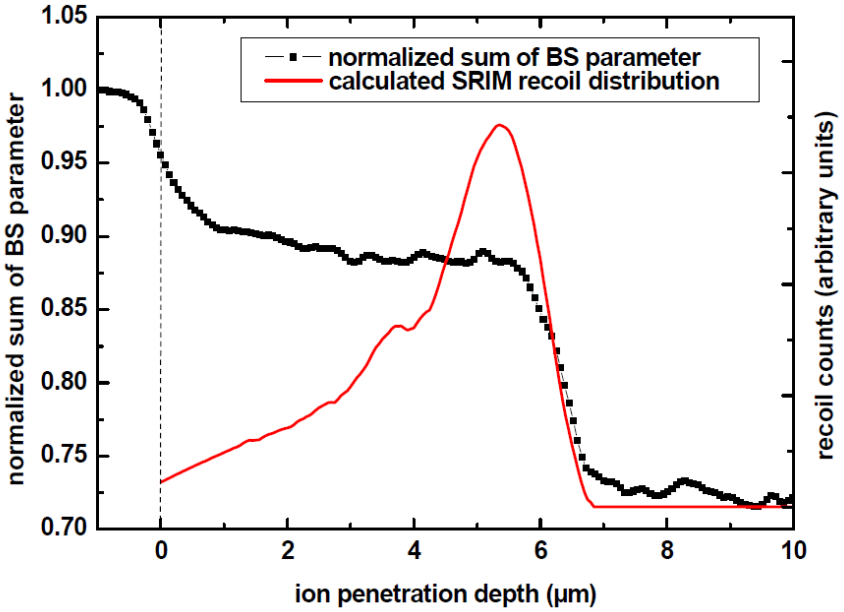

Figure 4.2: Depth dependent normalized sum of the band slope (BS) parameter compared to the SRIM calculation results (M5®, 40 MeV Zr irradiated at 300°C)

The irradiated layer can be clearly distinguished from the bulk by its darker coloring in the band slope map (see Fig. 4.1). Also, the width of the irradiated layer is approximately constant along the specimen. This shows that, even though the material is hexagonal and might thus be expected to be prone to channeling effects that are disregarded by the SRIM code, channeling does not occur to a significant level, and the damage range does not depend on the grain orientation. The peaked recoil distribution which was calculated with SRIM is not reflected in the depth dependent distribution of the normalized sum of the BS parameter (see Fig. 4.2); the sum is approximately constant over the total depth of the irradiated layer. This is assumed to be an effect of saturation: As observed during the in-situ-TEM ion irradiation, the Kikuchi lines become invisible in the TEM in specimens irradiated to high doses due to the high density of defect structures that disturb the lattice planes' periodicity. From the EBSD results, that effect can be assumed to occur already at the comparatively low recoil densities as they are given on the material's surface. Then, the higher recoil density and subsequent higher defect density deeper in the sample cannot be resolved by EBSD as the Kikuchi lines are already completely dark at the much lower dose.
The damage level at which the saturation occurs has to be lower than the damage level at the specimen's surface, otherwise a part of the peak would be seen in the EBSD signal. The SRIM calculated surface recoil density is about 6% of the peak recoil density. It can thus be concluded that EBSD saturation is reached for recoil densities of 6% of the peak density or lower in the irradiated sample. For the chosen irradiation conditions, and assuming that 70% of the recoils are concentrated in the recoil peak with a full width half maximum of 1.2 μm, the peak damage level is 21 dpa. Then, the calculated damage level at the sample's surface is 1.3 dpa, which can be regarded as the upper limit for EBSD saturation under the chosen measurement conditions.
The measured maximal damage range corresponds very well to the calculated maximal recoil range; it can thus be concluded that the SRIM calculations for heavy ion ranges in Zr-based alloys produce reliable results and can be used as a basis for damage level calculations in the specimens with a level of accuracy that is significantly higher than the typical measurement errors in the irradiation experiments.

4.2 Comparability of Light Water Reactor Neutron and Heavy Ion Damage

The most distinguished features of neutron induced microstructural damage in Zr-based alloys are the <a>- and <c>-type dislocation loops, as described in chapter 2; also, the dislocation loops are reported to be the dominant force in irradiation induced deformation. Therefore, the formation and characteristics of these dislocation loops are the primary criterion to assess the comparability of ion damage with neutron damage in the context of irradiation induced deformation.
The results of the feasibility study whether heavy ion irradiation is suited to simulate neutron damage, and under which parameters, will be presented in three parts: first, <a>-loop formation and characteristics, then <c>-loop nucleation and properties, and finally the observations regarding additional microstructural features. To be sure that the experimental method is applicable not only in the single case of one specific alloy, or reproducible only at one accelerator, two different Zr-based alloys were used, M5® representing the group of Zr-Nb alloys, and Zry-4 as an example of the Zr-Sn-Fe-Cr alloys. Also, irradiations were done at two different acceler-

ators with two different projectiles: 1 MeV Kr at the ANL's 500 kV tandem accelerator of the IVEM Tandem Facility, and 1 MeV Zr at the Max-Planck-Institute für Plasmaphysik's 3 MV tandem accelerator. Finally, irradiations were carried out with both in-situ TEM imaging at ANL, and with pre-irradiating the samples to their final dose and subsequent post irradiation TEM imaging. It was thus assured that the irradiation mode (stepwise or in one run) did not have a significant effect on the irradiation induced microstructure.

4.2.1 <a>-Loops

The development of <a>-component dislocation loops was observed in one grain of the M5® sample A1 from the unirradiated state to an ion fluence of $5.0 \times 10^{15} \mathrm{cm}^{-2}$. Diffraction vector $\vec{g} = (11\bar{2}0)$ or equivalent was used, which leads to an invisibility of all <c>-type contrasts and shows all emerging <a>-type contrasts (see chapter 3). The grain's thickness was not measured; to estimate the ion dose, a thickness of 150 nm was assumed, based on the grain's distance from the hole. This leads to a calculated final ion dose of 18 dpa. As soon as the irradiation was started, small <a>-type contrasts in dot- or loop-like shape started to develop and to slightly migrate in the grain; their density increased with the dose (see Fig. 4.3). Fig. 4.4 shows the <a>-loop contrast in higher magnification; contrasts of loop form are designated by the arrows. At high damage levels, the <a>-component dislocation network shows regions of very dense contrasts alternating with lower contrast regions. Therefore, it is difficult to tell whether the loop density increases further with the damage level or reaches a state of saturation which is described for neutron irradiated Zr-based alloys [36]. The [0001] zone axis diffraction pattern after 18 dpa shows significant deviations from the lower dose state (see Fig. 4.5): While the initial hexagonal diffraction pattern is barely recognizable, additional reflexes are present. They might be an indication of recrystallization of grain regions into small grains with a slight deviation of orientation or lattice parameters from the original grain. This recrystallization could be a consequence of very strong bending of the grain in combination with the high defect density, as it was observed in a grain close to the hole at high damage levels. Even though the temperature of 300°C is much lower than the recrystallization temperature range of Zr-based alloys, it is assumed that the effect might have been triggered by strong bending of the single grain in combination with the irradiation. Oxidation as a cause for these changes in the images and diffraction pattern is deemed unlikely because comparable samples did not show the observed effects, neither while being irradiated at corresponding pressure and damage level conditions nor during annealing experiments at up to 750°C.

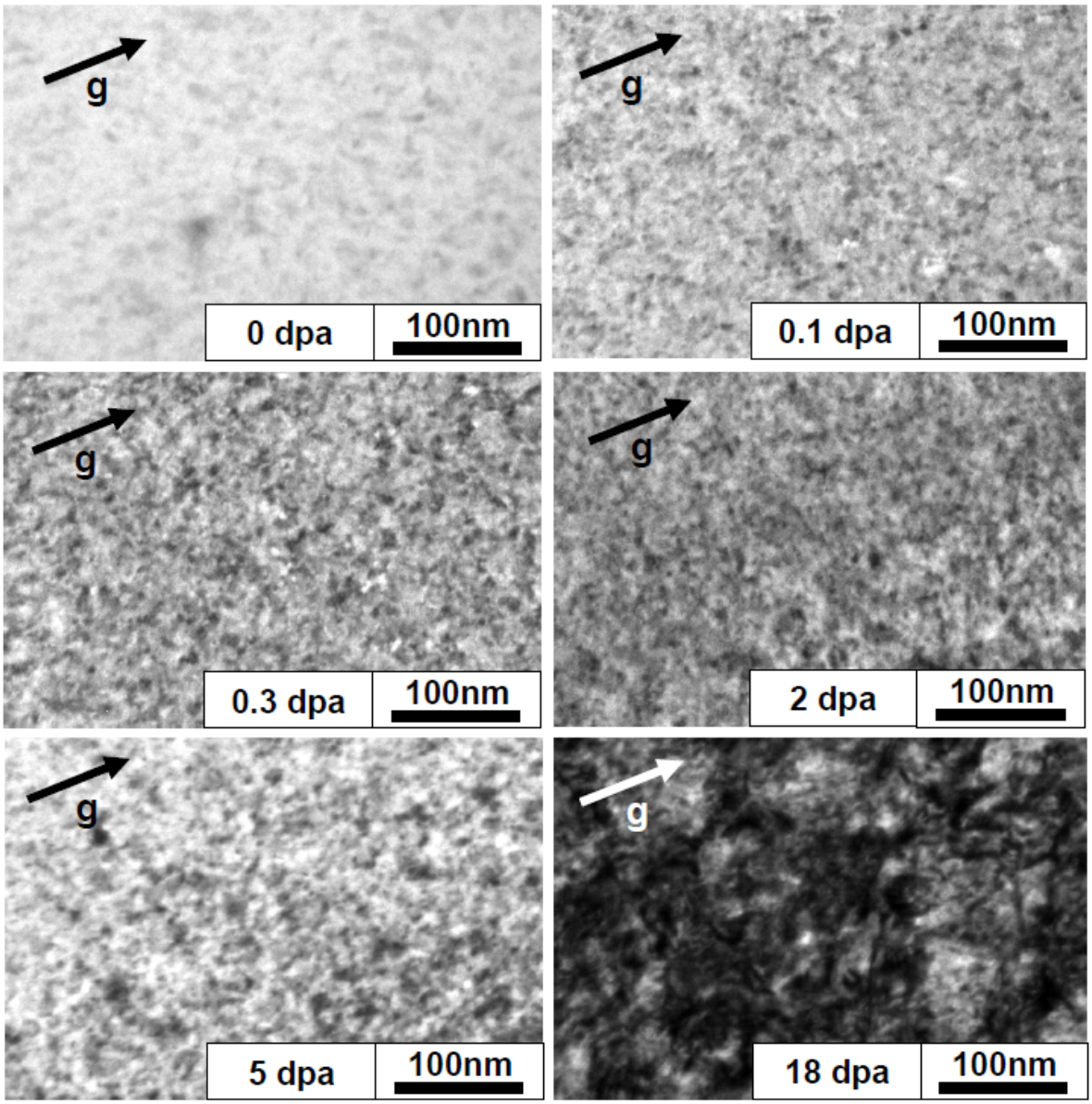

Figure 4.3: <a>-loop development in M5® vs. ion dose (1 MeV Kr at 300°C); $\vec{g} = (11\bar{2}0)$ or equivalent

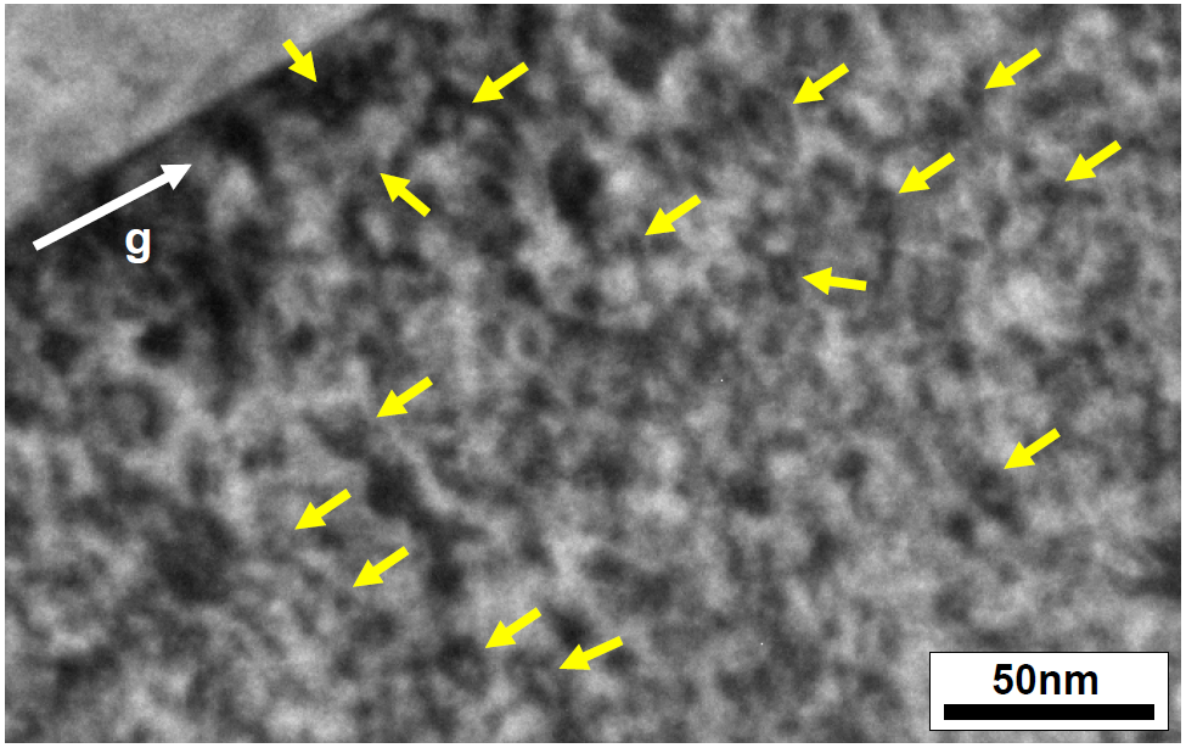

Figure 4.4: <a>-loop contrast in M5® in higher magnification (5 dpa 1 MeV Kr at 300°C); $\vec{g} = (11\bar{2}0)$ or equivalent

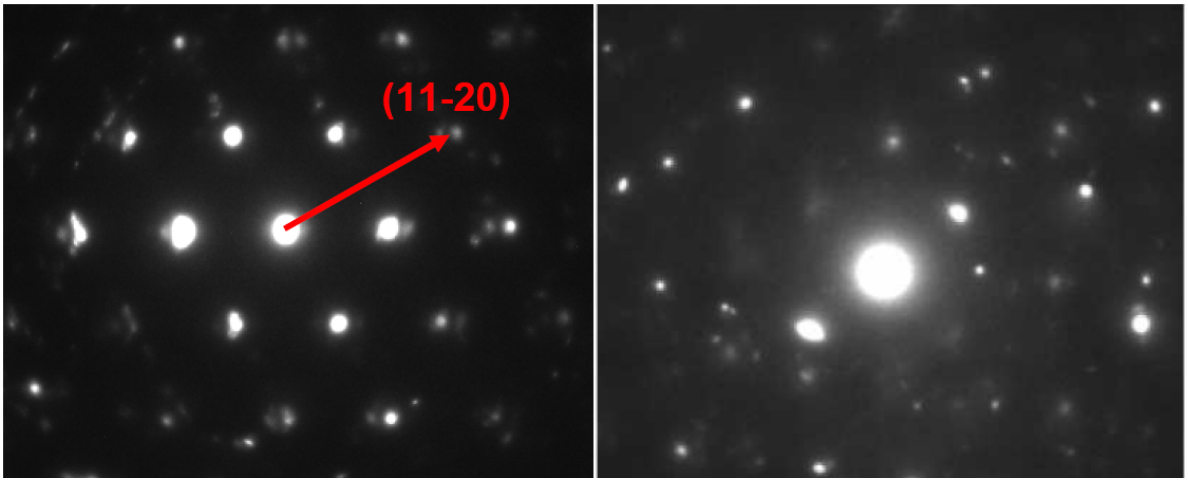

Figure 4.5: [0001] zone axis diffraction pattern of M5® at 0 dpa and 18 dpa (1 MeV Kr at 300°C)

In Zry-4, <a>-loops were studied at the high damage level of 25 dpa; Fig. 4.6 shows the observed <a>-loop contrast at high magnification with diffraction vector $\vec{g} = (01\bar{1}0)$ or equivalent, which allows for visibility of two thirds of the <a>-type contrasts and two thirds of the mixed <c+a>-types. Analogously as in M5®, the <a>-loops formed from the beginning of the irradiation and built a dense network at high damage level. The diffraction pattern given in figure 4.6 is taken after the final dose of 25 dpa and does not show signs of recrystallization. It is therefore assumed that the strong diffraction pattern degradation observed in the M5® sample was caused by the low grain thickness and the close position of the grain to the hole which allowed for strong bending. The Zry-4 grain had a higher thickness of 247 nm.
Fig. 4.7 shows the <a>-loop size distribution in both samples, at damage level 2 dpa in the M5® sample and for the high dose of 25 dpa in Zry-4.

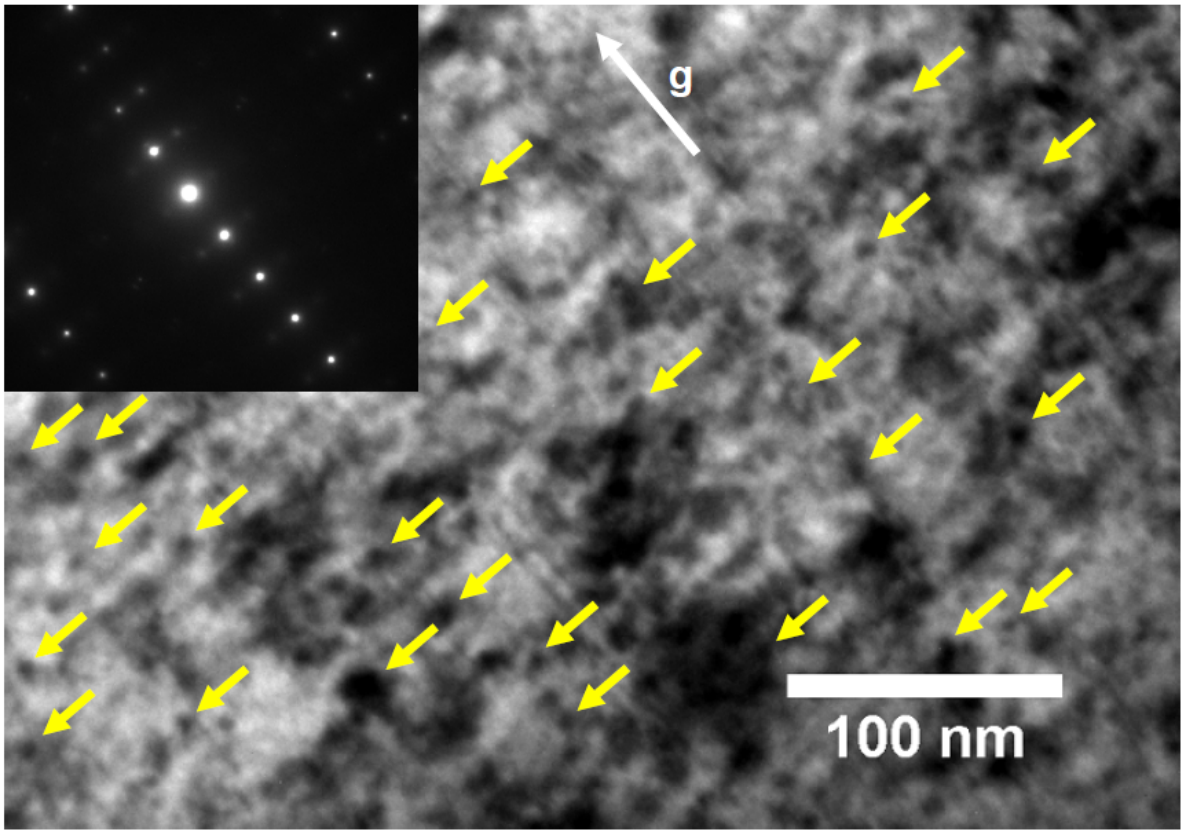

Figure 4.6: <a>-loops in Zry-4 (25 dpa, 1 MeV Kr at 300°C); $\vec{g} = (01\bar{1}0)$ or equivalent

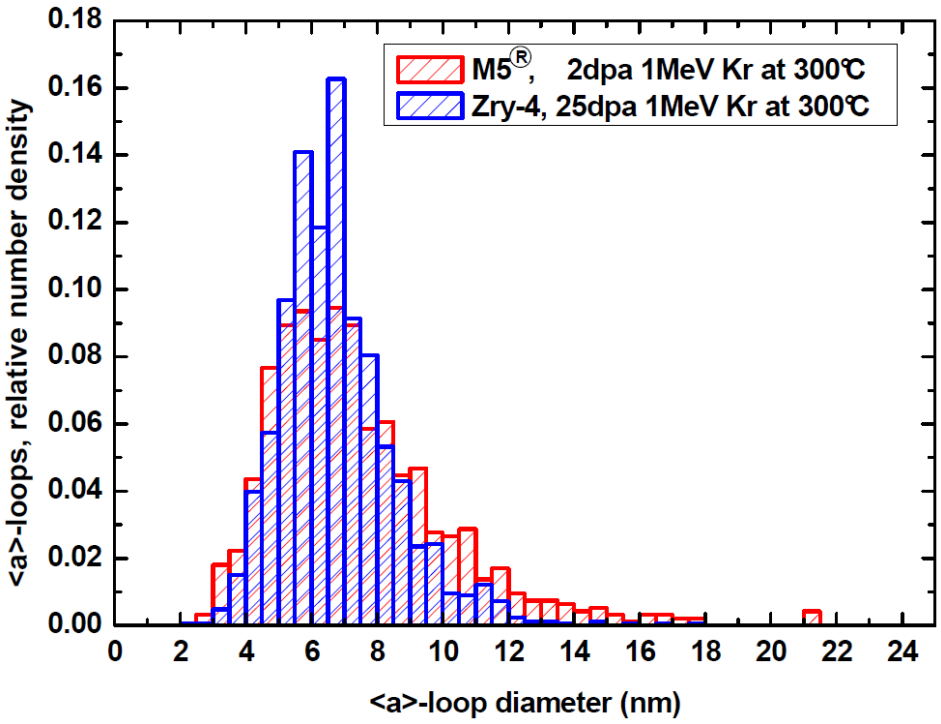

Figure 4.7: <a>-loop size distribution in M5® and Zry-4 (1 MeV Kr at 300°C)

The <a>-loops' measured average sizes are 7.4 nm at 2 dpa for M5® and 6.8 nm at 25 dpa for Zry-4. These sizes correspond well to the typical <a>-loop diameters in neutron irradiated Zr alloys of about 8 nm stated in the literature [10]. <a>-loops are expected to be of both interstitial and vacancy type [10]; however, the <a>-loop types could not be studied experimentally due to the high loop density and the resulting strong contrasts.

To quantitatively determine the loop densities, the so-called "linear density" is used; it is defined as the sum of the lengths of all loop contrasts of the specific type in one image section, divided by the imaged material's volume. For the irradiated Zry-4 sample, the grain thickness was measured by the grain boundary method described in chapter 3; therefore, a linear <a>-loop density could be calculated from the loop length measurements. At 25 dpa, the linear <a>-loop density as measured for one observed grain was $(1.7\pm0.12)\,\mathrm{x}\,10^{14}\mathrm{m}^{-2}$; the given measurement error is calculated based on one standard deviation of the foil thickness. As the chosed diffraction vector $\vec{g} = (01\bar{1}0)$ allows for visibility of two thirds of all <a>-type contrasts, the total <a>-loop linear density is thus 3/2 of the measured linear density, $(2.6\pm0.18)\,\mathrm{x}\,10^{14}\mathrm{m}^{-2}$. There are only few published values of <a>-loop linear densities in neutron-irradiated Zr-based alloys. Gilbon et al. studied <a>-loop densities in a recrystallized high tin and oxygen version of Zry-4 (1.73 wt.-% Sn, 1640wt.-ppm O) which had been neutron irradiated at 400°C at the Phénix reactor; they report linear densities of $7.5\,\mathrm{x}\,10^{14}\mathrm{m}^{-2}$ at 5 dpa and $9.1\,\mathrm{x}\,10^{14}\mathrm{m}^{-2}$ at 13 dpa [100]. These values are higher than the ones observed in the Kr irradiated sample, but within the same order of magnitude. The deviation between the values might be due to possible variations in the linear density measurement techniques, the different Sn and O content or the 100 K difference in irradiation temperature. It should also be kept in mind that the <a>-loop densities at such damage

levels are high and that loop contrast overlap is probable, which would be an error source in the loop density determination.

To conclude, the <a>-loops observed in 1 MeV Kr irradiated M5® and Zry-4 agree very well in their characteristics with the <a>-loops reported for neutron irradiated Zr-based alloys:

- The <a>-loops begin to form directly with the beginning of the irradiation, without a dose threshold; then, they increase in density with increasing damage level.
- The average <a>-loop size corresponds very well to the average <a>-loop size in neutron irradiated Zr-based alloys of about 8 nm reported in the literature [10].
- <a>-loop linear densities measured in Kr irradiated Zry-4 are in the same range as the linear densities reported for high Sn and O Zry-4, neutron irradiated at 400°C in the Phénix reactor [100].

4.2.2 <c>-Loops

The <c>-loop contrast development with the ion dose in M5® was studied in one grain of sample A2. An overview TEM picture of the observed grain in its unirradiated state can be seen in Fig. 4.8. The grain's diffraction pattern of pole $(2\bar{1}\bar{1}0)$ with the (0002) reflex location is shown next to the BF image.

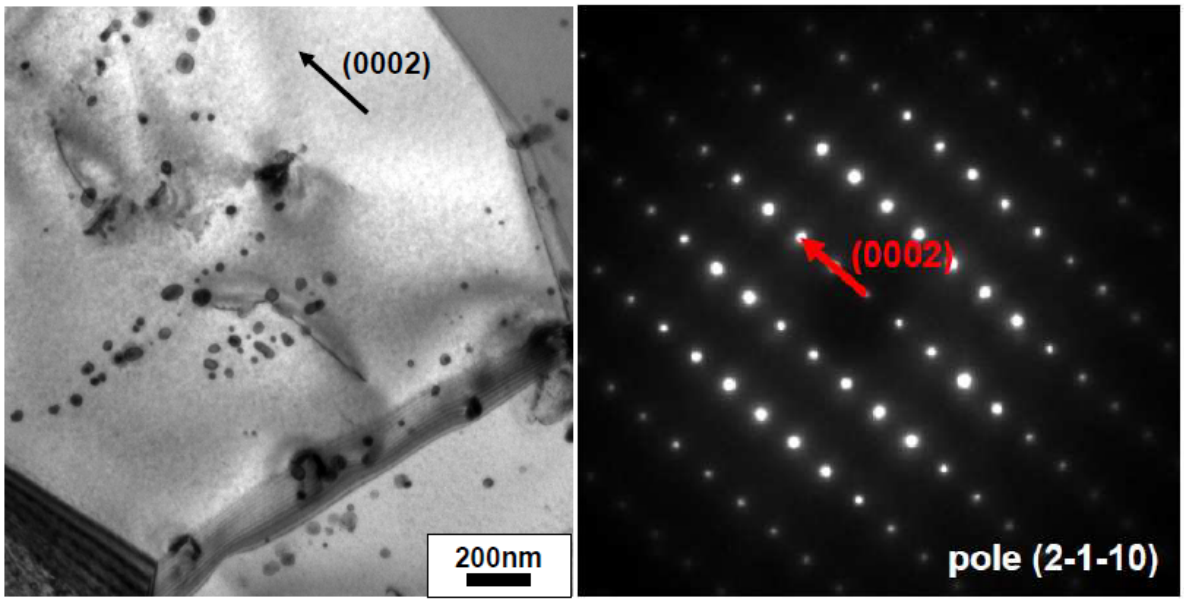

Figure 4.8: M5® sample A2, unirradiated grain, $\vec{g}$ = (0002) (left); $(2\bar{1}\bar{1}0)$ pole diffraction pattern (right)

The thickness of the grain was determined by the grain boundary method to be 181 nm.
Fig. 4.9 shows the development of the <c>-loops with the ion dose. In Fig. 4.10, a grain area of sample A2 at a damage level of 22 dpa imaged at a lower magnification demonstrates that the <c>-loops are homogeneously distributed over the grain. The darker contrast to the right

is caused by a more dynamic diffraction condition in that grain region, with the contrast being sensitive to weak lattice strains, while the lighter contrast to the left is given by a more kinematical diffraction condition with the contrast more confined to the physical size of the dislocation loops [97]. The difference in the diffraction conditions is caused by a slight bending of the grain.

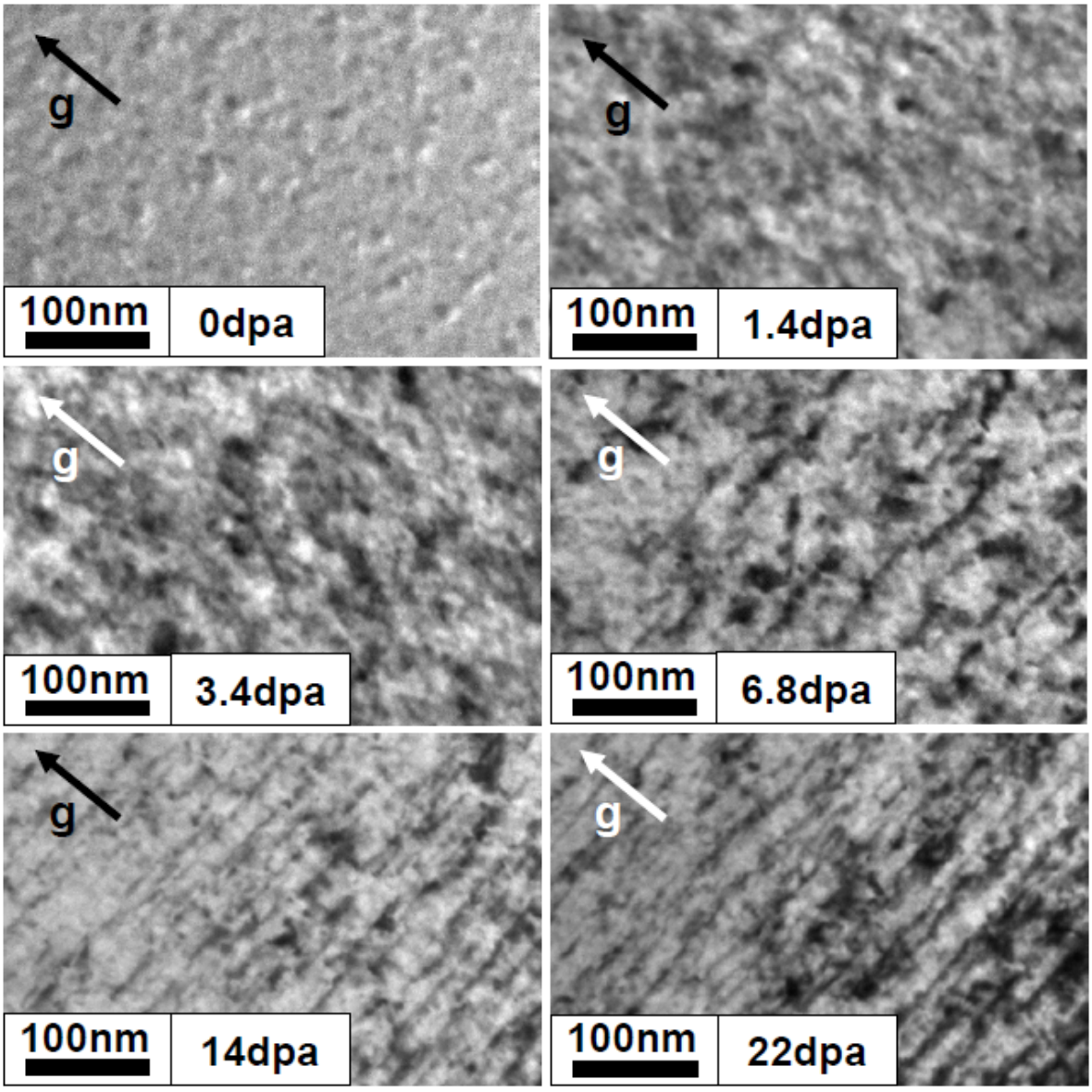

Figure 4.9: <c>-loop development in M5® with the ion dose (1 MeV Kr at 300°C); $\vec{g} = (0002)$

Contrary to the <a>-loops, <c>-loops are not observed in the early stages of irradiation. Sample A2 was irradiated stepwise; after the step to 6.8 dpa, <c>-loop contrasts were clearly observed, while they were absent up to 3.4 dpa. It can be seen in several of the imaged regions that the <c>-type contrasts are each composed of several smaller contrasts, suggesting small loops which are ordered in a chain-like structure to form the typical line contrast, as indicated by the arrows in Fig. 4.11.

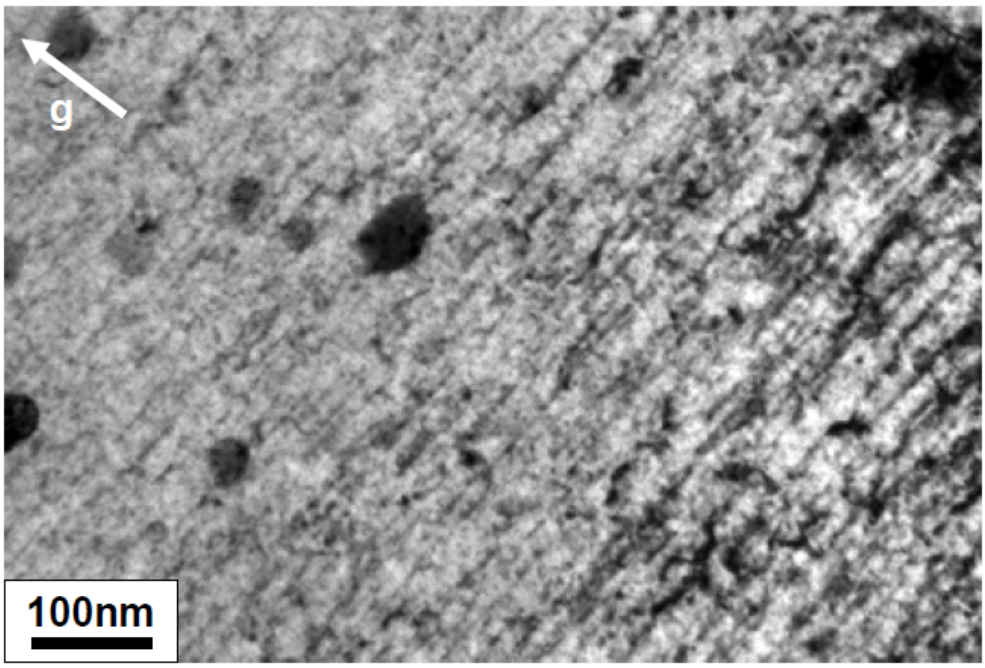

Figure 4.10: <c>-loop distribution in M5® sample A2 at 22 dpa (1 MeV Kr at 300°C); $\overrightarrow{g} = (0002)$

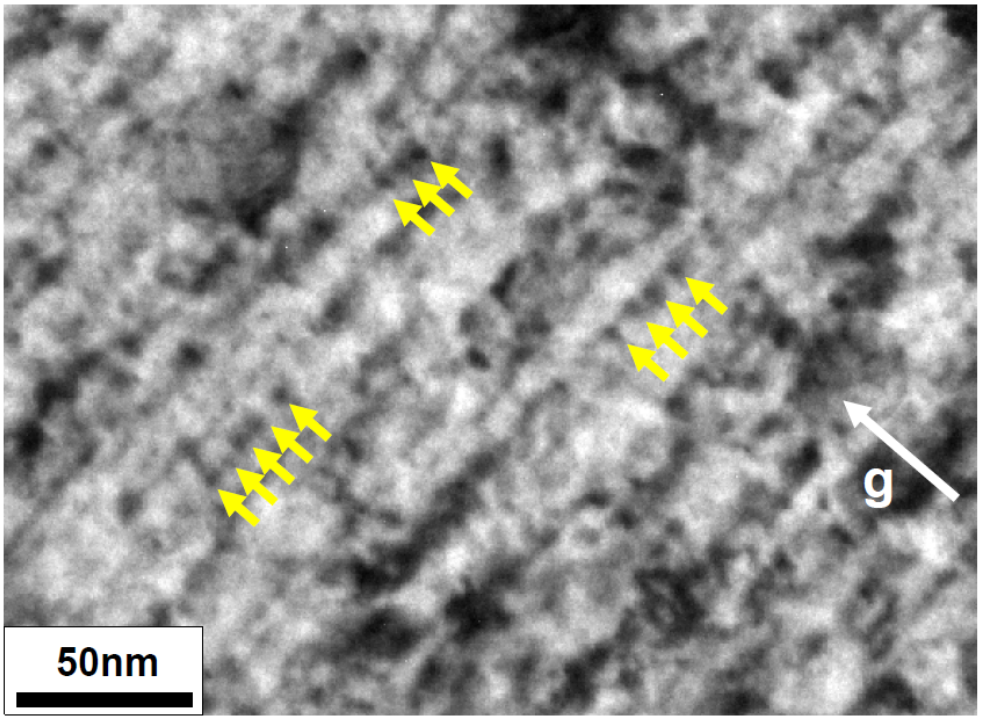

Figure 4.11: <c>-type contrasts formed by small loops (1 MeV Kr at 300°C) in M5®; $\overrightarrow{g} = (0002)$

A Zry-4 sample, PA2, was imaged as well during in-situ irradiation to study the <c>-loop formation; for this sample, movies were taken during the irradiation process from the beginning, to determine the threshold damage level for <c>-loop nucleation. The imaged grain in PA2 had an orientation towards the beam that allowed for imaging of both <a>- and <c>-loops. Fig. 4.12 shows both contrasts with their respective diffraction conditions for the final dose of 25 dpa. The <a>-loops, as described above, were imaged with diffraction vector $(01\bar{1}0)$, which leads to a complete invisibility of the <c>-loops (see left image). By tilting the sample away from this diffraction condition to excite the (0002) reflex, all <a>-contrasts are invisible and the <c>-loops appear (see right image). The diffraction pattern added to the images show the perpendicular position of the two diffraction vectors to each other in the reciprocal lattice.

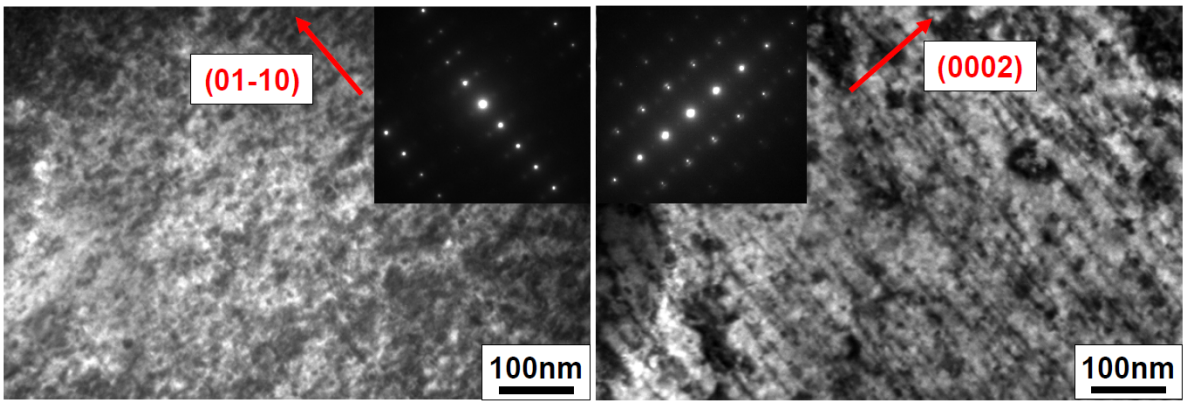

Figure 4.12: <a>- and <c>-loop imaging conditions in the same grain in Zry-4 sample PA2 (25 dpa 1 MeV Kr at 300°C)

For a detailed observation of the <c>-loop development with the dose, the grain was set up for <c>-loop imaging, and one grain region was observed from its unirradiated state up to 25 dpa. Fig. 4.13 shows the development of the <c>-loops with the damage level.
The left lower corner of the imaged position shows a part of a Laves precipitate. As expected from previous studies on Zr-based alloys [77] and from neutron irradiated material, the <c>-loops form only after a threshold dose in the Zr-matrix. From the movies taken during the irradiation, the point of first observation of small <c>-loops was found to be at 5.5 dpa. However, in direct vicinity of the precipitate, <c>-loop contrasts can be observed to nucleate at a lower damage level; the image taken at 3 dpa (see Fig. 4.13) already shows small loops. This is in agreement with observations for neutron irradiated Zr-based alloys, where <c>-loops at the beginning of their formation are reported to be located close to the intermetallic precipitates [36]. This is assumed to be due to a gradual dissolution of the Fe in the SPP into the matrix, which might then provide <c>-loop nucleation points or lead to faster <c>-loop growth. This effect of faster <c>-loop nucleation near SPPs under heavy ion irradiation in Zry-4 has been shown for the first time. It confirms the good agreement between PWR neutron damage and heavy ion damage under the chosen experimental parameters. As in the Kr irradiated M5® sample, the <c>-loops are distributed homogeneously throughout the grain.

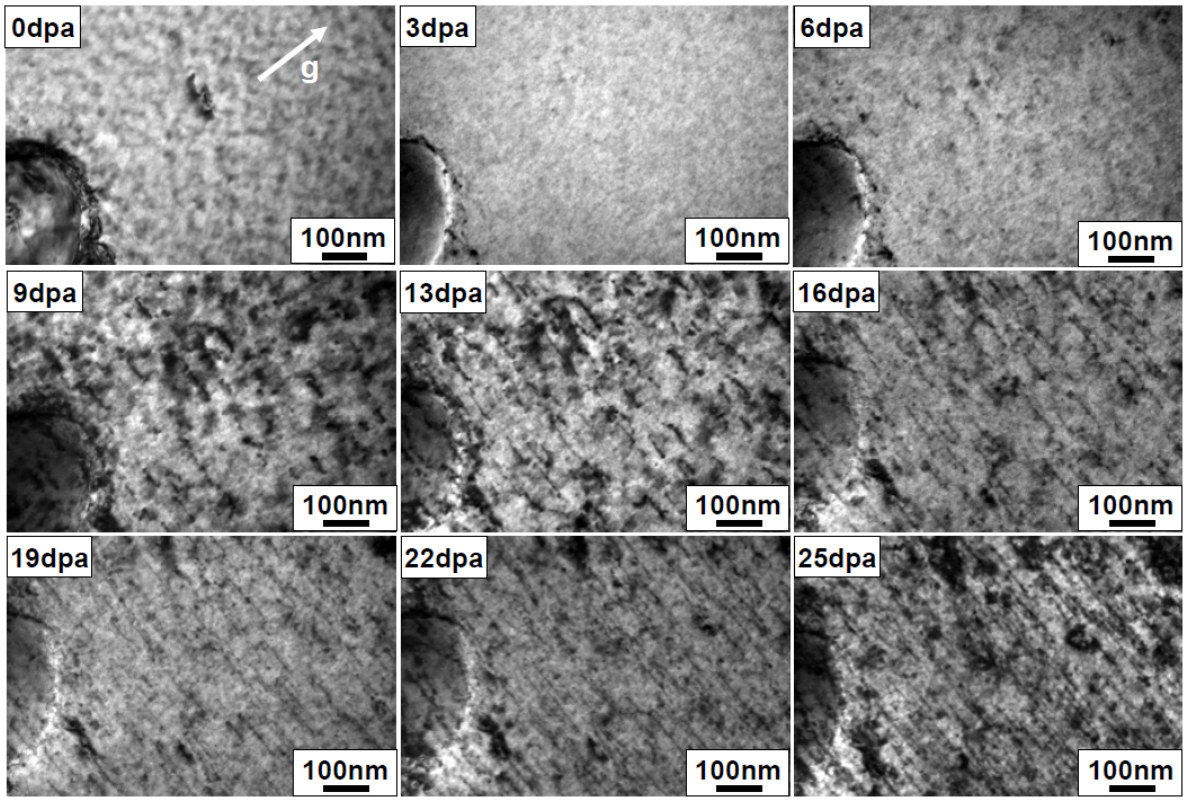

Figure 4.13: <c>-loop development with the dose in Zry-4; $\overrightarrow{g} = (0002)$

The <c>-loop density is also quantified by the linear density, dividing the sum of the lengths of all <c>-loop contrasts in one image section by the imaged material's volume. The <c>-loop linear density is a widely-used quantity [26,74,100] and allows to compare the measured <c>-loop densities with literature data. For each sample, several grain regions were chosen to determine the linear density from images taken at a magnification of 30'000. The received densities for M5® sample A2 and Zry-4 sample PA2 are shown in Fig. 4.14, together with literature values for heavy ion and neutron irradiated Zr-based alloys [26, 74, 100]. From the M5® sample A2, a movie was taken for damage levels from 7 dpa to 22 dpa with a higher magnification of 70'000; the received linear densities from this high magnification image series are added to the diagram for the sake of completeness. This higher magnification leads to a visibility of loop contrasts that cannot be observed in the lower magnification images; thus, the linear densities measured in frames taken from the movie are higher.

The <c>-loops show an approximately homogeneous distribution over the grains; the statistical variation can be seen by comparing the linear densities calculated from the loop size measurements at different grain positions. A general change in the <c>-loop density near outstanding microstructural features like grain boundaries or precipitates was not observed (with exception of the earlier onset of <c>-loop nucleation near the Laves precipitate in Zry-4). It is thus concluded that, if these possible defect sinks have any influence on the general <c>-loop densities, the effect is not significant under the chosen experimental conditions.

For the linear densities in the Zry-4 sample, error bars are given. They were calculated based on one standard deviation of the grain thickness measurements at about 8 different tilting angles,

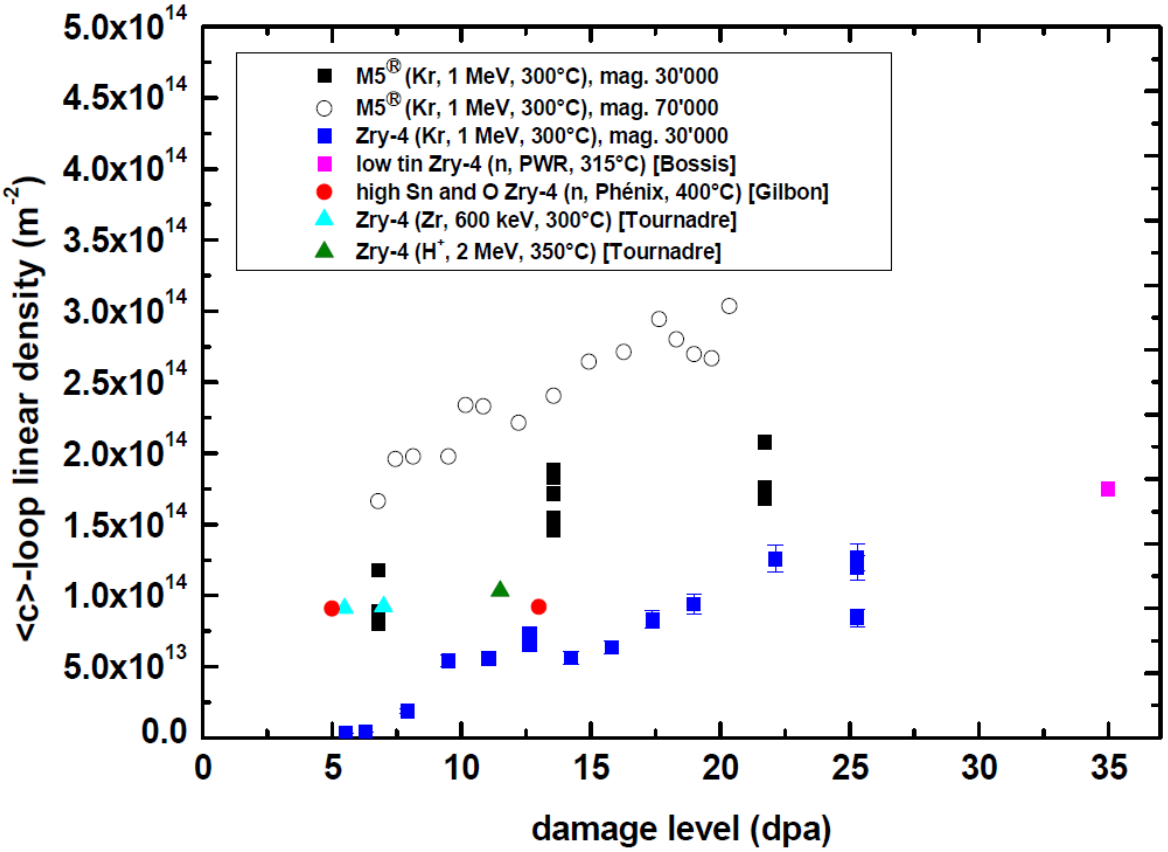

Figure 4.14: Measured <c>-loop linear densities compared to literature data by Tournadre [74], Bossis [26] and Gilbon [100]

using the grain boundary method. As these thickness measurements had only been done twice for the grain in the M5® sample, the M5® density values do not contain error bars.
Different literature values for the linear <c>-loop densities are added to the diagram. As far as the information is contained in the literature, the linear densities were taken from images with magnification of 30'000; thus, the following comparison to literature data is done for the densities measured at 30'000.
The ion irradiation induced <c>-loops' linear densities measured in Zry-4 agree very well with the densities reported by Bossis et al. in 2007 for PWR neutron irradiated low tin Zry-4 [26]. Also, they correspond well to high Sn and O Zry-4 irradiated in the Phénix fast breeder reactor as described by Gilbon et al. in 1994 [100], specifically with the density given for about 13 dpa. The deviation in the range of 5 dpa can be expected, since <c>-loop densities are very low near the nucleation threshold which would increase the measurement error. In addition, the measured <c>-loops' linear densities in both alloys are in the same range as data on ion irradiated Zry-4 presented by Tournadre et al. in 2011 [74], for both Zr and proton irradiation.

Fig. 4.15 shows the observed <c>-loop size distributions for the maximal damage level reached in the samples A2 (M5®) and PA2 (Zry-4). The given values include the measurements of 4 different positions within one grain in A2 and 3 different positions within one grain in PA2. The perception of the loops as several small ones or one long loop may vary for each person doing the

measurements. Also, the actual observed length can depend on the specific imaging conditions in each TEM image. To keep this bias as low as possible, all length measurements were done by the author of this work; also, images with the same magnification were chosen. The average <c>-loop diameters are 36 nm for M5® and 16 nm for Zry-4. As a comparison, two TEM images taken from publications on neutron induced <c>-loops in annealed Zry-4 were measured analoguously to the TEM images from the ion irradiated samples. Remeasuring the published images is expected to avoid the possible bias in length measurement. The images chosen are from a Zry-4 sample irradiated at 290°C in a BWR [101] and a Zry-4 sample irradiated at 290°C in a CANDU [12], both to a neutron fluence of 8.5×10^{21}n/cm^2 (E>1 MeV). Using the neutron flux-dpa conversion suggested by Shishov et al. [25] for PWR as an approximation, due to the absence of a BWR or CANDU conversion factor in the open literature, the given fast fluence corresponds to 14 dpa. The magnification was in the same range as for the ion irradiated samples, but image quality was comparatively low as the images were taken in the 1980s. For the BWR irradiated sample, the received average <c>-loop length is 27 nm; in the CANDU-irradiated sample, it is 19 nm. This provides an estimate of the measured loop length variation for different neutron irradiated samples. The <c>-loop size distribution of these neutron irradiated samples is also included in Fig. 4.15.

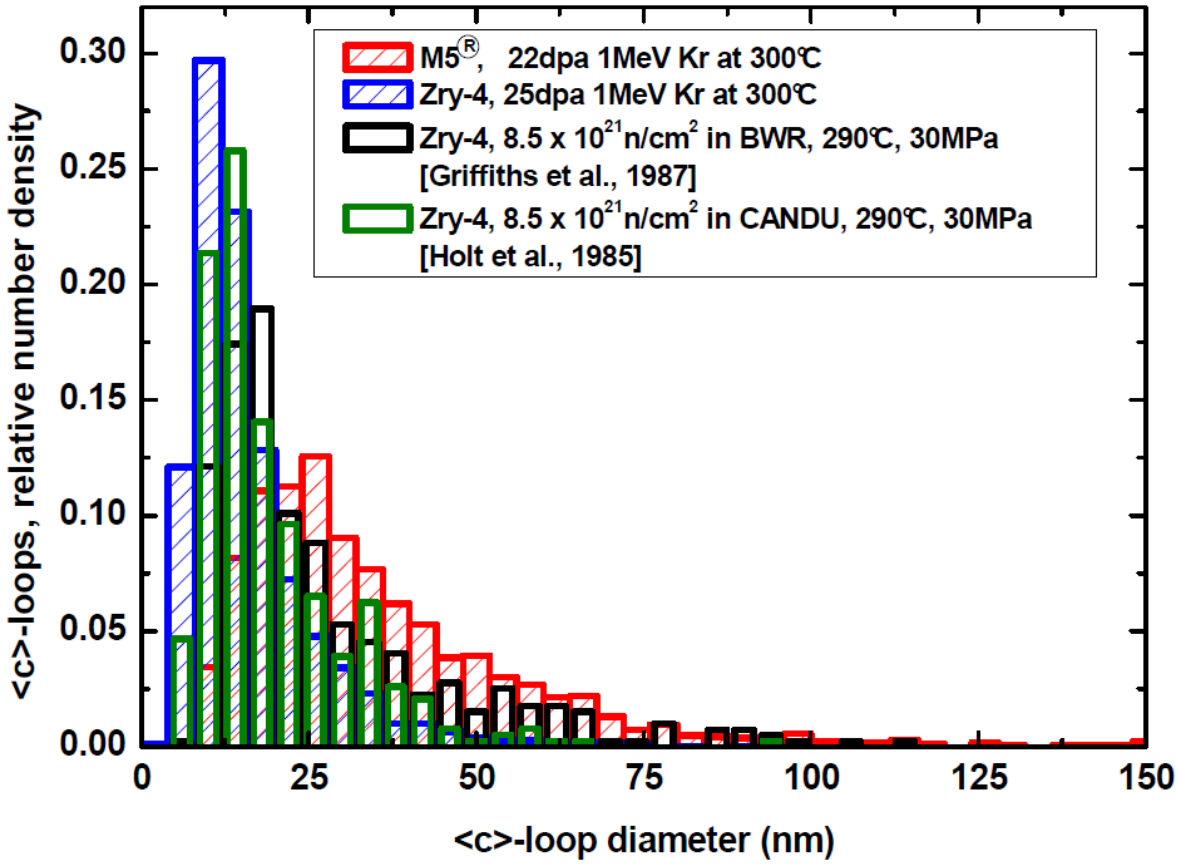

Figure 4.15: <c>-loop size distribution in ion irradiated M5® and Zry-4 (1 MeV Kr at 300°C)

The <c>-loop size distribution is rather comparable for all four samples; especially the three Zry-4 samples' distributions are very similar. This confirms the general agreement between the <c>-loop characteristics for heavy ion irradiated and neutron irradiated samples.

In addition to the in-situ TEM irradiations, experiments were also carried out using ion irradiation to the final dose with the TEM imaging afterwards. Fig. 4.16 shows two examples of Zry-4 grains, one of them irradiated with 1 MeV Kr at ANL and the other with 1 MeV Zr at IPP. They both received an ion fluence of $5 \times 10^{15} \mathrm{cm}^{-2}$, which corresponded to 25 dpa in the ANL sample; for the IPP sample, the grain thickness was not measured but estimated to be 200 nm, which results in a calculated final damage level of 27 dpa.

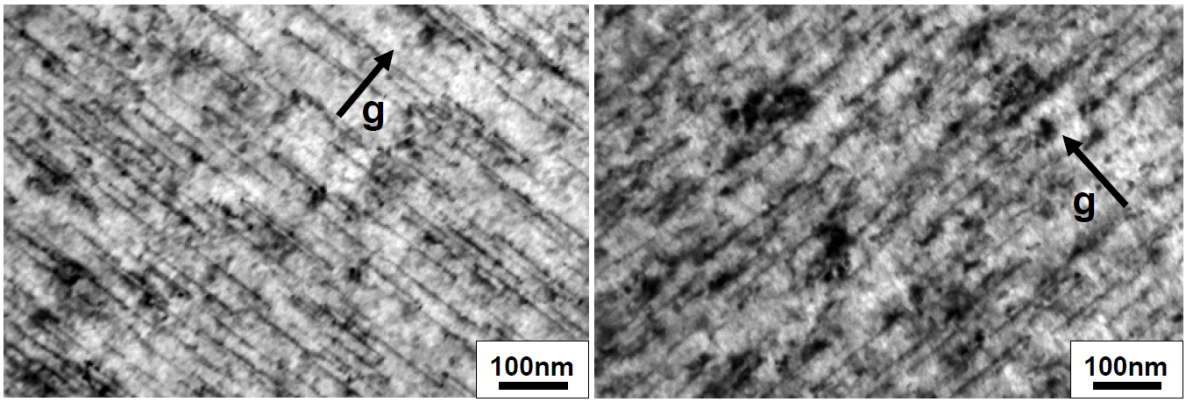

Figure 4.16: <c>-loops in Zry-4 pre-irradiated at 300°C with 1 MeV Kr at ANL (left) and with 1 MeV Zr at IPP (right); $\vec{g} = (0002)$

Both samples show a homogeneous network of <c>-loops with significant density, analogous to the samples studied with in-situ TEM. The loops in both samples, which were irradiated with different projectiles with significantly different damage rates (see table 3.3), are comparable in their size and distance distribution. It can therefore be concluded that the irradiation microstructures produced by Zr and Kr irradiation are in agreement. Also, a significant influence of the accelerator and damage rate with regard to the final loop structure was not found.

Discussion of the <c>-Loops' Characteristics

There was one specific observation of the <c>-loops' characteristics in all studied samples irradiated at 300°C that was not reported in the literature before and should thus be emphasized: The <c>-loop contrasts which are typically described in the literature as being large loops viewed edge-on give strong indications in their contrast appearance of not being single large loops, but instead chain-like structures of many aligned, small loops. There are some details which support this hypothesis: High magnification bright field images show the <c>-type contrasts to actually consist of a number of small contrasts (see e.g. Fig. 4.11). This general loop appearance was observed in all TEM samples when viewed at sufficiently high magnification. Also, the loops when imaged at the usual magnification of about 30000 x show kinks and jogs along their lengths, which would be more obvious to emerge for aligned small loops than for one large loop. An experimental verification of the hypothesis by tilting the <c>-loops from their edge-on orientation towards a plane orientation was impossible in the samples, due to the high <a>-type contrast

densities. A possibility would be the heating of the samples to 450°C where the <a>-type contrasts should have annealed (see DBS studies to be described in the following); however, such a change in sample temperature could easily lead to changes in the <c>-loop characteristics, such that the <c>-loops would not keep their original features. There is no straightforward explanation from the imaging conditions as to why those contrast features should emerge as an imaging artifact. There might be a possibility that strain fields from the <a>-loops on the prism planes lead to lattice distortions which produce the observed effect. However, thinking of possible <c>-loop nucleation and development processes, the nucleation of small <c>-loops and their gradual alignment to chain-like structures when their number increases with the damage level could be a valid physical process, perhaps similarly probable as the generally assumed formation of single large <c>-loops.

A central point in the interpretation of the results of this work is the degree of possible correlation between the observed irradiation induced microstructures, specifically the <c>-loop structure, and the macroscopic irradiation growth phenomenon. This issue contains several different aspects which will be discussed one at a time.

- The experimental work described in this thesis covered the irradiation induced microstructures forming after heavy ion irradiation. The measurement of irradiation induced material deformation, either in single grains or macroscopic samples, was not an objective of this work. Therefore, a direct experimental correlation between irradiation induced microstructures and material growth cannot be provided by this work. However, the formation of <c>-loops is correlated by both experimental and theoretical work in the literature with the onset of breakaway growth (see chapter 2). Based on this reported correlation, indirect conclusions to possible material deformation can be drawn from the observed microstructures.

- Based on the reported correlation between <c>-loop appearance and breakaway growth, the first information that can be gathered from ion irradiated samples would be the tendency of different materials to show breakaway growth. A low <c>-loop nucleation threshold would indicate an early onset of breakaway growth, while a higher threshold would lead to a later occurrence of the phenomenon.

- Following the literature argument that the presence of <c>-loops enhances irradiation growth, it can be assumed that a higher density of <c>-loops would lead to a stronger material growth. Thus, the absolute <c>-loop density increase rate in the ion irradiated samples can be used as an indicator for the growth rate with the damage level after the onset of breakaway growth.

- It should be discussed in more detail which point of the <c>-loop formation is actually the one that correlates with the onset of breakaway growth. As was already shown in the studies presented above, <c>-loops are rather small and have a low density when they are first observed after the threshold dose. It is also possible that they exist in a smaller state that is invisible with the chosen imaging conditions and magnification before the observed threshold. Referring to the growth model by Bacon [38] which describes the <c>-loops to act as a defect sink that disturbs the equilibrium between interstitial and vacancy type loops on prism planes, it is not highly probable that the few small loops in that first state of nucleation already show a significant effect on material growth. It would seem more likely that a certain <c>-loop density has to be present before significant effects on material

growth will emerge; this will be described in the following as "critical <c>-loop density". In this context, it should also be kept in mind that a low <c>-loop threshold with a high <c>-loop density increase rate could have the same effect on the onset of breakaway growth as a higher <c>-loop threshold with a lower <c>-loop density increase rate, reaching the critical <c>-loop density at the same damage level. According to the growth data of recrystallized Zry-2 and Zry-4 neutron irradiated at around 300°C presented by Holt et al. [12] (see Fig. 2.11 in chapter 2), the transition region from the rather moderate material growth in phase II to breakaway growth in phase III lies in a fast fluence range of about 4-6 x 10^{21}n/cm^2 (E>1 MeV). Based on the PWR fluence to damage level conversion, this transition range corresponds to a damage level range of 6.7 to 10.0 dpa, with the average being 8.3 dpa. The <c>-loop damage level thresholds found for the in-situ irradiated samples as presented above were between 3.4 and 6.8 dpa for standard M5® (sample A2) and 5.5 dpa for standard Zry-4 (sample PA2). These damage level thresholds correspond in general to the fast fluence regions reported by Holt et al., and thus confirm the hypothesis of the link between <c>-loop appearance and onset of breakaway growth. To narrow the value of the critical <c>-loop density down, the Zry-4 sample whose properties are similar to the material studied by Holt et al. [12] will be used. To demonstrate how the <c>-loop structure looks like in the damage level region where breakaway growth begins according to Holt et al., Fig. 4.17 shows three TEM images of sample PA2, taken at damage levels corresponding to the lower boundary, average value and upper boundary for the transition to breakaway growth.

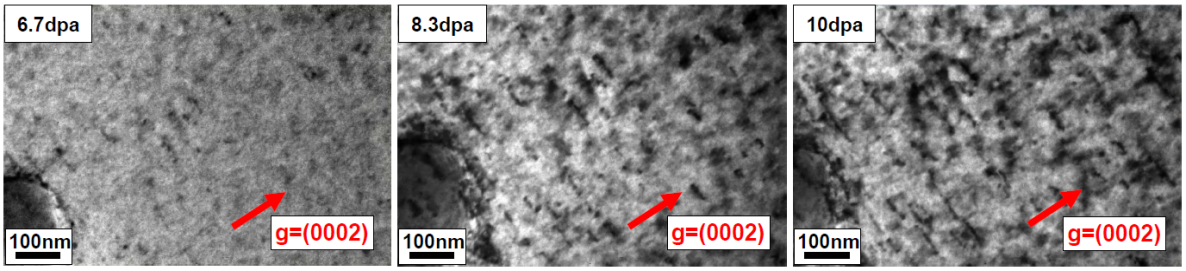

Figure 4.17: Zry-4 standard sample at damage levels representing the observed region of macroscopic growth transition to breakaway

Table 4.1 summarizes the average <c>-loop length and the <c>-loop linear densities measured for these damage levels.

damage level (dpa)	average <c>-loop length (nm)	<c>-loop linear density (m^{-2})
6.7	10.7	(4.48±0.260) x 10^{12}
8.3	11.5	(1.46±0.109) x 10^{13}
10.0	11.1	(3.46±0.259) x 10^{13}

Table 4.1: <c>-loop average length and linear densities for standard Zry-4 in the transition damage level region to macroscopic breakaway growth

From the comparison of the measurement results with the macroscopic growth data by Holt et al., it is concluded that the critical <c>-loop linear density which marks the be-

ginning of macroscopic breakaway growth in recrystallized Zry-4 irradiated at about 300°C lies in the range of $1.5 \times 10^{13}\,m^{-2}$ and shows an average loop length of about 11 nm. This critical <c>-loop distribution is close to the observed actual <c>-loop nucleation threshold at 5.5 dpa, but lies slightly above it. It should be mentioned that the growth samples used in the experiments by Holt et al. can be expected to have contained some amount of hydrogen, since they spent significant time being irradiated in a BWR and PWR. This might have an effect on the <c>-loop nucleation threshold in the samples. This issue will be taken up again in section 4.3.3.
Ion irradiation experiments by Tournadre et al. [74] using 600 keV Zr on Zry-4 at 300°C show a <c>-loop nucleation threshold between 4.1 and 5.5 dpa. This agrees well with the nucleation threshold of 5.5 dpa observed for sample PA2.

Summary of the <c>-Loops' Characteristics

In summary, the <c>-loop microstructure induced by heavy ion irradiation under the chosen experimental conditions shows good agreement with the microstructure observed under neutron irradiation:

- <c>-loops can be produced by heavy ion irradiation in both M5® and Zry-4, at different accelerators and with both Kr and Zr projectiles.
- As reported for neutron irradiated Zr-based alloys, the <c>-loops start to form after a threshold dose only, and then increase in density.
- The threshold dose found for the onset of <c>-loop formation in 1 MeV Kr irradiated Zry-4 confirms the correlation between <c>-loop nucleation and the onset of breakaway growth described by Holt et al. [12]. By comparing that growth data to the observed ion induced <c>-loop structures, the critical <c>-loop density at which macroscopic breakaway growth can be expected to start in Zry-4 LWR neutron irradiated at 300°C is determined to lie in the range of $1.5 \times 10^{13}\,m^{-2}$.
- The <c>-loops' length distribution in both ion irradiated alloys corresponds to the length distribution from BWR and CANDU neutron irradiated recrystallized Zry-4, when the same loop length measurement technique is applied by the same person.
- The <c>-loop linear densities for Kr irradiated Zry-4 agree with the linear density values for neutron irradiated Zry-4 found in the literature. For Kr irradiated M5®, the measured linear densities were found to correspond well to unpublished data from PWR guide tubes.
- In Kr irradiated Zry-4, a preferential nucleation of <c>-loops was observed in direct vicinity to a Laves phase, as reported in the literature for neutron irradiated Zry-4 [36].

4.2.3 Further Microstructural Characteristics

Apart from the investigation of dislocation loop formation, which was the major objective of the conducted experiments, other microstructural features were studied.

- All imaged grains in both M5® and Zry-4 were tested for voids at different dose levels by alternating over- and underfocus imaging and searching for contrast inversion; from

the chosen imaging conditions, voids with a diameter of about 2 nm or higher would have been visible if present in the samples. However, voids were not observed at any dose level. This is in agreement with the literature on neutron irradiated Zr-based alloys. While void formation under irradiation is a typical phenomenon observed in steels (which have a cubic lattice structure), there are no reports on void formation in Zr-based alloys under neutron irradiation [10, 36].

- In M5®, amorphization of the β_{Nb} precipitates was not observed; their alternating contrast between bright field and dark field images, and the absence of rings in the diffraction pattern showed them to be crystalline up to the highest ion dose of 22 dpa. This is in agreement with the reported stability of these precipitates in neutron irradiated M5®.

- Possible differences in the irradiation induced microstructures in the different alloys M5® and Zry-4 were not the primary objective of this work, but the agreements and differences found during the experiments should be noted. The general irradiation behavior of the two alloys was similar. The microstructures of both irradiated alloys at high damage level consisted of a high density of <a>-loops and a lower density of homogeneously distributed <c>-loops. Void formation was not seen in either alloy. The observed <a>-loop structures in both alloys appear comparable. Both alloys showed <a>-loop formation from the beginning of the irradiation, with an increasing loop density with the dose. For damage levels higher than 2 dpa, the average <a>-loops size is in the range of 8 nm for both alloys. <c>-loops formed after a dose threshold in both alloys; for Zry-4, that threshold was determined to be at 5.5 dpa. In M5®, it lies between 3.4 and 6.8 dpa. In both alloys, the increase of the linear <c>-loop density with the damage level shows a linear behavior with a comparable slope. However, Zry-4 showed a lower absolute <c>-loop linear density than M5®; it was by a factor 2.5 lower at 15 dpa and a factor of 1.9 lower at 20 dpa. The measured average <c>-loop size from images of magnification 30'000 x was 36 nm for M5® and 16 nm for Zry-4. However, deviations in the <c>-loop size can also be found between images from neutron irradiated samples of the same material, due to the generally difficult comparability of <c>-loop length measurements.

To sum up, the heavy ion irradiation induced microstructure under the chosen experimental conditions in both M5® and Zry-4 shows all essential characteristics of the microstructure after LWR neutron irradiation. Both <a>- and <c>-loops are produced with their features corresponding to neutron irradiated Zr-based alloys, and unexpected new microstructural effects were not observed. It can be concluded that, despite the large differences in the damage rate between heavy ions and LWR neutrons, and possible influences of the surfaces of the thin TEM foil on the microstructure, the chosen experimental conditions are well suitable for LWR neutron damage simulation.
Therefore, further experiments were carried out using these verified experimental conditions to study the effect of different parameters on the irradiation-induced microstructure.

4.3 Heavy Ion Induced Irradiation Damage in Guide Tube Alloys

As the first studies showed that the chosen experimental parameters were well suited for the simulation of LWR neutron damage in Zr-based alloys, they were applied to investigate the influence of different parameters on the irradiation induced microstructures: ion dose, temperature, hydrogen content and external stress.

4.3.1 Effect of Ion Dose

<a>-Loops

The <a>-loops were observed to nucleate from the very beginning of the irradiation and to increase in density with the dose. For the M5® sample A2, <a>-loop diameters were measured at different comparatively low dose levels; in Zry-4 sample PA2, the diameters were determined at high dose. Fig. 4.18 shows the <a>-loop size distribution in dependence of the damage level.

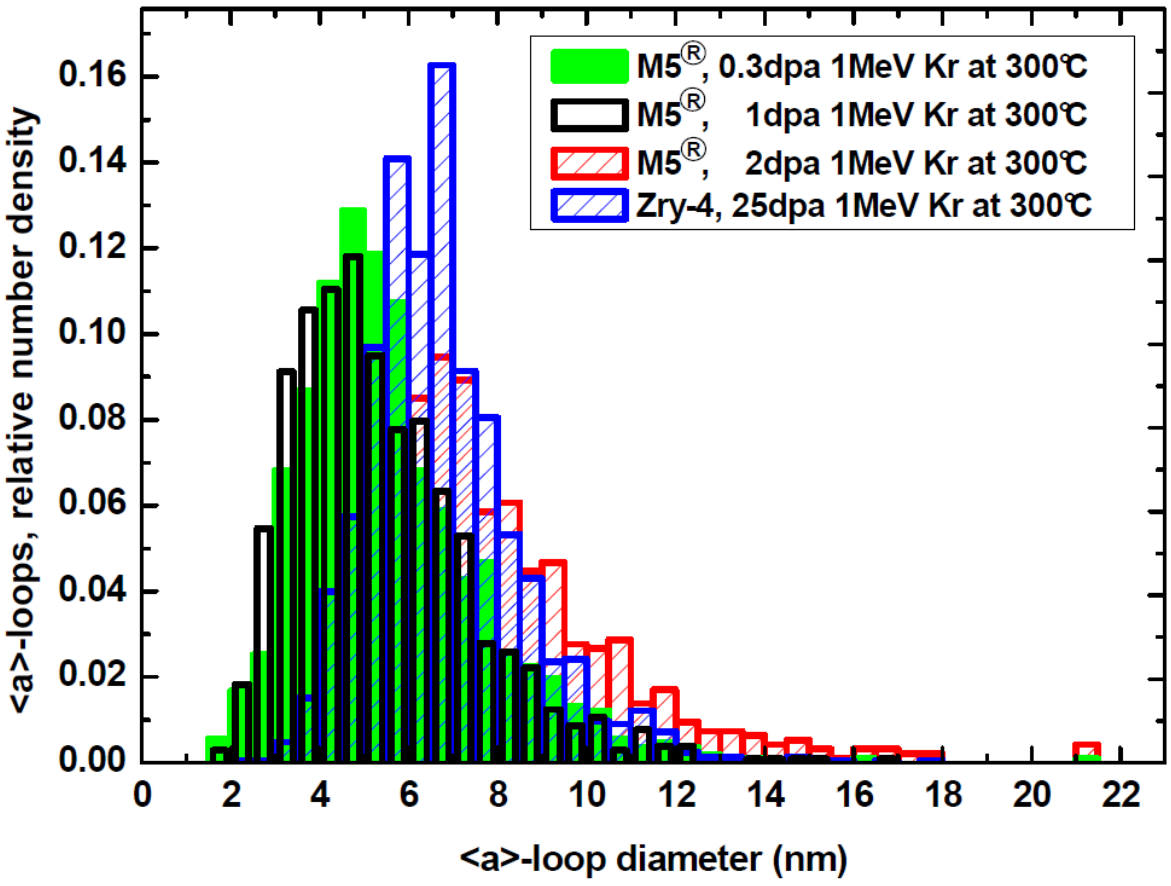

Figure 4.18: <a>-loop size distribution at different damage levels in M5® and Zry-4

The average <a>-loop diameters are given in Table 4.2.
There is a noticeable loop size increase between 1 dpa and 2 dpa; however, between 2 dpa and 25 dpa, assuming that the influence of the alloying on the loop size is insignificant, the loop size remains rather stable.

alloy	damage level (dpa)	<a>-loop diameter (nm)
M5®	0.3	5.6
M5®	1	5.4
M5®	2	7.4
Zry-4	25	6.8

Table 4.2: Average <a>-loop diameters

<c>-Loops

As described above, <c>-loops do not start to form from the beginning of the irradiation like the <a>-loops but only after a threshold dose, which was found to be 5.5 dpa for the Kr irradiated Zry-4 sample PA2. For damage levels exceeding this <c>-loop threshold, the <c>-loop linear densities L show an increase with the damage level which can be approximated by a linear correlation, as shown in Fig. 4.19.

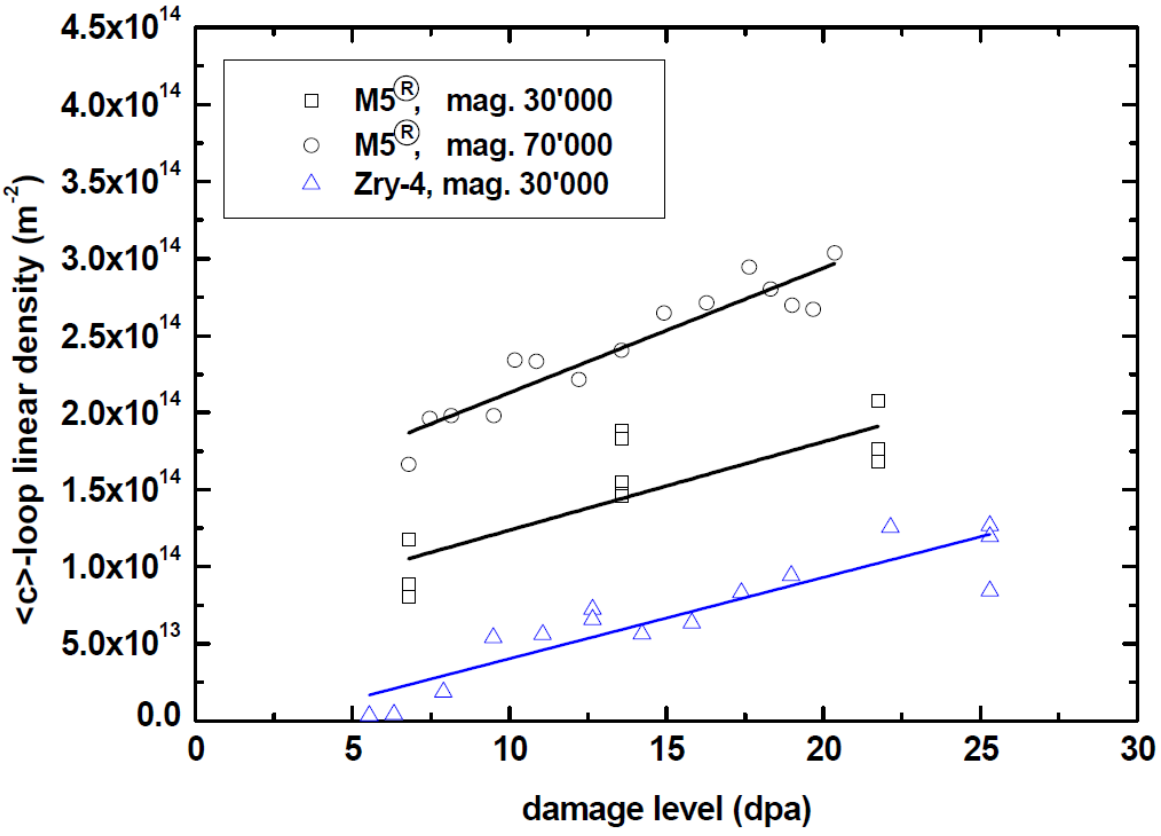

Figure 4.19: <c>-loop linear density increase with the damage level (1 MeV Kr at 300°C)

The assumed correlation is of the form

$$L = L_0 + \dot{L} \cdot D;$$

the fit parameters for the different magnifications and alloys are shown in Table 4.3.

	L_0 (m^{-2})	$\dot{L}$ ($m^{-2}dpa^{-1}$)
M5®, mag. 30'000	$(6.6 \pm 2) \cdot 10^{13}$	$(5.7 \pm 1) \cdot 10^{12}$
M5®, mag. 70'000	$(1.3 \pm 0.1) \cdot 10^{14}$	$(8.1 \pm 0.8) \cdot 10^{12}$
Zry-4, mag. 30'000	$(-1.2 \pm 1.1) \cdot 10^{13}$	$(5.3 \pm 0.6) \cdot 10^{12}$

Table 4.3: Fit parameters for the linear densities

The images taken with the higher magnification of 70'000 show a higher linear density due to the higher contrast resolution but do also have a 40% higher slope as compared to the densities from the images with magnification 30'000. It can thus be assumed that the density of small <c>-loop contrasts visible only at high magnification increases faster with the damage level than the density of larger loops visible also at lower magnification. This can be an indication that the clustering of small <c>-loops to larger alignments is a slower process than the small <c>-loop formation.
The absolute linear densities measured from the images with magnification 30'000 for M5® and Zry-4 are different, with Zry-4 being significantly lower. However, the slope of the fit function for the two materials agrees very well, with only a 8 % deviation. Thus, the increase of the linear <c>-loop density with the dose is very similar for the two materials, but Zry-4 shows a higher threshold dose for <c>-loop nucleation. In the dose region above the threshold, a damage level increase of 5 dpa leads to a <c>-loop linear density increase of about 25% of the final density reached at 25 dpa (calculated for the standard Zry-4 sample).
Such a correlation of the <c>-loop linear densities with the dose can be found comparatively fast when using ion irradiation for neutron damage simulation. For neutron irradiation, in-situ TEM imaging is impossible. A comparative study by stepwise in-pile material irradiation takes irradiation times in the range of months (in high-flux material test reactors) or years (in nuclear power plants), and the subsequent TEM preparation can induce preparation artifacts in the samples. Obviously, the imaged material regions would be different after each irradiation step. This shows the great advantage of the in-situ ion irradiation method as compared to in-pile neutron irradiation.

The <c>-loop size distribution for one grain in the M5® sample A2 at different damage levels is shown in Fig. 4.20; the length distribution is based on TEM images of 4 different positions in the grain (for 7 and 22 dpa) and on 5 different positions for 14 dpa. The average <c>-loop size increases slightly with the dose, by 17 % from 7 dpa to 22 dpa (see Table 4.4).

sample	damage level (dpa)	<c>-loop length (nm)
M5®	7	30.4
M5®	14	32.4
M5®	22	35.6
Zry-4	8	15.4
Zry-4	13	12.2
Zry-4	25	16.0

Table 4.4: Average <a>-loop lengths as a function of the damage level

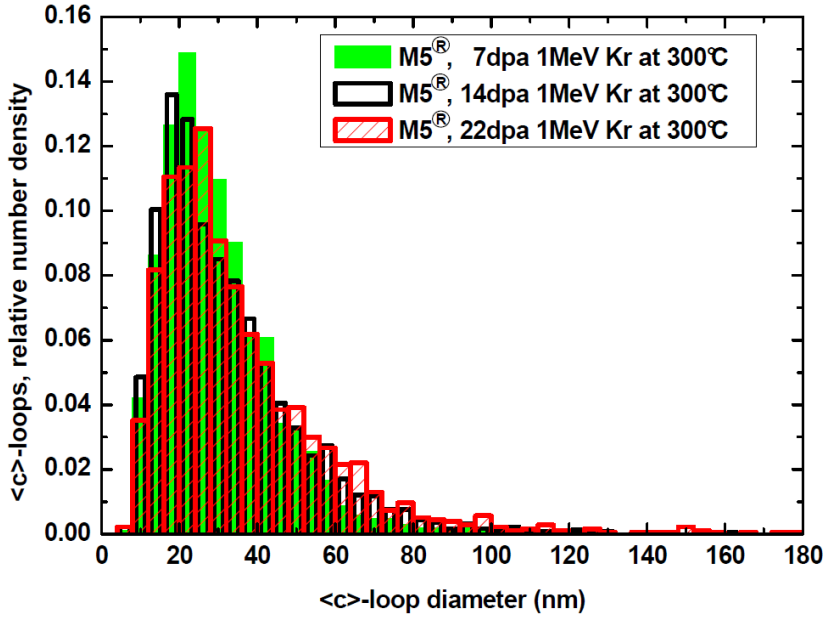

Figure 4.20: <c>-loop size distribution in ion irradiated M5® (1 MeV Kr at 300°C)

Fig. 4.21 shows the <c>-loop size distribution for different damage levels in Zry-4. The distributions are taken from TEM images of one position at 8 dpa, of 2 positions in the grain at 13 dpa and of 3 positions at 25 dpa. The average <c>-loop size does not show a clear trend as a function of the dose in Zry-4 (see Table 4.4).

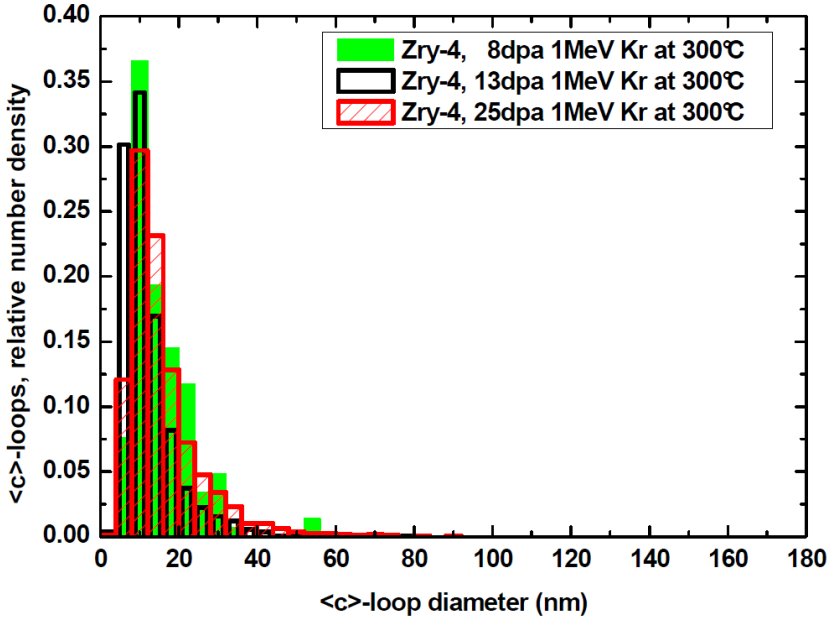

Figure 4.21: <c>-loop size distribution in ion irradiated Zry-4 (1 MeV Kr at 300°C)

Overall Vacancy-Type Defect Densities

While the observation of the <a>- and <c>-loops in the TEM is of most importance to study irradiation growth, positron Doppler Broadening Spectroscopy (DBS) as a complementary experimental technique was used to measure the overall vacancy-type defect density in the material. As a fraction of the <a>-loops and all <c>-loops are reported to be of vacancy-type, it can be assumed that the higher the overall vacancy-type defect density, the higher the general loop density. In addition, dislocation loop studies in the TEM do not provide information about defects in other forms than loops, like single vacancies, which can be expected to be equally part of the irradiation induced microstructure. Therefore, the vacancy-type defect density was studied by DBS, in several M5® foil samples irradiated under different conditions.
The S-parameter was measured in four M5® foil samples, consisting of one unirradiated standard and three samples (I1, I2 and I3) irradiated with 3 MeV Zr at 35°C at the IPP accelerator, to dose levels of 0.1, 0.2 and 0.4 dpa. Fig. 4.22 shows a lateral scan over an area of 2 cm x 2 cm of the four quadratic samples; the given S-parameter is normalized, using the S-parameter averaged over the central region of the unirradiated sample (x=3...7 mm, y=3...7 mm), 0.53, as a standard. The scan was taken with a positron energy of 25 keV which corresponds to a positron mean penetration depth of 880 nm.

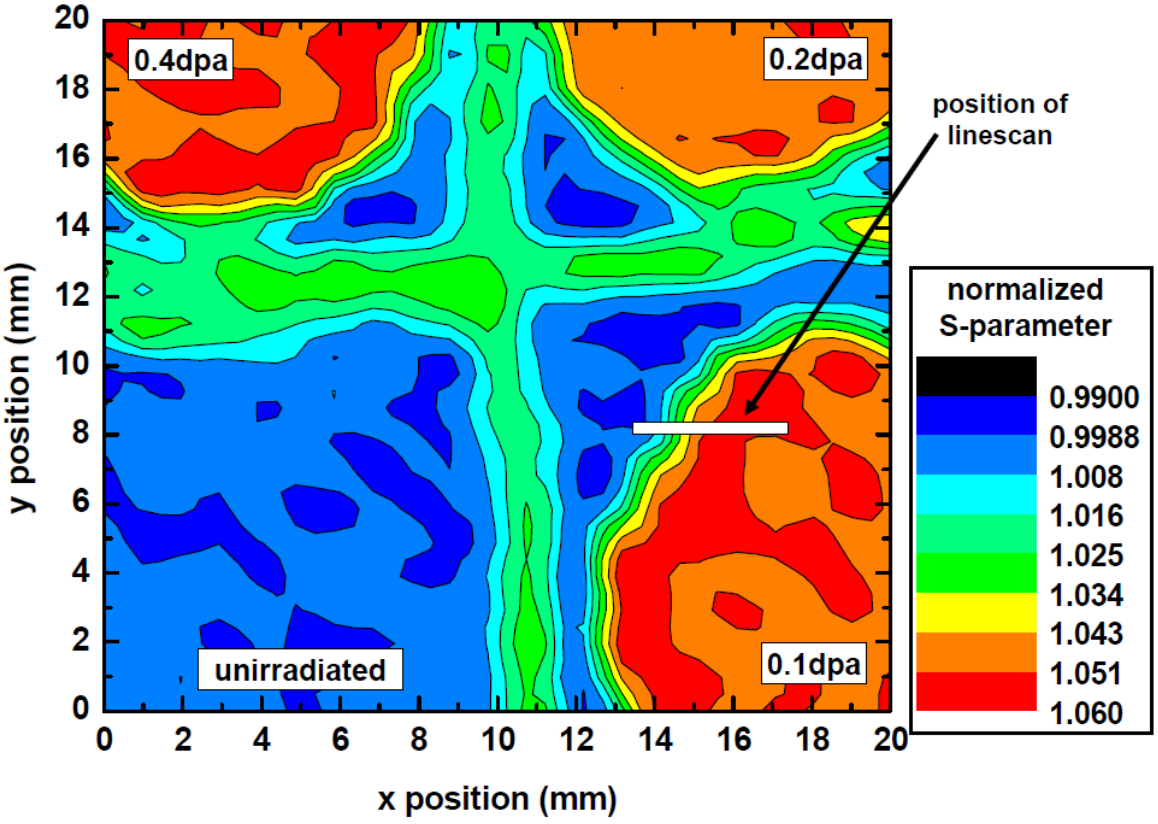

Figure 4.22: Lateral DBS scan at 25 keV (880 nm) of one unirradiated and 3 irradiated M5® samples

While the unirradiated sample shows the expected homogeneous low S-parameter, the circular beamspots in the irradiated samples can be clearly distinguished from the unirradiated sample rims. The area between the four samples appears as a cross-like shape of a different S-parameter color-coded in green. The irradiated areas show a significant S-parameter increase of about 6% as compared to the unirradiated standard, indicating a high vacancy-type defect density. However, the difference in the damage level does not show an influence on the vacancy-type defect density in the irradiated samples; the S-parameters of the three samples are in the same range. For a more detailed study, S(E) depth scans were conducted in each sample center from 1 to 12 keV, which corresponds to a mean positron implantation depth of 9 nm to 280 nm, to measure the S-parameter in dependence of the sample depth. The determined depth-dependent S-parameters are given in Fig. 4.23. The S-parameters are normalized, i.e. divided by the unirradiated standard's S-parameter for the bulk region; the standard S-parameter is calculated by averaging over the three values measured for the bulk at highest positron energies, designated in red.

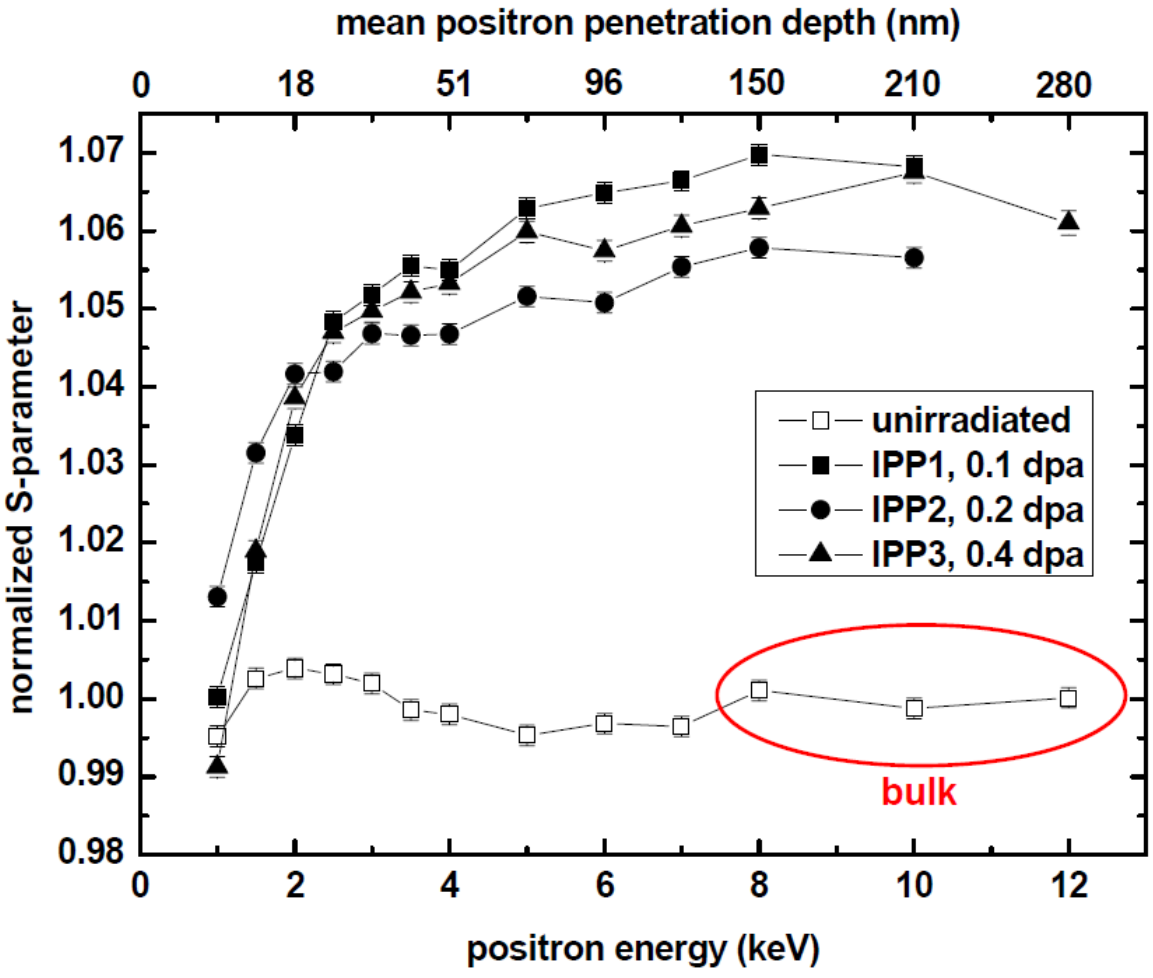

Figure 4.23: S-parameter depth profile of unirradiated and irradiated M5® (3 MeV Zr at 35°C)

The S-parameter depth profile for the unirradiated standard in Fig. 4.23 shows a slight buckling for positron energies between 1 keV and 4 keV before reaching an approximately constant value.

This is due to deviations from the material's bulk microstructure near the surface and positrons being scattered back to the surface; for energies higher than 4 keV, surface effects can apparently be neglected.
As observed for the lateral scan at 25 keV positron energy, the three irradiated samples do not show a significant difference in the S-parameter slope near the surface and reach a comparable S-parameter level in the bulk region of the sample, despite their different damage levels. Thus, it can be concluded that the vacancy-type defect density after 35°C Zr ion irradiation is not dependent on the damage level in the measured low damage level range. It can therefore be assumed that, under the chosen irradiation conditions and dose range, an equilibrium between vacancy-type defect production and recombination is given.
Sample I1 with a total damage level of 0.1 dpa was scanned depth-dependently along a line leading from the unirradiated to the irradiated layer (designated in Fig. 4.22), measuring S(x,E) (see Fig. 4.24). The step size in x-direction was 0.5 mm, the positron energy step size between 0.5 keV and 1.5 keV. The S-parameter is normalized, using the average of the unirradiated bulk region of the sample, 0.53, as standard.

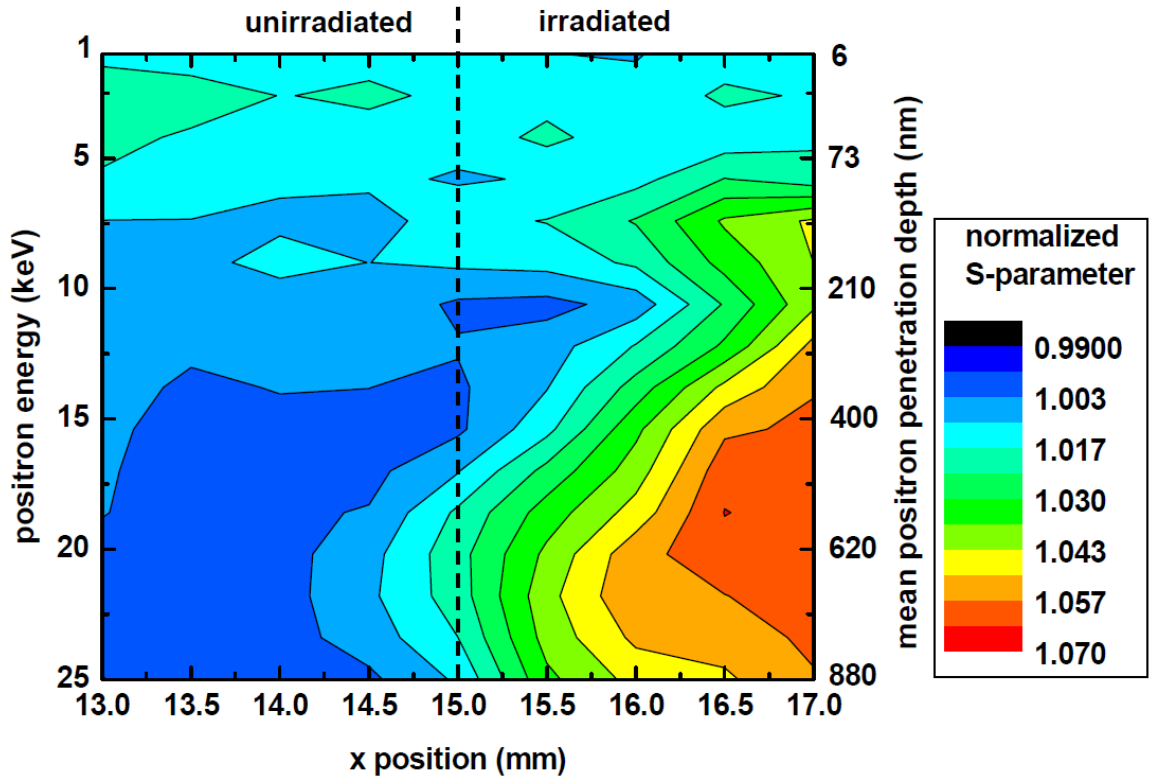

Figure 4.24: Normalized S-parameter as function of the positron energy (depth) and the sample's x-position (M5®, 3 MeV Zr at 35°C)

The unirradiated material to the left of the beamspot has a S-parameter corresponding to the S-parameter of the unirradiated standard (see Fig. 4.23), showing that sample handling before and after irradiation did not induce, e.g. by application of stress, any defects observable by DBS. The observed material changes in the irradiated regions are therefore solely caused by the ion irradiation. The irradiated material in the superficial material region has the same S-

parameter as the unirradiated material region, even though according to the SRIM calculations there should be a considerable recoil creation rate also near the surface. This can be due to positrons being scattered back to the surface. Another possible effect would be that point defects from this superficial layer annihilate at surface sinks or impurities that are present with a higher probability near the surface. In deeper material regions, the observed vacancy-type defect density shows a peaked profile as is to be expected from the SRIM calculations. The irradiated volume has a lower S-parameter at the border of the beamspot, located at x=15 mm. Especially for lower penetration depths, the S-parameter increases only slowly with the x position, in the direction of the beamspot center. The general region of S-parameter gradient around the irradiated material volume can be partly due to the stepwidth of 0.5 mm, leading to an averaging of the measurements of unirradiated and irradiated material. However, the irradiated region is broader for higher penetration depths, indicating that the defects in this region are more stable against recombination with the unirradiated bulk than in the regions closer to the surface. In the damage peak region the defect formation rate is higher compared to the surface region, where the ion-target interaction probability is lower. For this reason, a possible explanation for the observed variation in beamspot width would be a different production to recombination ratio of point defects at higher penetration depths, or the formation of point defect clusters, e.g. as loops, with a higher stability against recombination.

Summary of the Dose Effect

While <a>-loops begin to form with the beginning of the irradiation, <c>-loops form after a threshold dose only, which was determined to be 5.5 dpa in 1 MeV Kr-irradiated recrystallized Zry-4. The <a>-loops show a size increase with the dose for dose levels lower than 2 dpa, but remain rather stable in their average size afterwards, in the range of 8 nm up to high doses. Their density, however, increases with the dose and leads to a dense dislocation network at high doses. After the <c>-loop nucleation, their linear density increases approximately linearly with the dose up to damage levels in the range of 22 to 25 dpa. The <c>-loop contrasts' average lengths remain rather stable with increasing damage level, when the first few dpa after their nucleation have passed.
For the overall vacancy-type defect density at low temperatures (35°C), an effect of the damage level on densities between 0.1 and 0.4 dpa was not found, while a clear distinction between the unirradiated and irradiated material region was given. The vacancy-type defect densities followed the peaked damage distribution as predicted by the SRIM code.

4.3.2 Effect of Temperature

Temperature Dependence of the Overall Vacancy-Type Defect Densities

As described above, in the M5® foil samples irradiated at 35°C, a S-parameter increase of about 6% as compared to the unirradiated standard was observed. To study the influence of the irradiation temperature, a M5® foil sample (I10) was irradiated at 300°C with 2.5 MeV $^{90}Zr^{+}$; however, as further testing was planned with that sample, it was irradiated to a high final dose of 16 dpa. Fig. 4.25 shows S-parameter depth profiles of the unirradiated and irradiated sample I10 in combination with the calculated SRIM recoil production profile. The S-parameters are normalized, using the average of the unirradiated parameters at the three highest energies as standard, as designated in blue. After the initial increase between the surface and 0.25 μm, the measured S-parameters do not rise further, showing that the measured values are representative for the bulk material.

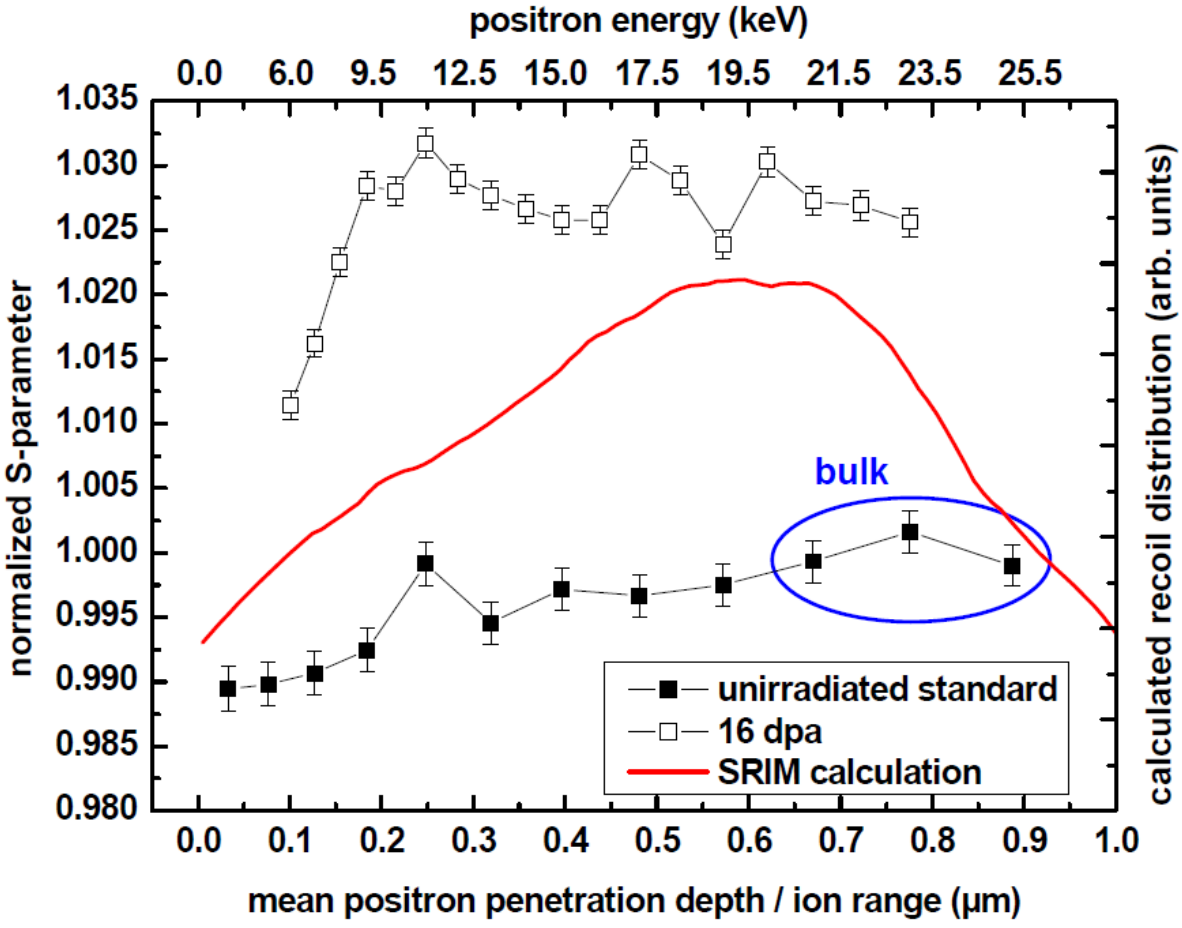

Figure 4.25: S-parameter depth profile of M5® sample I10 (2.5 MeV Zr at 300°C), observed at room temperature

The irradiated sample shows a significantly higher S-parameter than the unirradiated sample. However, the difference between material irradiated at 300°C and unirradiated material is in the range of about 2.5%, while it was about 6% for the samples irradiated at 35°C to significantly

lower doses. It can be concluded that a high fraction of the initially created vacancy-type defects in the ion induced recoil cascades are subject to recombination and annihilation at 300°C. This is in agreement with the annealing stages for irradiation induced defects in single-crystal zirconium, as they are proposed by G.M. Hood and W. Frank [37,58]: According to Hood's interpretation of measurements of electron irradiation induced defect annealing in single crystal pure Zr, the onset of free vacancy migration in α-Zr occurs between -23°C and +27°C [58]. W. Frank's interpretation of the annealing measurements predicts the onset of free vacancy migration to be at around 30°C [37], while he proposes self-interstitials to undergo long-range migration in the annealing stages I and III, with the higher temperature limit of stage III being around 30°C. This suggests that free vacancy migration is possible in the samples irradiated at 35°C only within certain limits, while it can be expected to have a significantly stronger effect at 300°C. Free vacancy migration can thus be assumed to be responsible for the significantly lower vacancy-type defect density in the samples irradiated at high temperature, even though the damage level was much higher. The significantly higher defect density at 35°C as compared to 300°C agrees with observations made for interstitial and vacancy-type <a>-loops in neutron-irradiated zirconium at 400°C as described by Jostsons et al. [33]. He concluded from his observations that the <a>-loop concentration decreases with increasing irradiation temperature at a given flux.

Post-Irradiation Damage Annealing

Annealing Studies with Positron Doppler Broadening Spectroscopy (DBS)

As DBS gives a measure of the vacancy-type defect density only and does not contain information about the defect being in mono-vacancy, cluster or loop form, it is not possible to decide from the DBS measurements alone whether the observed vacancies are in the form of loops or on which crystal planes the loops are located. To test which kind of dislocation loops can be resolved by DBS, the defects in sample I10 irradiated at IPP were annealed during in-situ DBS to image the S-parameter's development with the temperature and to compare the observed annealing effects with dislocation loop imaging results during in-situ defect annealing in the TEM. Another objective of the experiment was to compare the defect annealing characteristics with those known from the literature. A positron energy of 15 keV was used, which leads to a positron implantation profile clearly located in the bulk region of the irradiated sample (see Fig. 4.25). The sample I10 was heated from 230°C to 600°C, in steps of about 25°C. The temperature measurements were done with a two-color pyrometer, whose output had been calibrated with a Pt-Rh thermocouple spotwelded to an M5® standard sample. The dwell time at each temperature level was 15 min, the heating rate between the steps about 9 K/min. During the holding time at the different temperature levels, the S-parameters remained constant within the measurement accuracy. The measured S-parameter as a function of temperature, normalized to the S-value of the annealed sample (T=450°C) is shown in Fig. 4.26, in comparison to the annealing curve for single crystal Zr after 1.2 MeV electron irradiation at 120 K as reported by G.M Hood [58]. The annealing stages as suggested by W. Frank [37] are given in the plot.

As expected, the measured S-parameter remains constant between 230°C and 285°C; this confirms the irradiation temperature of the sample to have been higher than 285°C, as all diffusion processes up to that temperature range can be expected to already have taken place during irradiation. From 285°C to 400°C, the S-parameter decreases linearly before it approximates its lowest level at about 450°C, which corresponds to the S-parameter measured for the unirradiated sample. The overall vacancy type defect density between 300 and 400°C showed to decrease by

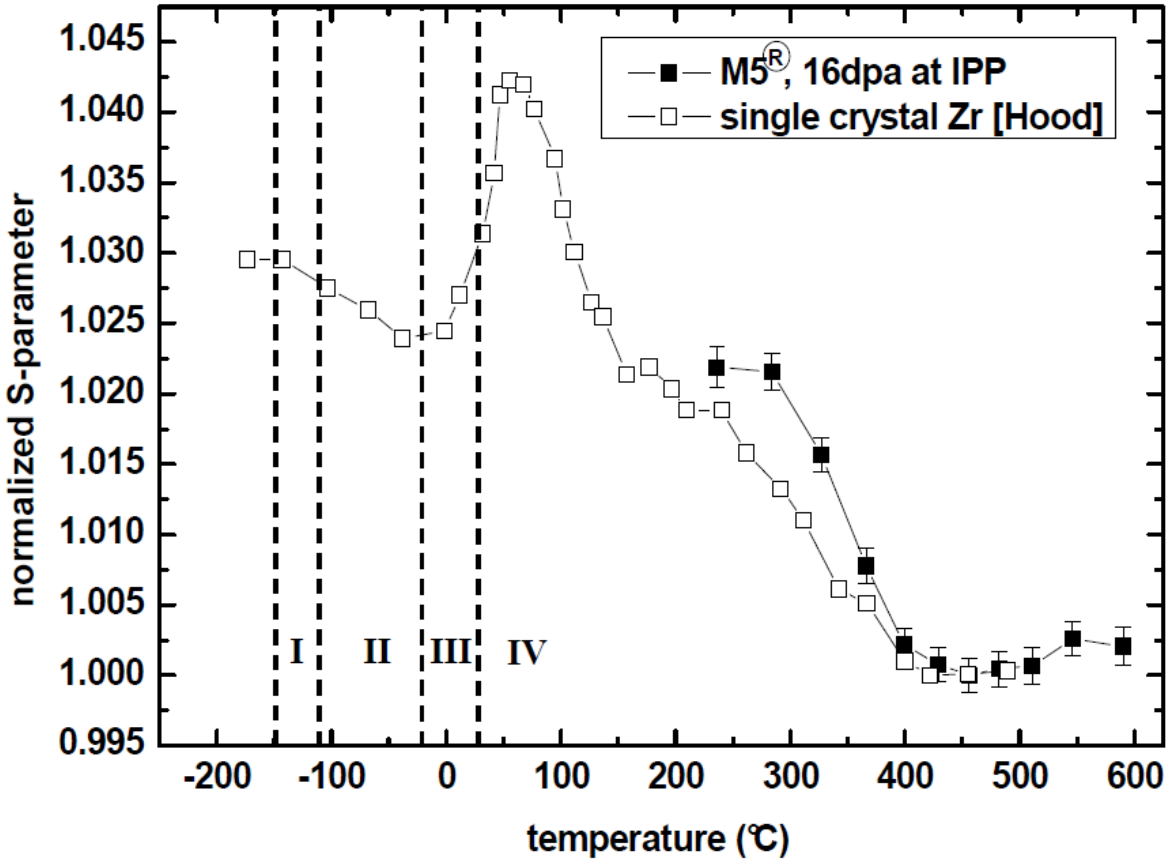

Figure 4.26: Defect annealing in I10 (M5® irradiated with 2.5 MeV Zr at 300°C), observed with in-situ DBS; comparison to literature data by Hood et al. [58]

about 7% of the initial density per 10 K temperature increase. An increase of the irradiation temperature by 50 K would thus lead to a decrease of the overall vacancy type defect density by 35%. The small increase of the S-parameter for temperatures higher than 450°C is caused by the thermal lattice expansion. While the normalized S-parameter's difference between irradiated and unirradiated state, which depends on the electron or ion implantation fluence and the irradiation temperature, is higher for the measured sample, the curve's lowest point is in very good agreement with the Zr single crystal values provided by G.M. Hood. As electron irradiation is expected not to form recoil cascades but Frenkel pairs only [10] and vacancy migration is assumed to be strongly limited at the irradiation temperature of 120 K, the single crystal vacancy-type defect structure can be assumed to consist of mainly mono-vacancies. The corresponding annealing behavior for sample I10 can be an indication of the dominating defect structures in sample I10. The sample could either host mostly mono-vacancies, or it could contain defect loops or clusters with the same annealing characteristics as mono-vacancies. Further studies of the defect annealing behavior were done by in-situ TEM annealing, as described below.
The observed S-parameter changes during annealing can be expected to be due to changes in the matrix material only, and to be independent of the SPP behavior. Steinberg et al. [102] reported in 1997 that no visible growth of SPPs was observed after annealing of Zircaloys at 510°C. This

was confirmed during the annealing studies in the TEM in this work, where changes of the SPPs with regard to size, number, distribution or crystallinity remained absent.

Annealing Studies with In-Situ TEM

As a complementary measurement to the in-situ defect annealing studied by DBS, a M5® sample irradiated with 1 MeV Kr at 300°C to doses corresponding to 27 dpa was heated up to 750°C to study the development of the <c>-loops with the annealing temperature. The irradiated sample was charged with 110 wt.-ppm hydrogen, due to an initially different testing purpose; however, this is approximated not to have significant influence on the defect annealing behavior. After each temperature step, the sample was held at the respective temperature for about five minutes. The average heating rate during the temperature steps was 7.5 K/min. The temperature was measured with a thermocouple integrated in the TEM sample holder; the measurement accuracy is assumed to be 5 K. Fig. 4.27 shows the <c>-loops in dependence of the annealing temperature, imaged at a magnification of 10'000.

While the DBS measurements described above found a complete annealing of the vacancy-type defects in the irradiated samples at 450°C, the <c>-loops observed during in-situ annealing in the TEM show only a slight tendency of linear density and number decrease and size increase for temperatures lower than 500°C. For temperatures higher than 520°C, the <c>-loops' linear densities and numbers decreased significantly while their length increased; at 750°C, a very low density of long <c>-type contrasts remained in the material. For the higher temperatures, the contrasts show darker, more even forms, without the short disruptions or kinks that were observed at lower temperatures. These changes found for higher temperatures suggest that, while a large part of the <c>-loops anneal during the heating process, the remaining chains of small loops transform into dislocation lines. The observed stability of the <c>-loops at temperatures in the range of 500°C is in agreement with dislocation annealing studies in PWR irradiated Zry-4 by Garzarolli et al. [103], where <a>-component dislocations were shown to be removed completely after 48 h annealing at 500°C while the <c>-component dislocations were still present.

At different times during the TEM annealing experiment, it was tested whether the TEM's electron beam acted as a trigger for the loop annealing by focussing the beam on a small area and looking for possible changes in the annealing characteristics. However, such an influence could not be found.

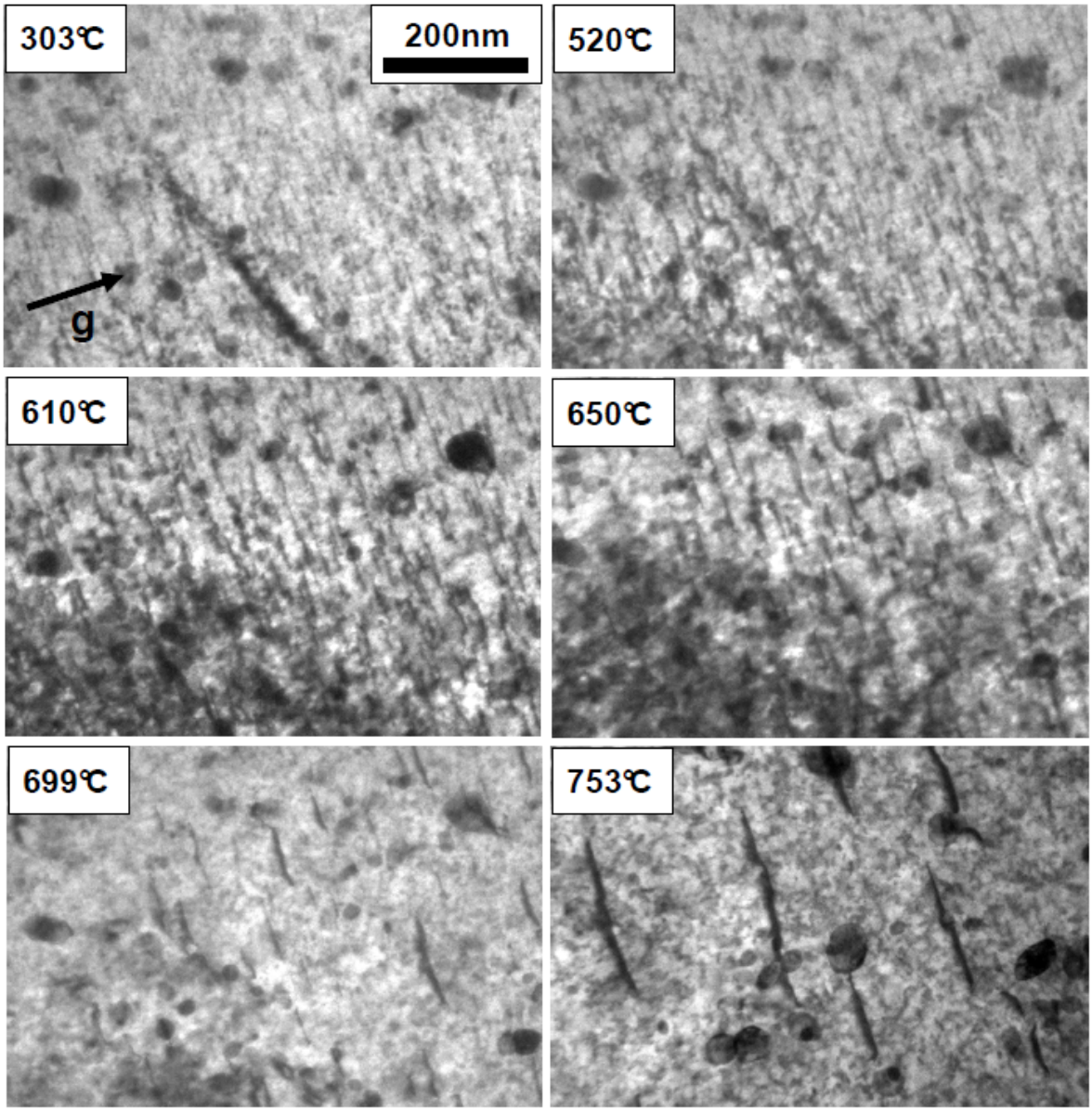

Figure 4.27: <c>-loop development in M5® during annealing (after irradiation with 1 MeV Kr at 300°C)

In Fig. 4.28, the increase of the average <c>-loop length and the decrease of the loops' number is given, normalized to the loops' structure at 303°C. The loops' sizes and numbers were measured three times for the image taken at each temperature; the errors given in the plots are one standard deviation for the average of these three values, corrected for the low number of measurements.
Another grain region was observed after 750°C was reached, to study the <c>-loop annealing behavior with the time until the equilibrium loop concentration at that temperature had formed. Fig. 4.29 shows the remaining <c>-loop fraction as compared to the total <c>-loop density at reaching 750°C, in dependence of the holding time.

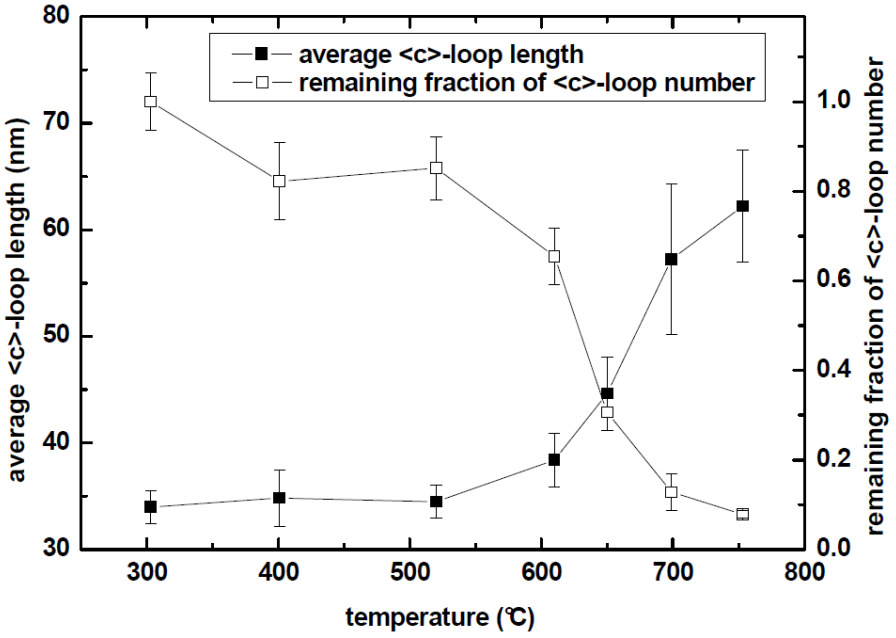

Figure 4.28: <c>-loop length and number development in M5® during annealing (after irradiation with 1 MeV Kr at 300°C)

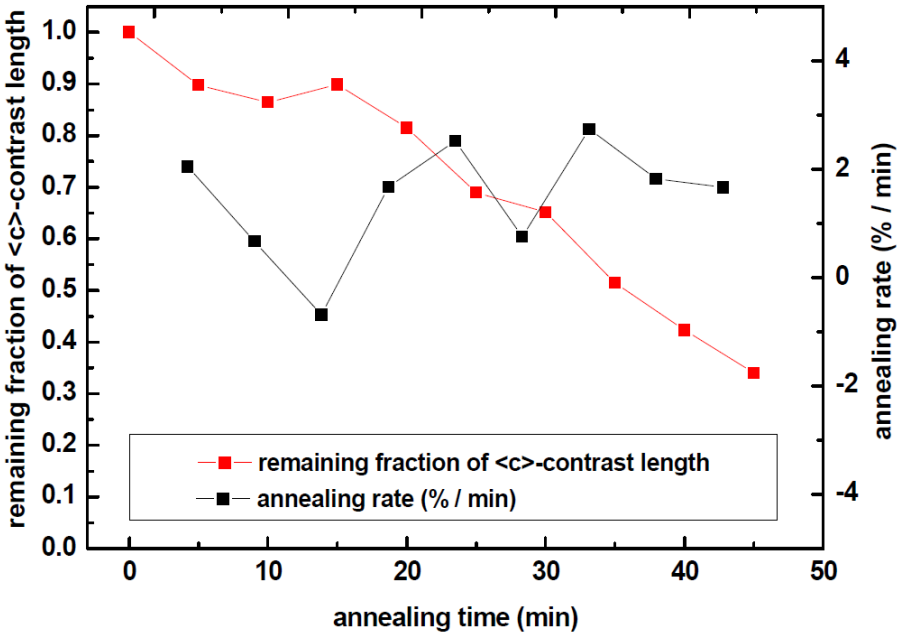

Figure 4.29: Total <c>-loop contrast length decrease and length annealing rate in M5® (after irradiation with 1 MeV Kr at 300°C)

After a holding time of 45 min, the total <c>-component contrast length had decreased to 34% of its original value at the start of holding. The remaining 34% did not show noticeable changes

during the additional subsequent holding time of about 30 min. The annealing rate fluctuated around its average value of 1.5%/min.

By observing the dislocation annealing, it has to be kept in mind that, due to the invisibility criterion, only <c>-component dislocations are visible, and possible defect structures on other lattice planes that might be involved in the annealing process cannot be seen. Also, as shown by the DBS in-situ defect annealing experiment, it can be assumed that at a temperature as high as 750°C, the vast majority of the vacancy-type defects have already annealed; this can be expected to include specifically vacancy-type point defects and <a>-loops. While the DBS measurements do not provide information about the interstitial-type point defects, it can be assumed that the majority of them was involved in the vacancy annealing processes and have therefore disappeared as well. <a>-loop annealing studies in the TEM by other authors show that for temperatures higher than 450°C to 500°C, only a very low density of <a>-loops is left [33]. It can therefore be expected that the observed sample material is, with exception of the remaining <c>-component dislocations, rather defect free, and that the dislocation annealing is dominated by thermal processes and interaction of the dislocations with each other, rather than interaction with remaining other defects in the sample.

The annealing of the dislocations was observed to follow several different processes. First, dislocations could be seen to remain rather stable or to migrate without changing their form or interacting with other dislocations, until their sudden disappearance. It is assumed that this effect is caused by dislocations migrating to the TEM foil surface and annihilating there. Also, locally static dislocations were observed to diminish from one or two ends, until total annealing. During the shrinking of the dislocations, parts of them showed vibration like behavior around their static location, possibly indicating interaction with point defects. Fig. 4.30 is an image series of such an annealing process. Another interesting observation was the shrinkage of a dislocation that led to the formation of a small loop-like contrast before sudden disappearance of the newly formed loop. This observation is demonstrated in the image series in Fig. 4.31. Dislocations were also observed to move towards each other, to merge partly or completely and to anneal afterwards. Fig. 4.32 is an image series of such a merging process.

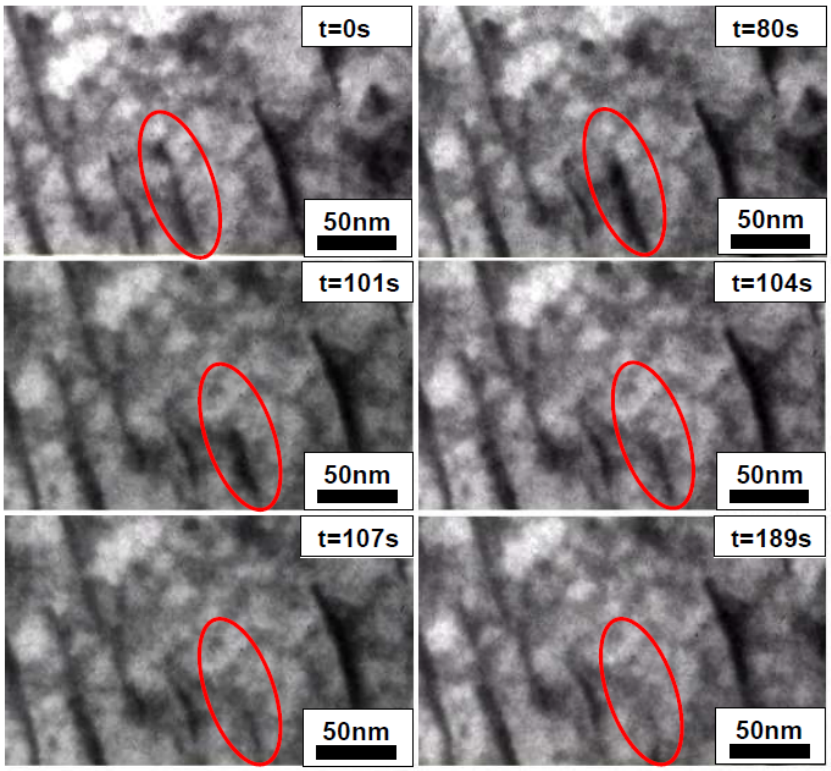

Figure 4.30: <c>-type dislocation annealing in 1 MeV Kr irradiated M5®: annealing of a locally static dislocation

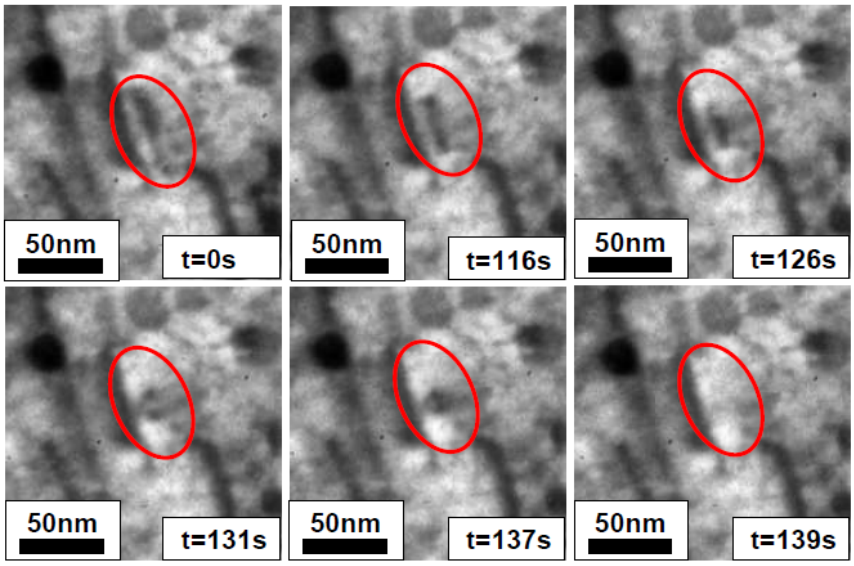

Figure 4.31: <c>-type dislocation annealing in 1 MeV Kr irradiated M5®: loop-like contrast before annealing

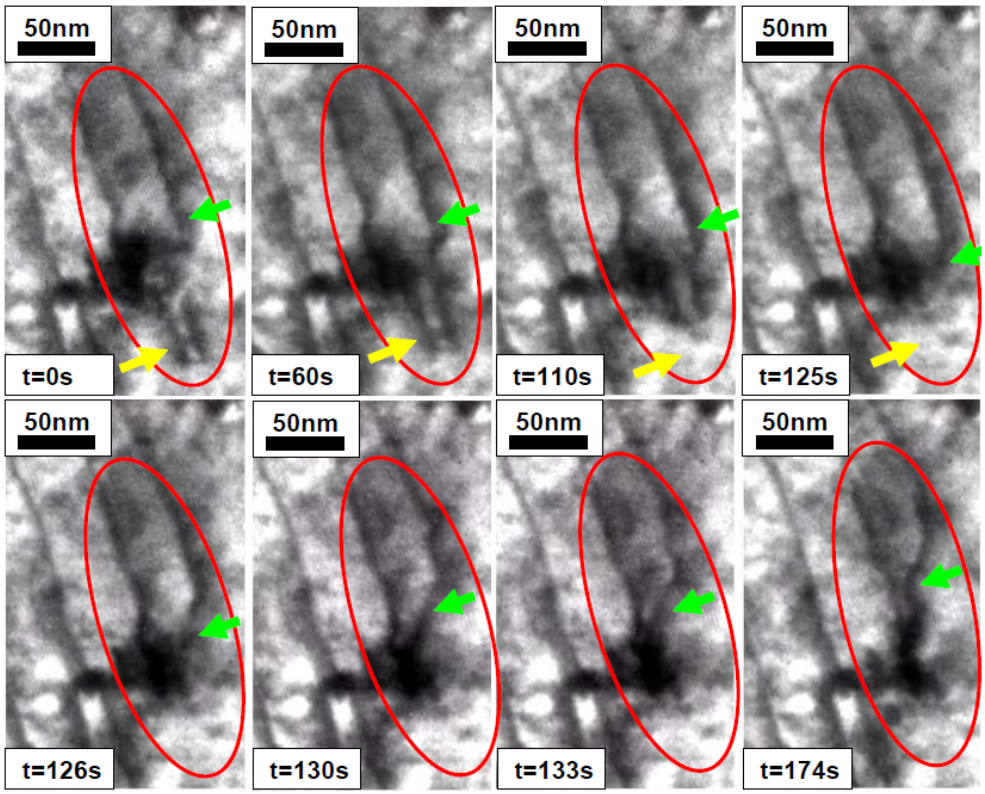

Figure 4.32: <c>-type dislocation annealing in 1 MeV Kr irradiated M5®: merging of two dislocations with subsequent partial annealing

Summary of the Temperature Effect

The DBS studies on Zr irradiation damage in M5® at irradiation temperatures of 35°C vs. 300°C showed that the irradiation temperature has a very strong influence on the overall vacancy-type defect densities created during the irradiation: The normalized S-parameter increase by irradiation was around 6% for 35°C and only about 2.5% at 300°C, even though the damage level at 300°C was about a factor 40 higher than at 35°C. This strong effect was confirmed and studied in more detail by in-situ DBS annealing of a sample irradiated at 300°C from 285°C to 600°C. A monotoneous decrease of the overall vacancy-type defect density from 300°C towards 450°C was observed, with the measured S-parameter at 450°C corresponding to the unirradiated standard. It was thus concluded that at 450°C, the significant part of the irradiation induced vacancy-type defects was annealed. From the similarity of the annealing characteristics to literature work on electron irradiated single-crystal Zirconium, it can be assumed that the vacancy-type defects are either mostly of point defect form or have the same annealing dynamics as point defects. The subsequent <c>-loop annealing studies in the TEM showed <c>-loops to be stable up to about 520°C. This leads to the conclusion that the <c>-loops only constitute an insignificant amount of all vacancy-type defects in the sample; following the literature, the majority of the vacancies are presumably in <a>-loop or point defect form. For temperatures higher than 520°C, the <c>-loops showed a decrease in their length and density, and a change in their contrast characteristics that suggests a change in their form from chains of small loops to dislocation lines. During holding of the sample at 750°C, the <c>-dislocation migration and annealing character-

istics were studied, and different mechanisms were observed. After 1h holding at 750°C, about a third of the original <c>-loop density remains.
Regarding the experimental technique, it should be mentioned that the positron Doppler broadening spectroscopy measurements showed a large potential as a complementary experimental method to in-situ TEM, especially with regard to irradiation microstructure studies in a larger material volume than accessible with a TEM. The constraint of this experimental method, that conclusions can only be drawn regarding the overall vacancy-type defect density and not the different forms in which the vacancies occur, could be dissolved by using Positron Annihilation Lifetime Spectroscopy (PALS). A continuation of the positron studies of irradiation effects in Zr-based alloys, especially at the unique positron source NEPOMUC at the FRM II research reactor, is therefore regarded as a promising project.

4.3.3 Effect of Hydrogen Content

To study the effect of the hydrogen content on the irradiation induced microstructure in Zr-based alloys was one main objective of this work. This section contains the hydrogen influence studies in Zry-4; in addition, experiments on the dissolution and precipitation of hydrides under temperature cycling in M5® are presented. The confidential studies on the effect of hydrogen content on the irradiation induced microstructure in M5® will be summarized in AREVA internal reports.

Hydride Precipitation Characteristics

Hydrogen in zirconium and Zr-based alloys precipitates as δ- and γ-hydrides, as described in chapter 2. Within the hydrogen-loaded Zry-4 samples, zirconium hydrides were present as intergranular as well as intragranular hydrides.

Intergranular Hydrides

Fig. 4.33 shows overview TEM images of the electrolytically thinned holes in the sample centers of Zry-4 samples which were loaded with 0, 68, 186 and 405 wt.-ppm hydrogen.
In the vicinity of the holes of all four samples, it can be seen that a preferential thinning of second phase particles occurred, or a preferential thinning of their boundaries with subsequent SPP loss - there are small spherical holes spread throughout the grains, which are assumed to be former SPP locations. While the samples with 0 and 68 wt.-ppm look rather similar, the sample with 186 wt.-ppm shows increased fissures at the lower right side of the hole, and for the sample with 405 wt.-ppm a very high amount of fissures are given throughout the hole periphery. Those fissures are assumed to originate from preferential etching of intergranular zirconium hydrides.

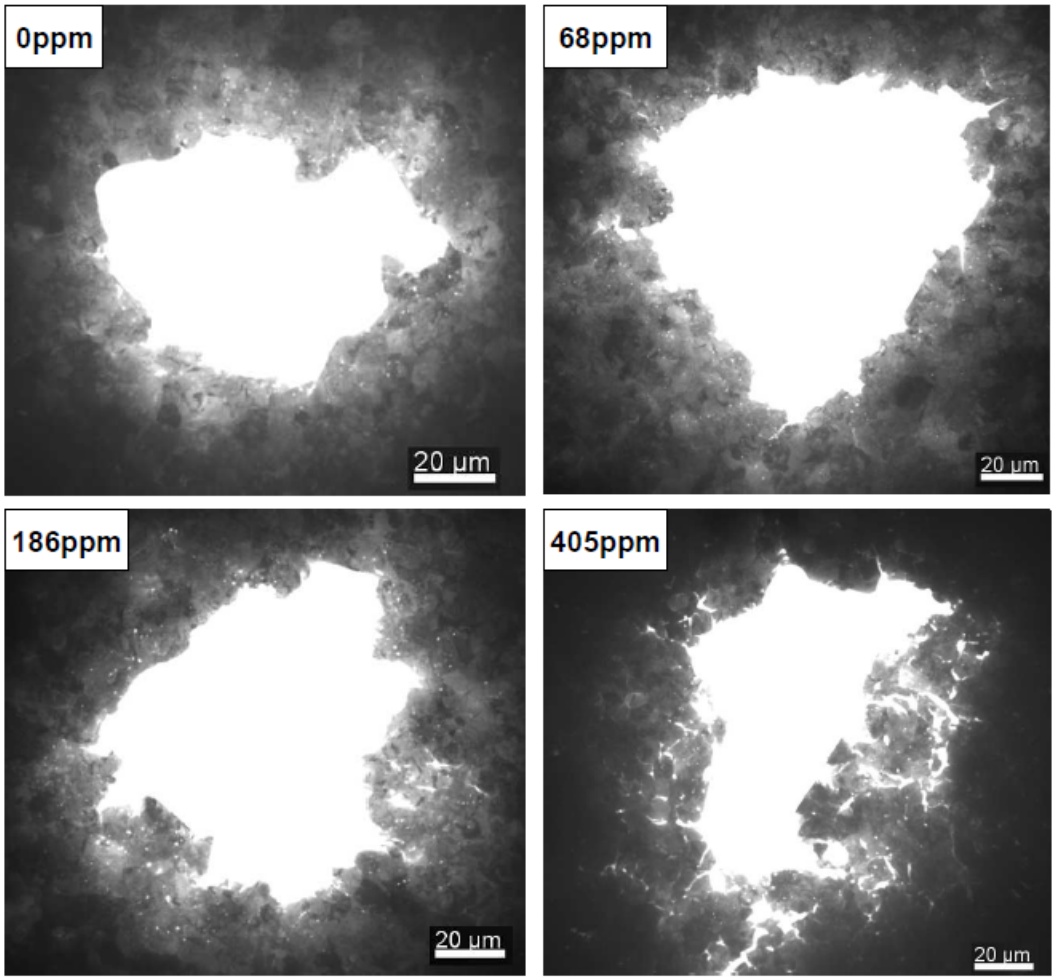

Figure 4.33: Zry-4 TEM samples with different hydrogen contents

Intragranular Hydrides

Fig. 4.34 shows overview TEM images of several grains in the samples with 186 and 405 wt.-ppm hydrogen content.

The samples show intragranular hydrides of needle-like shape; the hydride density is significantly higher in the sample with 405 ppm, as expected. The needle-like hydrides show a preferential orientation in coherence with the matrix of the respective grains. As was confirmed during later TEM work, the hydrides are oriented perpendicular to the c-direction of their surrounding matrix. When analyzing in-pile neutron irradiated samples after they received the total neutron dose, it is reported to be difficult to distinguish hydrides oriented parallel to the <c>-loops from the loops. This difficulty is overcome by in-situ TEM, as the hydride distribution in the unirradiated sample is known before the irradiation.
The technical aspect of this preferential orientation is that the hydrides can be used as markers to easily recognize the grains' c-direction, and to find grains with suitable orientation for <c>-loop imaging.

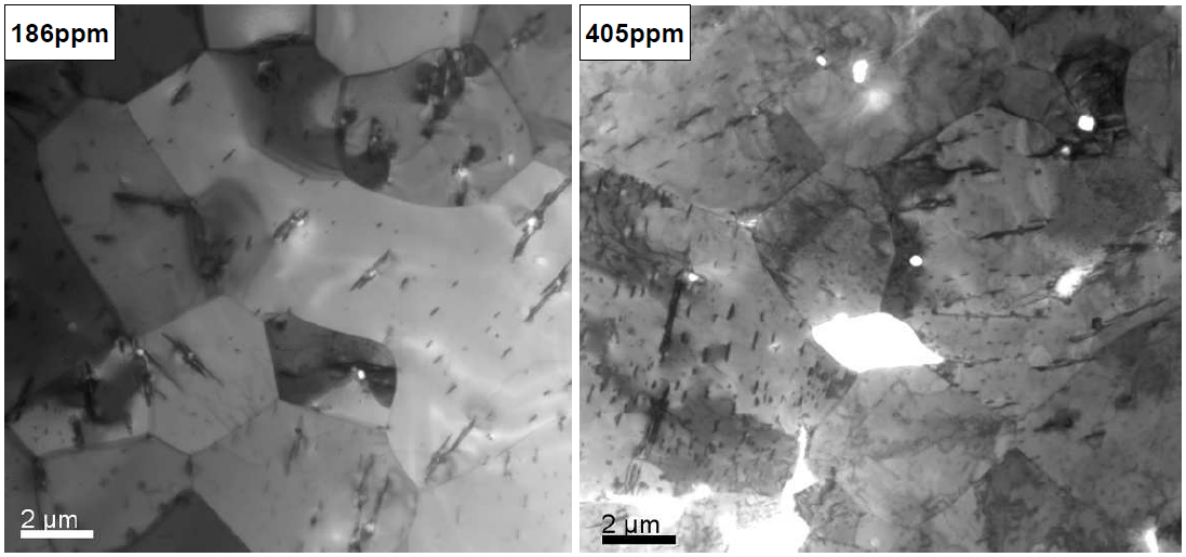

Figure 4.34: Zry-4 TEM samples with different hydrogen contents at room temperature, containing intragranular hydrides

Hydride Dissolution and Precipitation during Temperature Cycling

In the TEM samples containing hydrogen, hydrides were observed as part of the general microstructure during the experiments. The majority of the intragranular hydrides dissolved during heating from room temperature to 300°C. During cooling down of the samples in between or after the irradiation, hydrides were seen to re-precipitate; however, they were generally located at different positions than before their dissolution, appeared in different number, geometry and orientation and did not show any relation to the hydrides before the irradiation.

Fig. 4.35 gives an example of the temperature induced dissolution of a large hydride which had formed after cool-down of an M5® sample with 110 wt.-ppm that had been irradiated to a damage level of 11 dpa. The imaging conditions are close to $\vec{g}$=(0002); therefore, some <c>-loops can be seen in the images. During re-heating to 300°C, the hydride initially remained stable up to a temperature of about 190°C, then started to dissolve from its upper tip at around 205°C and gradually disintegrated downwards until its disappearance at 243°C. The time span between the start of the dissolution and the complete disintegration was about 3 min, at a heating rate in the range of 25 K/min.

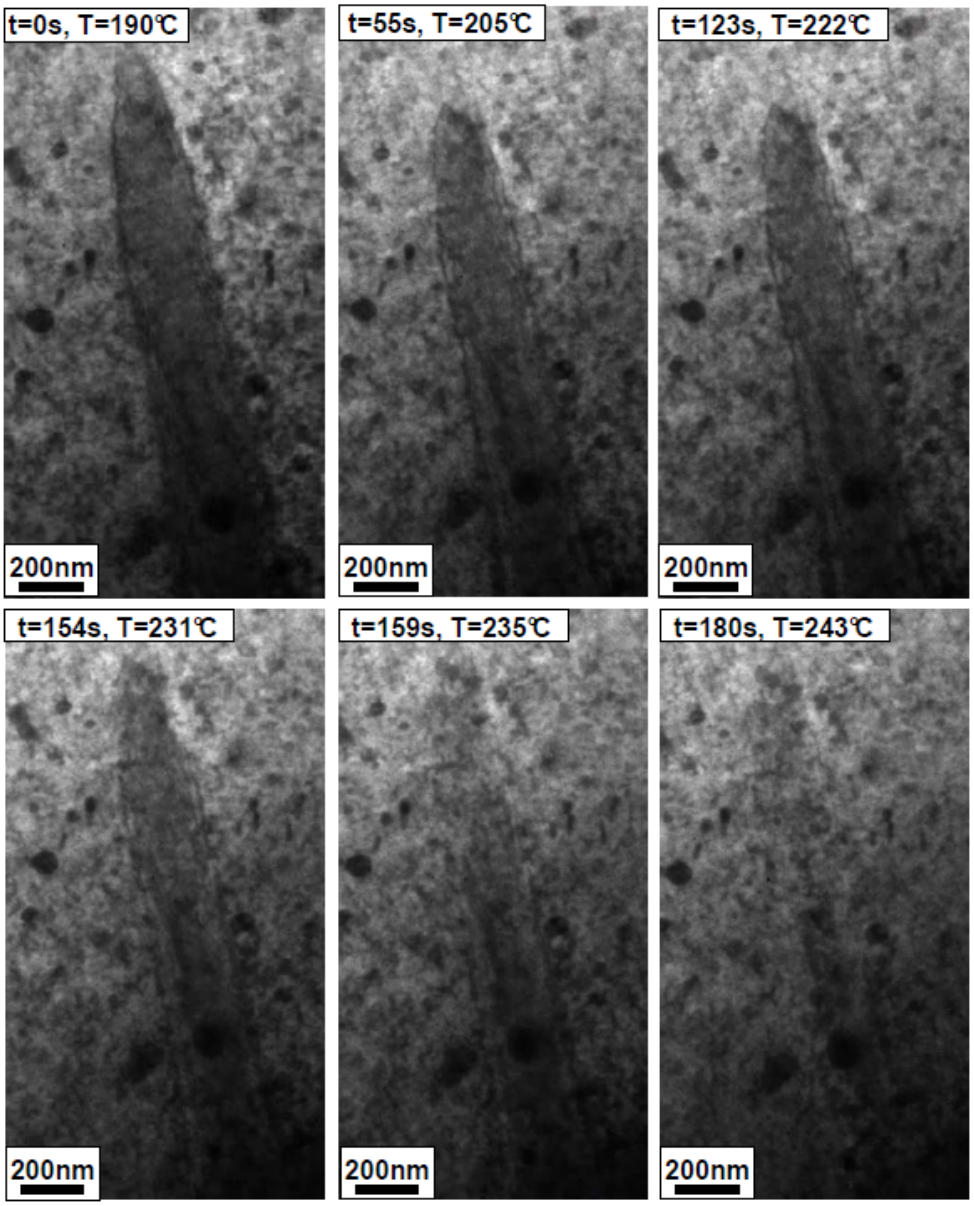

Figure 4.35: Dissolution of an intragranular hydride during heating up in 11 dpa irradiated M5® with 110 wt.-ppm H

After the heating up of the sample, it was further irradiated until a final damage level of 27 dpa. During the following cooling down from 300°C to room temperature, the precipitation of some hydrides was observed; one of them is shown in the image series in Fig. 4.36. The average cooling rate was about 100 K/min.

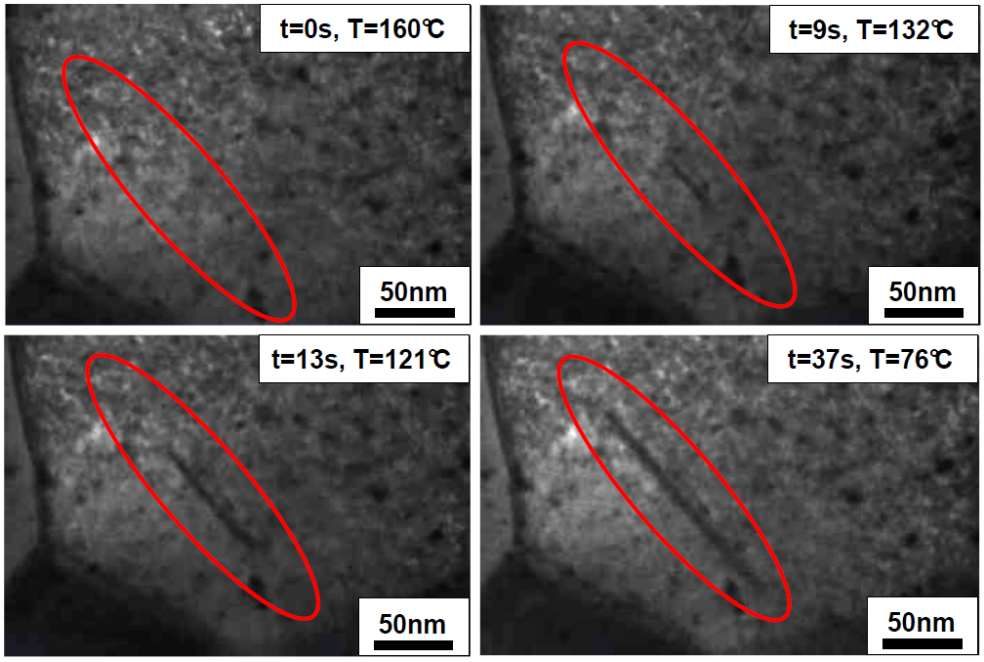

Figure 4.36: Precipitation of an intragranular hydride during cooling down in 27 dpa irradiated M5® with 110 wt.-ppm H

The observed hydride dissolution and precipitation behavior confirms that the hydride structure at room temperature before or in between an irradiation experiment at higher temperature is not related to the hydride structure after the irradiation. Therefore, correlations between the hydride and dislocation loop structures in irradiated samples should only be drawn from samples imaged at their temperature of irradiation, and not from images taken at room temperature.

<a>-Loops in Zry-4

Fig. 4.37 shows the <a>-loop size distribution in Zry-4 at high damage level, as a function of the samples' hydrogen content. The distribution shows a slight trend towards lower loop sizes with increasing H content. The average <a>-loop diamaters as well as the <a>-loop linear densities for the samples with different hydrogen content are summarized in Table. 4.5. The <a>-loop linear densities are 3/2 times the measured linear densities, due to the visibility of only two thirds of the <a>-loops under the chosen diffraction condition $\vec{g} = (01\bar{1}0)$. Those values are, however, to be regarded with caution, as the high damage level leads to a very high <a>-contrast density that makes <a>-contrast overlap probable. As a result, it is possible that the measured linear densities are too low.

The <a>-loop linear density does not follow a clear trend in dependence of the hydrogen content: The sample with 186 wt.-ppm hydrogen shows an increase of the linear density as compared to the hydrogen free sample, while the sample with 405 wt.-ppm has a lower loop density than the unloaded standard. The average <a>-loop sizes show a slight decrease with increasing hydrogen content.

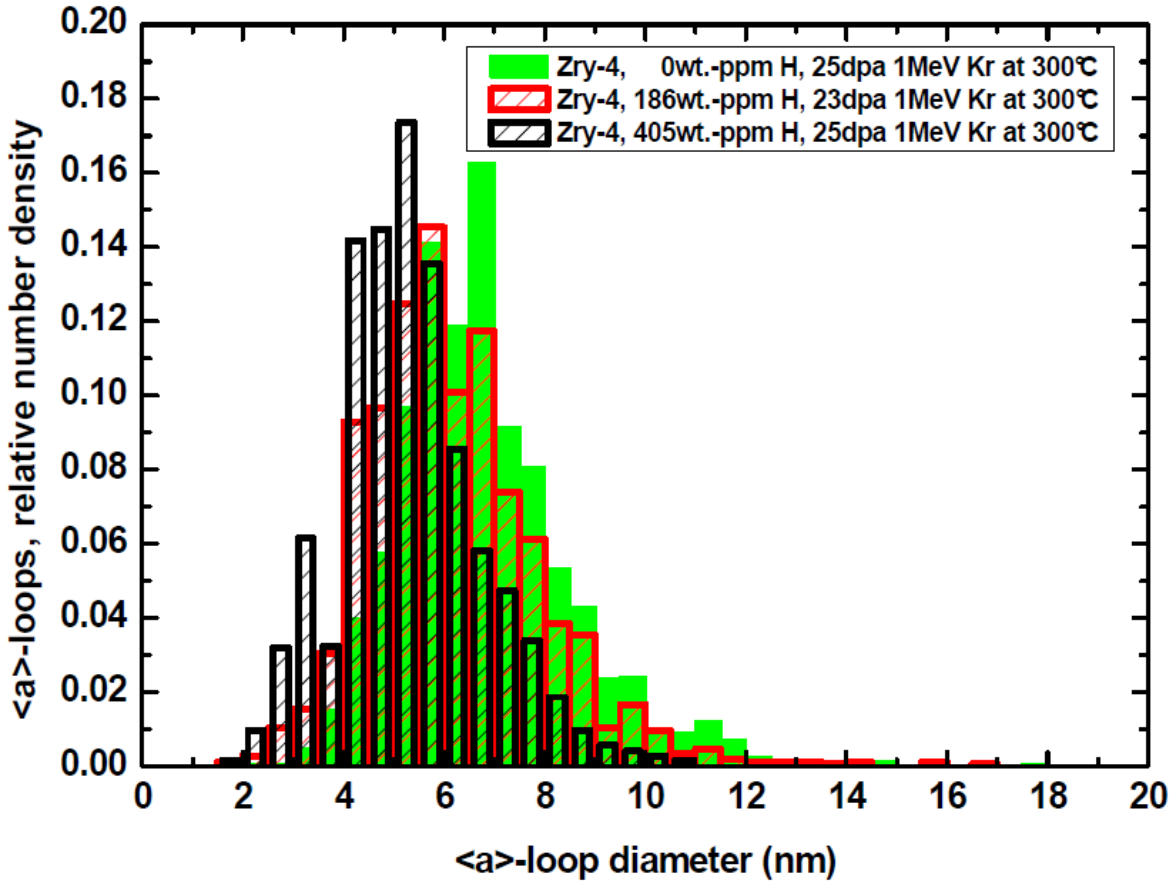

Figure 4.37: <a>-loop size distribution in Zry-4 at high damage level, as a function of the hydrogen content

Sample	H content (wt.- ppm)	D_{dpa}	<a>-loop lin. density ($10^{14}m^{-2}$)	<a>-loop diameter (nm)
PA2	0	25	(2.51±0.18)	6.8
PB3	186	23	(3.41±0.14)	6.2
PC4	405	25	(1.85±0.15)	5.4

Table 4.5: <a>-loop linear densities and average diameters in Zry-4 as a function of the hydrogen content

<c>-Loops in Zry-4

Fig. 4.38 shows the measured <c>-loop linear densities in the Zry-4 samples with different hydrogen content, as a function of the damage level. At the final damage level of each sample, 3 different positions in one grain of each sample were measured to assess the statistical variation within one grain. In addition, the loop densities were measured in 3 different grains in sample PC4 with 405 wt.-ppm hydrogen content (shown by different symbols in Fig. 4.38), with 3 measurement positions in each grain. It can be seen that the data from those 3 different grains do

not show significant deviation. The <c>-loop linear densities can therefore be assumed to be comparable within different grains of one sample.

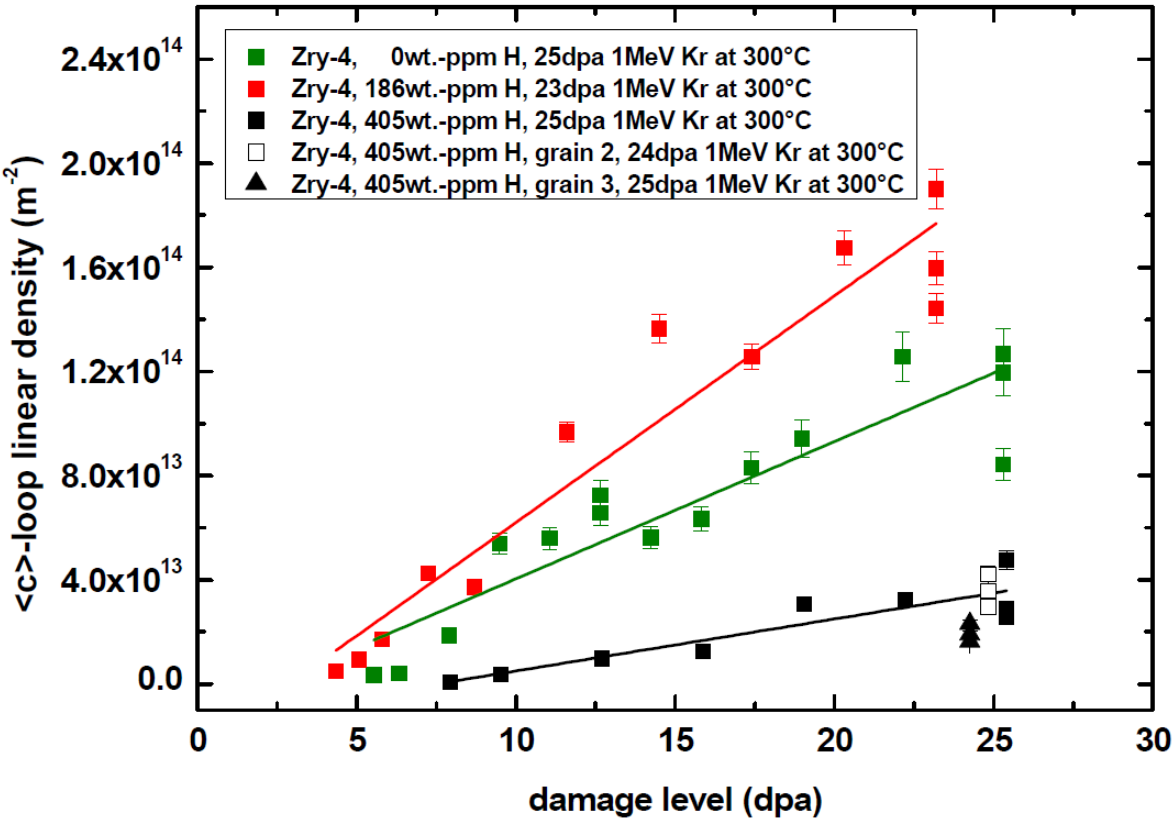

Figure 4.38: Linear <c>-loop densities in Zry-4 with different hydrogen content

Significant <c>-loop densities formed in all three samples; the loops nucleate at threshold damage levels between 4 and 8 dpa. Fig. 4.39 shows the <c>-loops in their early state of nucleation; Table 4.6 gives the respective damage levels.

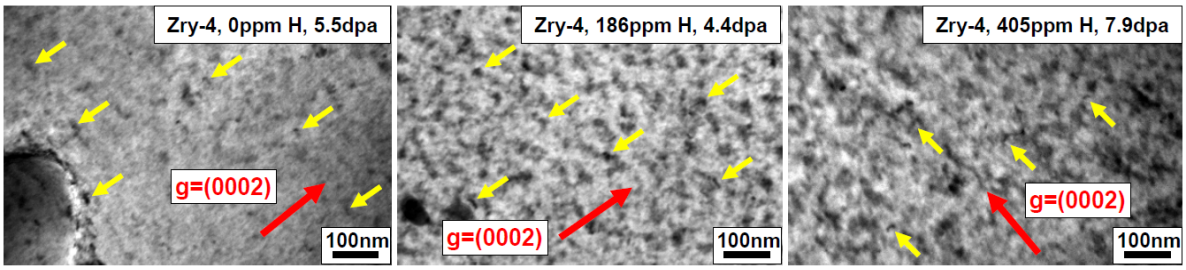

Figure 4.39: <c>-loop threshold in Zry-4 for different hydrogen contents

Even though the thresholds are significantly different, they do not show a clear trend in one direction. While the sample PB3 with a hydrogen content of 186 wt.-ppm has a lower <c>-loop

sample	H content (wt.- ppm)	<c>-loop threshold (dpa)
PA2	0	5.5
PB3	186	4.4
PC4	405	7.9

Table 4.6: <c>-loop nucleation threshold in Zry-4

threshold than the as-fabricated sample PA2, sample PC4 with 405 wt.-ppm H has a higher threshold than the as-fabricated sample. It should, however, be pointed out that the threshold decreases for hydrogen content with 186 wt.-ppm by only 20%, as compared to the standard sample, while it increases by 44% for the sample with 405 wt.-ppm. When comparing these observed <c>-loop nucleation thresholds with the average damage level for the onset of breakaway growth described by Holt et al., 8.3 dpa, it is noticeable that the observed threshold being closest to this literature value is the one for the sample with 405 wt.-ppm hydrogen. Holt et al. do not provide data on the hydrogen content of the samples, but from the irradiation time of the samples spent in the BWR and PWR environment, it can be expected that the hydrogen uptake was significant. It is therefore possible that the critical <c>-loop distribution for the onset of macroscopic breakaway growth lies actually closer to the <c>-loops' first point of nucleation than to the "critical" <c>-loop density determined in section 4.2.2. Still, due to the absence of the hydrogen data in the literature, and the observed discontinuity of the hydrogen effect, this phenomenon cannot be investigated in more detail. The determined "critical <c>-loop density" from section 4.2.2 is therefore assumed to be the most reliable value to can be gained from the available ion irradiation data; it can be regarded as an upper limit for the "critical <c>-loop density".
The discontinuous trend of the hydrogen effect is also reflected in the overall <c>-loop linear densities throughout the studied damage levels: The linear <c>-loop densities for the sample with 186 wt.-ppm H are highest for all damage levels, and the densities for the sample with 405 wt.-ppm are lowest (see Fig. 4.38). All three samples show an approximately linear increase of the <c>-loop linear density with the damage level, but the density increase rate varies with the hydrogen content. The given error bars are based on one standard deviation of the measured grains' thicknesses. At the highest damage level, the linear densities were determined at three different positions in the observed grain of each sample, to assess the statistical scattering during the <c>-loop measuring and the variations of the densities within one grain. The deviations of the linear densities between the three samples are, however, higher than this statistical scattering and the measurement errors of the grain thicknesses; therefore, it is concluded that the observed hydrogen effect is significant.
The linear <c>-loop densities were again approximated by a linear equation of type

$$L_{lin} = L_0 + \dot{L} \cdot D$$

with the fit parameters for the different hydrogen contents as given in Table 4.7.
For the damage level of 23 dpa, the linear <c>-loop densities (calculated by using the linear correlation described above) in sample PB3 with 186 wt.-ppm are 61 % higher than the as-fabricated sample; the densities in the sample PC4 with 405 wt.-pm are 71 % lower than in the sample without hydrogen.

sample	H content (wt.-ppm)	L_0 ($10^{13}m^{-2}$)	$\dot{L}$ ($10^{12}m^{-2}dpa^{-1}$)
PA2	0	(-1.23±1.05)	(5.27±0.628)
PB3	186	(-2.50±1.22)	(8.70±0.789)
PC4	405	(-1.58±0.931)	(2.06±0.482)

Table 4.7: Fit parameters for the linear densities as a function of hydrogen content and damage level

Fig. 4.40 shows the size distribution of the <c>-loops at the respective maximal damage level for the three samples with different hydrogen contents. The size distributions include measurements from 3 positions in sample PA2 without hydrogen, 3 positions from PB3 with 186 wt.-ppm H and 2 positions from PC4 with 405 wt.-ppm H. In Fig. 4.41, the average <c>-loop length is given as a function of the damage level for the different hydrogen contents.

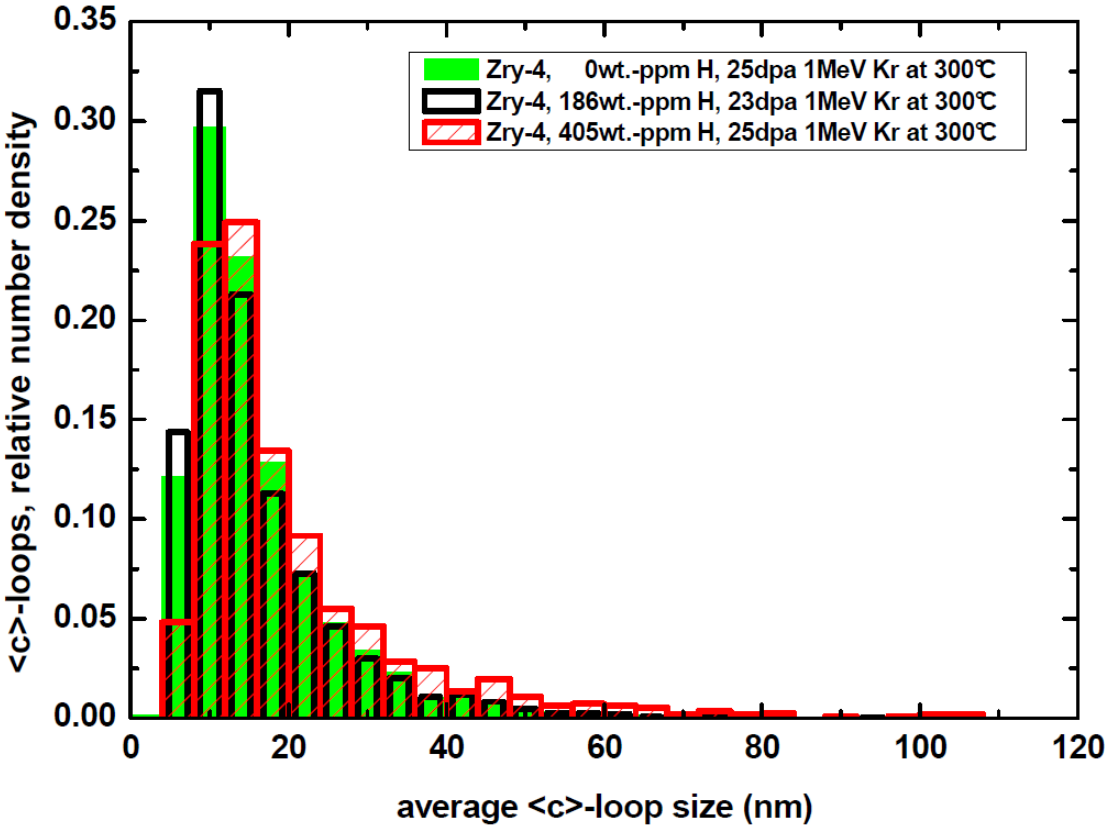

Figure 4.40: <c>-loop size distribution for different hydrogen contents

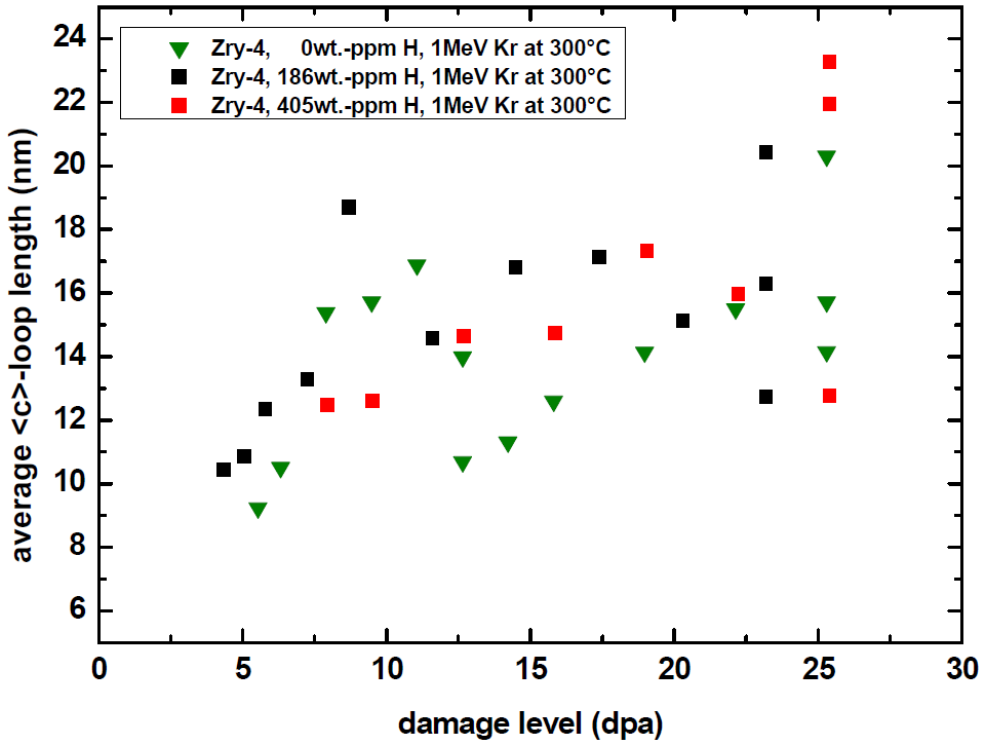

Figure 4.41: Average <c>-loop length in Zry-4 with different hydrogen contents

The <c>-loop length results for the different samples do not show a dependence on the hydrogen content; the scattering of the average loop length from different positions in the same grain of each sample, at highest dose level, is in the range of the overall scattering of the data points. Therefore, conclusions on the effect of hydrogen on the average <c>-loop length cannot be drawn.

Summary of the Hydrogen Effect

The hydrogen content of Zr-based alloys was one of the two parameters suspected to have a dominating influence on macroscopic irradiation deformation, not only by the known effect of zirconium hydride precipitation and the associated volume increase with a possibly preferred orientation, but by direct interaction of hydrides and dislocation loops, and direct involvement of dissolved hydrogen with loop nucleation, characteristics and stabilization. However, the experiments with Zry-4 conducted in this work do not show a straightforward, but rather a discontinuous influence of hydrogen on dislocation loop formation.
While the <a>-loops' average sizes decrease slightly with the hydrogen content, the average <c>-loop lengths are independent of the hydrogen level. The <c>-loop formation threshold and the <c>-loop linear densities at comparable damage levels show an influence of hydrogen content on the <c>-loop characteristics, but the observed effect does not point in a clear direction. While the sample with 186 wt.-ppm hydrogen showed a 20% lower <c>-loop nucleation threshold and an increase in <c>-loop density by 61% as compared to the standard sample at 23 dpa, the sample with 405 wt.-ppm demonstrated a 44% higher nucleation threshold and a decrease of the linear density by 71%, for a damage level of 25 dpa.

Discussion of the Hydrogen Effect

The observed increase of the <c>-loops' linear densities at 186 wt.-ppm H as compared to the standard, and the decrease at 405 wt.-ppm H seems unusual, as well as the effect of hydrogen on <c>-loop threshold which points in two different directions for the different amounts of hydrogen. However, the experimental conditions during the measurements do not seem to contain the possibility of an error in measurement that would lead to an explanation of the effect:

- The hydrogen contents of the samples before the irradiation experiments were determined in the middle of the sample preparation process, after the hydrogen diffusion loading of the parts that had been milled from the TREX (see chapter 3). Subsequent preparation steps included further milling, mechanical and chemical polishing, relaxation annealing, TEM disc punching and electrolytical etching. The order of these preparation steps was, however, chosen with care. The chemical thinning and polishing with the hydrofluoric acid based etchant is expected to lead to a thin oxide layer on the samples' surfaces, which is assumed to act as a diffusion barrier, to keep the hydrogen in the sample during relaxation annealing. That hydrogen did not leave the samples in significant amounts is confirmed by the appearance of the TEM samples before the irradiation, as shown in Fig. 4.33: The samples with 186 and 405 wt.-ppm show the presence of large intergranular hydrides in their hole periphery, where preferential thinning of the material occurred. Also, more detailed TEM imaging with higher magnification (see Fig. 4.34) shows the presence of intragranular hydrides in the materials, with a significantly higher hydride density for the sample with 405 wt.-ppm than in the sample with 186 wt.-ppm. This strong visibility of the hydrides in the TEM samples also guarantees that an unintended confusion of the samples with different hydrogen content during some step of the experimental process can be excluded.

- The TEM samples were thinned to perforation by electrolytical etching, a process that is reported to lead to slight hydrogen uptake. However, if an uptake of that kind occurred, it can be expected that it would affect all samples to the same degree, as they were thinned with the same parameters. Then, they would pick up a comparable amount of "excess hydrogen" which might increase the hydrogen content of the samples, but by the same amount in all samples. Therefore, the hydrogen content of all samples would be shifted upwards simultaneously, which would not lead to an explanation of the observed effect of hydrogen pointing in two different directions.

- It could be assumed that hydrogen leaves the samples during the irradiation due to the energy transferred to the atoms, which might enhance diffusion processes in the material and to the surface. However, the samples showed hydride precipitation during cool-down to room temperature after their final damage level was reached, which proves that a significant amount of hydrogen was still present in the samples after the irradiation. Also, since the loop densities are compared at similar dose levels, possible irradiation induced diffusion enhancement would have occurred in the different samples at that specific damage level to a comparable degree, and should thus have changed their hydrogen content into the same direction. Again, this would not be an obvious explanation for the observed effect in two different directions.

- The <c>-loop linear densities are calculated by summing up all loop lengths and dividing them by the observed material volume, which depends on the observed grain's thickness. Grain thickness measurements are therefore of high importance for the accuracy of the

calculated linear densities. Thus, the thicknesses of each observed grain was calculated by the grain boundary method (see Appendix C) from measurements at about 8 different tilting angles each, to assure a reliable grain thickness determination. The errors by the grain measurements are shown with the linear density data (see Fig. 4.38). They are not in an order of magnitude that could explain the deviation of the densities.

- As described in several parts of this work, there is a statistical variation when measuring the <c>-loop densities from different TEM images, caused by both a possible bias in the decision when a loop is actually a loop and not a background contrast, and variations in image quality and diffraction conditions that might lead to different degrees of loop visibility. The "human factor" in the analyses does not apply, as all measurements were done by the same person. The statistical variation of the measurements can be observed in the deviation of the linear densities at different damage levels from a straight line increasing with the dose, and also from the 3 measurements each that were taken at the final damage level of the samples. However, the scattering is smaller than the deviation between the data from the different samples, and can therefore not explain the effect.

It is therefore concluded that the observed phenomenon is a real experimental effect and not due to possible experimental or measurement errors. It is possible that the effect of hydrogen addition in the range of 186 wt.-ppm lowering the loop threshold and increasing the linear densities as opposed to the effect of 405 wt.-ppm is due to effects in the material that possess a certain hydrogen concentration threshold. For example, it should be noted that the different hydride densities due to the varying hydrogen content provide a different density of defect sinks in the samples. This could shift the interstitial to vacancy ratio locally or globally. With the sink bias playing an important role during the evolution of the irradiation induced microstructure, this difference in hydride density could have a significant effect on the dislocation loop nucleation and characteristics in the observed samples. Another possible and perhaps more obvious explanation would be that certain material or experimental parameters other than the hydrogen content have a dominating effect on the dislocation loop characteristics and cover any effect that the different hydrogen content might have.
To assess which of these explanations is the accurate one, further experiments with a higher number of samples are required. By measuring a higher number of samples with the same hydrogen content, the magnitude of the effect of unknown other material or experimental parameters on the dislocation loops could be tested. Also, by conducting experiments with samples of a higher number of different hydrogen contents, it could be determined at which hydrogen content the observed density effect changes its direction, i.e. up to which hydrogen level the hydrogen increases the loop density, and when it causes the loop density to fall again.

4.3.4 Effect of External Stress

The effect of external tensile stress on <c>-loop formation was studied in a Zry-4 sample, prepared for the heating-straining TEM stage. The straining sample is fixed to the straining stage by two screws at either end; then, the screws' distance can be increased in a defined way to apply the strain. However, an exact fit of the sample holes to the stage screw positions can only be guaranteed within limited accuracy. Thus, the zero point of the stress, where the sample is exactly flat in the stage but not yet under stress, cannot be defined accurately. To avoid this uncertainty in the sample's stress state, the sample was put into the sample holder and the

TEM, heated to 300°C and then strained until dislocation channels started to open in the grains. Fig. 4.42 shows a low magnification TEM image of the dislocation channels opening in the strain sample.

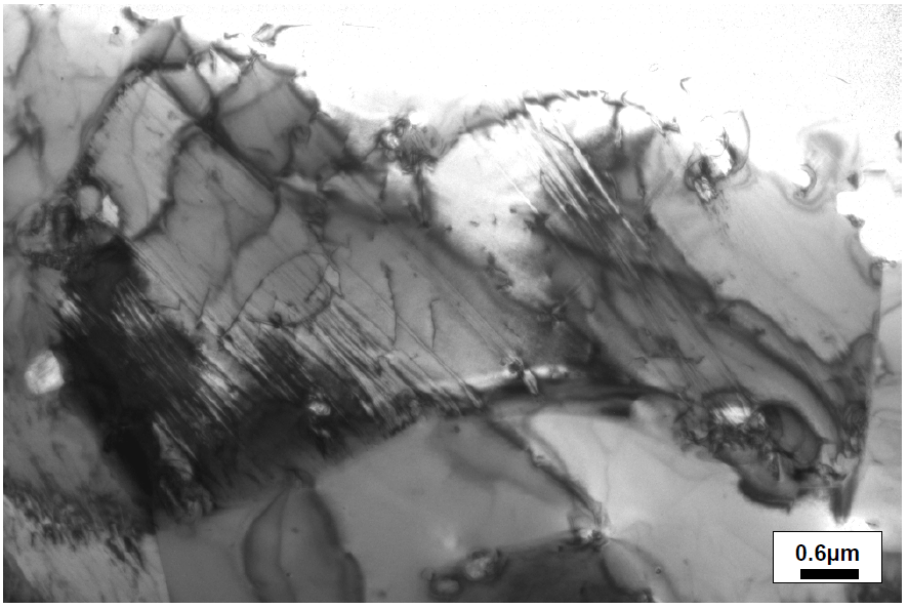

Figure 4.42: Dislocation channels opening in the Zry-4 TEM sample at yield strength

This value of external stress can then be assumed to be close to the material's yield strength, which is defined as the minimal stress which leads to a permanent plastic deformation of the material. For recrystallized Zry-4 ingots comparable to the ingot from which the samples were prepared, the average yield strength is 378 MPa at room temperature and 143 MPa at 343°C. Approximating the temperature dependence to be linear, the calculated yield strength at 300°C is 175 MPa.

Due to the inhomogeneous lattice structure of hcp α-Zr, a possible effect of grain orientation to the tensile direction was expected. Therefore, a sample region was chosen which contained four grains in close proximity to each other, with their c-axes in different orientations towards the stress direction. The angles α between c-axis and tensile direction were approximately 90°, 45°, 30° and 0°. As the grains were within the same sample region and close to each other (with maximal two grains in between), their grain thickness and general stress and temperature state can be assumed to be comparable. Differences in the irradiation induced microstructures are therefore expected to be due to the different c-axis to stress orientation only. The left image row of Fig. 4.43 shows overview images of the four grains, with their values of α indicated; all grains were imaged with g=(0002). In-situ irradiation was carried out at 300°C to high damage levels; the right image row of Fig. 4.43 shows the observed <c>-loop distributions in the four different grains after the final dose level. For the two grains with α=90° and α=45°, which showed significant loop densities, the grains' thicknesses were determined by the grain boundary method to be able to calculate reliable <c>-loop densities. The thicknesses correspond to damage levels of 27 dpa for α=90 and 24 dpa for α=45°. For the two other grains with low loop densities, the thicknesses were not measured; however, due to their close positions to the other grains, it can be assumed that their damage levels lie within the same range.

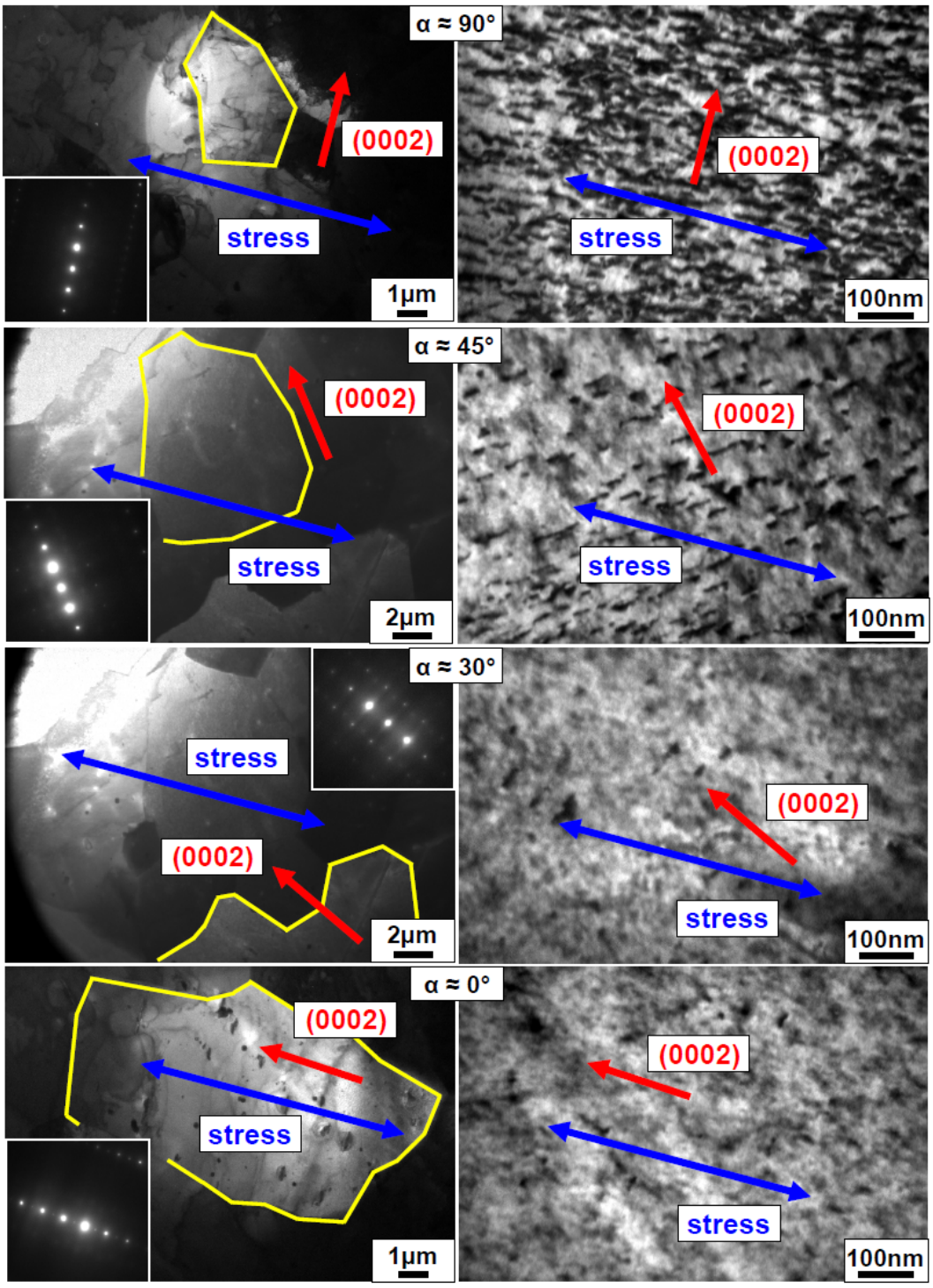

Figure 4.43: <c>-loop development in the Zry-4 strain sample, in dependence of the orientation of the tensile stress direction to the grains' c-axis; dose level = 24 - 27 dpa

The grain with its c-axis oriented perpendicular to the stress direction contains a high <c>-loop density as expected from the previous experiments for Zry-4 at comparable damage level. How-

ever, the grains where the stress vector has a component parallel to the c-axis show a decrease in <c>-loop density; the lower the angle α between tensile stress direction and c-axis, the lower the <c>-loop density in the grains. While the <c>-loop density in the grain with α=45° is still significant, the grain with α=30° shows only few small loops. Finally, the grain with the tensile stress direction parallel to the c-axis does not contain <c>-loops in a significant amount.
This most significant effect of external tensile stress on the <c>-loop characteristics in Zr-based alloys was observed for the first time. The consistency of the continuous <c>-loop density decrease in the four grains with decreasing angle α confirms the reliability of the results. It should also be emphasized that the effect of complete suppression of <c>-loop formation for α=0° is surprising in its magnitude, as 24 - 27 dpa is a damage level range at the upper end of end-of-life doses where <c>-loops with significant densities are found as a rule, both in ion irradiated samples as well as in neutron irradiated material. An oral presentation about these results was accepted at the Nuclear Materials Conference 2012 [104].

Fig. 4.44 shows the linear <c>-loop densities for the unstressed Zry-4 standard sample (black symbols) and two grains in the sample under strain, one with angle α=90° (blue symbols), the other with α=45° (green symbols). During the in-situ irradiation, the grain with angle 90° was observed; therefore, the densities measured in the grain at 45° were taken at the highest dose level only. For the grain with α about 30°, there were only a few single <c>-loops; therefore, their density was not measured. The observed <c>-loop threshold of the grain with α=90° is 5.0 dpa, which agrees with the threshold of 5.5 dpa for the standard sample without stress.

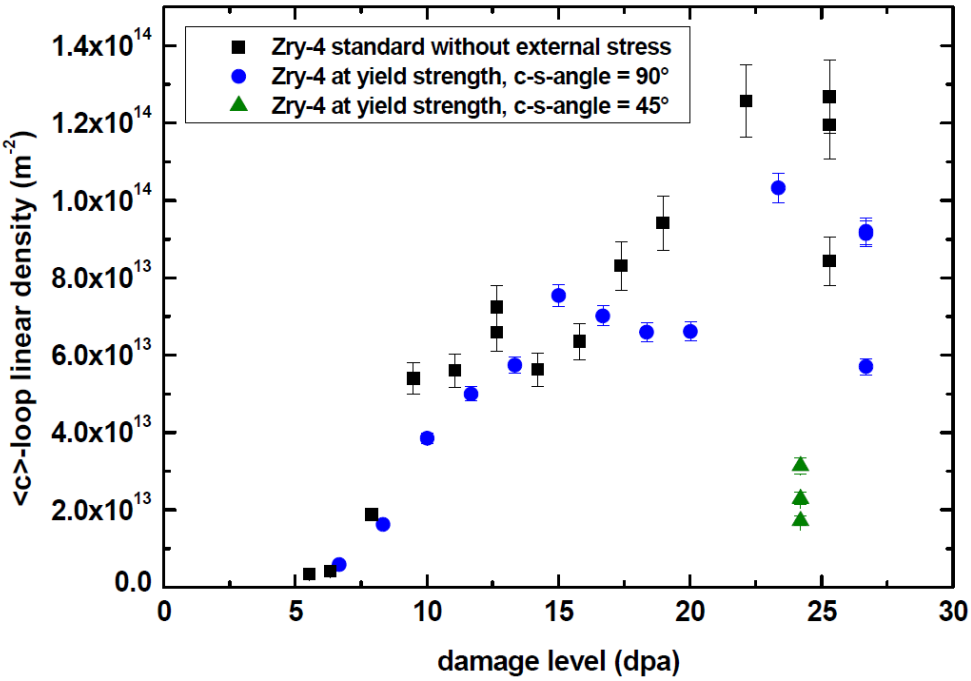

Figure 4.44: <c>-loop linear densities, in dependence of the damage level and the orientation of the tensile stress direction to the grains' c-axis

The measurement accuracy designated by the error bars was calculated from the statistical error of the grain thickness measurements and is one standard deviation of the grain thickness average for the respective grains. At the highest damage level, three grain positions were measured in each sample to demonstrate the <c>-loop density scattering, which can be assumed to be caused both by loop measurement statistics and actual inhomogeneities of the loop distribution over the samples.
The sample with α=90° shows similar <c>-loop linear densities as the sample without stress over the whole damage level range; however, the grain with α=45° has a significantly lower linear <c>-loop density. At the maximal damage level (27 dpa for the grain with α=90° and 24 dpa for the grain with α=45°), the <c>-loop linear density in the grain with α=45° is about 30% of the density of the grain with α=90°.

Fig. 4.45 shows the <c>-loop size distribution for Zry-4 samples with and without external stress. The distributions contain data from 3 observed positions in sample PA2 without strain, 3 positions in the grain with α=90° and 2 positions in the grain with α=45° in the strain sample. The average <c>-loop lengths as a function of the damage level for the standard sample without stress and the samples under stress with α being 90° and 45° are summarized in Fig. 4.46.

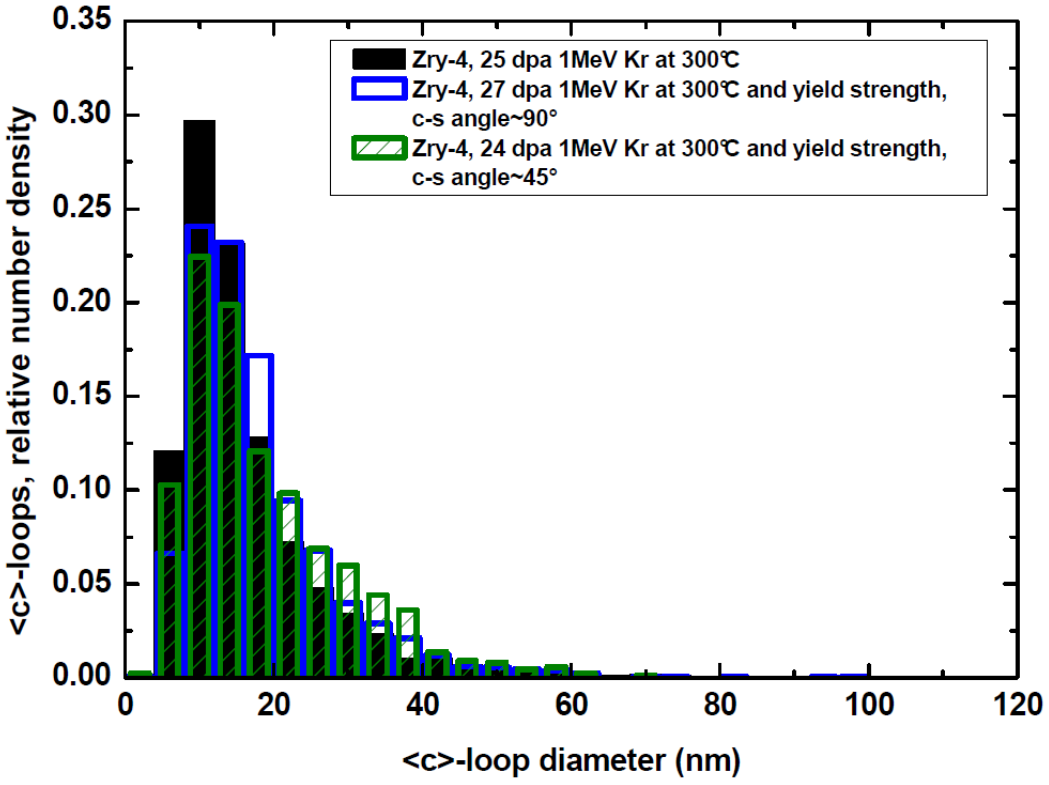

Figure 4.45: <c>-loop size distribution for samples with and without external stress

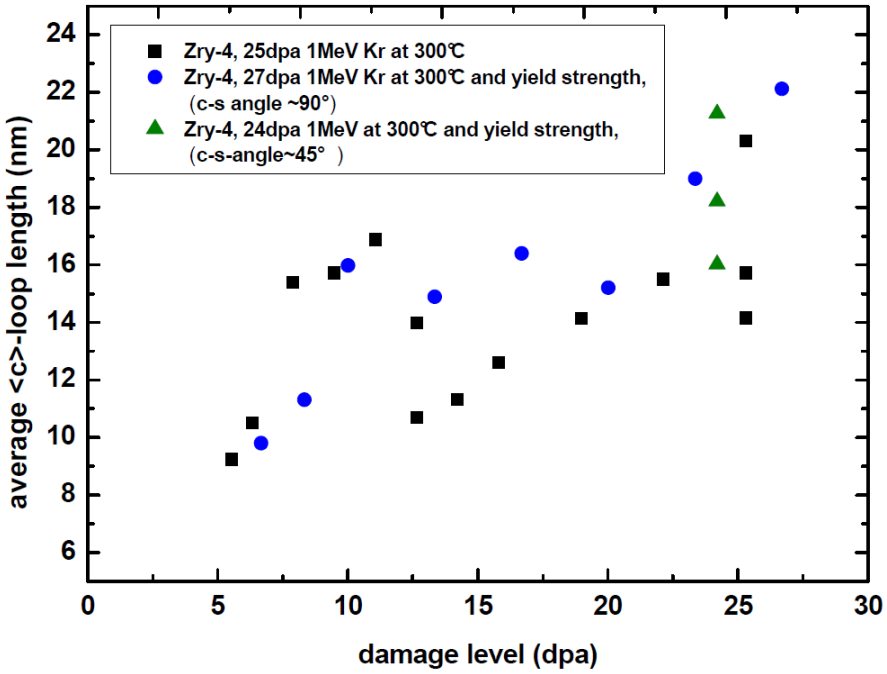

Figure 4.46: Average <c>-loop length for samples with and without external stress

The <c>-loop length distributions for the two grains with α=90°, α=45° and for the standard sample without stress in Fig. 4.45 do not show a significant influence of external stress and its orientation on the loop length. Fig. 4.46, which gives the average <c>-loop length development with the damage level, confirms that an effect of stress on loop length cannot be seen.

The <c>-loop distribution in the imaged grain from the sample without stress and the grain under stress with α=90° are comparatively homogeneous over the grains; however, the grain with α=45° shows an noticeable feature in the <c>-loop distribution which can be observed in a lower magnitude overview image of the grain: The loops' density is varying over the grain, with regions of higher densities following a pattern of "flow lines" (see Fig. 4.47). For the linear loop densities given in Fig. 4.44, grain regions of homogeneous densities within the matrix were chosen.

These flow lines are similar in form and characteristics to bending contours typically observed in thin TEM sample grains. Therefore, it is assumed that the origin of the phenomenon is an inhomogeneous stress state of the matrix over the grain. This inhomogeneous stress distribution would lead to the formation of a higher density of <c>-loops along the bending contours, where the stress state varies from the rest of the grain. This observation demonstrates that not only strain differences between different grains lead to different <c>-loop densities, but that the <c>-loop densities are also sensitive towards strain variations within single grains. Whether the deciding factor in this case is a difference of the absolute stress value within the contours or the difference in the stress orientation, or both, cannot be decided from the available data. This also raises the question whether reported enhanced <c>-loop densities in the vicinity of hydrides and second phase particles are really primarily due to possible dissolution of these phases and the related compositional changes in their surrounding matrix during irradiation, and not rather caused by the different strain level in the matrix surrounding the precipitates.

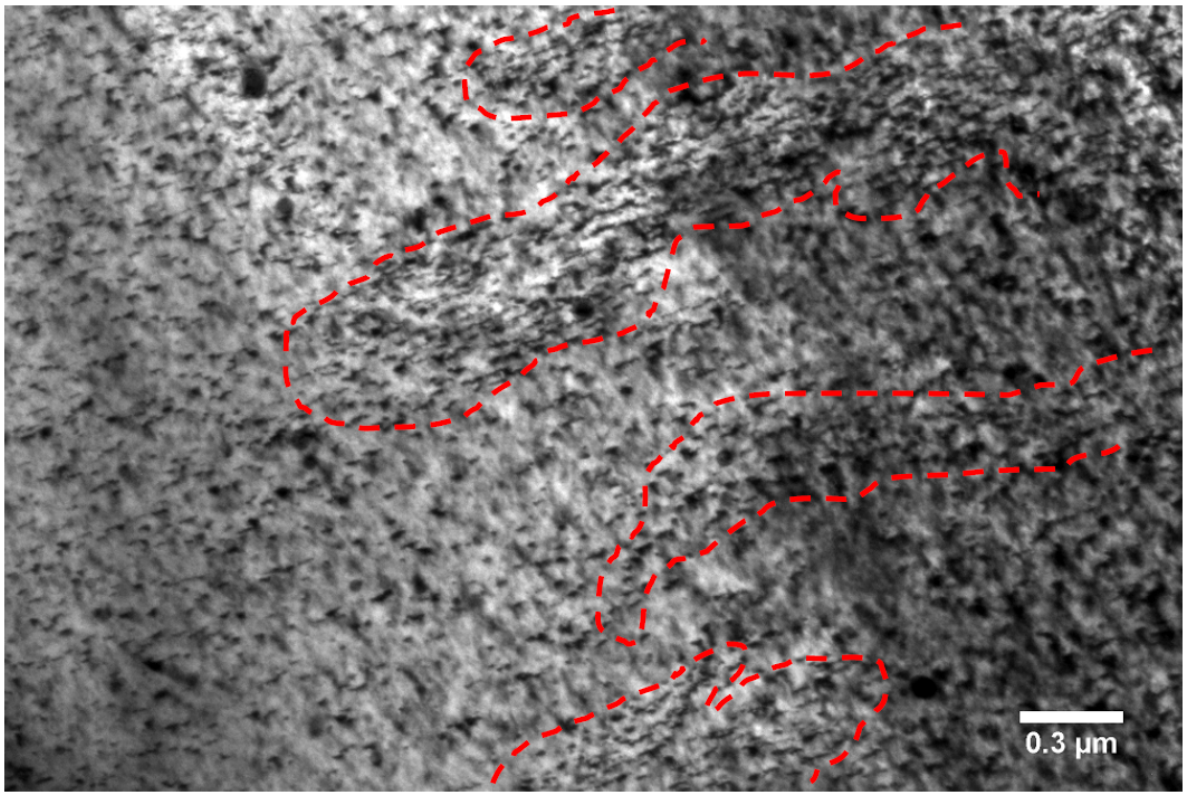

Figure 4.47: <c>-loop distribution varying within one grain; α=45°, damage level 24 dpa

Summary of the Stress Effect

A most significant effect of external tensile stress at yield strength level on the <c>-loop formation in Zry-4 was observed. The <c>-loop density decreases with decreasing angle between the direction of stress and the c-axis of the respective grain; for the stress direction parallel to the c-axis, <c>-loop formation is suppressed entirely, at the high damage level of 24 to 27 dpa which corresponds to high end-of-life LWR neutron fluences. This strong effect of external stress on <c>-loop densities in Zr-based alloys was shown for the first time and is surprising in its magnitude. In addition, the observation of <c>-loop density fluctuations within one grain following a "flow line" pattern is an indication that <c>-loop formation and/or stability is not only sensitive towards the orientation of the respective grain towards the tensile stress, but also to stress variations within single grains.
While the stress was observed to clearly affect the <c>-loop linear densities, <c>-loop lengths showed to be unaffected by the tensile stress.

Discussion of the Stress Effect

The observed effect of the orientation of external tensile stress on the <c>-loop linear densities can be explained as follows:
By applying an external tensile stress parallel to the c-axis of the sample, the grain is strained and its basal planes are pulled apart (see left schematic in Fig. 4.48).
The linear density of lattice planes in c-direction is therefore reduced as compared to the equilibrium state. Placing a <c>-loop, which is a two-dimensional cluster of vacancies, on one of the

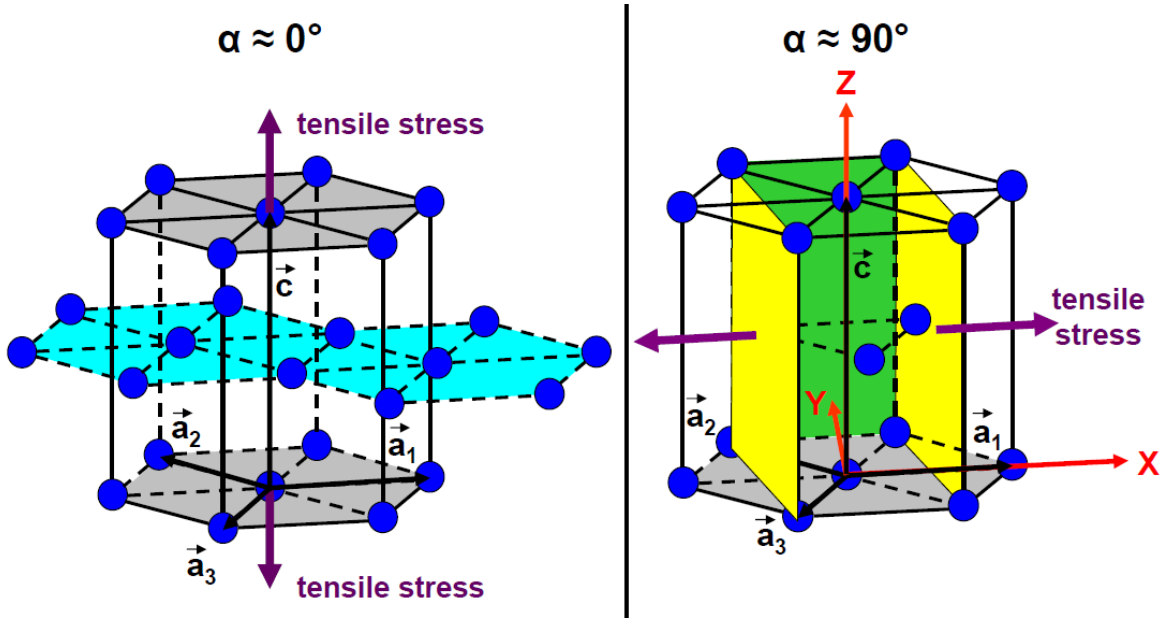

Figure 4.48: Tensile stress pulling on the basal planes, $\alpha \approx 0°$ (left); tensile stress pulling on the prism planes of type II, $\alpha \approx 90°$ (right)

basal planes, would correspond to a local removal of a part of the basal plane, and would therefore reduce the lattice plane density in c-direction even further. It would thus require additional energy, as compared to the formation of a c-loop on a basal plane in the crystal without external stress. Consequently, <c>-loop formation under tensile stress with a component parallel to the c-axis is not energetically favored, and the <c>-loop density is accordingly lower than in the grain without tensile stress. This is in accordance with the stress induced preferetial nucleation (SIPN) model described in section 2.2.2. and summarized in the statement that vacancy loops will be less likely to nucleate on planes perpendicular to the tensile stress and more likely to nucleate on planes parallel to the stress [10][1]. The larger the component of the stress in c-direction, the stronger the suppression of <c>-loop formation. The observed <c>-loop densities shown in Fig. 4.43 are in direct agreement with this hypothesis; for $\alpha \approx 45°$, a significant reduction in <c>-loop density is observed. For increasing stress component parallel to the c-axis, at $\alpha \approx 30°$, the <c>-loop density decreases further until the complete absence of <c>-loops for $\alpha \approx 0°$.
When tensile stress is applied perpendicular to the c-direction, it has only components in one or more of the a-directions, depending on the orientation of the grain. The right schematic in Fig. 4.48 shows the situation where the tensile stress is applied to one set of prism planes of type II, parallel to the crystal axis $\vec{a_1}$. The linear density of the prism planes in this direction is therefore reduced; consequently, in analogy to the explanation above, the density of vacancy-type <a>-loops on the respective prism planes should be reduced. <a>-loops were not studied in the strain sample which was imaged with the (0002) reflex only. Also, the interstitial or vacancy nature of the <a>-loops would not have been measureable due to the high defect density. Therefore, it was not possible to confirm or refute this hypothesis.

[1] This statement is not limited to anisotropic crystal structures.

When discussing the comparability of the conducted ion irradiation experiment on the effect of tensile stress to the guide tube situation during reactor operation, one major issue is the texture of the guide tubes. In consequence of the tube production process, the c-axes in the guide tubes are mainly in radial orientation. In radial direction, though, tensile stress is not applied during reactor operation. However, the hold-down system described in chapter 2 leads to a compressive stress in axial direction. Due to the elasticity of the material, it can be expected that such compressive stress in an a-direction would lead to an expansion of the grain in the other a-directions and, specifically, in c-direction. The magnitude of this indirect tensile strain component in c-direction can be estimated on the basis of the elastic properties of the hcp lattice:
The elastic behavior of a solid, in this case a single grain of the guide tube alloy, can be approximated by continuum theory, regarding the grain as a homogeneous continuous medium instead of a periodic array of atoms [105, 106]. Assuming the applied stress to be low, the strain in the elastic solid is directly proportional to the stress, as stated by Hooke's law. While there is a deviation from this direct proportionality for stress at the yield strength level, it will still be used as an approximation to illustrate the general material behavior. In the three-dimensional case, strain and stress are each tensors of 2^{nd} rank, which are connected by the elastic data of the solid, in the form of a tensor of 4^{th} rank. The displacement $\vec{R}$ of a material position $\vec{r}$ can be described as

$$\vec{R}(\vec{r}) = \begin{bmatrix} \epsilon_{xx} & \epsilon_{yx} & \epsilon_{zx} \\ \epsilon_{xy} & \epsilon_{yy} & \epsilon_{zy} \\ \epsilon_{xz} & \epsilon_{yz} & \epsilon_{zz} \end{bmatrix} \cdot \begin{bmatrix} x \\ y \\ z \end{bmatrix},$$

where the dimensionless coefficients ϵ_{ij} define the deformation. The strain components $\mathsf{e}_{\alpha\beta}$ are related to the ϵ_{ij} as follows [105]:

$$\mathsf{e_{xx}} = \epsilon_{\mathsf{xx}}$$

$$\mathsf{e_{yy}} = \epsilon_{\mathsf{yy}}$$

$$\mathsf{e_{zz}} = \epsilon_{\mathsf{zz}}$$

$$\mathsf{e_{xy}} = \epsilon_{\mathsf{yx}} + \epsilon_{\mathsf{xy}} = \mathsf{e_{yx}}$$

$$\mathsf{e_{yz}} = \epsilon_{\mathsf{zy}} + \epsilon_{\mathsf{yz}} = \mathsf{e_{zy}}$$

$$\mathsf{e_{zx}} = \epsilon_{\mathsf{zx}} + \epsilon_{\mathsf{xz}} = \mathsf{e_{xz}}$$

The strain components $\mathsf{e}_{\alpha\beta}$ are linear functions of the stress components; for example, $\mathsf{e_{xx}}$ is given as

$$\mathsf{e_{xx}} = \mathsf{S_{11}X_x} + \mathsf{S_{12}Y_y} + \mathsf{S_{13}Z_z} + \mathsf{S_{14}Y_z} + \mathsf{S_{15}Z_x} + \mathsf{S_{16}X_y}.$$

The $\mathsf{X_x}$, $\mathsf{Z_x}$ etc. represent the stress components; the capital letter describes the direction of the force, and the index gives the normal to the plane to which the force is applied. The $\mathsf{S_{mn}}$ are the so-called elastic compliance constants which can be calculated from the elastic moduli $\mathsf{C_{ab}}$ by inverting the 6x6 matrix containing the elastic moduli.
For hcp materials, the elastic data consists of 5 independent elastic moduli with the following structure [106]:

$$\mathsf{C} = \begin{bmatrix} & \mathsf{e_{xx}} & \mathsf{e_{yy}} & \mathsf{e_{zz}} & \mathsf{e_{yz}} & \mathsf{e_{zx}} & \mathsf{e_{xy}} \\ \mathsf{X_x} & \mathsf{C_{11}} & \mathsf{C_{12}} & \mathsf{C_{13}} & 0 & 0 & 0 \\ \mathsf{Y_y} & \mathsf{C_{12}} & \mathsf{C_{11}} & \mathsf{C_{13}} & 0 & 0 & 0 \\ \mathsf{Z_z} & \mathsf{C_{13}} & \mathsf{C_{13}} & \mathsf{C_{33}} & 0 & 0 & 0 \\ \mathsf{Y_z} & 0 & 0 & 0 & \mathsf{C_{44}} & 0 & 0 \\ \mathsf{Z_x} & 0 & 0 & 0 & 0 & \mathsf{C_{44}} & 0 \\ \mathsf{X_y} & 0 & 0 & 0 & 0 & 0 & \mathsf{C_{66}} \end{bmatrix}$$

with $\mathsf{C_{66}} = (\mathsf{C_{11}} - \mathsf{C_{12}})/2$.
For the described situation of compressive stress perpendicular to the c-direction, a suitable orientation of the coordinate system is the x-axis parallel to crystal axis $\vec{a_1}$ and the z-axis parallel to crystal axis $\vec{c}$ (compare the coordinate system on the right side of Fig. 4.48). This compressive stress applied in $\vec{a_1}$ direction, parallel to the x-axis, leads to a compressive strain of the material normal to one prism plane set of type II. The response of the prism planes of type I and the basal planes can then be calculated from the elastic data of the hcp lattice:
According to the chosen coordinate system, only the X_x out of the six independent stress components are unequal zero. Following the elastic material properties as described above, the resulting strain components are the $\mathsf{e_{ii}}$; the $\mathsf{e_{ij}}$ with i≠j are zero because of the respective elastic moduli being zero. Therefore, the strain components in x-, y- and z-direction are

$$\mathsf{e_{xx}} = \mathsf{S_{11}X_x}$$
$$\mathsf{e_{yy}} = \mathsf{S_{21}X_x}$$
$$\mathsf{e_{zz}} = \mathsf{S_{31}X_x}$$

The values of $\mathsf{S_{mn}}$ referring to the $\mathsf{e_{ii}}$ can be calculated by inverting the matrix C and are given as follows [106]:

$$S_{11} = \frac{1}{2}\left[\frac{1}{C_{11}-C_{12}} + \frac{C_{33}}{(C_{11}+C_{12})C_{33}-2C_{13}^2}\right]$$
$$S_{21} = \frac{1}{2}\left[\frac{C_{33}}{(C_{11}+C_{12})C_{33}-2C_{13}^2} - \frac{1}{C_{11}-C_{12}}\right]$$
$$S_{31} = \frac{-C_{13}}{(C_{11}+C_{12})C_{33}-2C_{13}^2}$$

The elastic moduli for α-Zr are summarized in table 4.8 [107].

C_{11}	C_{12}	C_{13}	C_{33}	C_{44}
1.43	0.728	0.653	1.65	0.320

Table 4.8: Elastic moduli for α-Zr, in $10^{11}\mathrm{N/m^2}$ [106]

The strain components are therefore given as:

$$\mathsf{e_{xx}} = 1.017 \cdot 10^{-11}\frac{\mathsf{m^2}}{\mathsf{N}} \cdot \mathsf{X_x}$$

$$\mathsf{e_{yy}} = -4.076 \cdot 10^{-12} \frac{\mathsf{m}^2}{\mathsf{N}} \cdot \mathsf{X_x}$$

$$\mathsf{e_{zz}} = -2.411 \cdot 10^{-12} \frac{\mathsf{m}^2}{\mathsf{N}} \cdot \mathsf{X_x}$$

For compressive stress in x-direction, the $\mathsf{X_x}$ are negative, which leads to a negative strain in x-direction and a positive strain in y- and z-direction. The resulting strain component in y-direction is about 40% of the strain component in x-direction, and the strain component in z-direction is about 24% of the strain in x-direction. For visualization of the absolute grain deformation, the absolute displacements will be calculated for an exemplary compressive stress of 100 MPa in x-direction. The resulting strain components are

$$\mathsf{e_{xx}} = -1.017 \cdot 10^{-4}$$

$$\mathsf{e_{yy}} = 4.076 \cdot 10^{-5}$$

$$\mathsf{e_{zz}} = 2.411 \cdot 10^{-5}$$

The position of atom $\vec{a_1} = (a, 0, 0)$ on the x-axis and atom $\vec{c} = (0, 0, c)$ on the c-axis, with a=3.231$\mathring{A}$ and c=5.147$\mathring{A}$ would then change as follows[2]:

$$\vec{a_1}^{\mathsf{new}} = \vec{a_1} + \vec{R}(\vec{a_1}) = \begin{bmatrix} 3.231\mathring{A}(1 - 1.017 \cdot 10^{-4}) \\ 0 \\ 0 \end{bmatrix} = \begin{bmatrix} 3.2307\mathring{A} \\ 0 \\ 0 \end{bmatrix}$$

$$\vec{c}^{\mathsf{new}} = \vec{c} + \vec{R}(c) = \begin{bmatrix} 0 \\ 0 \\ 5.147\mathring{A}(1 + 2.411 \cdot 10^{-5}) \end{bmatrix} = \begin{bmatrix} 0 \\ 0 \\ 5.1482\mathring{A} \end{bmatrix}$$

For completeness, the center of the prism plane I designated in green in Fig. 4.48, with position vector $\vec{a_y}$=(0,$\sqrt{3}$/3·a,0) would be affected as follows:

$$\vec{a_y}^{\mathsf{new}} = \vec{a_y} + \vec{R}(\vec{a_y}) = \begin{bmatrix} 0 \\ \sqrt{3}/3 \cdot 3.231\mathring{A} \cdot (1 + 4.076 \cdot 10^{-5}) \\ 0 \end{bmatrix} = \begin{bmatrix} 0 \\ 1.8655\mathring{A} \\ 0 \end{bmatrix}$$

The resulting changes in the axis intercepts of the different lattice planes in x-, y- and z-direction are summarized in table 4.9.

	prism planes II (yellow) x-axis	prism planes I (green) y-axis	basal planes (grey) z-axis
without stress	1.6155$\mathring{A}$	1.8654$\mathring{A}$	5.147$\mathring{A}$
100 MPa in a_1-direction	1.6153$\mathring{A}$	1.8655$\mathring{A}$	5.1482$\mathring{A}$

Table 4.9: Estimate of the changes in the lattice plane positions for a compressive stress of 100 MPa parallel to $\vec{a_1}$; color references are given with regard to Fig. 4.48

[2]The number of valid digits is increased by 1 in the new atom position vectors as compared to the original positions, to illustrate the strain effect which would not be visible otherwise.

Due to the texture of the guide tubes, a compressive stress in axial direction (which can be approximated as being parallel to one of the a-axes) thus leads to a significant indirect tensile strain component in c-direction, with a magnitude of about 24% of the compressive strain component in direction of the specific a-axis. Therefore, the axial compressive stress during reactor operation indeed creates a strain situation that is approximated with the tensile stress in c-direction during the ion irradiation experiment with α=0°. In consequence, the hypothesis can be formed that an increase of the axial hold-down forces during operation should lead to a decrease of the <c>-loop formation in the guide tubes.

The observed dependence of <c>-loop densities on the stress orientation, and the variation of <c>-loop-densities within a single grain observed in the "flow line" features lead to the formation of an additional hypothesis: In-pile irradiated Zr-based alloys are in some cases reported to show a preferred nucleation of <c>-loops, or just a higher <c>-loop density, in direct vicinity of second phase particles or hydrides. The effect of preferential nucleation near an SPP was also described for one sample ion irradiated in this work. Explanations of this phenomenon are mostly based on compositional changes of the matrix in the vicinity of the SPPs or hydrides during the irradiation, e.g. Fe diffusion from the dissolving SPP into the matrix. The observed strong effect of stress on <c>-loop formation indicates another obvious explanation for this preferential nucleation or loop formation to higher densities, which would be independent of changes of the chemical composition of the matrix: The presence of SPPs or hydrides leads, due to the different lattice structures and lattice parameters of those phases as compared to the matrix, to lattice strains in the matrix surrounding the particles. The strain state of the material in these regions is thus different from the rest of the grain, which would be a direct explanation for a different <c>-loop formation behavior in these areas. It is of course also possible that both the effects of the different stress state around the SPPs and the irradiation induced diffusion of alloying elements from the SPPs into the matrix contribute to the observed phenomenon.

An important issue from the experimental point of view is the estimation of the strain state of the respective grains. It was explained above that the determination of the zero strain state of a sample put into the straining stage is difficult because strains in the range of microns are to be measured while it is impossible to assess at which exact point the sample is in a perfectly flat state without external stress. To avoid this difficulty, the yield strength of the respective alloy was chosen; then, by straining until the occurrence of dislocation channels, the amount of stress can be well estimated. However, while this applies for initial stress before the irradiation, it is known that Zr-based alloys under neutron irradiation show irradiation hardening and thus change their elastic properties [108]. To assess whether the sample was still under stress during and after the irradiation, the screw distance of the straining stage was decreased by some microns to see the reaction of the sample after the final damage level was reached. The observed rim of the hole in the sample reacted immediately to the stress release by motion in negative stress direction. It was therefore confirmed that, even if the sample did experience relaxation during irradiation, there was still a significant amount of stress present at the final damage level.
For future experiments with a more detailed monitoring of the strain state in single grains during the irradiation, and also to be able to do reliable experiments at stress levels lower than the yield strength where the dislocation channel method can obviously not be applied, first tests were conducted to calculate the strain level from the distances of markers within the grains before and after the application of stress. Such markers could be second phase particles or, depending on grain size and geometry, grain boundary sections. The tests showed that the resolution of the strain in the applied levels would require images of significantly higher magnification than

30'000 which was used. Further work in succession to this thesis will therefore also focus on high magnification imaging of defined distances within single grains under stress, possibly by reconstruction of grain distances from a larger number of high magnification images taken from regions between the respective markers.
Since the effect of stress showed to be very clear and continuous, the reliability of this particular experiment should also be used to study the simultaneous effects of external stress and other parameters like hydrogen content or alloying. This would provide more details about the interaction of the different experimental parameters and would be of high interest for the transferability of the results to in-pile components, whose behavior is the result of a high number of interdependent experimental parameters.

4.4 General Discussion

4.4.1 Interaction of the Parameters during the Ion Irradiation Experiments

During the in-situ irradiations at the IVEM Tandem Facility, all samples were held at 300°C (with an assumed error of 5 K for the double-tilt heating stage and 10 K for the heating-straining stage), such that effects of temperature should be negligible when discussing the differences in irradiation microstructure in the various samples.
Looking at the effect and possible superpositions of hydrogen and stress state in the ion irradiated samples, the straining sample should not have experinced an effect of hydrogen. There is the possibility of hydrogen pickup during electrolytical etching, but since the imaged grains were close to each other in the sample, if such pick-up should have occurred, it should have affected the grains to a comparable degree. On the other hand, it cannot be excluded that the samples studied for the effect of hydrogen experienced deviations of the strain state in their different grains. Residual strains from sample preparation are not expected in the samples, as they were recrystallization annealed before the electrolytical etching. However, differences in strain might evolve during the irradiation, assuming that the dislocation loop formation leads to single grain growth, which would cause strains between adjacent grains, depending on their geometry. A more detailed assessment of this question would require a method to measure single grain's strain states during the irradiation experiments, which might be possible by the marker technique described above.

4.4.2 Relevance of the Results for the Fuel Assembly Deformation Issue

The objective of this work was to investigate the microstructural processes in Zr-based alloys under irradiation, in order to better understand the fuel assembly deformation phenomenon. The results of this work contribute to such a better understanding in several points.
First of all, there are a number of conclusions and practical recommendations regarding the experimental techniques in general and TEM sample preparation and TEM imaging, which are also relevant for TEM studies of in-pile irradiated material:

- The extensive experiments with in-situ ion irradiation proved the method to be an excellent tool for LWR irradiation damage simulation; the conducted parameter optimization can facilitate further experimental work in the field, and the good results can promote the method as a time- and cost-effective alternative to in-pile irradiation experiments. It was

also shown that, due to the possibility to observe dynamic microstructural processes in-situ, the method provides scientific insight into microstructural processes that would not be accessible in in-pile irradiation experiments.

- It has to be emphasized that TEM sample preparation by focussed ion beam (FIB) should be avoided whenever possible for the study of dislocations in Zr-based alloys. FIB tests at different facilities and with different instruments showed to lead to extensive irradiation damage, even when conducted at liquid nitrogen temperature, and additional problems occurred like TEM lamella bending or sample oxidation. Minimization of the FIB's ion beam incident angle, ion energy and beam current did not solve the issue; neither did subsequent usage of a precision ion polishing system (PIPS) even when set to the mildest parameters. From the preparation experience in this work, it has to be concluded that irradiation damage studies in Zr-based alloy samples prepared by FIB before or after the irradiation are not suitable to provide reliable results on the irradiation induced microstructures.

- When studying the relation between hydrides and irradiation damage, it is recommended not to draw conclusions regarding possible interactions between dislocation loops and intragranular hydrides from samples viewed in the TEM at room temperature (if the irradiation temperature was higher than room temperature). The observed hydride dissolution during heating of the samples to 300°C and hydride precipitation during cooling showed that the hydride distribution and characteristics at room temperature are not related in any direct way to the situation at 300°C. The hydrides did not precipitate in the same locations where they were before the heating up, and they were different in size, form and orientation. It is expected that their appearance after cooling down is also related to the cooling rate, which can vary for in-pile irradiated samples due to different procedures for reactor shutdown before the outage. For post irradiation examinations of irradiated material, it is therefore recommended to heat the samples in the TEM and image them at their former operating temperature, which would reproduce the hydrogen solution state during the irradiation.

- When comparing dislocation loop densities from different TEM images, it is essential to use images with similar magnification. To avoid bias in the density measurements, it is recommended that the different images are analyzed by the same person. Also, the accuracy of grain thickness measurements is essential for the calculation of reliable values for dislocation loop densities.

- The studies on the temperature effect showed that the irradiation temperature has a strong effect on the overall vacancy-type defect density. Microstructural observations from material irradiated at different temperature levels should therefore be compared with care.

Finally, the results contribute to a better scientific understanding of the origins and influencing factors of the fuel assembly deformation phenomenon, which was the main objective of this work.

- The damage level at which the <c>-loop nucleation threshold was observed for the ion irradiated samples confirmed the hypothesis of several authors that the onset of macroscopic breakway growth in Zr-based alloys is correlated to the appearance of <c>-loops in the material. The critical <c>-loop density corresponding to this onset was determined for Zry-4 at 300°C.

- While a correlation between <c>-loop appearance and macroscopic growth was described and assumed by many authors, it was never actually proven that the appearance of <c>-loops would trigger the onset of breakaway growth, and not the other way round. In theory, it could also be possible that breakaway growth is triggered by processes that are unrelated to the <c>-loops, and that the <c>-loops would form as a consequence of the breakaway growth. By the ion irradiation experiments in this work, it was shown that <c>-loop formation occurs in Zr-based alloys as a result of the irradiation in samples that are isolated from the in-pile environment, in the absence of parameters like stress, hydride precipitation, temperature gradients, corrosion or other possible factors that might be causing breakaway growth. Therefore, the results of this work confirm that <c>-loop formation is a trigger for breakaway growth, and not breakaway growth a trigger for <c>-loop formation.

- One of the main questions to be investigated in this work was the effect of hydrogen on the irradiation induced microstructure in Zr-based alloys. The studies of the effect of hydrogen as an isolated parameter, as it was done in the ion irradiation experiments, showed the influence of hydrogen content on the <c>-loop characteristics to be discontinuous, in the way that hydrogen addition in the range of 186 wt.-ppm led to a lower <c>-loop nucleation threshold and a higher <c>-loop linear density than in the standard material at comparable damage level, while the addition of 405 wt.-ppm had the opposite effect. The two most probable explanations for the observed phenomenon would be, on the one hand, that the effect of parameters other than hydrogen on the irradiation induced microstructure are so strong that they cover the effect of the hydrogen completely; or, on the other hand, that the different hydrogen levels which lead to a different hydride density could influence the defect sink bias and thus change the interstitial to vacancy ratio locally or globally. This could cause a <c>-loop stabilization for lower hydride densities as compared to a <c>-loop formation suppression for higher hydride densities. In the case of the dominant effect of other parameters, it is necessary to assess which parameters that would be. In the case of the different interactions between hydrides and irradiation defects for different hydrogen contents, this phenomenon has to be taken into consideration when discussing the effect of hydrogen on macroscopic fuel assembly growth. Since the hydrogen content in the structural material changes during the assembly lifetime, from a hydrogen-free state at beginning-of-life to concentrations significantly above the solubility limit for Zry-4, Zry-4 guide tubes can be assumed to pass these two observed hydrogen content regions which have an opposite effect on the <c>-loop structure and thus possibly on macroscopic irradiation growth. As the hydrogen uptake shows dependence on the operating conditions of the specific plants and fuel assemblies, the effects can differ for different assemblies. Disregarding the effect of other parameters, this would lead to non-linear or discontinuous effects in the growth behavior. The onset of breakaway growth would be accelerated if the hydrogen level was in the range of 186 wt.-ppm before the damage level triggering breakaway onset is reached, and it would be retarded if the material had already taken up a hydrogen level in the range of 405 wt.-ppm before reaching the "critical" damage level. Above the threshold dose, the ion irradiation results showed a lower <c>-loop formation rate for the 405 wt.-ppm level and a higher rate for the 186 wt.-ppm. It can therefore be expected that the <c>-loop density increase rate after the onset of breakaway growth will depend on the operating condition and lifetime dependent hydrogen content of the components and might lead to discontinuous growth behavior.
  To sum up, the ion irradiation results did not show an effect of the hydrogen content

pointing in a clear direction; the most probable explanations for this observation are that the hydrogen content is either negligible with regard to other dominating parameters, or that it has a discontinuous component. Both hypotheses lead to the conclusion that a direct correlation between hydrogen content and breakaway growth might not be suited to describe the phenomenon. Therefore, it is recommended to study the effect of hydrogen more extensively to assess this issue in more detail.

- The ion irradiation experiments showed a very significant and conclusive effect of external tensile stress on the <c>-loop formation in Zry-4: tensile stress with a component parallel to the c-direction of the grains reduces the <c>-loop density in the respective grains; the effect increases with the magnitude of the parallel component. For tensile stress at the yield strength level, <c>-loop formation was completely suppressed for the stress direction parallel to the c-axis.
  When comparing the experimental conditions during the ion irradiation experiment to in-pile fuel assembly operation, the main difference is the level of applied stress. The Zry-4 yield strength at 300°C of 175 MPa is by several factors higher than typical stress levels in PWR guide tubes under normal operation, which are described to vary between some 10 MPa compressive to several 10 MPa tensile axial load, caused by the hold-down spring force, hydraulic forces, the differential expansion of fuel rods and guide tubes, and bow forces created by cross flow and neighbouring fuel assemblies; in addition, the oxide layer on the guide tubes, growing during operation, can contribute up to 10 MPa axial tensile stresses [30]. Even though these stress levels during operation are smaller than the yield strength, they remain at a significant level; also, there is no obvious reason to assume that the conclusive effect of tensile stress observed at yield strength level should not occur, with a lower magnitude, analogously for lower stress levels. It is thus assumed that the observed orientation dependent stress effect is also relevant under in-pile conditions.
  As described in chapter 2, the guide tubes are produced with a texture that causes the majority of the grains' c-axes to be oriented radially, with their direction deviating in a range of 30° from the radial vector. A direct tensile stress in radial direction is not likely to occur in guide tubes during normal operation; the coolant pressure results in a radial compressive stress, and the other main stress contributors are oriented in axial direction. It should however be noted that radial tensile stress is relevant for fuel rods as a consequence of pellet swelling. On the other hand, due to the elastic properties of the alloy, an "indirect" tensile strain in radial direction would result from axial compressive stress e.g. applied by the hold-down springs. As calculated above from the elastic properties of α-Zr, a compressive stress in axial direction, corresponding to a compressive stress in one a-direction of the crystal lattice, would lead to a tensile strain component in c-direction with about one fourth of the magnitude of the compressive strain component in a-direction. Such tensile strain parallel to the c-axis would, according to the results of the ion irradiation at yield strength experiment, hinder the formation of <c>-loops. Therefore, the application of axial compressive stress on the guide tubes leads in theory to a reduction of <c>-loop formation which would in turn hinder the onset of macroscopic breakaway growth and slow down the growth process in general. However, to assess the magnitude of the effect and to study whether it is significant at typically applied hold-down forces, further ion irradiation experiments at lower tensile stress levels corresponding to typical PWR environments are necessary.
  Finally, the observed effect of grain orientation towards the stress direction leads to the conclusion that changes in the guide tubes' texture due to different production processes

might have a significant effect on <c>-loop formation under irradiation and thus on macroscopic component growth. Also, it was shown by Garzarolli et al. that Zry-4 with higher yield strength shows stronger irradiation growth [103]. Therefore, processes leading to a yield strength increase such as possible induction of residual strains from cold work after the final annealing, e.g. by final straightening of the tubes, might influence the tubes' growth behavior. Such variations in the tubes' texture or strain state should therefore be treated with caution.

- As a final comment, the effects of the different environmental parameters during in-pile irradiation are occurring simultaneously and can be expected to be interdependent. This can be expected to also apply for the effects of hydrogen and stress; deviations from the conclusions taken from the ion irradiation experiments that were conducted by isolating these single parameters can therefore be assumed for in-pile operation. Further insight into these interactions could be provided by additional ion irradiation studies on the simultaneous effects of stress and hydrogen content.

Chapter 5

Conclusion and Outlook

In the past years, unexpectedly high fuel assembly growth has been observed in some PWR plants, which was not predicted by the fuel assembly codes that are based on the operational experience and the theoretical knowledge of irradiation deformation. To explain this unexpected phenomenon, to improve the FA codes and to facilitate the development of advanced deformation resistant alloys, a better understanding of the microstructural processes in the alloys during neutron irradiation is necessary. The objective of this work was to contribute to such better understanding by specifically studying the influence of hydrogen content and external stress on the irradiation behavior of PWR guide tube alloys, two parameters whose effect on the observed unexpected growth is unclear. Irradiation induced macroscopic component deformation at high fluences is reported to be governed by a process of enhanced material growth ("breakaway growth"), which is associated by many authors with the formation of c-component vacancy-type dislocation loops. Therefore, the main focus during the conducted microstructural studies was on the formation and characteristics of those <c>-loops.

The unique feature of this work as compared to many other studies in the field is the highly successful application of out-of-pile experimental methods for the investigation of in-pile phenomena, and specifically for phenomena directly originating from the in-pile neutrons. That LWR typical irradiation damage can be produced out-of-pile, and particularly in modern Zr-based alloys currently being used for PWR assemblies, is despite previous reports in the literature far from self-evident.
The out-of-pile method this work is based on is heavy ion irradiation, in the majority of the experiments coupled with in-situ transmission electron microscopy. The huge advantages of heavy ion irradiation as compared to in-pile neutron irradiation are the vastly reduced irradiation times in the range of several hours, the absence of target activation, the easy experimental accessibility which allows to control and measure the experimental parameters with accuracy, and the capability to isolate single parameters. The unique asset of in-situ TEM is the possibility to observe defined material regions from their unirradiated state up to highest damage levels, to study the microstructural processes dynamically and to document the microstructural developments as a function of the damage level in the form of movies.
For additional studies of the properties of the overall irradiation induced vacancy-type defect density, positron Doppler broadening spectroscopy was used, as a post-irradiation examination method complementary to TEM.
In a first set of experiments after the optimization of the sample preparation techniques and the experimental parameters, a feasibility study was conducted to show that heavy ion irradiation in

combination with in-situ TEM is suitable for the simulation of in-pile irradiation damage. The criteria to decide upon the comparability of heavy ion and LWR neutron damage were set to be all main microstructural characteristics reported for LWR neutron damage in Zr-based alloys:
1) <a>-loop characteristics: <a>-loop formation from the beginning of the irradiation; increase of the <a>-loop density with the damage level; <a>-loop size
2) <c>-loop characteristics: <c>-loop producibility with ion irradiation; formation after a threshold damage level only; correspondence of that threshold level to the LWR neutron fluence range for the onset of breakaway growth; increase of the <c>-loop density with the damage level; <c>-loop size
3) Further microstructural characteristics: absence of void formation; preferential nucleation of <c>-loops in the vicinity of intermetallic precipitates in Zry-4
The in-situ irradiation experiments carried out with both guide tube alloys M5® and Zry-4 fulfilled all the criteria described above. It was therefore concluded that heavy ion irradiation under the chosen experimental conditions is a most suitable tool for the simulation of LWR neutron damage in Zr-based alloys, which is the first main result of this work.

The second main result is the confirmation of the generally assumed correlation between <c>-loop formation and breakaway growth, as the observed formation threshold damage level for <c>-loops lies in the same damage level range as the reported onset of macroscopic breakaway growth. Also, it was shown that <c>-loop formation occurs independently of in-pile parameters that might lead to breakaway growth without the <c>-loops' involvement; this allows the conclusion that breakaway growth as a trigger for <c>-loop formation can be excluded, and confirms the assumption of <c>-loops being the trigger for breakaway growth. The third important result is the observation that the <c>-loop linear density increases linearly with the damage level, and the determination of the slope (which agrees within the measurement accuracy for M5® and Zry-4). This <c>-loop density increase rate has been measured for the first time. In addition, the overall <c>-loop appearance during the experiments led to the hypothesis that <c>-loops are not, as generally assumed, single large loops, but chains of small aligned <c>-component dislocation loops.
Studies with both in-situ DBS and in-situ TEM showed, as expected from the literature, a large effect of the target temperature on the irradiation induced microstructure. Defect annealing measurements led to the conclusion that, while the majority of the vacancy-type defects is annealed for temperatures higher than 450°C, the <c>-loops are stable up to 500°C and therefore constitute only a small fraction of the overall vacancy-type defects. In addition, an annealing experiment at 750°C allowed to observe several different c-component dislocation annealing mechanisms dynamically.
The effect of hydrogen in Zry-4 under irradiation was studied by in-situ TEM in samples with different hydrogen contents. The experimental results showed an increase of the <c>-loop linear densities as compared to the standard material for an addition of a lower hydrogen content, and a decrease of the <c>-loop linear densities for a higher hydrogen content. This discontinuous nature of the hydrogen effect is surprising and is assumed to be due to one of two possible explanations: First, there might be another currently unknown experimental parameter with a strong influence on the <c>-loop characteristics, which is superimposed on the hydrogen effect and covers any effect the hydrogen might have partly or completely. Secondly, it seems possible that a lower hydrogen content and the related hydride concentration might have an effect on the sink bias in the Zr-matrix which would lead to an increase of <c>-loop formation as compared to the standard material, while higher hydrogen contents with the related higher hydride densities might cause a decrease in <c>-loop formation. The fourth main result of this thesis is therefore

the recommendation to investigate the hydrogen effect in more detail and with a higher number of studies, since the database provided by the herein described experiments is not sufficient to provide a clear correlation between the material's hydrogen content and macroscopic component growth.
External tensile stress, on the other hand, showed a very significant and direct correlation with the irradiation induced <c>-loop structure. In a Zry-4 sample under irradiation to a high dose at yield strength level, the <c>-loop linear density decreased continuously with an increase of the component of the tensile stress parallel to the c-axis, and the stress applied parallel to the c-axis suppressed the <c>-loop formation entirely. Such a dependence of the <c>-loop structure on the tensile stress direction can be explained in a straightforward way, but has been verified experimentally for the first time. The effect is surprising in both its clarity and its magnitude. In addition, the observation of the <c>-loop density following bending contour like "flow lines" in one of the grains suggests the assumption that <c>-loop densities are not only dependent on variations of the stress level between different grains, but also within single grains.
While the applied stress in the range of the yield strength is clearly higher than in-pile component stress levels during operation, is seems a valid conclusion that the observed effect should also occur for lower stress levels, with a respectively lower magnitude. The fifth major result of this thesis is thus the following: Tensile stress has a most significant effect on <c>-loop formation in Zr-based alloys, and the effect is highly dependent on the orientation of the stress direction towards the grains' orientation. Based on this result, the known typical guide tube textures and the elastic properties of α-Zr, it can be deduced that, in theory, an increase of the hold-down spring forces should lead to a reduction of <c>-loop formation in the majority of the grains, which could in turn lower the guide tubes' axial growth. Any such measures would, however, have to be taken in compliance with the known effect of stronger hold-down forces on creep and the resulting increase in fuel assembly bow.

The presented results showed that the experimental techniques applied in this work can contribute valuable information about the microstructural characteristics of irradiation induced damage in Zr-based alloys. It is therefore recommended to continue these studies in several different facets.
First of all, it should be mentioned that the promising positron experiments should be carried on, preferably by using positron annihilation lifetime spectroscopy.
Then, it has to be emphasized that the successful optimization of the experimental parameters of the in-situ TEM method, the feasibility studies and especially the clear results on the effect of external stress strongly suggest further use of this excellent tool for the investigation of LWR neutron damage in Zr-based alloys. The two major issues to be addressed in direct succession to this work are the following:
Firstly, more detailed studies of the influence of hydrogen should be conducted, to resolve the question of the observed discontinuous component of the effect. Secondly, the highly successful in-situ experiment under tensile stress should be continued, with the focus on two different areas: On the one hand, the experimental technique should be refined to allow for the reliable application and measurement of lower stress levels, which are closer to the actual operating conditions of the components. On the other hand, since the nature of the orientation dependent stress effect is now known from the previous experiments, a set of studies should be carried out to investigate the correlation of the stress effect with other material parameters. Since neutron irradiation under in-pile conditions occurs under a combination of a high number of interacting parameters, the investigation of the interaction of these parameters would contribute to a more detailed understanding of the in-pile irradiation behavior of Zr-based alloys.

Acknowledgements

This work was funded by Corporate Research and Development budget of AREVA NP GmbH (Erlangen, Germany).

The IVEM Tandem Facility within the Argonne National Laboratory's Electron Microscopy Center, which was used for a large part of the experiments described in this thesis, is supported by the US DOE Office of Science and operated under contract No. DE-AC02-06CH11357 by UChicago Argonne, LLC.

My thesis would not have been possible without the exceptional help and support of my supervisors, colleagues, collaboration partners, friends and family:

- **My Doktorvater, Prof. Dr. Winfried Petry** (Technische Universität München and FRM II, Garching)
  You were my mentor already during my years at university, and it is an honor that you agreed to supervise my doctoral thesis. Thank you so much for supporting me to do my thesis in cooperation with industry, for giving me the freedom to pursue even unexpected paths in my experimental work and for being open for the part-time PhD/AREVA employee agreement during the last two years. The inspiring discussions and your scientific advice were of highest value for me.

- **Dr. Petra Britt Hoffmann** (AREVA NP GmbH, Erlangen)
  Even if inofficially, I would like to call you my "Doktormutter"; thank you very much for accepting me as doctoral candidate, and for supervising my thesis from AREVA's side. You made me feel welcome in your department from my first day, and supported me ever since. Your free sharing of industrial background knowledge and your scientific and strategic advice were of highest importance for me. I also want to thank you especially for providing the support for my research trips abroad, which led to the successful experiments at ANL. Finally, thank you for offering my staff position in your department, and for allowing the flexible time management to finish my thesis while simultaneously being your employee.

- **Marquis A. Kirk, PhD** (Argonne National Laboratory, Lemont, USA)
  During one of our beamtimes, Pete said to me: "I don't know how you've been running with luck so far in your life, but meeting Mark was definitely one of your best moments." Mark, I couldn't agree more. You've been the key to my successful experimental work, by accepting my beamtime proposal in the first place, even though I came with minimal TEM and irradiation damage experience; by teaching me how to really use a TEM, and by engaging into all those scientific and technical discussions. If I think of how I would

imagine the ideal researcher to be, it would be you: open-minded, ready and happy to try any new idea, openly sharing your knowledge, supporting and encouraging new people in your field, and most of all, being so enthusiastic and inspiring about you research. You have become a mentor, a role model and a dear friend to me, and I am so thankful we have met. I hope to be back at Argonne for continuative experiments, it would be wonderful to have the opportunity to learn even more from you.

- **Prof. Dr. Erdmann Spiecker** (Arbeitsgruppe Elektronenmikroskopie, FAU Erlangen-Nürnberg)
  Your scientific and technical advice on the TEM sample preparation and TEM imaging, and the possibility for the preparation tests in your labortory and the access to your CM30 were very valuable for my work. I also want to thank you for agreeing to act as referee and examiner for my thesis.

- **PD Dr. Christoph Hugenschmidt and Dr. Philip Pikart** (FRM II, Garching)
  I want to thank you very much for allowing and supporting my work at NEPOMUC, for your help with the experiments and their interpretation and for all those scientific discussions. Philip, thank you especially for spending that time on the weekends and during the night in the experimental hall, just for another measurement we were not even sure we could use, and for the repeated analyses of our data.

- **Dr. Karl Ertl and Joachim Dorner** (Max-Planck-Institut für Plasmaphysik, Garching)
  Thank you for the repeated access to your accelerator, for your support during the beamtimes and your scientific and technical advice.

- **Dr. Volker Lansmann** (AREVA NP GmbH, Erlangen)
  Thank you for offering me the opportunity to start my thesis in your department, and for the scientific and strategic support.

- **Dr. Volker Schoß** (AREVA NP GmbH, Erlangen)
  Thank you for the helpful scientific and technical discussions, for your support and especially for giving me the flexibility in my working hours to combine my regular work and my thesis.

- The scientists, engineers, colleagues and mentors who supported me during my experimental work and helped me with their advice:
  My colleagues Willi Braun, Christine Bretting, Peter Dewes, Jens Diecke, Christoph Gebhardt, Dr. Wolfgang Goll, Karl Gösswein, Josef Heilmann, Angela Hergenhan, Harald Kalup, Günter Klose, Dieter Kreuter, Gerd Maussner, Andreas Möckel, Wolfgang Pflaum, Alexey Rempel, Frank Salzhuber, Dr. Wolfgang Schmid, Markus Schriefer, Dr. Hans-Jürgen Sell, Rainer Schumann, Angela Schwarzenbach, Dr. Elmar Schweitzer, Siegrun Trapp-Pritsching, Juliane Vidal, Dr. Nico Vollmer, Elisabeth Witt, Dieter Ziegler (AREVA NP GmbH, Erlangen); **My colleagues Dr. Jean-Paul Mardon and Dr. Jean-Marc Cloué** (AREVA SAS, France);
  Dr. Ron Adamson (Zircology Plus, USA); **Peter Baldo** (Argonne National Laboratory, USA); **Dr. Ludwig Beck, Walter Carli and the MLL operators group** (MLL, Garching); **Ass. Prof. Dr. Johannes Bernardi and Sabine Schwarz** (USTEM, TU Wien); **Dr. Harald Breitkreutz and Dr. Lea Canella** (FRM II, Garching);

Dr. Werner Egger (Universität der Bundeswehr München, Neubiberg); **Dr. Wilhelm Frey** (Robert Bosch GmbH, Reutlingen); **Benedikt Hecking** (E.ON Kernkraft GmbH, Hannover); **Dr. Mercedes Hernández-Mayoral** (CIEMAT, Spain); **Ass. Prof. Dr. Djamel Kaoumi** (University of South Carolina, USA); **Prof. Dr. Arthur T. Motta** (Penn State University, USA); **Dr. Saskia Mimietz-Oeckler** (Leica Microsysteme Vertrieb GmbH, Wetzlar); **Dr. Fabien Onimus and Léa Tournadre** (CEA, France); **Dr. Ralf Röhlsberger, Dr. Oliver Seeck, Dr. André Beerlink and Kathrin Pflaum** (DESY HASYLAB, Hamburg); **Dr. Julius Schneider** (Ludwigs-Maximilians-Universität, München); **Dr. Jörg Starke** (TIMCONCEPT GmbH, München); **Dr. Axel Stepken** (TÜV Süd AG, München); **Katrin Sulzbacher** (Siemens AG, München); **Prof. Dr. Gary Was** (University of Michigan, USA); **Dr. Thierry Wiss, Bert Cremer and Hartmut Thiele** (Institute for Transuranium Elements, Karlsruhe).

- **My friends**
  Some who have been with me nearly forever, and some whom I met just a short time ago. Thank you so much for your support and the time we spent together, and for still being in touch even after I've let contact run low for weeks and months; thank you for being there.

- **My Sensei, Werner Bachhuber**
  For 14 years of training, and for teaching me that giving up is never an option. Domo arigato gozai mashita.

- **My parents and sisters, Martha and Dr. Norbert Hengstler, Dr. Michaela Lurz and Julia Hengstler**
  You are my home; I could not have done it without you.

- **My husband, Dr. Peter Eger**
  Thank you for all our scientific discussions, for your support and advice during the last years which were of great help for my thesis. But much more important, sharing your life is the best that ever happened to me. This work is dedicated to you.

Appendix

A Abbreviations and Acronyms

This section provides lists of the abbreviations and acronyms used throughout this work.

Abbreviation	Meaning
ANL	**A**rgonne **N**ational **L**aboratory
ASTM	**A**merican **S**ociety for **T**esting and **M**aterials
bcc	**b**ody-**c**entered **c**ubic
BF	**B**right **F**ield
BS	**B**and **S**lope
BWR	**B**oiling **W**ater **R**eactor
CANDU	**Can**adian **D**euterium **U**ranium Reactor
CCD	**C**harge-**C**oupled **D**evice
DAD	**D**iffusional **A**nisotropy **D**ifference
DBS	**D**oppler **B**roadening **S**pectroscopy
DF	**D**ark **F**ield
DP	**D**iffraction **P**attern
dpa	**d**isplacements **p**er **a**tom
E110	Zr-1Nb
E635	Zr-1Nb-1.2Sn-0.35Fe
EBSD	**E**lectron **B**ackscatter **D**iffraction
EID	**E**lastic **I**nteraction **D**ifference
FA	**F**uel **A**ssembly
FBR	**F**ast **B**reeder **R**eactor
FIB	**F**ocussed **I**on **B**eam
FR	**F**uel **R**od
GGR	**G**as-Cooled **G**raphite-Moderated **R**eactor
hcp	**h**exagonal **c**lose-**p**acked
HP	**H**igh **P**ressure
IAEA	**I**nternational **A**tomic **E**nergy **A**gency
IPP	Max-Planck-**I**nstitut für **P**lasma**p**hysik
ITU	**I**nstitute for **T**ransuranium **E**lements
IVEM	**I**ntermediate **V**oltage **E**lectron **M**icroscope
LWGR	**L**ight-Water Cooled **G**raphite-Moderated **R**eactor
LWR	**L**ight-**W**ater Moderated and Cooled **R**eactor

continued on next page

Table 1: List of Abbreviations

Table 1 – continued from previous page

Abbreviation	Meaning
MLL	**M**aier-**L**eibnitz **L**aboratorium
MOX	**M**ixed **Ox**ide
NEPOMUC	**Ne**utron Induced **Po**sitron Source **Mu**nic**h**
NFIR	**N**uclear **F**uel **I**ndustry **R**esearch
PALS	**P**ositron **A**nnihilation **L**ifetime **S**pectroscopy
PHWR	**P**ressurized **H**eavy-**W**ater Moderated and Cooled **R**eactor
PIPS	**P**recision **I**on **P**olishing **S**ystem
PKA	**P**rimary **K**nock-on **A**tom
PWR	**P**ressurized **W**ater **R**eactor
RPV	**R**eactor **P**ressure **V**essel
SAD	**S**elected **A**rea **D**iffraction
SEM	**S**canning **E**lectron **M**icroscope
SIPA	**S**tress-**I**nduced **P**referential **A**bsorption
SIPN	**S**tress-**I**nduced **P**referential **N**ucleation
SPP	**S**econd **P**hase **P**article
SRIM	**S**topping and **R**ange of **I**ons in **M**atter
TEM	**T**ransmission **E**lectron **M**icroscope / **M**icroscopy
TREX	**T**ube **R**educed **Ex**trusion
USTEM	**U**niversitäre **S**erviceeinrichtung für **T**ransmissions**e**lektronen**m**ikroskopie
Zry	**Zr**calo**y**

Table 1: List of Abbreviations

Acronym	Meaning
A	nucleon number
A	beam spot area
a_0	Bohr radius
b	scattering parameter
$\vec{B}$	Burgers vector
β	v/c
c	speed of light in vacuum
C	ion charge state
d	TEM sample thickness / Bragg peak thickness
D	damage level
e	elementary charge
E	energy
$\mathsf{E}_{\mathsf{ion}}$	ion energy
E_{R}	Rydberg constant
ϵ_0	electric field constant

continued on next page

Table 2: List of Acronyms

Table 2 – continued from previous page

Acronym	Meaning
f	fraction of total recoil number produced in the damage peak region
F	ion fluence
F	amplitude of the Bragg reflex
$\mathsf{F_S}$	structure factor
φ	neutron flux
Φ	neutron fluence
ϕ	ion flux
$\vec{g}$	diffraction vector
I	mean excitation energy
I	ion beam current
k	multiplication factor
$\mathsf{L_{lin}}$	linear loop density
$\dot{\mathsf{L}}_{\mathsf{lin}}$	linear loop density increase rate
λ	neutron mean free path
λ	electron beam wavelength
m	mass
$\mathsf{M_{mol}}$	molar mass
n	number of neutrons per unit volume
n	number of electrons per unit volume
ν	number of neutrons produced per fission reaction
N	number of atoms per unit volume
N_0	initial number of target atoms per unit volume
$\mathsf{N_A}$	Avogadro's constant
$\dot{\mathsf{N}}_{\mathsf{d}}$	atom diplacement rate
$\mathsf{N_d}$	total number of displaced atoms per unit volume
$\mathsf{N_d^{1ion}}$	average number of displacements produced by 1 incident ion
P	positron probability distribution
R	total number of reactions
$\dot{\mathsf{R}}$	reaction rate
ρ	mass density
S	stopping power
$\vec{s}$	excitation error
σ	(microscopic) neutron reaction cross section
σ_D	damage cross section
Σ	macroscopic neutron absorption cross section
$\mathsf{\Sigma_f}$	macroscopic fission cross section
$\mathsf{\Sigma_{total}}$	total macroscopic neutron reaction cross section
$\mathsf{\Sigma_{transformation}}$	macroscopic nuclear reaction cross section, without (n,γ)
t	time
$\bar{t}$	average time between two neutron generations

continued on next page

Table 2: List of Acronyms

Table 2 – continued from previous page

Acronym	**Meaning**
T	transferred energy
θ	scattering angle
θ	Bragg angle
$\mathsf{U}_{\mathsf{acc}}$	accelerating voltage
v	neutron velocity
V	volume
x	distance
Z	atomic number

Table 2: List of Acronyms

B Zirconium Phase Diagrams

Fig. 1 shows the binary phase diagrams for Sn-Zr and for Zr-Nb.

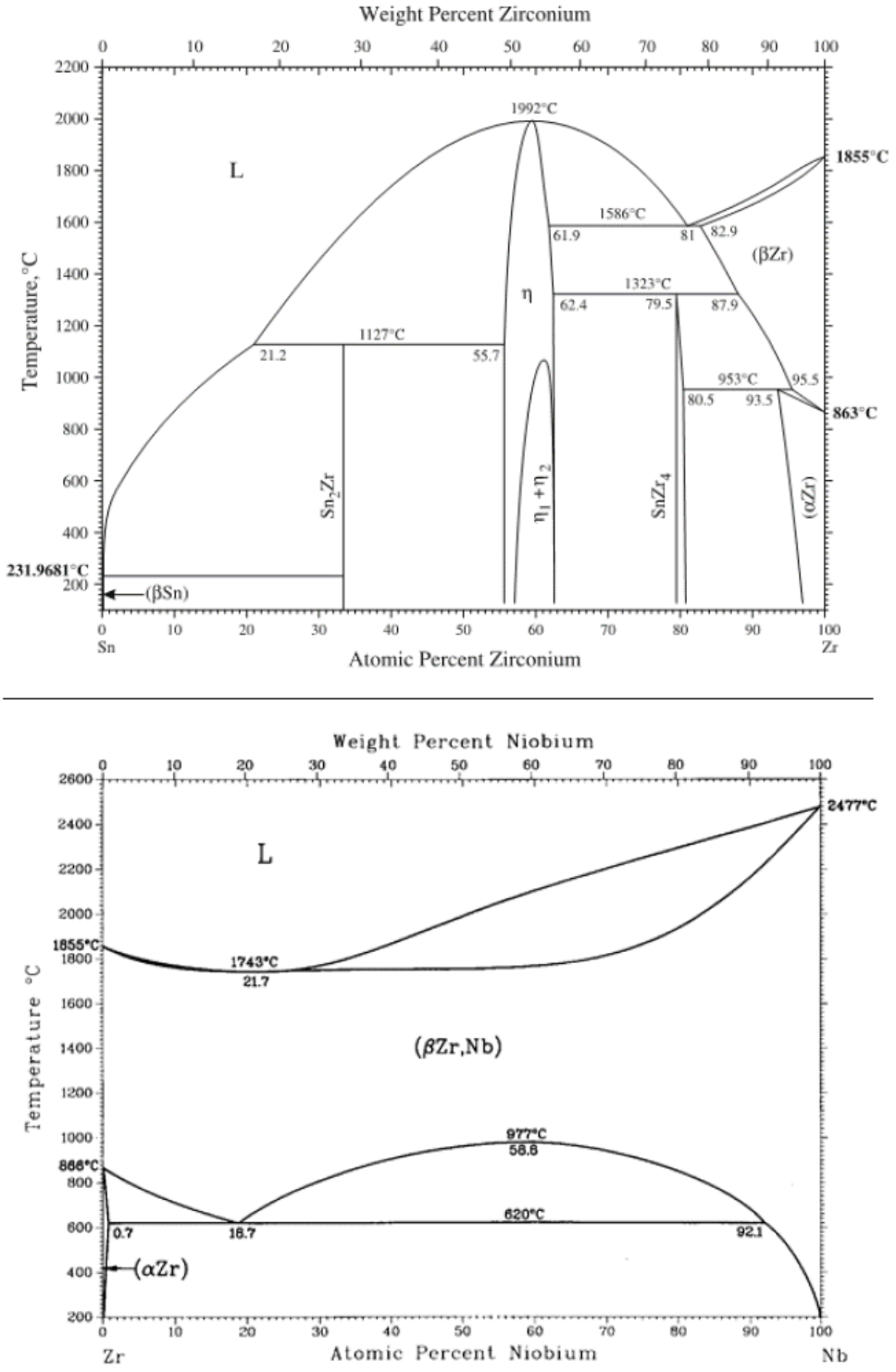

Figure 1: Binary phase diagrams of Sn-Zr [109] and Zr-Nb [78]

C Foil Thickness Determination by the Grain Boundary Method

For the calculation fo the dislocation loop linear densities, the thickness of the observed grains in the TEM had to be determined. This was done by imaging a grain boundary lying parallel to the main tilt axis of the sample holder at different tilting angles and measuring the observable thickness of the boundary. Fig. 2 gives a schematic of a TEM sample with a tilted grain boundary at different tilting angles.

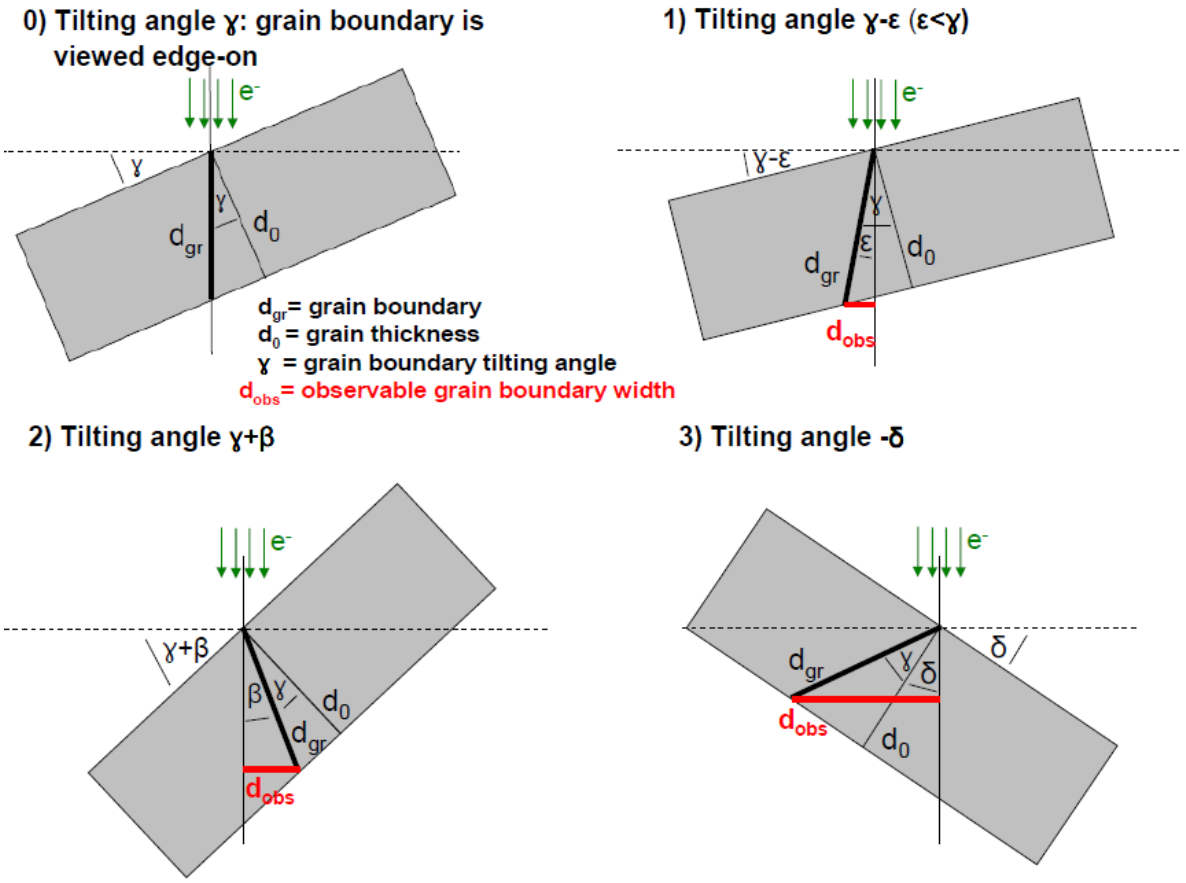

Figure 2: Schematic for the grain thickness calculation

In the first step, the sample is tilted to the angle where the grain boundary is viewed edge-on. That tilting angle, γ, corresponds to the tilting angle of the grain boundary to the sample normal. The relation between the grain thickness d_0 and the grain boundary length d_{gr} is given as

$$d_{gr} = \frac{d_0}{\cos(\gamma)}.$$

The sample can then be tilted in two directions, and with the tilting angle smaller or larger than γ. For the three cases demonstrated in Fig. 2, the trigonometric relations for the grain thickness are the following:

1) Tilting angle γ-ϵ:

$$\mathsf{d_{obs}} = \mathsf{d_{gr}} \cdot \sin(\epsilon) \Rightarrow \mathsf{d_0} = \mathsf{d_{obs}} \frac{\cos(\gamma)}{\sin(\epsilon)}$$

2) Tilting angle γ+β:

$$\mathsf{d_{obs}} = \mathsf{d_{gr}} \cdot \sin(\beta) \Rightarrow \mathsf{d_0} = \mathsf{d_{obs}} \frac{\cos(\gamma)}{\sin(\beta)}$$

3) Tilting angle -δ:

$$\mathsf{d_{obs}} = \mathsf{d_{gr}} \cdot \sin(\gamma + \delta) \Rightarrow \mathsf{d_0} = \mathsf{d_{obs}} \frac{\cos(\gamma)}{\sin(\gamma + \delta)}$$

Fig. 3 shows exemplary TEM images for the calculation of the thickness of one of the Zry-4 samples. The grain boundary was edge-on at γ=+1.4°; the observed boundary thicknesses therefore corresponded to the cases 2 (positive tilting angles) and 3 (negative tilting angles).

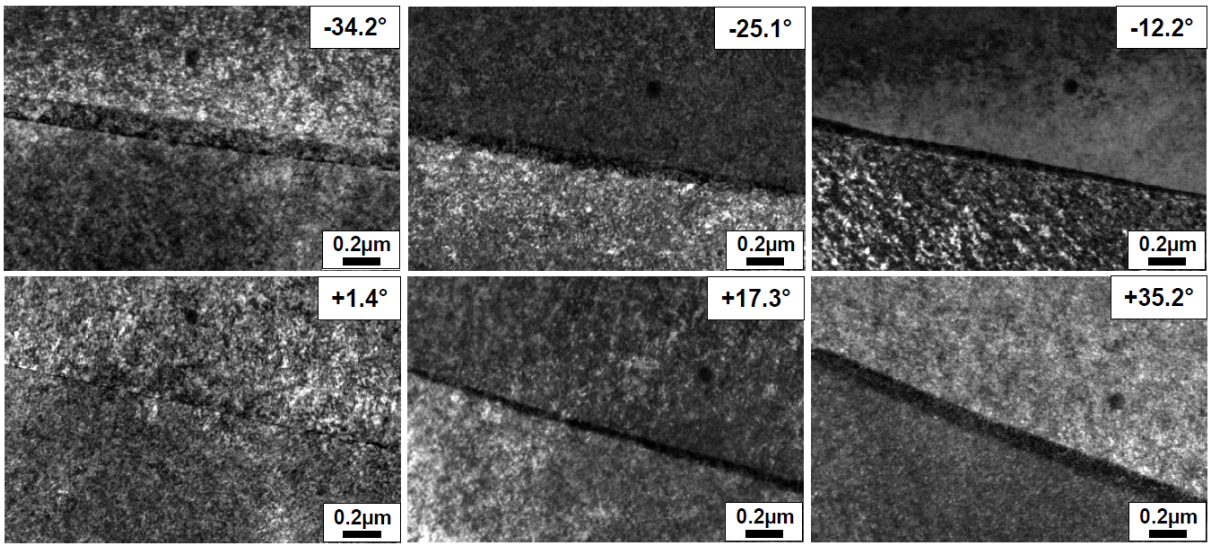

Figure 3: TEM imaging of a grain boundary for grain thickness determination

D List of Publications

In the course of the thesis, parts of the work were published in printed form as well as poster and oral presentations:

- **R.M. Hengstler**: "Fuel Development for Nuclear Research and Power Reactors". Oral presentation at the *Neutrons in Science and Industry* seminar at Technische Universität München. Garching, June 2009
- **R.M. Hengstler**: "Irradiation induced creep and growth of zirconium-based alloys for PWR guide tubes". *Physik Department E13, Annual Report.* 2009
- **R.M. Hengstler-Eger**: "Irradiation induced creep and growth of zirconium-based alloys for PWR guide tubes". *Physik Department E13, Annual Report.* 2010
- **R.M. Hengstler-Eger**: "Heavy ion irradiation for LWR neutron damage simulation in Zr-based alloys". Oral presentation at the *Wall Forum* of the Max-Planck-Institut für Plasmaphysik. Garching, July 2011.
- **R.M. Hengstler-Eger**, P.B. Hoffmann, P. Baldo, M.A. Kirk, J. Dorner, K. Ertl, C. Hugenschmidt, W. Petry and P. Pikart: "Heavy Ion Irradiation Induced Dislocation Loops in AREVA's M5®Alloy". Poster presentation at the *Workshop on Ion Implantation as a Neutron Irradiation Analogue.* Oxford, 26-28 Sept. 2011
- **R.M. Hengstler-Eger**, P. Baldo, L. Beck, J. Dorner, K. Ertl, P.B. Hoffmann, C. Hugenschmidt, M.A. Kirk, W. Petry, P. Pikart and A. Rempel: "Heavy ion irradiation induced dislocation loops in AREVA's M5®alloy". *Journal of Nuclear Materials 423, pp. 170-182.* Feb. 2012
- **R.M. Hengstler-Eger**, W. Petry, P. Baldo, M.A. Kirk and P.B. Hoffmann: "Ion Irradiation Studies of the Microstructural Origins of PWR Guide Tube Deformation". Poster at the *Department of Energy Review of the Argonne National Laboratory's Electron Microscopy Center.* Lemont, 18-19 July 2012
- **R.M. Hengstler-Eger**, P.B. Hoffmann, W. Petry, M.A. Kirk and P. Baldo: "The Effect of External Stress on Irradiation Induced c-Loop Formation in Zircaloy-4". Oral presentation at the *Nuclear Materials Conference 2012.* Osaka, 22-25 Oct. 2012.

Bibliography

[1] E. Fermi, E. Amaldi, O. D'Agostino, F. Rasetti, and E. Segre. Artificial Radioactivity Produced by Neutron Bombardment. *Proceedings of the Royal Society A*, 146:483–500, 1934.

[2] L. Meitner, O. Hahn, and F. Strassmann. Über die Umwandlungsreihen des Urans, die durch Neutronenbestrahlung erzeugt werden. *Zeitschrift für Physik A Hadrons and Nuclei*, 106:249–270, 1937.

[3] O. Hahn and F. Strassmann. Über die Entstehung von Radiumisotopen aus Uran durch Bestrahlen mit schnellen und verlangsamten Neutronen. *Naturwissenschaften*, 26:755–756, 1938.

[4] L. Meitner and O.R. Frisch. Disintegration of Uranium by Neutrons: A New Type of Nuclear Reaction. *Nature*, 143:239–240, Feb. 1939.

[5] U.S. Department of Energy. The First Reactor. *DOE/NE-0046*, Dec. 1982.

[6] European Nuclear Society. Nuclear Power Plants, World-wide. *ENS website: http://www.euronuclear.org/1-information/map-worldwide.html*, April 2012.

[7] Eisenhower Presidential Library & Museum Web Site Information. Official Program by General Dynamics Corp., for the Launching of the U.S.S. Nautilus, January 21, 1954 . *Arthur L. Minnich Papers, Box 16, General Dynamics Corporation; http://eisenhower.archives.gov/Research/Digital_Documents/Nautilus/Nautilusdocuments.html*, May 6, 2011.

[8] European Nuclear Society (ENS). Nuclear Power Plants, World-Wide. *ENS website: http://www.euronuclear.org/1-information/npp-ww.htm*, July 2012.

[9] European Nuclear Society (ENS). ENS website of the Research Reactor Fuel Management Conference. *http://www.euronuclear.org/1-networking/rrfm.htm*, July 2012.

[10] G.S. Was. Fundamentals of Radiation Materials Science. Metals and Alloys. *Springer-Verlag Berlin Heidelberg*, 2007.

[11] V. Fidleris. The Irradiation Creep and Growth Phenomena. *Journal of Nuclear Materials*, 159:22–42, 1988.

[12] R.A. Holt and R.W. Gilbert. c-Component Dislocations in Annealed Zircaloy Irradiated at about 570K. *Journal of Nuclear Materials*, 137:185–189, 1986.

[13] S.J. King, R.L. Kesterson, K.H. Yueh, R.J. Comstock, W.M. Herwig, and S.D. Ferguson. Impact of Hydrogen on Dimensional Stability of ZIRLO Fuel Assemblies. *Zirconium in the Nuclear Industry: Thirteenth International Symposium*, ASTM STP 1423, 2002.

[14] G.M. Hood. Point Defect Diffusion in α-Zr. *Journal of Nuclear Materials*, 159:149–175, 1988.

[15] W.M. Stacey. Nuclear Reactor Physics. *WILEY-VCH Verlag GmbH&Co. KGaA, Weinheim*, 2nd Edition, completely revised and enlarged, 2007.

[16] K. Schreckenbach. Einführung in die Reaktorphysik. *Vorlesungsskript, Technische Universität München*, 2007.

[17] J. Magill, G. Pfennig, and J. Galy. Karlsruher Nuklidkarte, 7th edition. 2006.

[18] Ide creation Play Bac and AREVA. A Nuclear Power Plant. *Ide creation Play Bac, Editions Speciales*, 2011.

[19] E.ON Kernkraft. Kernkraftwerk Isar, Hintergrundinformationen. *website: http://www.eon-kernkraft.com/pages/ekk_de/Standorte/Isar/index.htm*, Nov. 2011.

[20] G. Oestberg. Determination of Hydride Solubility in Alpha Phase Zirconium, Zircaloy-2 and Zircaloy-4. *Journal of Nuclear Materials*, 5:208–215, 1962.

[21] P. Haasen. Physikalische Metallkunde, 3. Auflage. *Springer-Verlag Berlin Heidelberg*, 1994.

[22] M. Le Saux, J. Besson, S. Carassou, C. Poussard, and X. Averty. Behavior and Failure of Uniformly Hydrided Zircaloy-4 Fuel Claddings between 25°C and 480°C under Various Stress States, including RIA Loading Conditions. *Engineering Failure Analysis*, 17:683–700, 2010.

[23] G.P. Sabol. Precipitation Behavior in Zr/2.5wt.-% Nb Alloys. *Journal of Nuclear Materials*, 34:142–150, 1970.

[24] Y.H. Jeong, H.G. Kim, and T.H. Kim. Effect of β-Phase, Precipitate and Nb-Concentration in Matrix on Corrosion and Oxide Characteristics of Zr-xNb Alloys. *Journal of Nuclear Materials*, 317:1–12, 2003.

[25] V. Shishov. The Evolution of Microstructure and Deformation Stability in Zr-Nb-Fe(Sn,O) Alloys under Neutron Irradiation. *Zirconium in the Nuclear Industry: 16th International Symposium, Chengdu, Sichuan, China*, ASTM STP 1529, 2010.

[26] P. Bossis, B. Verhaeghe, S. Doriot, D. Gilbon, V. Chabretou, A. Dalmais, J.P. Mardon, M. Blat, and A. Miquet. In PWR Comprehensive Study of High Burn-up Corrosion and Growth Behavior of M5 and Recrystallized Low-Tin Zircaloy-4. *Zirconium in the Nuclear Industry: 15th International Symposium*, ASTM STP 1505, 2007.

[27] J.P. Mardon, D. Charquet, and J. Senevat. Influence of Composition and Fabrication Process on Out-of-Pile and In-Pile Properties of M5 Alloy. *Zr in the Nuclear Industry: 12th International Symposium*, ASTM STP 1354, 2000.

[28] E. Gebhardt and H.-D. Seghezzi. Reaktorwerkstoffe Teil 1. Metallische Werkstoffe. *B. G. Teubner Verlagsgesellschaft, Stuttgart, Darmstadt*, 1964.

[29] K. Kopitzki and P. Herzog. Einführung in die Festkörperphysik. *B.G. Teubner Verlag/GWV Fachverlag GmbH, Wiesbaden*, 5. Auflage, 2004.

[30] R.B. Adamson, F. Garzarolli, and C. Patterson. In-Reactor Creep of Zirconium Alloys. *Advanced Nuclear Technology International: www.antinternational.com*, 2009.

[31] G.J.C. Carpenter, R.H. Zee, and A. Rogerson. Irradiation Growth of Zirconium Single Crystals: a Review. *Journal of Nuclear Materials*, 159:86–100, 1988.

[32] D.O. Northwood, R.W. Gilbert, L.E. Bahen, P.M. Kelly, R.G. Blake, P.K. Madden, D. Faulkner, W. Bell, and R.B. Adamson. Characterization of Neutron Irradiation Damage in Zirconium Alloys - an International "Round-Robin" Experiment. *Journal of Nuclear Materials*, 79:379–394, 1979.

[33] A. Jostsons, P.M. Kelly, and R.G. Blake. The Nature of Dislocation Loops in Neutron Irradiated Zirconium. *Journal of Nuclear Materials*, 66:236–256, 1977.

[34] A. Jostsons, R.G. Blake, J.G. Napier, P.M. Kelly, and K. Farrell. Faulted Loops in Neutron-Irradiated Zirconium. *Journal of Nuclear Materials*, 68:267–276, 1977.

[35] J. Ribis, F. Onimus, L. Béchade, S. Doriot, C. Cappelaere, C. Lemaignan, A. Barbu, and O. Rabouille. Experimental and Modeling Approach of Irradiation Defects Recovery in Zirconium Alloys: Impact of an Applied Stress. *Journal of ASTM International*, 5, Issue 3, 2008.

[36] F. Onimus and J.L. Béchade. Radiation Effects in Zirconium Alloys. *Comprehensive Nuclear Materials*, 4:1–31, 2012.

[37] W. Frank. Intrinsic Point Defects in Hexagonal Close-Packed Metals. *Journal of Nuclear Materials*, 159:122–148, 1988.

[38] D.J. Bacon. Point Defects and Clusters in the hcp Metals: their Role in Dose Transition. *Journal of Nuclear Materials*, 206:249–265, 1993.

[39] C.H. Woo and X. Liu. Generation of c-Component Edge Dislocations in α-Zirconium during Neutron Irradiation-An Atomistic Study. *Journal of Nuclear Materials*, 393:513–517, 2009.

[40] C.H. Woo. Defect Accumulation Behaviour in hcp Metals and Alloys. *Journal of Nuclear Materials*, 276:90–103, 2000.

[41] C.H. Woo. Theory of Irradiation Deformation in Non-Cubic Metals: Effects of Anisotropic Diffusion. *Journal of Nuclear Materials*, 159:237–256, 1988.

[42] O.T. Woo. c-Component Dislocations in Zirconium Alloys. *Journal of Nuclear Materials*, 87:70–80, 1979.

[43] G.J.C Carpenter, R.A. Murgatroyd, A. Rogerson, and J.F. Watters. Irradiation Growth of Zirconium Single Crystals. *Journal of Nuclear Materials*, 101:28–37, 1981.

[44] R.A. Holt, M. Griffiths, and R.W. Gilbert. c-Component Dislocations in Zr-2.5wt.%Nb Alloy. *Journal of Nuclear Materials*, 149:51–57, 1987.

[45] R.W. Gilbert, K. Farrell, and C.E. Coleman. Damage Structure in Zirconium Alloys Neutron Irradiated at 537 to 923 K. *Journal of Nuclear Materials*, 84:137–148, 1979.

[46] G.J. Field. Problems Caused by Irradiation Deformation in CANDU Reactors. *Journal of Nuclear Materials*, 159:3–11, 1988.

[47] D.G. Franklin and R.B Adamson. Implications of Zircaloy Creep and Growth to Light Water Reactor Performance. *Journal of Nuclear Materials*, 159:12–21, 1988.

[48] A. Rogerson. Irradiation Growth in Zirconium and its Alloys. *Journal of Nuclear Materials*, 159:43–61, 1988.

[49] M. Koike and T. Asada. Irradiation Creep and Growth of Pressure Tubes in HWR Fugen. *Journal of Nuclear Materials*, 159:62–74, 1988.

[50] R.G. Fleck, R.A. Holt, V. Perovic, and J. Tadros. Effects of Temperature and Neutron Fluence on Irradiation Growth of Zr-2.5 wt.-%Nb. *Journal of Nuclear Materials*, 159:75–85, 1988.

[51] R.A. Holt. Mechanisms of Irradiation Growth of Alpha-Zirconium Alloys. *Journal of Nuclear Materials*, 159:310–338, 1988.

[52] R. Dutton. General Discussion of Creep and Growth Mechanisms: their Theoretical and Practical Implications. *Journal of Nuclear Materials*, 159:339–347, 1988.

[53] R.A. Herring and D.O. Northwood. Microstructural Characterization of Neutron Irradiated and Post-Irradiation Annealed Zircaloy-2. *Journal of Nuclear Materials*, 159:386–396, 1988.

[54] R.B. Adamson. NFIR V; Dimensional Stability Project - Irradiation Growth in BOR 60. *Electric Power Research Institute; CPAG Working Group Summary, Charlotte (NC)*, April 2011.

[55] T. Mayer-Kuckuck. Kernphysik. Eine Einführung. *Teubner Verlag; B.G. Teubner GmbH, Stuttgart/Leipzig/Wiesbaden*, 2002.

[56] Korean Atomic Energy Research Institute. ENDFPLOT-2. *website: http://atom.kaeri.re.kr/endfplot.shtml*, Jan. 2012.

[57] M. W. Thompson. Defects and Radiation Damage in Metals. *Cambridge University Press*, 1969.

[58] G.M. Hood, R.J. Schultz, and J.A. Jackman. The Recovery of Single Crystal α-Zr from Low Temperature Electron Irradiation - a Positron Annihilation Spectroscopy Study. *Journal of Nuclear Materials*, 126:79–82, 1984.

[59] C. Abromeit. Aspects of Simulation of Neutron Damage by Ion Irradiation. *Journal of Nuclear Materials*, 216:78–96, 1994.

[60] C. Abromeit, V. Naundorf, and H. Wollenberger. Phase Stability Criteria for Ion and Neutron Irradiated Alloys. *Journal of Nuclear Materials*, 155-157:1147–1178, 1988.

[61] V.N. Shishov, M.M. Peregud, A.V. Nikulina, P.V. Shebaldov, A.V. Tselischev, A.E. Novoselov, G.P. Kobylyansky, Z.E. Ostrovsky, and V.K. Shamardin. Influence of Zirconium Alloy Chemical Composition on Microstructure Formation and Irradiation Induced Growth. *Zirconium in the Nuclear Industry: Thirteenth International Symposium*, ASTM STP 1423, 2002.

[62] P. Vizcaino, P.B. Bozzano, A.V. Flores, A.D. Banchik, R.A. Versaci, and R.O. Rios. Hydrogen Solubility and Microstructural Changes in Zircaloy-4 due to Neutron Irradiation. *16th International Symposium: Zirconium in the Nuclear Industry*, 2010.

[63] C.D. Cann, M.P. Puls, E.E. Sexton, and W.G. Hutchings. The Effect of Metallurgical Factors on Hydride Phases in Zirconium. *Journal of Nuclear Materials*, 126:197–205, 1984.

[64] A. McMinn, E.C. Darby, and J.S. Schofield. The Terminal Solid Solubility of Hydrogen in Zirconium Alloys. *Zirconium in the Nuclear Industry: Twelfth International Symposium*, ASTM STP 1354:173–195, 2000.

[65] A. Strasser, R.B. Adamson, and F. Garzarolli. IZNA8 Special Topic Report: The Effect of Hydrogen on Zirconium Alloy Properties. *A.N.T. International, Sweden*, 2008.

[66] A.E. Gorodetsky, A.P. Zakharov, V.M. Sharapov, and V.Kh. Alimov. Interaction of Hydrogen with Radiation Defects in Metals. *Journal of Nuclear Materials*, 93&94:588–593, 1980.

[67] J. E. Turner. Atoms, Radiation and Radiation Protection. *Wiley-VCH*, 2007.

[68] B.T. Kelly. Irradiation Damage in Solids. *United Kingdom Atomic Energy Authority Reactor Materials Laboratory, Cultech*, 1966.

[69] J.F. Ziegler. SRIM-The Stopping and Range of Ions in Matter. *website: www.srim.org*, 2012.

[70] V.N. Shishov, M.M. Peregud, A.V. Nikulina, Yu.V. Pimenov, G.P. Kobylyansky, A.E. Novoselov, Z.E. Ostrovsky, and A.V. Obukhov. Influence of Structure-Phase State of Nb Containing Zr Alloys on Irradiation Induced Growth. *Journal of ASTM International*, 2 (8):666–685, 2005.

[71] S. Zinkle. Roles of Ion Irradiation in Materials Research. *Ion Implantation as a Neutron Irradiation Analogue, Workshop at Oxford University*, Sept. 26-28, 2011.

[72] A.T. Motta, F. Lefebvre, and C. Lemaignan. Amorphization of Precipitates in Zircaloy under Neutron and Charged-Particle Irradiation. *Zirconium in the Nuclear Industry: Ninth International Symposium*, ASTM STP 1132:718–739, 1991.

[73] A. Ryanzanov. Using of Charged Particle Accelerators for Investigation of Physical Mechanisms. Radiation Resistance of Fission and Fusion Structural Materials. *IAEA Technical Meeting TM34567: Accelerator Simulation and Theoretical Modelling of Radiation Effect*, 2008.

[74] L. Tournadre, F. Onimus, J.-L. Béchade, D. Gilbon, J.-M. Cloué, J.-P. Mardon, X. Feaugas, O. Toader, and C. Bachelet. Experimental Study of c-Component Loops Nucleation and Growth under Charged Particles Irradiation in Recrystallized Zry-4. *TMS Meeting 2011, San Diego*, Feb. 27-March 3, 2011.

[75] M. Terasawa, M. Shimada, M. Iimura, K. Suzuki, T. Yasuda, and K. Noro. Proton Irradiation Creep of Zirconium. *Journal of Nuclear Science and Technology, 21*, 2:149–151, 1984.

[76] O.J.V. Chapman, R.J. McElroy, and B.E. Sheldon. Irradiation Creep and Growth during Proton and Neutron Bombardment of Zircaloy-2 Plate. *Zirconium in the Nuclear Industry: Sixth International Symposium*, ASTM STP 824:343–375, 1984.

[77] R.M. Hengstler-Eger, P. Baldo, L. Beck, J. Dorner, K. Ertl, P.B. Hoffmann, C. Hugenschmidt, M.A. Kirk, W. Petry, P. Pikart, and A. Rempel. Heavy Ion Irradiation Induced Dislocation Loops in AREVA's M5®Alloy. *Journal of Nuclear Materials*, 423:170–182, 2012.

[78] H. Okamoto. Nb-Zr (Niobium-Zirconium). *Journal of Phase Equilibria*, 13, No. 5:577, 1992.

[79] R. Stoller. Displacement Calculations: Neutron Damage vs. Ion Near-surface Damage. *Workshop on Ion Implantation as a Neutron Irradiation Analogue, Oxford*, 2011.

[80] R.M. Hengstler. Thermal and Electric Conductivity of a Monolithic Uranium-Molybdenum Alloy for Research Reactor Fuels. *Diplomarbeit at the Technische Universität München*, 2008.

[81] W. Schmid. Forschungsneutronenquelle Heinz Maier-Leibnitz, private communication. 2008.

[82] W. Carli. Maier-Leibnitz Laboratorium, private communication. 2008.

[83] L. Beck. Maier-Leibnitz Laboratorium - Tandem Operation and Experiments. *Heavy Ion Accelerator Technology Conference, Venice*, 2009.

[84] A. Kolitsch. Sputter-Ionenquelle. *website: http://www.hzdr.de/db/Cms?pOid=11878&pNid=0*, 2012.

[85] D. Gerthsen and P.F. Schmidt. Praxis der Transmissionselektronenmikroskopie, Lehrgang TEM: Transmissionselektronenmikroskopie, Grundlagen und Anwendungen. *Lecture series at Karlsruher Institut für Technologie*, 2010.

[86] E. Fuchs, H. Oppolzer, and H. Rehme. Particle Beam Microanalysis: Fundamentals, Methods and Applications. *VCH Verlagsgesellschaft mbH, Weinheim*, 1990.

[87] Oxford Instruments. EBSD. *website: http://www.ebsd.com/*, 2012.

[88] D.B. Williams and C.B. Carter. Transmission Electron Microscopy. *Springer Science+Business Media, LLC*, 2009.

[89] W. Zhou and Z.L. Wang. Scanning Microscopy for Nanotechnology. Techniques and Applications. *Springer Science+Business Media, LLC*, 2007.

[90] C. Hugenschmidt, B. Löwe, J. Mayer, C. Piochacz, P. Pikart, R. Repper, M. Stadlbauer, and K. Schreckenbach. Unprecedented Intensity of a Low Energy Positron Beam. *Nuclear Instruments and Methods A*, 593 (3):616–618, 2008.

[91] Research Neutron Source Heinz Maier-Leibnitz (FRM II). NEPOMUC: Neutron Induced Positron Source Munich. *website: http://www.frm2.tum.de/wissenschaftliche-nutzung/kern-amp-teilchenphysik/nepomuc/index.html*, Jan. 2012.

[92] Research Neutron Source Heinz Maier-Leibnitz. FRM II: Die Neutronenquelle. *website: http://www.frm2.tum.de/technik/index.html*, Jan. 2012.

[93] M.J. Puska and R.M. Nieminen. Theory of Positrons in Solids and on Solid Surfaces. *Reviews of Modern Physics*, 66:841–897, 1994.

[94] P. Coleman. Some Experimental Aspects of Positron Beams. *International School on Positron Studies*, Kolkata, Jan. 2009.

[95] C. Hugenschmidt. Von der Oberfläche ins Volumen - Monoenergetische Positronen als Sonden im Festkörper. *Seminar talk at Technische Universität München*, 2008.

[96] M. Haaks. M_Spec2. *http://agmaier.hiskp.uni-bonn.de/en/material_science/software/-mspec_2.html*, 2011.

[97] M.L. Jenkins and M.A. Kirk. Characterization of Radiation Damage by Transmission Electron Microscopy. *Series in Microscopy in Materials Science*, Institute of Physics Publishing, Bristol, 2001.

[98] E. Spiecker. Elektronenmikroskopie I. *Lecture at Friedrich-Alexander-Universität Erlangen-Nürnberg*, 2008.

[99] P.B. Hirsch. Electron Microscopy of Thin Crystals. *Krieger Publishing Company*, 1977.

[100] D. Gilbon and C. Simonot. Effect of Irradiation on the Microstructure of Zry-4. *Zirconium in the Nuclear Industry: 10th International Symposium*, ASTM STP 1245, 1994.

[101] M. Griffiths and R.W. Gilbert. The Formation of c-Component Defects in Zirconium Alloys during Neutron Irradiation. *Journal of Nuclear Materials*, 150:169–181, 1987.

[102] E. Steinberg, I. Pohlmeyer, and A. Schaa. Annealing Parameter for Quality Control of Cladding and Structural Material. *Top Fuel Conference, Manchester*, June 1997.

[103] F. Garzarolli, P. Dewes, G. Maussner, and H.-H. Basso. Effects of High Neutron Fluences on Microstructure and Growth of Zircaloy-4. *Zirconium in the Nuclear Industry: Eighth International Symposium*, ASTM STP 1023:641–657, 1989.

[104] Elsevier. NuMat 2012: The Nuclear Materials Conference (Osaka, Japan). *http://www.nuclearmaterialsconference.com/*, 22 - 25 Oct. 2012.

[105] C. Kittel. Introduction to Solid State Physics, eighth edition. *John Wiley & Sons*, 2005.

[106] G. Leibfried and N. Breuer. Point Defects in Metals I; Introduction to the Theory. *Springer-Verlag Berlin/Heidelberg/New York*, 1978.

[107] G. Leibfried. Bestrahlungseffekte in Festkörpern. *B. G. Teubner Verlagsgesellschaft, Stuttgart*, 1965.

[108] H.R. Higgy and F.H. Hammad. Effect of Neutron Irradiation on the Tensile Properties of Zircaloy-2 and Zircaloy-4. *Journal of Nuclear Materials*, 44:215–227, 1972.

[109] H. Okamoto. Sn-Zr (Tin-Zirconium). *Journal of Phase Equilibria and Diffusion*, 31, No. 4:411–412, 2010.